

Neuroscience Bulletin

The Official Journal of The Chinese Neuroscience Society

神经科学通报

Volume 36

Number 2

February 2020

NRG1-ErbB4/GABA signaling



Sensorimotor cortical-striatal
deficits in schizophrenia

  Springer

www.neurosci.cn

About the Cover

The sensorimotor-striatal network might be a key systems-level marker of schizophrenia. Zhang *et al.*, by investigating both knockout of the type I receptor tyrosine kinase ErbB4 in parvalbumin interneurons in mice and first-episode, treatment-naïve patients with schizophrenia, found that disruption of specific molecular pathways in the cerebral cortex causes structural deficits in sensorimotor cortical-striatal circuits. The cover image indicates that anomalous neuregulin 1-ErbB4 signaling and GABA transmission may be an important molecular mechanism underlying the anatomical changes in the sensorimotor-striatal network in schizophrenia. The grid and starlights indicate NRG1-ErbB4/GABA signaling and sensorimotor-striatal deficits, respectively. See pages 97–109. (Cover image provided by Prof. Tao Li).



Volume 36 Number 2
February 2020

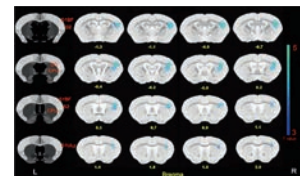
Original Articles

- 97 GABAergic Abnormalities Associated with Sensorimotor Cortico-striatal Community Structural Deficits in ErbB4 Knockout Mice and First-Episode Treatment-Naïve Patients with Schizophrenia**
Chengcheng Zhang · Peiyan Ni · Yikang Liu · Yang Tian · Jinxue Wei · Bo Xiang · Liansheng Zhao · Xiaojing Li · Xiaohong Ma · Wei Deng · Wanjun Guo · Rongjun Ni · Yamin Zhang · Qiang Wang · Hailiang Huang · Nanyin Zhang · Tao Li

- 110 MiR-125a-5p Regulates Vitamin D Receptor Expression in a Mouse Model of Experimental Autoimmune Encephalomyelitis**
Han-Chun Long · Rui Wu · Chun-Feng Liu · Fei-Long Xiong · Zu Xu · Dian He · Yi-Fan Zhang · Bing Shao · Ping-An Zhang · Guang-Yin Xu · Lan Chu

- 121 Failure of Placebo Analgesia Model in Rats with Inflammatory Pain**
Xiang-Sha Yin · Jin-Yu Yang · Shuai Cao · Yun Wang

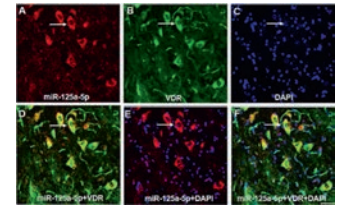
- 134 Hes1 Knockdown Exacerbates Ischemic Stroke Following tMCAO by Increasing ER Stress-Dependent Apoptosis via the PERK/eIF2 α /ATF4/CHOP Signaling Pathway**
Yueyong Li · Yingjun Zhang · Huangde Fu · Huadong Huang · Qifeng Lu · Houji Qin · Yingning Wu · Huatuo Huang · Guizhen Mao · Zhongheng Wei · Pinhu Liao



p 101

143 Chemical Stimulation of Renal Tissue Induces Sympathetic Activation and a Pressor Response *via* the Paraventricular Nucleus in Rats

Chao Ye · Yun Qiu · Feng Zhang · Ai-Dong Chen · Hong Zhou · Jue-Jin Wang · Qi Chen · Yue-Hua Li · Yu-Ming Kang · Guo-Qing Zhu



p 117

153 Ketamine Alleviates Fear Generalization Through GluN2B-BDNF Signaling in Mice

Muhammad Asim · Bo Hao · Yu-Han Yang · Bu-Fang Fan · Li Xue · Yan-Wei Shi · Xiao-Guang Wang · Hu Zhao

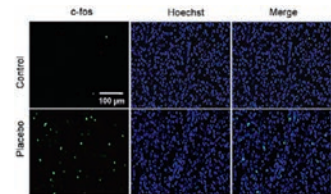
165 L-type Calcium Channels are Involved in Iron-induced Neurotoxicity in Primary Cultured Ventral Mesencephalon Neurons of Rats

Yu-Yu Xu · Wen-Ping Wan · Sha Zhao · Ze-Gang Ma

Letters to the Editor

174 A Familial Phenotypic and Genetic Study of Mutations in *PFN1* Associated with Amyotrophic Lateral Sclerosis

Jieshan Chi · Junling Chen · Yan Li · Zhiheng Huang · Lijuan Wang · Yuhu Zhang



p 129

179 A *De Novo* Variant Identified in the *PPP2R1A* Gene in an Infant Induces Neurodevelopmental Abnormalities

Yanghai Zhang · Haoxian Li · Hua Wang · Zhengjun Jia · Hui Xi · Xiao Mao

Review

183 Biomarkers for Parkinson's Disease: How Good Are They?

Tianbai Li · Weidong Le

Research Highlight

195 Early Intervention in Alzheimer's Disease: How Early is Early Enough?

Dong-Yu Fan · Yan-Jiang Wang



GABAergic Abnormalities Associated with Sensorimotor Cortico-striatal Community Structural Deficits in ErbB4 Knockout Mice and First-Episode Treatment-Naïve Patients with Schizophrenia

Chengcheng Zhang^{1,2} · Peiyan Ni^{1,2} · Yikang Liu³ · Yang Tian^{1,2} · Jinxue Wei^{1,2} · Bo Xiang^{1,2} · Liansheng Zhao^{1,2} · Xiaojing Li^{1,2} · Xiaohong Ma^{1,2} · Wei Deng^{1,2} · Wanjun Guo^{1,2} · Rongjun Ni^{1,2} · Yamin Zhang^{1,2} · Qiang Wang^{1,2} · Hailiang Huang^{4,5} · Nanyin Zhang³ · Tao Li^{1,2}

Received: 24 December 2018 / Accepted: 1 May 2019 / Published online: 6 August 2019
© Shanghai Institutes for Biological Sciences, CAS 2019

Abstract The current study was designed to explore how disruption of specific molecular circuits in the cerebral cortex may cause sensorimotor cortico-striatal community structure deficits in both a mouse model and patients with schizophrenia. We used prepulse inhibition (PPI) and brain structural and diffusion MRI scans in 23 mice with conditional ErbB4 knockout in parvalbumin interneurons and 27 matched controls. Quantitative real-time PCR was used to assess the differential levels of GABA-related transcripts in brain regions. Concurrently, we measured structural and diffusion MRI and the cumulative contribution of risk alleles in the GABA pathway genes in first-

episode treatment-naïve schizophrenic patients ($n = 117$) and in age- and sex-matched healthy controls ($n = 86$). We present the first evidence of gray and white matter impairment of right sensorimotor cortico-striatal networks and reproduced the sensorimotor gating deficit in a mouse model of schizophrenia. Significant correlations between gray matter volumes (GMVs) in the somatosensory cortex and PPI as well as glutamate decarboxylase 1 mRNA expression were found in controls but not in knockout mice. Furthermore, these findings were confirmed in a human sample in which we found significantly decreased gray and white matter in sensorimotor cortico-striatal networks in schizophrenic patients. The psychiatric risk alleles of the GABA pathway also displayed a significant negative correlation with the GMVs of the somatosensory cortex in patients. Our study identified that ErbB4 ablation in parvalbumin interneurons induced GABAergic dysregulation, providing valuable mechanistic insights into the sensorimotor cortico-striatal community structure deficits associated with schizophrenia.

Chengcheng Zhang and Peiyan Ni have contributed equally to this work.

Electronic supplementary material The online version of this article (<https://doi.org/10.1007/s12264-019-00416-2>) contains supplementary material, which is available to authorized users.

✉ Nanyin Zhang
nuz2@psu.edu

✉ Tao Li
litaohx@scu.edu.cn

¹ Mental Health Center and Psychiatric Laboratory, State Key Laboratory of Biotherapy, West China Hospital of Sichuan University, Chengdu 610041, China

² West China Brain Research Center, West China Hospital of Sichuan University, Chengdu 610041, China

³ Department of Biomedical Engineering, Pennsylvania State University, University Park, PA 16802, USA

⁴ Analytic and Translational Genetics Unit, Massachusetts General Hospital, Harvard Medical School, Boston, MA 02114, USA

⁵ Broad Institute of MIT and Harvard, Cambridge, MA 02141, USA

Keywords ErbB4 · Schizophrenia · MRI · Gene pathway · Mouse

Introduction

Schizophrenia is a heritable psychiatric disorder characterized by a heterogeneous collection of symptoms including altered perception and cognitive deficits [1–3]. Previous association studies, including by our group, have uncovered susceptibility genes for schizophrenia, such as the genes encoding neuregulin-1 (NRG1) and the only autonomous receptor tyrosine kinase erbB-4 (ErbB4) [4–8]. NRG1-ErbB4 signaling has been implicated in

neural development, and variation of the ErbB4 gene is associated with abnormal brain structure in schizophrenics [9]. Null mutations of the NRG1 and ErbB4 genes cause a spectrum of abnormal behaviors in mice, including hyperactivity, disrupted pre-pulse inhibition (PPI), and spatial learning and memory deficits, which are thought to be associated with schizophrenia [10, 11]. The PPI deficit, which has been widely shown in the ErbB4 knockout rodent model [12], is a characteristic feature of schizophrenia [13].

In addition to evidence at the behavioral level, transgenic rodent models have shown that GABAergic transmission, a major target of NRG1-ErbB4 signaling, is also critically involved in schizophrenia [14]. Almost all ErbB4-positive cells in the cortex, basal ganglia, and most of the amygdala in neonatal and adult mice are GABAergic with the highest enrichment in parvalbumin (PV) fast-spiking interneurons [15]. Specific ErbB4 deletion in PV neurons results in schizophrenia-relevant phenotypes in mice similar to those found in NRG1- or ErbB4-null mutant mice, including hyperactivity, impaired working memory, and a deficit in PPI. Using single-cell RNA sequencing of striatal cells, studies have shown that the main interneuron types are GABAergic, and most striatal interneurons signal *via* releasing GABA to inhibit target cells [16]. Thus, ErbB4-knockout (KO) in PV interneurons might provide a useful animal model in which to investigate how disturbances of the GABAergic system underlie the neurodevelopmental condition, schizophrenia, at the mechanistic level [17–19].

Despite the molecular- and behavioral-level evidence found in the transgenic rodent model of ErbB4 that is associated with key aspects of schizophrenia, we still do not understand the system-level alterations in this model and their relationship with behavioral and molecular changes. Specifically, there has been no research aiming to investigate the effects of knocking out the ErbB4 gene in PV neuron on brain structure in animals. Elucidating the relationship between ErbB4 and brain structural network change in a non-invasive and not hypothesis-driven MRI scanning manner is essential for understanding the pathophysiology of schizophrenia. In addition, it remains unknown whether gene expression abnormalities are present in the brain regions that exhibit morphological changes. Furthermore, how structural changes in the brain of KO animals are linked to clinical relevance remains elusive [20].

Previous studies have highlighted the importance of eliminating the confounder of drugs, particularly when investigating the molecular mechanisms of schizophrenia. Using both a mouse model with specific depletion of ErbB4 in PV-expressing interneurons and first-episode, treatment-naïve patients with schizophrenia, we set out to

analyze the brain sensorimotor-striatum network and gene expression abnormalities, which can completely eliminate the effects of antipsychotic treatment.

Materials and Methods

A flowchart of the experimental design is shown in Figure S1. Specific details of the methods and materials are provided in Supplementary Materials. All methods were in accordance with the relevant guidelines and regulations approved by the Institutional Review Board and local animal committee of West China Hospital of Sichuan University.

Animals

Conditional ErbB4-KO mice were generated by breeding PV-Cre mice with mice carrying loxP-flanked ErbB4 alleles [19]. Twenty-three KO mice (PV-Cre; ErbB4^{-/-}) and 27 age- and sex-matched controls (PV-Cre; ErbB4^{+/+}) were subjected to behavioral procedures and neuroimaging scans at ~ 3 months postnatal.

Behavioral Test and Mouse MRI

As many behavior tests have been conducted on the KO mice, we focused on their sensorimotor gating by measuring PPI. All MRI data were acquired on a 7.0 T MRI scanner (Bruker Biospec 70/30, Ettlingen, Germany). Brain structures were assessed using T2-weighted MRI and diffusion tensor imaging (DTI). T2-weighted anatomical images were analyzed using optimized voxel-based morphometry following Diffeomorphic Anatomical Registration Through Exponentiated Lie (DARTEL) algebra [21]. DTI images were analyzed using the FMRIB Diffusion Toolbox in FSL (<http://fsl.fmrib.ox.ac.uk/fsl/fslwiki/>) [22] as well as custom-written scripts in MatLab (MathWorks, Natick, MA).

Reverse Transcription Quantitative Real-Time Polymerase Chain Reaction (PCR)

As sensorimotor gating deficits may be relevant to schizophrenia, we next addressed the question of whether schizophrenia-related neuropathological and molecular changes exist. We analyzed the brain mRNA expression levels of the NRG1, PLCG1, GABR α 3, GABR α 2, and GAD1 genes, which have frequently been reported to be associated with the etiology of schizophrenia [23–27]. Total RNA was extracted from brain regions based on the results of image analysis, using TRIzol reagent (Life Technologies, Carlsbad, CA) [28]. The relative mRNA

levels in individual brain regions were measured in 19 KO mice and 21 controls. Details are provided in the Supplementary Materials. All assays were performed in triplicate.

Human Study

We also performed MRI scanning and examined cumulative contribution of risk alleles in the GABA pathway genes using polygenic risk scores (PRS) in 117 first-episode treatment-naïve patients with schizophrenia and 86 age- and sex-matched healthy controls (details in Supplementary Information).

Human MRI and Genetic Analysis

All participants were scanned on a 3.0 T MRI scanner (GE EXCITE, General Electric, Milwaukee, 8-channel head-coil). T1 images were processed using the DARTEL toolbox in Statistical Parametric Mapping (SPM8) (<https://www.fil.ion.ucl.ac.uk/spm/>) [29]. Diffusion anisotropy indices and diffusion shape measures were calculated from the tensor element output of the FMRIB Software Library in FSL (<http://fsl.fmrib.ox.ac.uk/fsl/fslwiki/>). Detailed procedures of scanning and pre-processing are presented in the Supplementary Materials.

DNA from whole-blood samples was obtained with the standard isolation method and genotyped using the HumanOmniZhongHua-8 BeadChip (Illumina, San Diego, CA). The resulting single-nucleotide polymorphism set was then used to calculate four multidimensional scaling (MDS) components to assess population stratification. Genome-wide summary statistics for schizophrenia were generated using fixed-effect meta-analysis across 13 cohorts, consisting of 13,305 individuals with schizophrenia and 16,244 healthy controls of Asian ancestry (unpublished work). We used these results to calculate the pathway-based PRS for GABAergic pathway genes selected from Reactome [30, 31], a well-annotated molecular pathway database, including genes involved in the synthesis, release, receptor-reuptake, and degradation of GABA. For each individual, a PRS was calculated using PRSice software [32] (http://prsice.info/PRSice_MANUAL_v1.25.pdf), which runs a linkage disequilibrium (LD)-based clumping for multiple stepwise P -value thresholds (P_T) to find the optimal P_T based on the largest variance explained (Nagelkerke R^2). We used the default settings for clumping (LD window: 250 kb, $r^2 < 0.1$) and generated six sets of scores using P_T cut-offs at 0.05, 0.1, 0.2, 0.3, 0.4, and 0.5. For each P_T cut-off, a set of SNPs with P values below the cutoff were selected. All PRS quantifications were controlled for MDS.

Statistical Analysis

Imaging data were compared between control and KO mice using two-sample t -test after controlling for age and the whole brain. Imaging data across the whole brain were compared on a voxel-by-voxel basis. To further evaluate the correlation between brain morphometric changes and behavioral measures, we first defined each cluster of voxels that showed significant differences between the control and KO groups as a region of interest (ROI). We set the significance of differences at a threshold of $P < 0.05$ at a false discovery rate (FDR) corrected and cluster > 100 voxels. For each mouse, the gray matter volume (GMV) of each ROI was quantified by averaging the GMVs of all voxels within the ROI. Since PPI was measured at three noise amplitudes, principal component analysis (PCA) was applied to the three results, and the first principal component was used to quantify the PPI measure for each mouse. The participant-specific ROI GMV and PPI values were then separately correlated in control and KO mice, after controlling for age. Owing to skewed distributions of NRG1, PLCG1, GABR α 3, GABR α 2, and GAD1 values, their mRNA values were log-transformed [33]. Multivariate analysis of covariance was next performed on each of the normalized gene expression values and the effect size was calculated using Cohen's d . Age was set as covariate. The correlations between ROI GMV and mRNA expression level were separately calculated in control and KO mice after controlling for age.

For human imaging data, the GMVs of the left and right somatosensory cortex, as well as the GMVs and fractional anisotropy values (FAs) in the caudate were separately extracted and compared between healthy controls and patients with schizophrenia using univariate analysis with age, sex, education years, and the whole brain as covariates. For each P_T cutoff, the GABA-pathway PRS and the GMV of the somatosensory cortex were separately correlated in controls and schizophrenics after controlling for age, sex, education years, and the first four MDS components. All statistical analyses were performed using SPSS 22 statistical software (SPSS Inc., Chicago, IL) and MatLab (MathWorks, Natick, MA).

Results

In this study, we characterized alterations in behavior, brain structure, and gene expression of the GABAergic pathway in KO mice. We also examined the clinical relevance of our preclinical findings in first-episode patients with schizophrenia.

PPI Deficit

KO mice demonstrated impairment in somatosensory gating, reflected by significantly lower PPI amplitudes for

all three pre-pulse intensities relative to controls (Fig. 1B, $P = 0.02$, 0.004 , and 0.04 for 74 dB, 78 dB, and 86 dB, respectively). There was no significant difference in age

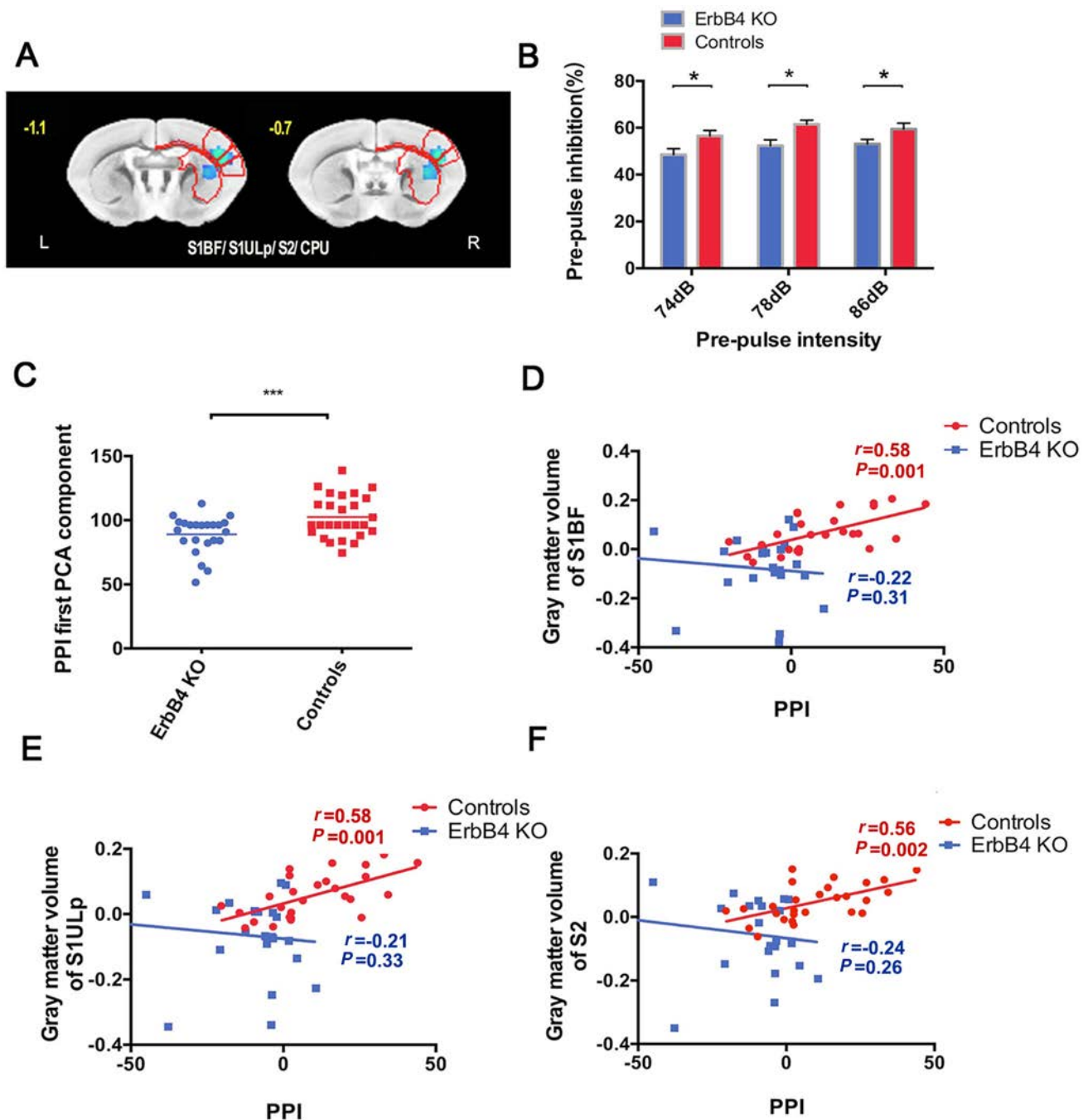


Fig. 1 Relationship between brain structures and PPI in ErbB4-KO mice. **A** Colored voxels represent clusters showing significant gray matter volume difference between controls and ErbB4-KO mice. **B** PPI tests in ErbB4-KO and control mice, quantified as the percentage decrease of the startle response amplitude at three pre-pulse intensities (74 dB, 78 dB, and 86 dB). Values are the mean \pm SEM. **C** The first PCA component of PPI amplitude in ErbB4-KO

and control mice. **D–F** Significant correlations of the first PCA component of PPI and the GMVs of the right S1BF, S1ULp, and S2 in control mice. However, these correlational relationships did not occur in KO mice. Age was included as the covariate. PCA, principal component analysis; S1BF and S1ULp, primary somatosensory cortex, barrel field and upper lip region; S2, secondary somatosensory cortex. * $P < 0.05$, *** $P < 0.001$.

between control and KO mice. The PPI data in both groups are summarized in Table S1.

Changes in Brain Structure

KO mice exhibited altered brain structures in both GMV and white matter integrity. Voxel-wise analysis of T2-weighted structural images revealed a significantly smaller GMV in an extended area covering the barrel field (S1BF) and upper lip region (S1ULp) in the right primary somatosensory area, the right secondary somatosensory

cortex (S2), and the right lateral striatum (CPU) ($P < 0.05$, FDR-corrected, Fig. 2A–F; details in Table S2). In addition, significantly smaller FAs in the right parasubiculum (Pas) and CPU were found in KO mice relative to the controls (Fig. 2G–J; $P < 0.05$, FDR-corrected). Detailed information of these clusters is summarized in Table S3.

mRNA Expression Levels

The mRNA expression levels of both NRG1 and PLCG1 genes in the right somatosensory cortex were significantly

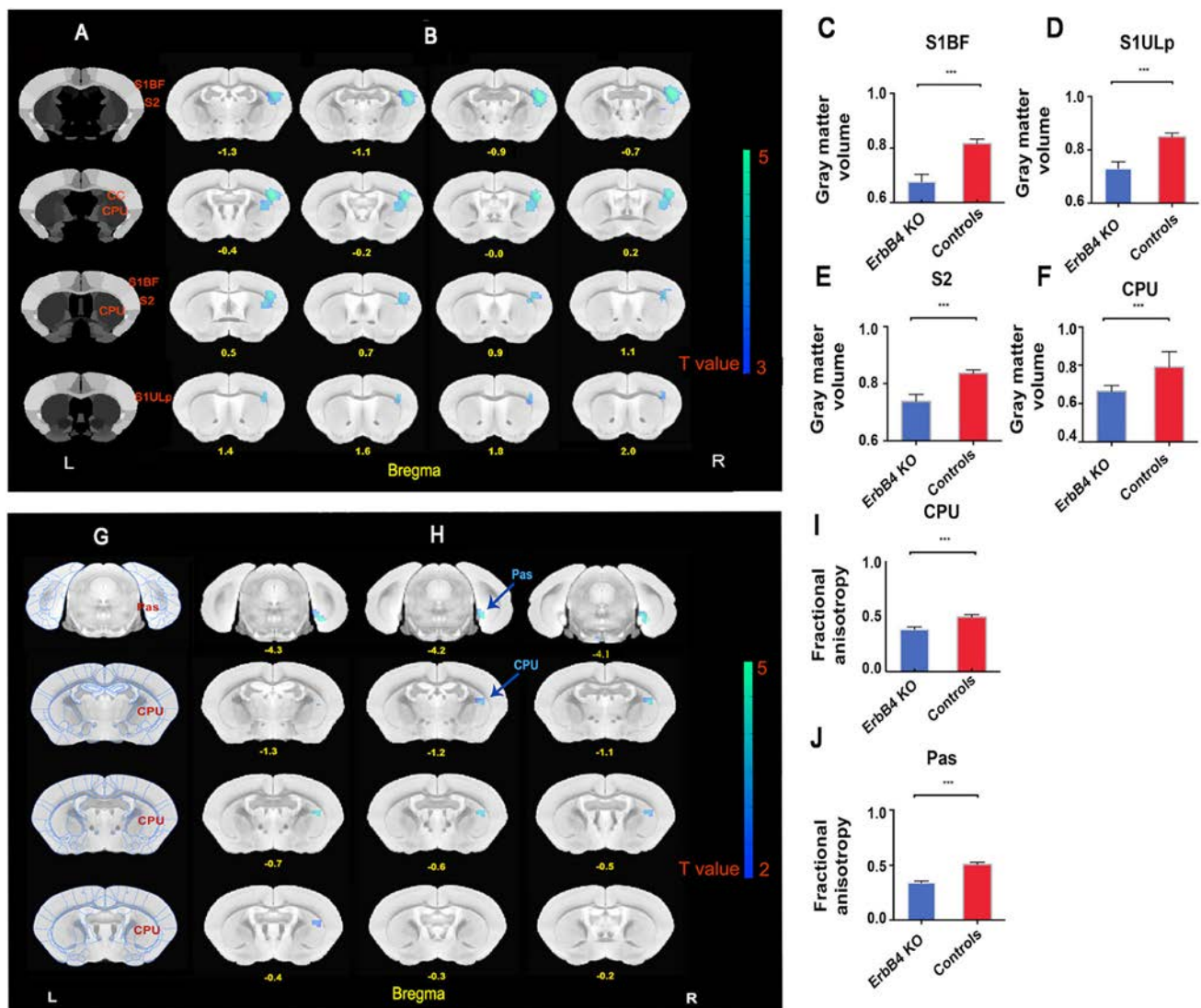


Fig. 2 Gray matter volume (GMV) and white matter integrity changes in ErbB4-KO mice. **A** Mouse brain atlas. **B** Colored voxels represent significant regional GMV decreases in ErbB4-KO mice ($P < 0.05$, FDR-corrected, after controlling for age and the whole brain), overlaid on structural MRI images. **C–F** GMVs of clusters. L, Left; R, Right; S1BF, barrel field of primary somatosensory cortex; S1ULp, upper lip region of primary somatosensory cortex; S2, secondary somatosensory cortex; CPU, lateral striatum. Values are

the mean \pm SEM. **G** Mouse brain atlas. **H** Colored voxels represent significant regional decreases in fractional anisotropy values in ErbB4-KO mice ($P < 0.05$, FDR-corrected, after controlling for age and the whole brain), superimposed on anatomical MRI atlas. **I, J** Fractional anisotropy values of clusters. L, left; R, right; Pas, parasubiculum; CPU, lateral striatum. Values are the mean \pm SEM. The colorbar shows the T -values of the statistical analysis. *** $P < 0.001$.

difference in the mRNA levels of these genes was found in the left striatum (Table S4).

By using these genes as query genes (i.e., *NRG1*, *GABRa2*, *GABRa3*, *GAD1*, *ErbB4*, and *PV*), we further expanded the set of genes examined and assessed functional gene networks in the somatosensory cortex in *ErbB4*-KO mice. Functional gene networks were constructed by connecting query and related genes including co-expression, co-localization, predicted, and shared protein domains. The 6 query genes noted above were given the maximum node size. The size of nodes for related genes was inversely proportional to the rank of the gene in a list sorted by the gene scores, which were assessed by using GeneMANIA software (<http://genemania.org/>). By analyzing the gene networks using GeneMANIA, we found prominent networks, including the GABA A receptor activity network (Coverage [number of genes in the network with a given function/all genes in the genome with that function] = 7/14, FDR $q = 6 \times 10^{-14}$) and the GABAergic synaptic transmission network (Coverage = 4/31, FDR $q = 1.9 \times 10^{-4}$). Taken together, these results indicated that GABA receptor activity and GABAergic synaptic transmission in the somatosensory cortex were altered in KO mice.

Correlations Between Brain Structure, Behavior, and mRNA Levels

We found that both the behavioral data and mRNA levels of the *GAD1* gene were significantly correlated to brain morphometric measures in control animals. By contrast, these correlation relationships were absent in KO mice. Specifically, PPI was positively associated with the GMV of S1BF ($r = 0.58$, $P = 0.001$), S1ULp ($r = 0.58$, $P = 0.001$) and S2 ($r = 0.56$, $P = 0.002$) in controls but not in KO mice (for S1BF, $r = -0.22$, $P = 0.31$; for S1ULp, $r = -0.21$, $P = 0.33$; for S2, $r = -0.24$, $P = 0.26$; Fig. 1D–F). In addition, the mRNA level of the *GAD1* gene was positively associated with the GMV of S1BF ($r = 0.55$, $P = 0.01$), S1ULp ($r = 0.52$, $P = 0.02$) and S2 ($r = 0.52$, $P = 0.02$) in controls, but again, not in KO mice (for S1BF, $r = -0.07$, $P = 0.79$; for S1ULp, $r = -0.11$, $P = 0.68$; for S2, $r = -0.12$, $P = 0.68$; Fig. 3L–N). No other significant associations between behavioral data, mRNA levels, and changes in brain structure were found.

GMV and FA Differences Between Patients with Schizophrenia and Controls

To further examine the clinical relevance of our preclinical findings in mice, we compared GMV in the somatosensory cortex between first-episode patients with schizophrenia

and healthy controls. Our data demonstrated reduced GMV in the left primary somatosensory cortex ($t = 2.93$, $P = 0.001$), right somatosensory cortex ($t = 2.86$, $P = 0.002$), and right caudate body ($t = 3.1$, $P < 0.001$), after controlling for age, sex, and education years. We also compared FA in the striatum region in first-episode patients with schizophrenia and healthy controls. Our data showed reduced FA in the right caudate ($t = 4.45$, $P < 0.001$), after controlling for age, sex, and education years (Table S5 and Fig. 4A–E). There was no significant difference in age, sex, and education years between controls and patients. Details of intelligence quotient and the duration of untreated psychosis in both groups are summarized in Table S5. These data suggest that our brain imaging findings in KO mice have significant translational value in patients.

Relationship Between PRS and GMV

The PRS of GABAergic pathway genes for schizophrenia was negatively associated with the GMV of the left somatosensory cortex at all five GWAS (genome-wide association study) P_T cutoffs (P_T ranging from 0.05 to 0.5) in patients with schizophrenia, but not in controls. In addition, the PRS values of GABAergic pathway genes were negatively associated with the GMV of the right somatosensory cortex at three GWAS P_T cutoffs (0.05, 0.1 and 0.2) in patients with schizophrenia, but not in controls (Table S6 and Fig. 4F–N). These results suggested that, like *ErbB4*-KO mice, altered GABA function might contribute to morphological changes in sensorimotor areas in schizophrenia patients.

Discussion

Here, we showed for the first time that a mouse model of schizophrenia (*ErbB4*-KO in PV neurons) displays significantly reduced GMVs and white matter integrity in the right sensorimotor cortico-striatal networks and reduced mRNA expression in the *ErbB4*-*NRG1* signaling pathway, as well as increased mRNA expression in the GABAergic pathway in the right somatosensory cortex and striatum. In addition, we found that correlations between GMVs of the S1BF, S1ULp, S2, and PPI as well as *GAD1* mRNA expression that were present in control mice, were absent in KO mice. The data provide a possible link between the GABA pathway and schizophrenia-related pathobiology. In parallel, we also confirmed changes in the schizophrenia-associated GABAergic pathway in sensorimotor structures of patients. We found reduced GMVs and white matter integrity in regions in the same sensorimotor cortico-striatal networks in patients with schizophrenia and this structural alteration was further associated with the PRS of

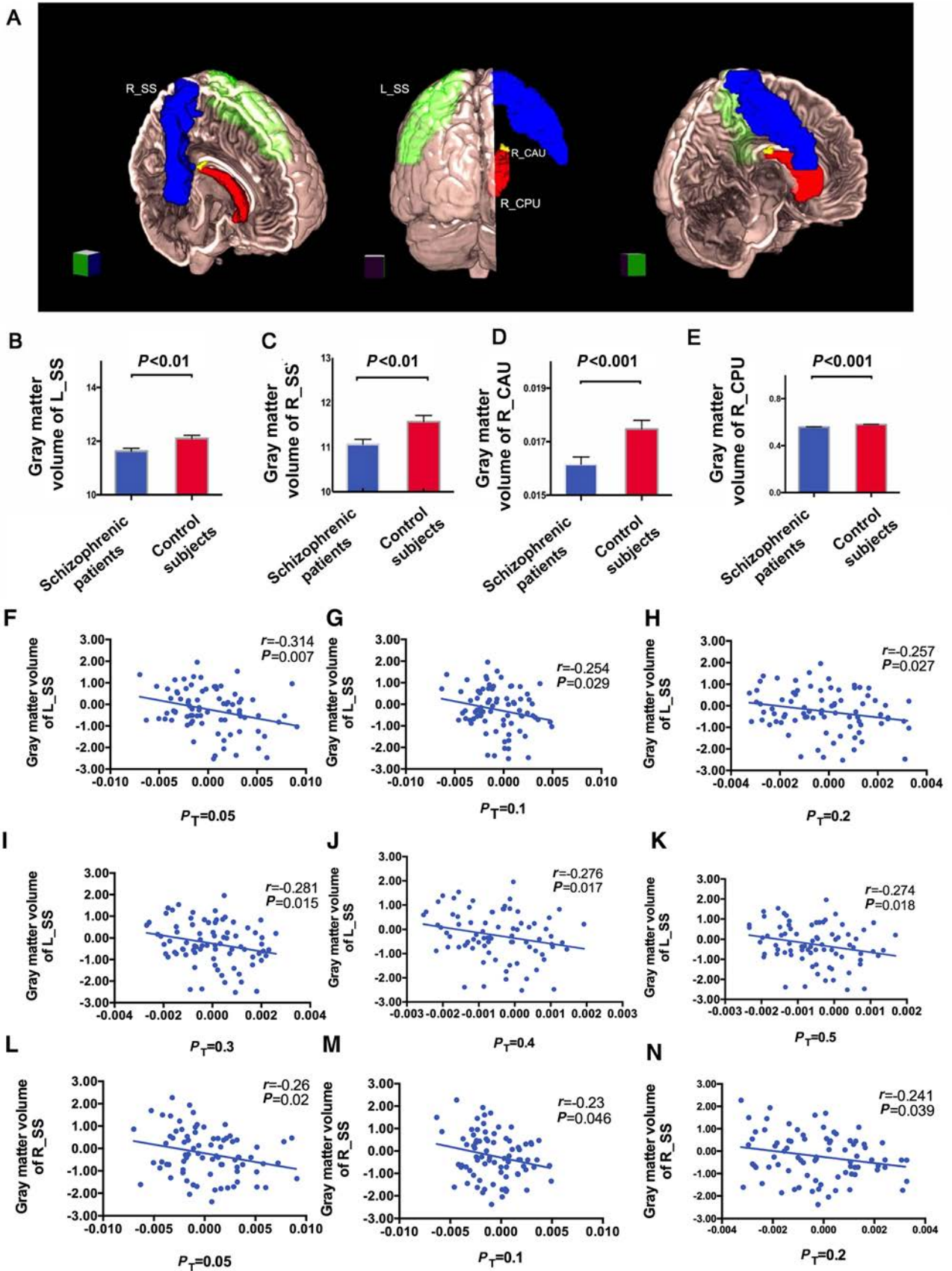


Fig. 4 Clinical relevance. **A** Patients with schizophrenia showed significant reductions in the gray matter volume in the sensorimotor cortico-striatal community. **B–E** GMV and FA values of clusters. Values are the mean \pm SEM. GMV, gray matter volume; FA, fractional anisotropy; L_SS, left somatosensory cortex; R_SS, right somatosensory cortex; R_CAU, right lateral caudate body; R_CPU, right caudate. **F–N** Polygenic risk scores of genes in the GABAergic pathway showing negative correlations with the GMV of the somatosensory cortex in patients with schizophrenia. Age, sex, and education years and the whole brain were included as covariates. P_T cutoffs, P_T ranging from 0.05 to 0.5.

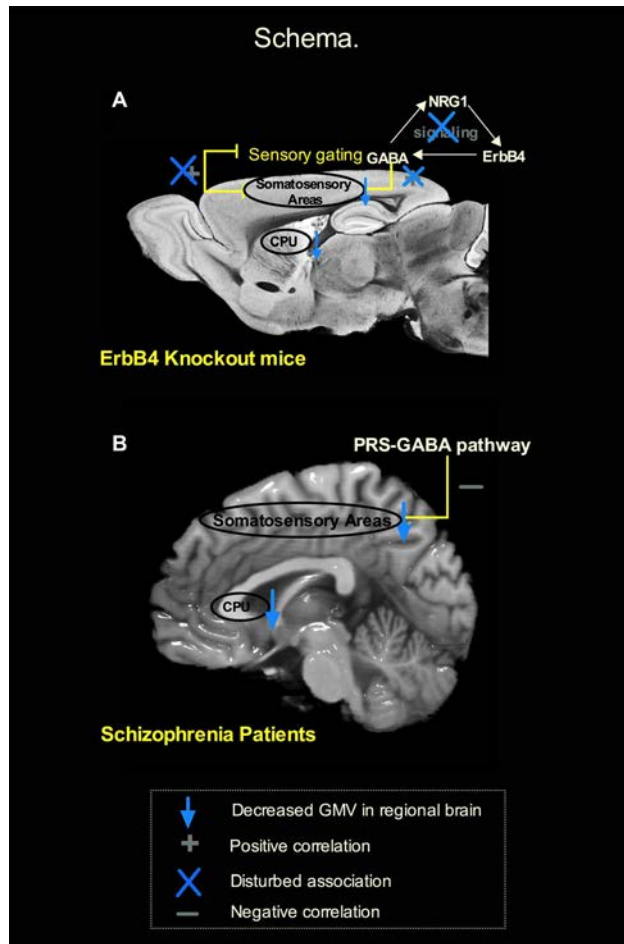


Fig. 5 Schematic illustration of major findings in the present study. Using both a mouse model and first-episode, treatment-naïve patients with schizophrenia, we identified sensorimotor cortico-striatal community structure deficits associated with schizophrenia. **A** ErbB4 deletion in PV interneurons might be critically involved in schizophrenia as manifested by the genes in the GABAergic pathway, abnormal structure in the sensorimotor cortico-striatal networks and sensory gating deficit. **B** Abnormal sensorimotor cortico-striatal network structure in patients with schizophrenia associated with the polygenic risk score of genes in the GABAergic pathway. GMV, gray matter volume; FA, fractional anisotropy; CPU, lateral striatum; PRS, polygenic risk scores.

genes in the GABAergic pathway. All these findings are summarized in Fig. 5. Taken together, these results suggest that ErbB4 in PV interneurons is critically involved in schizophrenia at the molecular (genes in the GABAergic pathway), systems (abnormal brain structure in the somatosensory-striatum regions), and behavioral levels (the PPI deficit).

Relationship between ErbB4 and Sensorimotor Gating Deficit in Schizophrenia

PPI provides an operational method to measure sensorimotor gating, a process by which an organism filters extraneous information from the internal and external milieu. A PPI deficit is a characteristic feature of schizophrenia both in patients and animal models [34–37]. However, less is known about the possible genetic underpinnings of this phenotypic PPI deficit in schizophrenia [38]. In the present study, we demonstrated a significant PPI deficit in ErbB4-KO mice. Our results confirmed that the ErbB4 gene plays an important role in the impaired sensorimotor gating in schizophrenia.

Relationships of ErbB4, Brain Structure, and PPI in Schizophrenia

The association between ErbB4 gene polymorphism and brain structure alterations in schizophrenia has been investigated in several studies [39, 40]. However, most of these studies investigated this relationship at the correlational level, while the causal effect of knocking out ErbB4 on brain structures remained unclear. Our study uncovered this effect on the sensorimotor cortical-lateral striatal networks. ErbB4-KO mice showed decreased GMVs of the right somatosensory cortex and CPU, as well as decreased FA in the right CPU relative to control mice, highlighting the impact of ErbB4 deletion on brain structures subserving sensorimotor-related functions.

These changes in brain structure in ErbB4-KO mice also echoed their behavioral deficit in sensorimotor gating. We found that in control mice, the GMV of the somatosensory cortex was positively correlated with PPI. This result is consistent with the human data demonstrating a linkage between the somatosensory cortex and PPI in healthy participants [41]. By contrast, this correlation disappeared in KO mice. These data collectively suggest that the somatosensory cortex is critical to somatosensory gating, and alteration in this brain structure can lead to a loss of a brain-behavior association in a right-hemisphere function. This brain-behavior relationship is consistent with anatomical studies in humans linking the right sensorimotor striatum to cognitive control, and suggests a loss of a brain-behavior association in schizophrenia [42]. Considering

that both the structural and behavioral changes are consequences of ErbB4-KO, ErbB4 might be the key genetic basis of somatosensory cortex changes and the somatomotor gating deficit in schizophrenia.

In contrast to the somatosensory cortex, we did not find any significant correlation between the deficit in the CPU and PPI, although the GMV of the CPU was also reduced in KO mice. These data are in line with a study that reported no significant correlation between the synaptic density in the striatum and PPI in either healthy participants or those at high risk of psychosis [35]. Taken together, these results indicate that the structural change in the striatum is not directly related to the PPI deficit in schizophrenia.

NRG1-ErbB4 Signaling, GABA Transmission, and Their Relationship to Brain Structure

On the basis of our imaging results, we identified abnormal mRNA levels of genes in the NRG1-ErbB4 and GABA pathways in the right somatosensory cortex and right striatum. It has been reported that NRG1 and PLCG1 are tightly connected to the ErbB4 pathway, and they are highly expressed in cortical interneurons and the striatum [43]. Our data confirmed that the NRG1 and PLCG1 mRNA levels were significantly decreased in the right somatosensory cortex and striatum in ErbB4-KO mice, suggesting changes in ErbB4-NRG1 signaling in this schizophrenia-like mouse model. In line with this result, previous studies have also reported decreased ErbB4 protein and NRG1-related cellular activity in the somatosensory cortex in schizophrenic patients [17, 44].

In addition, we found that the GAD1 (GAD67, an enzyme associated with GABA synthesis) [45] and GABR α 2 mRNA levels were increased in the right striatum in KO mice. This result is consistent with a previous report of stronger GABA expression in the dorsal caudate in ultra-high-risk patients with schizophrenia relative to healthy controls [46]. Moreover, previous researchers have shown that ErbB4 is enriched in GABAergic neurons. Although the exact mechanisms underlying the increases in GABR α 2 mRNA and GAD1 are unknown, it is possible that they are an up-regulated response to compensate for the deficit in GABA transmission [47–49]. Moreover, we found that the GMV of the right somatosensory cortex was positively correlated with the GAD1 mRNA expression in the same region in control mice, but this correlation was absent in ErbB4-KO mice. These data suggest that the structural alterations resulting from ErbB4 deletion can lead to impairment of transcriptional changes in NRG1-ErbB4 signaling and GABA transmission. These results demonstrate that anomalous NRG1-ErbB4 signaling and GABA transmission might be important molecular mechanisms

underlying the anatomical changes in the sensorimotor-striatum network in schizophrenia [50–52].

Clinical Relevance

Since ErbB4-KO mice displayed behavioral phenotypes that are characteristic of schizophrenia (e.g. PPI deficit) as shown in present study and others [17, 38], this animal model has been suggested to be a valuable model of schizophrenia. The sensorimotor gating deficits in ErbB4 mice provide an opportunity to understand the mild sensorimotor dysfunctions frequently reported in patients with schizophrenia. However, it is unclear whether our imaging and genetic findings in this animal model are clinically relevant. Thus, we concurrently examined in patients with schizophrenia the GMV and FA in the same sensorimotor cortical-lateral striatal networks identified in KO mice. Interestingly, we found decreased GMV in the somatosensory cortex and dorsal caudate in first-episode, treatment-naïve patients with schizophrenia relative to matched healthy controls. The results agree with our previous studies that showed decreased GMV of the somatosensory cortex in first-episode patients with schizophrenia [53]. It has also been shown that the GMV of the right primary somatosensory is still significantly smaller in schizophrenic patients than in healthy controls at 1-year follow-up [54]. Furthermore, we found that the FA in the right dorsal caudate was lower in patients than in controls, and this result is consistent with the report that the avolition in schizophrenia is linked to dorsal caudate hypoactivation [55–59]. Taken together, these results show that ErbB4-KO mice are a valuable model of schizophrenia and have high translational utility. Our results also indicate that abnormalities in the sensorimotor-striatum network might be a key systems-level marker of schizophrenia.

Since invasive procedures could not be considered in such a large and unique sample of first-episode and treatment-naïve patients with schizophrenia, brain-specific changes in gene expression could not be obtained. To further assess the clinical relevance of our molecular-level findings in mice, we used the polygenic risk-profiling method. Schizophrenia is a highly polygenic disorder, so PRS based on risk alleles derived from GWAS provides an ideal method to quantify the overall burden of the many risk allele carried by individuals. In addition, at the biological level, imaging genetics has demonstrated that psychiatric risk alleles are more closely tied to variance at the systems level as compared with clinical diagnoses [60]. Consistent with our findings in ErbB4-KO mice, we found that the additive contribution of risk alleles of genes in the GABAergic signaling pathway is clearly associated with decreased GMV of the somatosensory cortex in patients with schizophrenia. Our findings further support the role of

GABA dysfunction in schizophrenia and suggest that anomalous GABA transmission might be a significant factor contributing to the structural changes in the somatosensory cortex. This finding is striking because humans and mice use different modalities and levels (structural and diffusion MRI, expression levels and genetic variation) as a primary means of sensorimotor gating, suggesting that the physiological underpinnings of the sensorimotor network have remained evolutionarily conserved at the multi-system level and further supporting the use of such intermediate phenotypes as a way to enhance translational analyses.

The results of this study should be interpreted in the context of the following limitations. As we did not measure PPI or the ErbB4 expression level in the schizophrenic patients, further studies to confirm the relationship between the structural change in the somatosensory cortex and the PPI deficit as well as ErbB4 alterations in patients as in our animal study need to be conducted. The preliminary findings of the current study supported the possibility that deregulated ErbB4 signaling may be a joint mechanism between sensorimotor gating and GABAergic dysfunction, providing a working hypothesis for future research. It should be noted that the correlations between the PRS of GABAergic pathway genes and GMV of somatosensory cortex in schizophrenic patients reported in the current study are uncorrected with multiple comparisons. Further longitudinal studies in patients are required to verify the multi-system level changes in schizophrenia. In addition, the present study has several advantages. The whole-brain imaging method avoids the empirical preselection of brain regions. Animal models also avoid the confounding effects of medications. Indeed, researchers have measured GABA levels in the medial prefrontal cortex of medicated and un-medicated schizophrenics. They found significant elevations of the neurotransmitter only in un-medicated but not medicated patients [61], highlighting the importance of eliminating the confounder of drugs, particularly when investigating the molecular mechanisms of schizophrenia. As a result, in the human study, we used first-episode, treatment-naïve patients (or patients on drugs for < 3 days) and completely eliminated the effects of antipsychotic treatment on the sensorimotor-striatum network.

Conclusions

In this study, ErbB4 KO mice showed deficits in PPI, neuroanatomical changes (GMV and FA) in the sensorimotor cortical-lateral striatal networks, and abnormalities in the ErbB4-*NRG1* signaling and GABAergic pathways. The structural changes were replicated in first-episode treatment-naïve patients with schizophrenia. In addition,

the cumulative contribution of risk alleles of genes in the GABAergic pathway was negatively associated with the GMV of the somatosensory cortex in schizophrenic patients. We identified a critical function of ErbB4 in balancing brain circuits, and identified GABAergic abnormalities as a target of *NRG1*/*ErbB4* signaling in sensorimotor cortico-striatal community structural deficits and key behaviors relevant to schizophrenia.

Acknowledgements This work was supported by the National Natural Science Foundation of China (81630030, 81130024, and 81528008); the National Natural Science Foundation of China/Research Grants Council of Hong Kong Joint Research Scheme (81461168029); the National Basic Research Development Program of China (2016YFC0904300); the Science and Technology Project of the Health Planning Committee of Sichuan (19PJ090); and the National Natural Science Foundation of China for Distinguished Young Scholars (81501159).

Conflict of interest The authors declare that they have no conflict of interest.

References

1. Kavanagh DH, Tansey KE, O'Donovan MC, Owen MJ. Schizophrenia genetics: emerging themes for a complex disorder. *Mol Psychiatry* 2015, 20: 72–76.
2. Fioravanti M, Carlone O, Vitale B, Cinti ME, Clare L. A meta-analysis of cognitive deficits in adults with a diagnosis of schizophrenia. *Neuropsychol Rev* 2005, 15: 73–95.
3. Silverstein SM, Keane BP. Perceptual organization impairment in schizophrenia and associated brain mechanisms: review of research from 2005 to 2010. *Schizophr Bull* 2011, 37: 690–699.
4. Stefansson H, Petursson H, Sigurdsson E, Steinthorsdottir V, Bjornsdottir S, Sigmundsson T, *et al.* Neuregulin 1 and susceptibility to schizophrenia. *Am J Hum Genet* 2002, 71: 877–892.
5. Silberberg G, Darvasi A, Pinkas-Kramarski R, Navon R. The involvement of ErbB4 with schizophrenia: association and expression studies. *Am J Med Genet B Neuropsychiatr Genet* 2006, 141: 142–148.
6. Lu CL, Wang YC, Chen JY, Lai IC, Liou YJ. Support for the involvement of the *ERBB4* gene in schizophrenia: a genetic association analysis. *Neurosci Lett* 2010, 481: 120–125.
7. Li T, Stefansson H, Gudfinnsson E, Cai G, Liu X, Murray RM, *et al.* Identification of a novel neuregulin 1 at-risk haplotype in Han schizophrenia Chinese patients, but no association with the Icelandic/Scottish risk haplotype. *Mol Psychiatry* 2004, 9: 698–704.
8. Yang JZ, Si TM, Ruan Y, Ling YS, Han YH, Wang XL, *et al.* Association study of neuregulin 1 gene with schizophrenia. *Mol Psychiatry* 2003, 8: 706–709.
9. Zuliani R, Moorhead TWJ, Bastin ME, Johnstone EC, Lawrie SM, Brambilla P, *et al.* Genetic variants in the ErbB4 gene are associated with white matter integrity. *Psychiatry Res Neuroimaging* 2011, 191: 133–137.
10. Barros CS, Calabrese B, Chamero P, Roberts AJ, Korzus E, Lloyd K, *et al.* Impaired maturation of dendritic spines without disorganization of cortical cell layers in mice lacking *NRG1*/*ErbB* signaling in the central nervous system. *Proc Natl Acad Sci U S A* 2009, 106: 4507–4512.

11. O'Tuathaigh CMP, Babovic D, O'Meara G, Clifford JJ, Croke DT, Waddington JL. Susceptibility genes for schizophrenia: characterisation of mutant mouse models at the level of phenotypic behaviour. *Neurosci Biobehav Rev* 2007, 31: 60–78.
12. Powell SB, Zhou X, Geyer MA. Prepulse inhibition and genetic mouse models of schizophrenia. *Behav Brain Res* 2009, 204: 282–294.
13. Cadenhead KS, Swerdlow NR, Shafer KM, Diaz M, Braff DL. Modulation of the startle response and startle laterality in relatives of schizophrenic patients and in subjects with schizotypal personality disorder: evidence of inhibitory deficits. *Am J Psychiatry* 2000, 157: 1660–1668.
14. Woo RS, Li XM, Tao Y, Carpenter-Hyland E, Huang YZ, Weber J, *et al.* Neuregulin-1 enhances depolarization-induced GABA release. *Neuron* 2007, 54: 599–610.
15. Bean JC, Lin TW, Sathyamurthy A, Liu F, Yin DM, Xiong WC, *et al.* Genetic labeling reveals novel cellular targets of schizophrenia susceptibility gene: distribution of GABA and non-GABA ErbB4-positive cells in adult mouse brain. *J Neurosci* 2014, 34: 13549–13566.
16. Muñoz-Manchado AB, Gonzales CB, Zeisel A, Munguba H, Bekkouche B, Skene NG, *et al.* Diversity of interneurons in the dorsal striatum revealed by single-cell RNA sequencing and patchseq. *Cell Rep* 2018, 24: 2179–2190. e2177.
17. Del Pino I, García-Frigola C, Dehorter N, Brotons-Mas JR, Alvarez-Salvado E, de Lagrán MM, *et al.* ErbB4 deletion from fast-spiking interneurons causes schizophrenia-like phenotypes. *Neuron* 2013, 79: 1152–1168.
18. Chen YJ, Zhang M, Yin DM, Wen L, Ting A, Wang P, *et al.* ErbB4 in parvalbumin-positive interneurons is critical for neuregulin 1 regulation of long-term potentiation. *Proc Natl Acad Sci U S A* 2010, 107: 21818–21823.
19. Wen L, Lu YS, Zhu XH, Li XM, Woo RS, Chen YJ, *et al.* Neuregulin 1 regulates pyramidal neuron activity via ErbB4 in parvalbumin-positive interneurons. *Proc Natl Acad Sci U S A* 2010, 107: 1211–1216.
20. Donaldson ZR, Hen R. From psychiatric disorders to animal models: a bidirectional and dimensional approach. *Biol Psychiatry* 2015, 77: 15–21.
21. Biedermann S, Fuss J, Zheng L, Sartorius A, Falfan-Melgoza C, Demirakca T, *et al.* In vivo voxel based morphometry: detection of increased hippocampal volume and decreased glutamate levels in exercising mice. *Neuroimage* 2012, 61: 1206–1212.
22. Sahara N, Perez PD, Lin WL, Dickson DW, Ren Y, Zeng H, *et al.* Age-related decline in white matter integrity in a mouse model of tauopathy: an in vivo diffusion tensor magnetic resonance imaging study. *Neurobiol Aging* 2014, 35: 1364–1374.
23. Yu H, Bi W, Liu C, Zhao Y, Zhang D, Yue W. A hypothesis-driven pathway analysis reveals myelin-related pathways that contribute to the risk of schizophrenia and bipolar disorder. *Prog Neuropsychopharmacol Biol Psychiatry* 2014, 51: 140–145.
24. Gebicke-Haerter PJ. Differential expression of presynaptic genes in a rat model of postnatal hypoxia: relevance to schizophrenia. *Eur Arch Psychiatry Clin Neurosci* 2010, 260 Suppl 2: S81–89.
25. Straub RE, Lipska BK, Egan MF, Goldberg TE, Callicott JH, Mayhew MB, *et al.* Allelic variation in GAD1 (GAD 67) is associated with schizophrenia and influences cortical function and gene expression. *Mol Psychiatry* 2007, 12: 854–869.
26. Marengo S, Geramita M, van der Veen JW, Barnett AS, Kolachana B, Shen J, *et al.* Genetic association of ErbB4 and human cortical GABA levels *in vivo*. *J Neurosci* 2011, 31: 11628–11632.
27. Volk DW, Pierri JN, Fritschy JM, Auh S, Sampson AR, Lewis DA. Reciprocal alterations in pre- and postsynaptic inhibitory markers at chandelier cell inputs to pyramidal neurons in schizophrenia. *Cereb Cortex* 2002, 12: 1063–1070.
28. Simms D, Cizdziel PE, Chomczynski P. TRIzol: A new reagent for optimal single-step isolation of RNA. *Focus* 1993, 15: 532–535.
29. Ashburner J, Barnes G, Chen C, Daunizeau J, Flandin G, Friston K, *et al.* SPM8 manual. Functional Imaging Laboratory, Institute of Neurology, UCL 2012.
30. Power RA, Steinberg S, Bjornsdottir G, Rietveld CA, Abdellaoui A, Nivard MM, *et al.* Polygenic risk scores for schizophrenia and bipolar disorder predict creativity. *Nat Neurosci* 2015, 18: 953–955.
31. Jia P, Wang L, Meltzer HY, Zhao Z. Common variants conferring risk of schizophrenia: a pathway analysis of GWAS data. *Schizophr Res* 2010, 122: 38–42.
32. Euesden J, Lewis CM, O'reilly PF. PRSice: polygenic risk score software. *Bioinformatics* 2014, 31: 1466–1468.
33. Pillai AK, Howell KR, Ahmed AO, Weinberg D, Allen KM, Bruggemann JM, *et al.* Association of serum VEGF levels with prefrontal cortex volume in schizophrenia. *Mol Psychiatry* 2016, 21: 686–692.
34. Cheng CH, Chan PY, Niddam DM, Tsai SY, Hsu SC, Liu CY. Sensory gating, inhibition control and gamma oscillations in the human somatosensory cortex. *Sci Rep* 2016, 6: 20437.
35. De Koning MB, Bloemen OJN, Van Duin EDA, Booij J, Abel KM, De Haan L, *et al.* Pre-pulse inhibition and striatal dopamine in subjects at an ultra-high risk for psychosis. *J Psychopharmacol* 2014, 28: 553–560.
36. Brody SA, Dulawa SC, Conquet F, Geyer MA. Assessment of a prepulse inhibition deficit in a mutant mouse lacking mGlu5 receptors. *Mol Psychiatry* 2004, 9: 35–41.
37. Mena A, Ruiz-Salas JC, Puentes A, Dorado I, Ruiz-Veguilla M, De la Casa LG. Reduced prepulse inhibition as a biomarker of schizophrenia. *Front Behav Neurosci*. 2016, 10: 202.
38. Lazar NL, Neufeld RW, Cain DP. Contribution of nonprimate animal models in understanding the etiology of schizophrenia. *J Psychiatry Neurosci* 2011, 36: E5–29.
39. Chong VZ, Thompson M, Beltaifa S, Webster MJ, Law AJ, Weickert CS. Elevated neuregulin-1 and ErbB4 protein in the prefrontal cortex of schizophrenic patients. *Schizophr Res* 2008, 100: 270–280.
40. Konrad A, Vucurevic G, Musso F, Stoeter P, Dahmen N, Winterer G. ErbB4 genotype predicts left frontotemporal structural connectivity in human brain. *Neuropsychopharmacology* 2009, 34: 641–650.
41. Nakagawa K, Inui K, Yuge L, Kakigi R. Inhibition of somatosensory-evoked cortical responses by a weak leading stimulus. *NeuroImage* 2014, 101: 416–424.
42. Levitt JJ, Nestor PG, Levin L, Pelavin P, Lin P, Kubicki M, *et al.* Reduced structural connectivity in frontostriatal white matter tracts in the associative loop in schizophrenia. *Am J Psychiatry* 2017, 174: 1102–1111.
43. Villarcervino V, Kappeler C, Nobregapereira S, Henkemeyer M, Rago L, Nieto MA, *et al.* Molecular mechanisms controlling the migration of striatal interneurons. *J Neurosci* 2015, 35: 8718–8729.
44. Barz CS, Bessaih T, Abel T, Feldmeyer D, Contreras D. Altered resonance properties of somatosensory responses in mice deficient for the schizophrenia risk gene Neuregulin 1. *Brain Struct Funct* 2016, 221: 4383–4398.
45. Addington AM, Gornick M, Duckworth J, Sporn A, Gogtay N, Bobb AJ, *et al.* GAD1 (2q31.1), which encodes glutamic acid decarboxylase (GAD67), is associated with childhood-onset schizophrenia and cortical gray matter volume loss. *Mol Psychiatry* 2005, 10: 581–588.
46. de la Fuente-Sandoval C, Reyes-Madrigal F, Mao X, León-Ortiz P, Rodríguez-Mayoral O, Solís-Vivanco R, *et al.* Cortico-striatal GABAergic and glutamatergic dysregulations in subjects at ultra-

- high risk for psychosis investigated with proton magnetic resonance spectroscopy. *Int J Neuropsychopharmacol* 2015, 19: pyv105.
47. Frankle WG, Cho RY, Prasad KM, Mason NS, Paris J, Himes ML, *et al.* *In vivo* measurement of GABA transmission in healthy subjects and schizophrenia patients. *Am J Psychiatry* 2015, 172: 1148–1159.
 48. Deng C, Huang XF. Increased density of GABA A receptors in the superior temporal gyrus in schizophrenia. *Exp Brain Res* 2006, 168: 587–590.
 49. Geng HY, Zhang J, Yang JM, Li Y, Wang N, Ye M, *et al.* ErbB4 deletion from medium spiny neurons of the nucleus accumbens core induces schizophrenia-like behaviors via elevated GABA α 1 subunit expression. *J Neurosci* 2017, 37: 7450–7464.
 50. Hintiryan H, Foster NN, Bowman I, Bay M, Song MY, Gou L, *et al.* The mouse cortico-striatal projectome. *Nat Neurosci* 2016, 19: 1100–1114.
 51. Yin DM, Sun XD, Bean JC, Lin TW, Sathyamurthy A, Xiong WC, *et al.* Regulation of spine formation by ErbB4 in PV-positive interneurons. *J Neurosci* 2013, 33: 19295–19303.
 52. Shamir A, Kwon OB, Karavanova I, Vullhorst D, Leiva-Salcedo E, Janssen MJ, *et al.* The importance of the NRG-1/ErbB4 pathway for synaptic plasticity and behaviors associated with psychiatric disorders. *J Neurosci* 2012, 32: 2988–2997.
 53. Xiao Y, Lui S, Deng W, Yao L, Zhang W, Li S, *et al.* Altered cortical thickness related to clinical severity but not the untreated disease duration in schizophrenia. *Schizophr Bull* 2013, 41: 201–210.
 54. Ferro A, Roiz-Santianez R, Ortiz-Garcia de la Foz V, Tordesillas-Gutierrez D, Ayesa-Arriola R, de La Fuente-Gonzalez N, *et al.* A cross-sectional and longitudinal structural magnetic resonance imaging study of the post-central gyrus in first-episode schizophrenia patients. *Psychiatry Res* 2015, 231: 42–49.
 55. Scanlon C, Anderson-Schmidt H, Kilmartin L, McInerney S, Kenney J, McFarland J, *et al.* Cortical thinning and caudate abnormalities in first episode psychosis and their association with clinical outcome. *Schizophr Res* 2014, 159: 36–42.
 56. Ebdrup B. Hippocampal and caudate volume reductions in antipsychotic-naïve first-episode schizophrenia. *J Psychiatry Neurosci* 2010, 35: 95–104.
 57. Mucci A, Dima D, Soricelli A, Volpe U, Bucci P, Frangou S, *et al.* Is avolition in schizophrenia associated with a deficit of dorsal caudate activity? A functional magnetic resonance imaging study during reward anticipation and feedback. *Psychol Med* 2015, 45: 1765–1778.
 58. Li H, Tang J, Chen L, Liao Y, Zhou B, He Y, *et al.* Reduced middle cingulate gyrus volume in late-onset schizophrenia in a Chinese Han population: a voxel-based structural MRI study. *Neurosci Bull* 2015, 31: 626–627.
 59. Zhou D, Pang F, Liu S, Shen Y, Liu L, Fang Z, *et al.* Altered motor-striatal plasticity and cortical functioning in patients with schizophrenia. *Neurosci Bull* 2016, 33: 307–311.
 60. Torkamani A, Wineinger NE, Topol EJ. The personal and clinical utility of polygenic risk scores. *Nat Rev Genet* 2018, 19: 581–590.
 61. Kegeles LS, Mao X, Stanford AD, Girgis RR, Ojeil N, Xu X, *et al.* Elevated prefrontal cortex γ -aminobutyric acid and glutamate-glutamine levels in schizophrenia measured in vivo with proton magnetic resonance spectroscopy. *Arch Gen Psychiatry* 2012, 69: 449–459.



MiR-125a-5p Regulates Vitamin D Receptor Expression in a Mouse Model of Experimental Autoimmune Encephalomyelitis

Han-Chun Long^{2,4} · Rui Wu³ · Chun-Feng Liu^{2,3} · Fei-Long Xiong^{2,4} · Zu Xu¹ · Dian He¹ · Yi-Fan Zhang¹ · Bing Shao¹ · Ping-An Zhang³ · Guang-Yin Xu³ · Lan Chu^{1,2}

Received: 19 February 2019 / Accepted: 8 May 2019 / Published online: 19 August 2019
© Shanghai Institutes for Biological Sciences, CAS 2019

Abstract Multiple sclerosis (MS) is a chronic and incurable autoimmune neurodegenerative disease of the central nervous system. Although the symptoms of MS can be managed by vitamin D3 treatment alone, this condition cannot be completely eradicated. Thus, there might be unknown factors capable of regulating the vitamin D receptor (VDR). Genome-wide analysis showed that miRNAs were associated with VDRs. We sought to determine the role and mechanism of action of miRNA-125a-5p and VDRs in a model of MS, mice with experimental autoimmune encephalomyelitis (EAE), which was induced by myelin oligodendrocyte glycoprotein 35–55 peptides. EAE mice showed decreased mean body weight but increased mean clinical scores compared with vehicle or control mice. And inflammatory infiltration was found in the lumbosacral spinal cord of EAE mice. In addition, VDR expression was significantly lower while the expression of miR-125a-5p was markedly higher in the spinal ventral horn of EAE mice than in vehicle or control

mice. Importantly, activation of VDRs by paricalcitol or inhibition of miR-125a-5p by its antagomir markedly decreased the mean clinical scores in EAE mice. Interestingly, VDR and miR-125a-5p were co-localized in the same neurons of the ventral horn. More importantly, inhibition of miR-125a-5p remarkably blocked the decrease of VDRs in EAE mice. These results support a critical role for miR-125a-5p in modulating VDR activity in EAE and suggest potential novel therapeutic interventions.

Keywords Multiple sclerosis · Experimental autoimmune encephalomyelitis · Vitamin D receptor · MiR-125a-5p · Myelin oligodendrocyte glycoprotein 35–55 peptides

Introduction

Multiple sclerosis (MS) is a genetically [1–3] and immunologically complex disease defined by both myelin loss and neurodegeneration. It is characterized by infiltration of T lymphocytes and monocytes, inflammatory mediators, loss of oligodendrocytes, formation of reactive astrocytes, and axonal injury and loss [4–7]. The therapeutic interventions for MS are very limited and poorly effective [8], resulting in repeated attacks of the condition [9, 10]. Moreover, the molecular mechanisms underlying MS are poorly understood. Therefore, investigation of the pathogenic mechanism of MS is essential. The experimental autoimmune encephalomyelitis (EAE) mouse is a useful experimental model of MS in which inflammation provokes neurological and pathological symptoms similar to those of MS patients [4].

A growing body of evidence has pointed out that environmental factors might play a major role in MS

Han-Chun Long and Rui Wu have contributed equally to this work.

✉ Guang-Yin Xu
guangyinxu@suda.edu.cn

✉ Lan Chu
chulan8999@yeah.net

¹ Department of Neurology, The Affiliated Hospital of Guizhou Medical University, Guiyang 550001, China

² Department of Neurology, The Second Affiliated Hospital of Soochow University, Suzhou 215008, China

³ Institute of Neuroscience, Soochow University, Suzhou 215123, China

⁴ Department of Neurology, The Affiliated Xingyi City Hospital of Guizhou Medical University, Xingyi 562400, China

[11, 12]. Studies have shown that deficiency of vitamin D3 (D3) increases the incidence of EAE. Direct immunomodulatory effects of D3 on cells of the central nervous system (CNS), including astrocytes [13] and microglia [14], have recently been reported, and the D3 signals in a variety of immune cells are mediated by the vitamin D receptors (VDRs) [15–17]. The regulatory role of VDRs in adaptive immune responses also includes an inhibitory effect on dendritic cell maturation and differentiation [18, 19]. Vitamin D analogs like paricalcitol (PC) attenuate the inflammatory process and preserve the myelin sheath [20, 21]. However, the regulation of VDR expression and its involvement in MS are still unclear.

MicroRNAs (mRNAs) are small non-coding RNAs that regulate gene expression and stabilize the translation of mRNAs. They are involved in many biological and pathological processes such as development, functional dysregulation, differentiation, regeneration, and ontogenesis [2, 22–24], as well as several autoimmune diseases including MS [25, 26]. However, in autoimmune diseases, promising miRNA candidates for therapeutic development remain severely limited. MiRNAs exert their functions by binding to the 3' untranslated regions (UTRs) of their target mRNAs, thus promoting mRNA degradation or repressing protein translation [27, 28]. However, the regulation of VDR expression by miRNAs in MS remains unclear. According to bioinformatics analysis (TargetsCan and miRNA.org), miR-125-5p can bind to the 3' UTR of VDR mRNA. MiR-125a-5p has been confirmed to be functionally relevant in the context of immune cell activation, and inflammation – particularly in the settings of rheumatoid arthritis, neuroinflammation [29], and autoimmune diseases [30], but its role in MS remains unclear.

Based on these findings, we focused on roles of miR-125a-5p and VDRs. We hypothesized that miR-125a-5p regulates VDR expression in the spinal ventral horn in a mouse model of EAE.

Materials and Methods

Animals

Adult female C57BL/6 mice ($n = 60$, 8–12 weeks old, 18–20 g) were housed at a constant temperature of 24 ± 2 °C, 40%–60% relative humidity, and a 12-h light-dark cycle in a clean-level animal facility at the Experimental Animal Center of Soochow University. Animals were provided by the Animal Care and Use Committee of Soochow University. Food and water were given *ad libitum*. Animals were used for behavioral experiments and detection of molecular biological changes.

All procedures were performed according to the guidelines of the International Association for the Study and the Animal Care Committee of the Soochow University and were approved.

Experimental Design

Mice were separated into the following groups ($n = 60$ in total, Fig. 1): 1. Control group (CON, $n = 10$), mice did not receive any injection; 2. Vehicle group (Vehicle, $n = 10$), each mouse was injected with 0.1 mL complete Freund's adjuvant (CFA) (Sigma-aldrich, St. Louis, MO) only; 3. EAE group (EAE, $n = 10$), each mouse was immunized by injecting 0.1 mL myelin oligodendrocyte glycoprotein (MOG) 35–55 peptide (A Peptide Co., Ltd, Shanghai, China) subcutaneously – this formulation comprised 8 mg MOG 35–55 peptides emulsified in 4 mL CFA at a final concentration of 2 mg/mL, and contained 4 mg/mL of mycobacterium tuberculosis (Kaichuang, Shijiazhuang, China). This was followed by intraperitoneal injection of 0.1 mL of pertussis toxin (300 ng/0.1 mL, Sigma) in phosphate buffered saline (PBS) 1 h after MOG injection. A second identical dose of pertussis toxin was given 48 h after immunization (by intraperitoneal injection). 4. EAE + PC group ($n = 10$), mice were anesthetized by isoflurane and PC was administered by intraperitoneal injection (0.1 mL, 1 µg/kg). 5. EAE + miR-125a-5p antagomir ($n = 10$), MOG-injected mice were given miR-125a-5p antagomir or antagomir NC (10 µL, 200 nmol) ($n = 10$) daily after EAE induction [31].

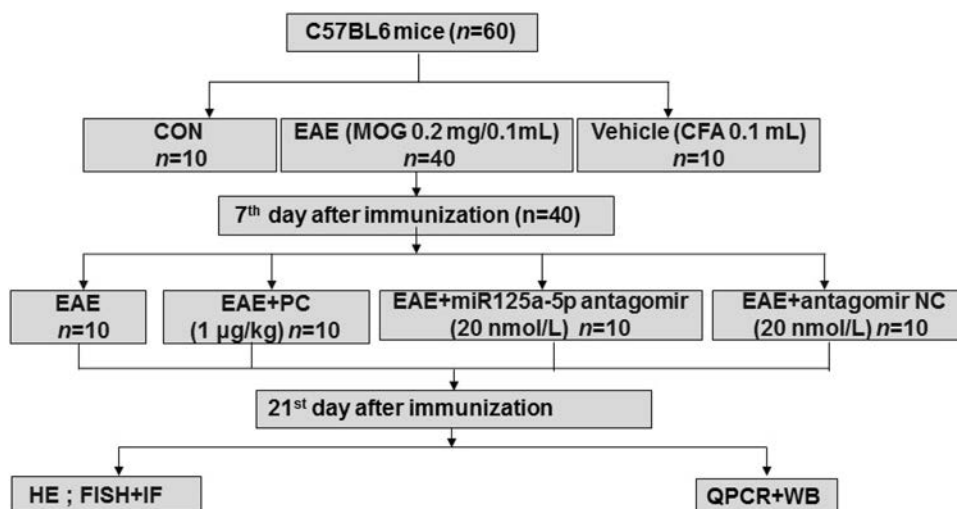
The total number of animals used was 72, but 12 were excluded (rule out models that are not successful), leaving 60.

EAE severity was determined by body weight and clinical scores. Body weight and symptoms were recorded daily. The clinical scores were assigned according to the following scale: Grade 0, no clinical signs; Grade 1, tail paralysis; Grade 2, abnormal gait; Grade 3, hind limb paralysis; Grade 4, complete paralysis; Grade 5, death or euthanasia with scoring intervals of 0.5 as described previously [32, 33]. Twenty-one days after EAE induction, mice were sacrificed and spinal cord tissue was collected and stored at -80 °C for further analyses.

Hematoxylin and Eosin Staining

Histopathological analysis was performed on day 21 after EAE induction. After euthanasia, lumbar spinal cord specimens were removed and fixed in 10% neutral buffered formalin. The tissue was dehydrated in graded ethanols and embedded in Paraplast Plus (McCormick, St. Louis, MO). Serial sections were cut at 10 µm and stained with hematoxylin and eosin (HE). Five photomicrographs were

Fig. 1 Flowchart of the experimental design.



captured from each animal with a Nikon microscope (Olympus, Shinjuku-ku, Tokyo, Japan). CNS inflammation was assessed using a semi-quantitative scoring system according to the following previously-described criteria [34]: 0, no infiltrates; 1, partial meningeal infiltration; 2, pronounced meningeal infiltration; 3, pronounced meningeal and some parenchymal infiltration.

Immunofluorescence

Mice were deeply anesthetized by isoflurane inhalation and then transcardially perfused with normal saline and 4% paraformaldehyde (Sinopharm Chemical Reagent Co. Ltd, Shanghai, China). Next, the lumbar enlargement was removed, post-fixed for 2 h with paraformaldehyde, and then dehydrated successively in 10%, 20% and 30% sucrose (dissolved in PBS; Sinopharm Chemical Reagent Co. Ltd.) until the tissue sank. The tissue was embedded in optimal cutting temperature compound (Sakura, Tokyo, Japan) and stored at -80°C until sectioning. The tissue was cut at $10\ \mu\text{m}$ on a freezing microtome (Leica, Wetzlar, Germany). For immunofluorescence, the sections were washed with PBS, blocked with 2% bovine serum albumin in PBS for 2 h, and then incubated overnight with primary antibodies against VDR (1:1000, Santa Cruz Biotechnology, CA, USA), NeuN (1:50, Merck Millipore, MA, USA), GFAP (1:300, Millipore), and CD11b (1:200, Abcam, Cambridge, UK) at 4°C overnight. The sections were washed three times with PBS for 5 min, and then incubated with the secondary antibodies Alexa Fluor488 (1:500, Molecular Probes, New York, USA) and Alexa Fluor555 (1:100, Molecular Probes) for 2 h at room temperature (RT). Primary antibodies were omitted to provide negative controls.

Fluorescence *In Situ* Hybridization (FISH)

FISH was performed with an enhanced sensitivity ISH detection Kit I (POD, Boster, Wuhan, China). A locked nucleic acid probe complementary to miR-125a-5p was labeled with 5' and 3'-digoxigenin and synthesized by Exiqon (Woburn, MA, USA). The slides were incubated in blocking buffer for 30 min at RT before they were pre-hybridized for 2 h at 37°C , and then exposed to a $1\ \mu\text{g}/\text{mL}$ probe in $60\text{--}120\ \mu\text{L}$ of hybridization mixture that was added to each slide and incubated overnight at 37°C . After washing with $2 \times$ Saline Sodium Citrate (SSC), $0.5 \times$ SSC, and $0.2 \times$ SSC, the slides were blocked in blocking solution, biotinylated mouse anti-digoxin was added and left for 1–2 h, then after 3 washes with $0.5\ \text{mol}/\text{L}$ PBS for 5 min each, the slides were incubated with POD-CY3 (1:100) for 1 h (Boster). The slides were blocked with 2% bovine serum albumin in PBS for 2 h and then incubated overnight with primary antibodies and fluorogenic secondary antibodies. All images were captured with a confocal microscope (Leica, TCS SP8).

Western Blot

Spinal ventral horns isolated from control and EAE mice were homogenized by ultrasonication in lysate. The re-suspended pellets were kept on ice for 2 h, centrifuged at $15,000\ \text{rpm}$ for 30 min at 4°C , and the supernatant retained to estimate proteins. The quantity of protein was determined with a BCA protein assay kit (MultiSciences, Hangzhou, China). After denaturation in a water bath at 75°C for 10 min, protein samples ($40\ \mu\text{g}$) were loaded onto 10% sodium dodecyl sulfate polyacrylamide gels (Bio-Rad, Hercules, CA) and transferred onto polyvinylidene difluoride membranes (Millipore). After transfer, the membranes were blocked with Tris-HCl buffer solution

(TBS) (50 mmol/L Tris-HCl, 133 mmol/L NaCl, pH = 7.4) containing 5% non-fat dried milk for 2 h at RT, and incubated overnight at 4 °C with the following specific antibodies: VDR (1:1000; Santa Cruz Biotechnology, USA) and GAPDH (1:2000, Santa Cruz Biotechnology). Then, membranes were washed in TBST (TBS containing 0.5% Tween) and incubated with horseradish peroxidase-conjugated anti-mouse (1:2000, Multi sciences, Hangzhou, China) or anti-rabbit IgG secondary antibody (1:2000, Jackson ImmunoResearch Laboratories, PA, USA) for 2 h at RT. Then, protein bands were quantified by enhanced chemiluminescence (Tanon, Shanghai, China) followed by optical density analysis. All images were captured using ImageJ software (Bio-Rad, CA, USA).

Real-Time Quantitative PCR (qPCR)

According to the manufacturer's instructions, RNA was extracted with TRIzol reagent (Ambion, Shanghai, China). The first-strand cDNA of the VDR was synthesized and analyzed from total RNA using a standard protocol with a reverse transcription kit (Transgen Biotech, Beijing, China). The PCR denaturation temperature curve was composed of 40 cycles at 95 °C for 15 s, with an annealing and elongation reaction at 60 °C for 1 min. The primers used for qPCR were utilized by Sangon Biotech (Shanghai, China). U6 was used as an internal control for miRNA. The primers used in this study were as follows:

GAPDH-F: 5'-GGTTGTCTCCTGCGACTTCA-3';
 GAPDH-R: 5'-TGGTCCAGGGTTTCTTACTCC-3';
 mmu-miR-125b-5p-F: 5'-CGCGTCCCTGAGACCCTAAC-3';
 mmu-miR-125b-5p-RT: 5'-GTCGTATCCAGTGCAGGTCCGAGGTATTCGCACTGGATACGACTCACAA-3';
 mmu-miR-351-5p-F 5'-GTCCCTGAGGAGCCCTTTG-3';
 mmu-miR-351-5p-RT: 5'-GTCGTATCCAGTGCAGGGTCCGAGGTATTCGCACTGCATACGACCAGGCT-3';
 mmu-miR-125a-5p-F: 5'-GCGTCCCTGAGACCCTTAAAC-3';
 mmu-miR-125a-5p-RT: 5'-GTCGTATCCAGTGCAGGTCCGAGGTATTCGCACTGGATACGACTCACAG-3';
 U6-F: 5'-AGAGAAGATTAGCATGGCCCCTG-3';
 U6-R: 5'-AGTGCAGGGTCCGAGGTATT-3';
 U6-RT: 5'-GTCGTATCCAGTGCAGGGTCCGAGGTATTCGCACTGGATACGACAAAAAT-3';
 VDR-F: 5'-GCAGCGTAAGCGAGAGATGAT-3';
 VDR-R: 5'-AGGGGGTGTACAGATCAGAGTTTG-3'.
 Common primer downstream of stem loop: 5'-AGTGCAGGGTCCGAGGTATT-3'.

Levels of gene expression are presented as relative fold difference using the method of the delta-delta threshold ($2^{-\Delta\Delta Ct}$).

Statistical Analysis

All results are expressed as the mean \pm SEM. Prior to analysis, all data were tested for normality. When the comparisons involved two means, Student's *t*-test was used. When multiple comparisons were involved, a single factor analysis of variance (ANOVA) or Friedman ANOVA was first performed to obtain a global test of the null hypothesis. If the overall *P*-value (alpha value) of the null hypothesis test was $P < 0.05$, subsequent comparison of different groups was conducted using the Dunn's subsequent test. The Mann-Whitney test was used when the means were not normally distributed. When an alpha value of $P < 0.05$ was evident, the comparison was considered statistically significant. Quantitative statistical data were analyzed using Prism software for multi-group comparisons (Version 8, GraphPad-Prism, San Diego, CA).

Results

Mean Clinical Scores are Higher and Body Weight Lower in EAE Mice

From the day of administration, EAE animals were less active and responsive, with a weak tail and rough unkempt fur. By comparing the mean clinical scores of the three groups, we found that the scores in the EAE group were significantly higher, but their body weights were clearly lower than the control and vehicle groups from day 7 after immunization ($n = 6$). The mean clinical score of the control and vehicle groups was 0 ± 0 on all days, and body weight gradually increased from day 0 to 21 ($n = 6$). However, the mean clinical score of the EAE group gradually increased (Fig. 2A), and their body weight gradually decreased from day 0 to 21 (Fig. 2B).

Inflammatory Infiltration in Lumbar Spinal Cord of EAE Mice

On day 21 post-immunization, the lumbar spinal cord was removed from mice of each group, paraffin sectioned, and stained with HE (Fig. 2C, D). The results showed that there was no phenomenon of "vascular cuff" and inflammatory infiltration in control mice (Fig. 2C, left). However, diffuse inflammatory infiltration and a phenomenon of "vascular cuff" were found in EAE mice (Fig. 2C, right). Pathological scores were 0 ± 0 ($n = 3$) in control mice and

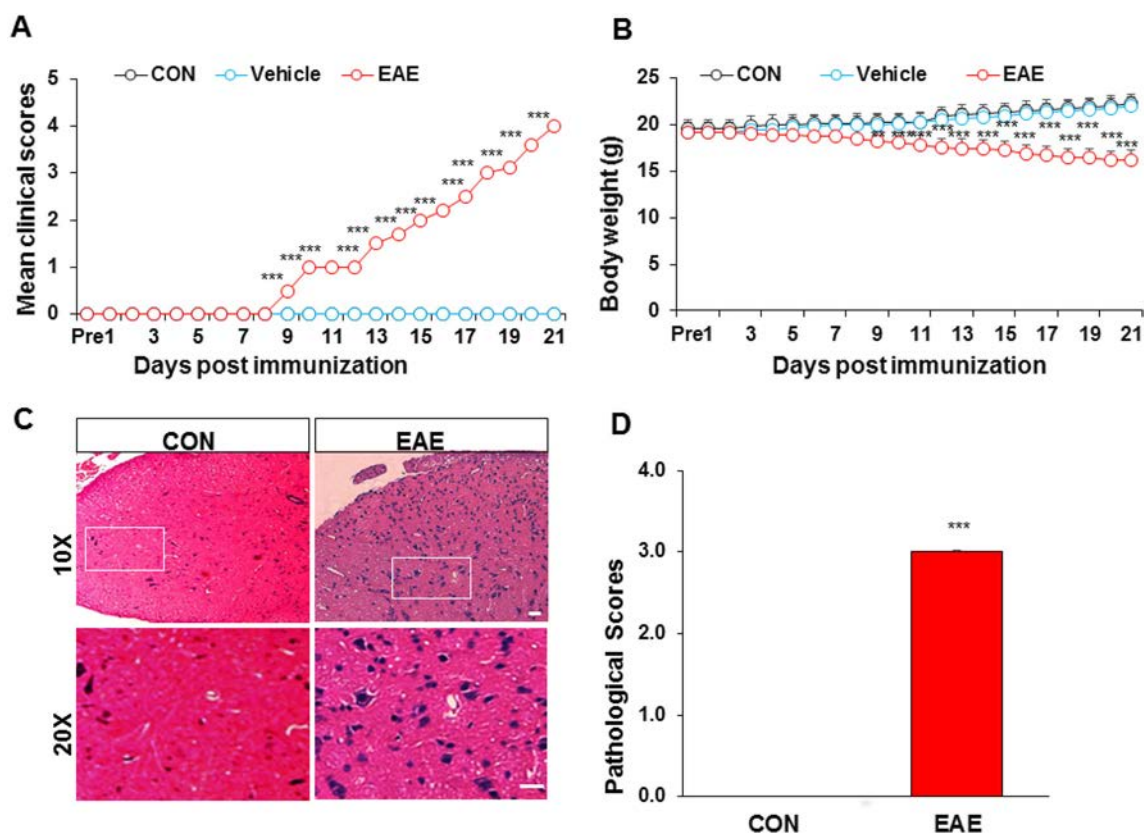


Fig. 2 Changes in mean clinical scores, body weight, and HE staining in EAE mice. **A** The mean clinical score was higher in the EAE than in the control (CON) and vehicle groups ($n = 6$, $***P < 0.001$, two-way ANOVA). **B** The body weight of EAE mice decreased gradually, while that of control and vehicle mice increased

significantly higher at 3.00 ± 0.02 ($n = 3$) in EAE mice (Fig. 2D).

VDR Expression is Lower in the Ventral Horn of EAE Mice

VDR expression in the ventral horn was assessed by qPCR and Western blot. The results showed that the relative mRNA levels of VDR were 1.00 ± 0.24 ($n = 4$) in control mice, 0.97 ± 0.16 ($n = 4$) in vehicle mice, and 0.11 ± 0.04 ($n = 4$) in EAE mice. Statistical analysis showed that the VDR mRNA in EAE mice was markedly lower than that in control or vehicle mice (Fig. 3A). Western blots showed that the relative protein levels of VDR were 0.83 ± 0.07 ($n = 4$) in control mice, 0.67 ± 0.02 ($n = 4$) in vehicle mice, and 0.43 ± 0.01 ($n = 4$) in EAE mice, and VDR expression was significantly lower in EAE mice than in age-matched control or vehicle mice (Fig. 3B).

($n = 6$, $**P < 0.01$, $***P < 0.001$, two-way ANOVA). **C**, **D** Control mice had no phenomenon of “vascular cuff” or inflammatory infiltration. However, EAE mice showed diffuse inflammatory infiltration, some of which showed a phenomenon of “vascular cuff”. $n = 3$; $***P < 0.001$, Mann–Whitney test; scale bars, 50 μm .

VDR is Mainly Expressed in Neurons of the Ventral Horn

Localization of VDRs in the ventral horn of EAE mice was determined by immunofluorescence staining. As shown in Fig. 4, cells were stained red by NeuN (a marker of neurons), CD11b (a marker of microglia), or GFAP (a marker of astrocytes) (Fig. 4A, D, G), and VDR-positive cells were stained green (Fig. 4B, E, H). The merged images showed that VDR was mainly expressed in neurons (Fig. 4C), but not in microglia (Fig. 4F) or astrocytes (Fig. 4I).

EAE Enhances the Expression of MiR-125a-5p in the Ventral Horn

Using bioinformatics prediction software (Targetscan and miRNA.org), we found that miR-125a-5p, miR-125b-5p, and miR-351-5p targeted to the 3' UTR of VDR mRNA. To test whether these selected miRNAs are involved in EAE, qPCR was used to assess their expression in the lumbar enlargement. The relative miRNA levels of miR-

Fig. 3 VDR expression was decreased in the ventral horn of EAE mice. VDR expression assessed by qPCR and Western blot. **A** The VDR mRNA level in EAE mice was markedly lower than in control (CON) or vehicle mice ($n = 4$, $**P < 0.01$, one-way ANOVA). **B** Western blots and statistics showing that VDR expression was lower in EAE than in age-matched control or vehicle mice ($n = 4$, $***P < 0.001$, one-way ANOVA).

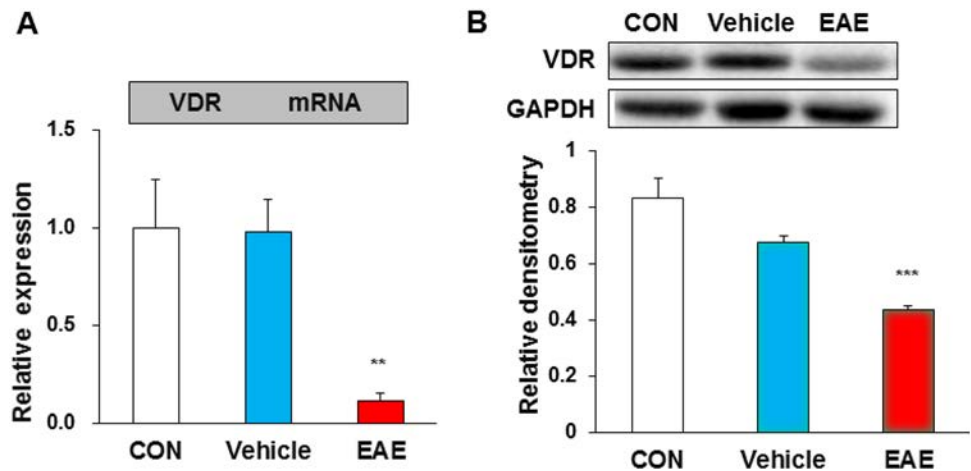
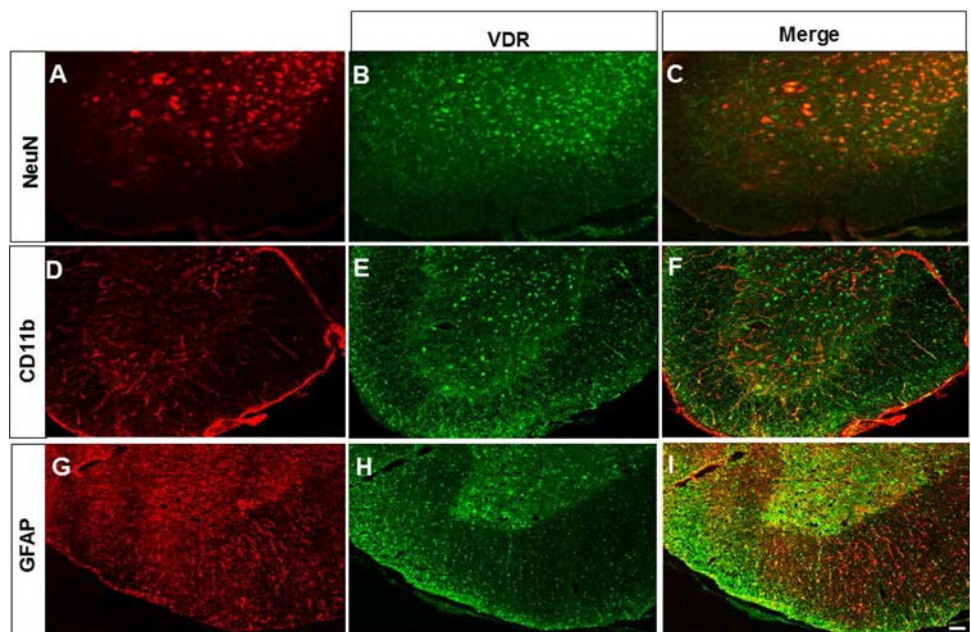


Fig. 4 VDR was mainly expressed in neurons of the ventral horn. **(A, D, G)** Cells stained red by NeuN (a marker of neurons), CD11b (a marker of microglia), or GFAP (a marker of astrocytes), and **(B, E, H)** VDR-positive cells stained green. The merged images show that VDR was mainly expressed in neurons **(C)**, but not in microglia **(F)**, or astrocytes **(I)** in the ventral horn of EAE mice. Scale bar, 50 μm .



125a-5p were 1.00 ± 0.87 in control, 1.32 ± 1.04 in vehicle, and 4.76 ± 0.54 in EAE mice ($n = 4$ for each). Statistical analysis showed significantly higher miRNA levels of miR-125a-5p in EAE than that in control or vehicle mice (Fig. 5A). The relative miRNA levels of miR-125b-5p were 1.00 ± 0.50 , 2.02 ± 0.57 , and 0.74 ± 0.19 ($n = 4$ for each), respectively. The same values for miR-351-5p were 1.00 ± 0.31 , 1.78 ± 0.34 , and 1.97 ± 0.25 ($n = 4$ for each). There were no significant differences in the miRNA levels of miR-125b-5p and miR-351-5p for EAE compared with control or vehicle mice (Fig. 5B, C). These results suggested that the expression of miR-125a-5p is enhanced in the ventral horn of EAE mice, but miR-125b-5p and miR-351-5p are unchanged.

MiR-125a-5p is Mainly Expressed in Neurons of the Ventral Horn

FISH was conducted to detect miR-125a-5p localization. Cells were stained green by NeuN (a marker of neurons, Fig. 6A), CD11b (a marker of microglia, Fig. 6E), or GFAP (a marker of astrocytes, Fig. 6I), while miR-125a-5p-positive cells were stained red (Fig. 6B, F, J), and DAPI stained nuclei blue (Fig. 6C, G, K). The merged images showed that miR-125a-5p was mainly expressed in neurons (Fig. 6D), but not in microglia (Fig. 6H) or astrocytes (Fig. 6L).

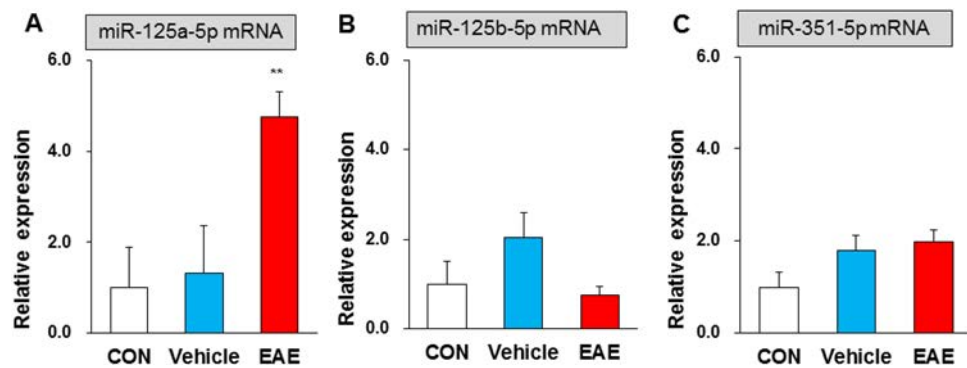
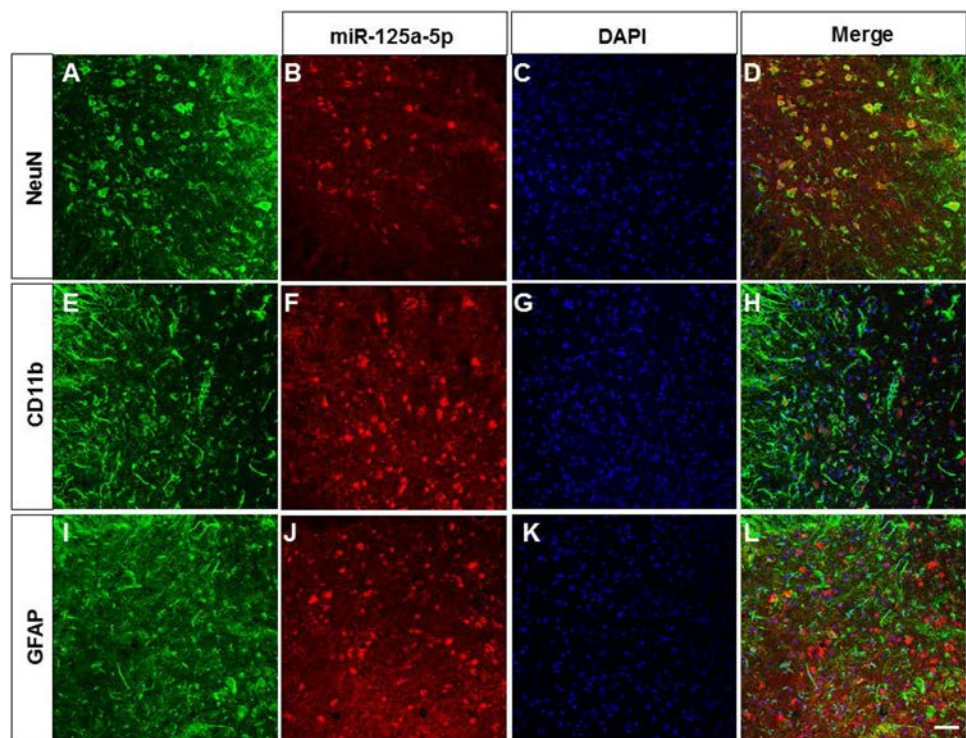


Fig. 5 EAE enhanced the expression of miR-125a-5p in the ventral horn. **A** Statistical analysis showing significantly higher miRNA levels of miR-125a-5p in EAE than in control (CON) and vehicle mice ($n = 4$, $**P < 0.01$, one-way ANOVA). **B, C** Statistical analysis

showing no significant differences in miRNA levels of miR-125b-5p and miR-351-5p for EAE compared with control and vehicle mice ($n = 4$, $P > 0.05$, one-way ANOVA).

Fig. 6 MiR-125a-5p was mainly expressed in neurons of the ventral horn. The merged images showed that miR-125a-5p was mainly co-expressed with NeuN (**A–D**). MiR-125a-5p was not co-labelled with CD11b (**E–H**) or GFAP (**I–L**) in the ventral horn of EAE mice. Scale bar, 50 μm .



MiR-125a-5p and VDRs are Co-Localized

A precondition of the reaction between miR-125a-5p and VDRs is that they must be co-expressed in the same cell, so we used FISH to detect their co-localization. MiR-125a-5p-positive cells were stained red (Fig. 7A), VDR-positive cells were stained green (Fig. 7B), and DAPI stained nuclei blue (Fig. 7C). The merged results for VDRs and miR-125a-5p showed that they were co-expressed in the same neurons (Fig. 7D). The results for merged DAPI and miR-125a-5p showed that miR-125a-5p was mainly expressed in the cytoplasm (Fig. 7E, F).

Agonist of VDR or miR-125a-5p Antagomir Attenuates the Symptoms of EAE Mice

To verify the involvement of VDR in EAE mice, we used PC, an efficient agonist of VDR. On day 9 after PC treatment, the mean clinical score of EAE mice was lower and remained at a lower level than untreated EAE mice (Fig. 8A). Similarly, by day 9 after intraperitoneal injection of PC, the mean body weight of EAE mice gradually increased (Fig. 8B). These data suggested that VDR is involved in the MS of EAE mice. To further confirm the involvement of miR-125a-5p in MS, we used its antagomir. As expected, the miR-125a-5p antagomir (intrathecal

Fig. 7 MiR-125a-5p and VDR were co-localized. **A, B** MiR-125a-5p-positive cells were stained red (**A**), and VDR-positive cells were stained green (**B**). **C** DAPI stained the nuclei blue. **D** VDR and miR-125a-5p merged showing that both were co-expressed in the same neurons. **E** DAPI and miR-125a-5p merged showing that miR-125a-5p was mainly expressed in the cytoplasm. **F** Merged images showing that miR-125a-5p and VDR were mainly co-expressed in the cytoplasm of EAE mice. Scale bar, 25 μ m. Arrow indicates a representative cell which co-expressed miR-125a-5p dyed in red and VDR dyed in green.

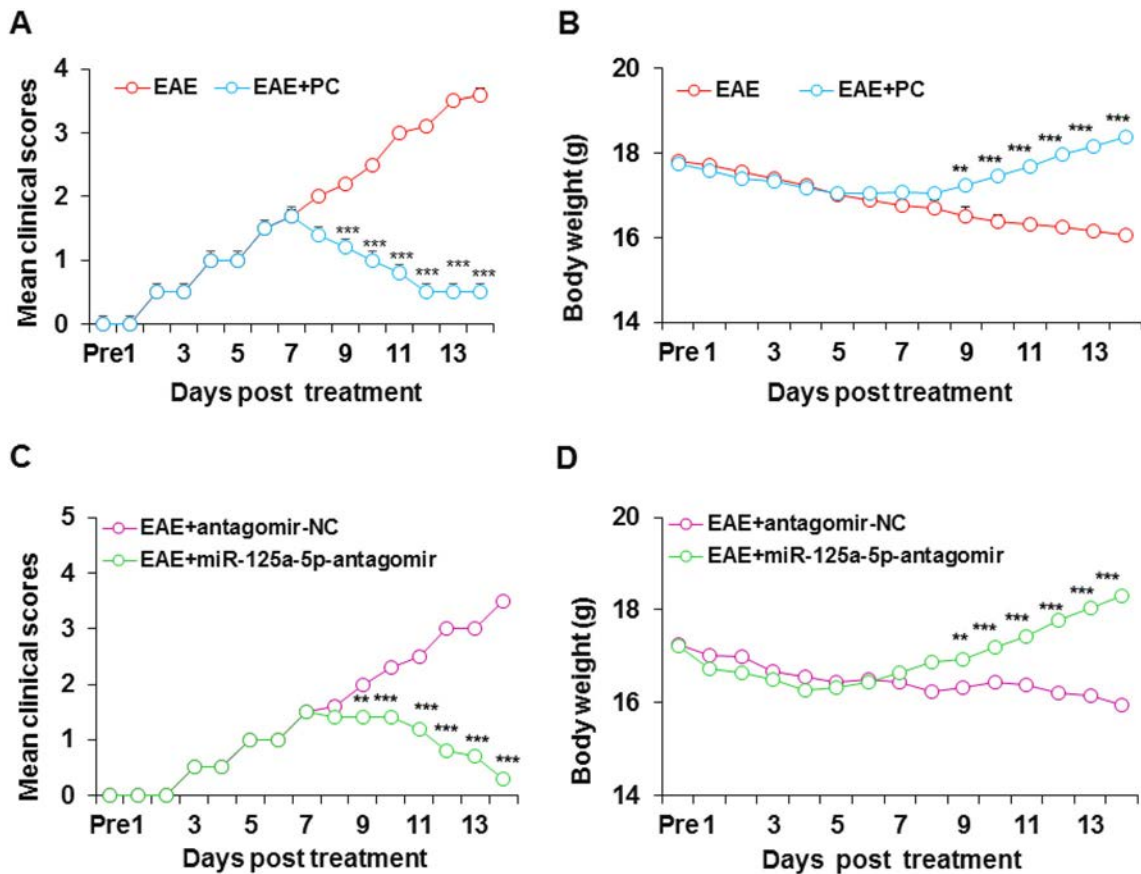
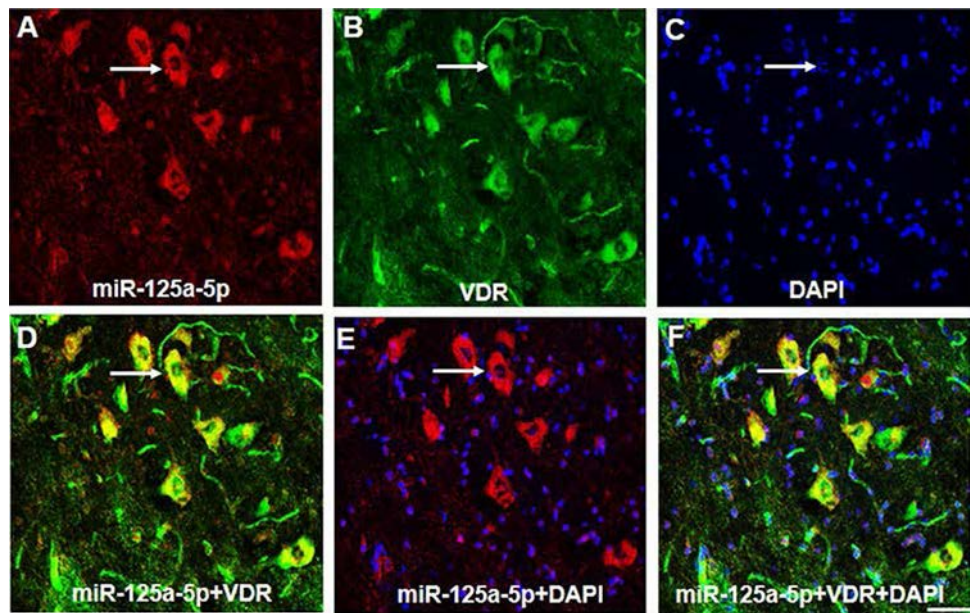


Fig. 8 Agonist of VDR or miR-125a-5p antagonist attenuated the symptoms of EAE mice. **A** Mean clinical scores of EAE mice were lower from day 9 after PC treatment than in untreated EAE mice ($n = 6$, $***P < 0.001$, two-way ANOVA). **B** The body weight of mice in the EAE + PC group gradually increased from day 9 after PC treatment, while the body weight of the untreated EAE group gradually decreased ($n = 6$, $**P < 0.01$, $***P < 0.001$, two-way

ANOVA). **C** Intrathecal injection of miR-125a-5p antagonist decreased mean clinical scores of EAE mice and attenuated the paralysis ($n = 6$, $**P < 0.01$, $***P < 0.001$, two-way ANOVA). **D** Intrathecal injection of miR-125a-5p antagonist increased the body weight of EAE mice ($n = 6$, $**P < 0.01$, $***P < 0.001$, two-way ANOVA).

injection) significantly improved the clinical scores (Fig. 8C) and body weight (Fig. 8D) of EAE mice compared with the antagomir-NC group.

MiR-125a-5p Antagomir Reverses the Decreased VDR Expression and Pathogenesis in EAE Mice

To determine how VDRs are regulated by miR-125a-5p, we assessed the mRNA and protein expression levels of VDR after intrathecal injection of miR-125a-5p antagomir or antagomir-NC. QPCR showed that the relative mRNA levels of VDR were 1.00 ± 0.92 ($n = 4$, EAE), 1.01 ± 0.67 ($n = 4$, antagomir-NC), and 12.62 ± 0.14 ($n = 4$, miR-125a-5p antagomir). Statistical analysis suggested that the VDR mRNA level was significantly higher in EAE mice after intrathecal injection of the miR-125a-5p antagomir than in the antagomir-NC and EAE groups (Fig. 9A). Western blot assays showed that VDR protein expression in EAE mice was significantly increased after intrathecal injection of the miR-125a-5p antagomir compared with the antagomir-NC or EAE groups (Fig. 9B). The relative densitometry of VDR was 0.34 ± 0.03 ($n = 4$) in EAE mice, 0.33 ± 0.00 ($n = 4$) in EAE mice treated with antagomir-NC, and 0.75 ± 0.06 ($n = 4$) in EAE mice treated with miR-125a-5p antagomir. These results suggested that miR-125a-5p targets VDRs in the mouse model of EAE.

Discussion

Vitamin D and its receptor VDR are closely associated with the development and appearance of autoimmune diseases, especially in MS [19, 35–37]. Although the symptoms of MS can be managed by vitamin D3 (D3)

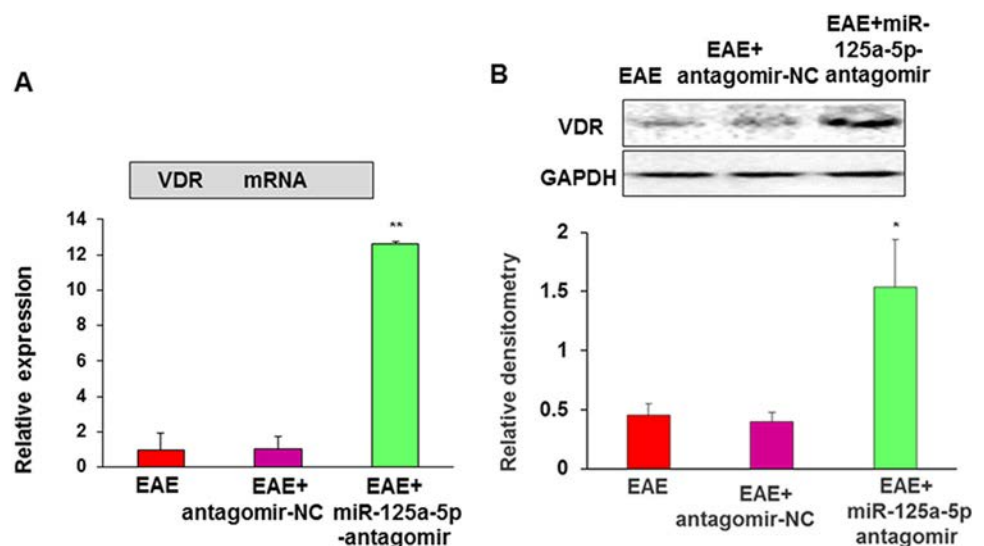
treatment alone, this condition cannot be completely eradicated. Thus, we suspected that there might be some unknown factors capable of regulating VDRs. The extensive involvement of miRNAs in human diseases has strengthened our understanding of pathogenesis and could help guide therapy [38]. However, candidates for miRNAs that have the potential to control autoimmune pathogenesis remain limited. Bioinformatics prediction software (Targets can and miRNA.org) revealed three small molecules that can regulate VDRs as identified *via* a systematic combination of bioinformatics resources [39]. However, we found that only miR-125a-5p was up-regulated and the others were not changed in EAE mice.

MiR-125a-5p is a key regulator of the tight integrity of brain endothelial cells and the egress of migrating immune cells [40, 41]. Studies have shown that miR-125a-5p is down-regulated in systemic lupus erythematosus [42], in oral mucosal disease [43], and in blood samples from pediatric patients with MS [44]. These findings provide a valuable candidate biomarker for some autoimmune diseases. In the present study, we demonstrated for the first time that miR-125a-5p in the spinal ventral horn (lumbar enlargement) is involved in an EAE model induced by MOG. We provided the following supporting evidence: first, miR-125a-5p expression was increased at both the protein and mRNA levels in the ventral horn of the lumbar enlargement of EAE mice; second, and importantly, application of the miR-125a-5p antagomir significantly reduced the clinical symptoms in EAE mice.

So far, how miR-125-5p contributes to the development of autoimmunity is unclear. Some researchers have demonstrated that miR-125a-5p inhibits inflammation by disrupting the differentiation of other effector molecules, thereby stabilizing regulatory T cell commitment and immunoregulation [40, 45]. This finding identified miR-

Fig. 9 MiR-125a-5p antagomir enhanced VDR expression.

A QPCR showed that the VDR mRNA level was significantly higher in EAE mice after intrathecal injection of the miR-125a-5p antagomir than in the antagomir-NC and EAE groups of mice ($n = 4$, $**P < 0.01$, one-way ANOVA). **B** Western blot assays showed that VDR protein expression in EAE mice was significantly higher after intrathecal injection of the miR-125a-5p antagomir than in the antagomir-NC and EAE groups ($n = 4$, $*P < 0.01$, one-way ANOVA).



125a-5p as a key regulator of CD4⁺ T-cell differentiation that prevents autoimmune pathogenesis by controlling the balance between immune tolerance and the development of autoimmunity [46, 47]. We showed here that miR-125-5p specifically targeted VDRs in the spinal ventral horn; this might be one of mechanisms of MS development, although miR-125a-5p has > 100 targets. We showed that inhibition of miR-125a-5p reversed the pattern of decreased VDR expression at the protein and mRNA levels. Importantly, the results of immunofluorescence analysis and FISH demonstrated that miR-125a-5p was co-localized with VDRs in the same spinal neurons – an observation that indicated the anatomical possibility of the regulation of VDR expression by miR-125a-5p. More importantly, application of the miR-125a-5p antagomir clearly reversed the decreased VDR expression both at the protein and at the mRNA levels.

In summary, we demonstrated that miR-125a-5p/VDR signaling plays a critical role in EAE, and suggested a potential novel therapeutic application in MS and other autoimmune disease states.

Acknowledgements This work was supported by the International Science and Technology Cooperation Plan of Guizhou Province, China [(2013) 7027] and the National Natural Science Foundation of China (81471137 and 31730040).

Conflict of interest The authors declare that they have no competing interests.

References

- Lau A, Qiu W, Kermod A, Au C, Ng A, Wong A, *et al.* High prevalence and indexes of anti-John Cunningham virus antibodies in a cohort of Chinese patients with multiple sclerosis. *Mult Scler J Exp Transl Clin* 2018, 4: 2055217318788699.
- Li WY, Zhang WT, Cheng YX, Liu YC, Zhai FG, Sun P, *et al.* Inhibition of KLF7-targeting MicroRNA 146b promotes sciatic nerve regeneration. *Neurosci Bull* 2018, 34: 419–437.
- Zhang Z, Chen W, Zhao Y, Yang Y. Spatiotemporal imaging of cellular energy metabolism with genetically-encoded fluorescent sensors in brain. *Neurosci Bull* 2018, 34: 875–886.
- Hauser SL, Oksenberg JR. The neurobiology of multiple sclerosis: genes, inflammation, and neurodegeneration. *Neuron* 2006, 52: 61–76.
- Li Z, Li K, Zhu L, Kan Q, Yan Y, Kumar P, *et al.* Inhibitory effect of IL-17 on neural stem cell proliferation and neural cell differentiation. *BMC Immunol* 2013, 14: 20.
- Popescu BF, Pirko I, Lucchinetti CF. Pathology of multiple sclerosis: where do we stand? *Continuum (Minneapolis)* 2013, 19: 901–921.
- Lu Y, Zhu ZG, Ma QQ, Su YT, Han Y, Wang X, *et al.* A critical time-window for the selective induction of hippocampal memory consolidation by a brief episode of slow-wave sleep. *Neurosci Bull* 2018, 34: 1091–1099.
- Chang Y, Shu Y, Sun X, Xu C, He D, Fang L, *et al.* Ectrodactyly in a Chinese patient born to a mother with neuromyelitis optica spectrum disorder. *Mult Scler Relat Disord* 2018, 19: 70–72.
- Butzkueven H, Calabresi PA. Is my MS patient failing treatment? *Neurology* 2016, 87: 124–125.
- Giovannoni G, Butzkueven H, Dhib-Jalbut S, Hobart J, Kobelt G, Pepper G, *et al.* Brain health: time matters in multiple sclerosis. *Mult Scler Relat Disord* 2016, 9 Suppl 1: S5–S48.
- Ascherio A, Munger KL, Simon KC. Vitamin D and multiple sclerosis. *Lancet Neurol* 2010, 9: 599–612.
- Burden of illness of multiple sclerosis: Part II: Quality of life. The Canadian burden of illness study group. *Can J Neurol Sci* 1998, 25: 31–38.
- Jiao KP, Li SM, Lv WY, Jv ML, He HY. Vitamin D3 repressed astrocyte activation following lipopolysaccharide stimulation in vitro and in neonatal rats. *Neuroreport* 2017, 28: 492–497.
- Boontanrart M, Hall SD, Spanier JA, Hayes CE, Olson JK. Vitamin D3 alters microglia immune activation by an IL-10 dependent SOCS3 mechanism. *J Neuroimmunol* 2016, 292: 126–136.
- Baeke F, Takiishi T, Korf H, Gysemans C, Mathieu C. Vitamin D: modulator of the immune system. *Curr Opin Pharmacol* 2010, 10: 482–496.
- Takahashi K, Nakayama Y, Horiuchi H, Ohta T, Komoriya K, Ohmori H, *et al.* Human neutrophils express messenger RNA of vitamin D receptor and respond to 1 α ,25-dihydroxyvitamin D3. *Immunopharmacol Immunotoxicol* 2002, 24: 335–347.
- Yang JT, Wang ZJ, Cai HY, Yuan L, Hu MM, Wu MN, *et al.* Sex differences in neuropathology and cognitive behavior in APP/PS1/tau triple-transgenic mouse model of Alzheimer's disease. *Neurosci Bull* 2018, 34: 736–746.
- Penna G, Adorini L. 1 α ,25-dihydroxyvitamin D3 inhibits differentiation, maturation, activation, and survival of dendritic cells leading to impaired alloreactive T cell activation. *J Immunol* 2000, 164: 2405–2411.
- Sazci A, Uren N, Idrisoglu HA, Ergul E. The rs2228570 variant of the Vitamin D receptor gene is associated with essential tremor. *Neurosci Bull* 2019, 35: 362–364.
- Sochorova K, Budinsky V, Rozkova D, Tobiasova Z, Dusilova-Sulkova S, Spisek R, *et al.* Paricalcitol (19-nor-1,25-dihydroxyvitamin D2) and calcitriol (1,25-dihydroxyvitamin D3) exert potent immunomodulatory effects on dendritic cells and inhibit induction of antigen-specific T cells. *Clin Immunol* 2009, 133: 69–77.
- Gonzalez-Mateo GT, Fernandez-Millara V, Bellon T, Liappas G, Ruiz-Ortega M, Lopez-Cabrera M, *et al.* Paricalcitol reduces peritoneal fibrosis in mice through the activation of regulatory T cells and reduction in IL-17 production. *PLoS One* 2014, 9: e108477.
- Campos-Melo D, Hawley ZCE, Strong MJ. Dysregulation of human NEFM and NEFH mRNA stability by ALS-linked miRNAs. *Mol Brain* 2018, 11: 43.
- Oakes JA, Davies MC, Collins MO. TBK1: a new player in ALS linking autophagy and neuroinflammation. *Mol Brain* 2017, 10: 5.
- Wu R, Zhang PA, Liu X, Zhou Y, Xu M, Jiang X, *et al.* Decreased miR-325-5p contributes to visceral hypersensitivity through post-transcriptional upregulation of CCL2 in rat dorsal root ganglia. *Neurosci Bull* 2019. <https://doi.org/10.1007/s12264-019-00372-x>.
- Ambros V. The functions of animal microRNAs. *Nature* 2004, 431: 350–355.
- Nicoloso MS, Spizzo R, Shimizu M, Rossi S, Calin GA. MicroRNAs—the micro steering wheel of tumour metastases. *Nat Rev Cancer* 2009, 9: 293–302.
- Guerrou-de-Arellano M, Alder H, Ozer HG, Lovett-Racke A, Racke MK. miRNA profiling for biomarker discovery in multiple sclerosis: from microarray to deep sequencing. *J Neuroimmunol* 2012, 248: 32–39.

28. Junker A, Hohlfeld R, Meinel E. The emerging role of microRNAs in multiple sclerosis. *Nat Rev Neurol* 2011, 7: 56–59.
29. Li X, Kroin JS, Kc R, Gibson G, Chen D, Corbett GT, *et al.* Altered spinal microRNA-146a and the microRNA-183 cluster contribute to osteoarthritic pain in knee joints. *J Bone Miner Res* 2013, 28: 2512–2522.
30. Pan W, Zhu S, Dai D, Liu Z, Li D, Li B, *et al.* MiR-125a targets effector programs to stabilize Treg-mediated immune homeostasis. *Nat Commun* 2015, 6: 7096.
31. Su S, Shao J, Zhao Q, Ren X, Cai W, Li L, *et al.* MiR-30b attenuates neuropathic pain by regulating voltage-gated sodium channel Nav1.3 in rats. *Front Mol Neurosci* 2017, 10: 126.
32. Becher B, Durell BG, Noelle RJ. Experimental autoimmune encephalitis and inflammation in the absence of interleukin-12. *J Clin Invest* 2002, 110: 493–497.
33. Garay L, Gonzalez Deniselle MC, Lima A, Roig P, De Nicola AF. Effects of progesterone in the spinal cord of a mouse model of multiple sclerosis. *J Steroid Biochem Mol Biol* 2007, 107: 228–237.
34. Fraga-Silva TF, Mimura LA, Zorzella-Pezavento SF, Ishikawa LL, Franca TG, Thome R, *et al.* Tolerogenic vaccination with MOG/VitD overcomes aggravating effect of *C. albicans* in experimental encephalomyelitis. *CNS Neurosci Ther* 2016, 22: 807–816.
35. Smolders J, Menheere P, Kessels A, Damoiseaux J, Hupperts R. Association of vitamin D metabolite levels with relapse rate and disability in multiple sclerosis. *Mult Scler* 2008, 14: 1220–1224.
36. Munger KL, Aivo J, Hongell K, Soilu-Hanninen M, Surcel HM, Ascherio A. Vitamin D status during pregnancy and risk of multiple sclerosis in offspring of women in the finnish maternity cohort. *JAMA Neurol* 2016, 73: 515–519.
37. Munger KL, Levin LI, Hollis BW, Howard NS, Ascherio A. Serum 25-hydroxyvitamin D levels and risk of multiple sclerosis. *JAMA* 2006, 296: 2832–2838.
38. Abidin AZ, Chockanathan U, AM DS, Inglese M, Wismuller A. Using large-scale granger causality to study changes in brain network properties in the clinically isolated syndrome (CIS) stage of multiple sclerosis. *Proc SPIE Int Soc Opt Eng* 2017, 10137.
39. Wang Y, Yang Z, Le W. Tiny but mighty: Promising roles of microRNAs in the diagnosis and treatment of Parkinson's disease. *Neurosci Bull* 2017, 33: 543–551.
40. Zhang J, Shi K, Li Z, Li M, Han Y, Wang L, *et al.* Organ- and cell-specific immune responses are associated with the outcomes of intracerebral hemorrhage. *FASEB J* 2018, 32: 220–229.
41. Mo JL, Pan ZG, Chen X, Lei Y, Lv LL, Qian C, *et al.* MicroRNA-365 knockdown prevents ischemic neuronal injury by activating oxidation resistance 1-mediated antioxidant signals. *Neurosci Bull* 2019. <https://doi.org/10.1007/s12264-019-00371-y>.
42. Zhao X, Tang Y, Qu B, Cui H, Wang S, Wang L, *et al.* MicroRNA-125a contributes to elevated inflammatory chemokine RANTES levels via targeting KLF13 in systemic lupus erythematosus. *Arthritis Rheum* 2010, 62: 3425–3435.
43. Hu JY, Zhang J, Cui JL, Liang XY, Lu R, Du GF, *et al.* Increasing CCL5/CCR5 on CD4 + T cells in peripheral blood of oral lichen planus. *Cytokine* 2013, 62: 141–145.
44. Liguori M, Nuzziello N, Licciulli F, Consiglio A, Simone M, Viterbo RG, *et al.* Combined microRNA and mRNA expression analysis in pediatric multiple sclerosis: an integrated approach to uncover novel pathogenic mechanisms of the disease. *Hum Mol Genet* 2018, 27: 66–79.
45. Wang J, Li X, Zhang DQ, Yang CS, Qi Y, Li MS, *et al.* Quantitative analysis of aquaporin-4 antibody in longitudinally extensive transverse myelitis. *J Neuroimmunol* 2015, 278: 26–29.
46. Maldonado RA, Irvine DJ, Schreiber R, Glimcher LH. A role for the immunological synapse in lineage commitment of CD4 lymphocytes. *Nature* 2004, 431: 527–532.
47. O'Shea JJ, Paul WE. Mechanisms underlying lineage commitment and plasticity of helper CD4 + T cells. *Science* 2010, 327: 1098–1102.



Failure of Placebo Analgesia Model in Rats with Inflammatory Pain

Xiang-Sha Yin¹ · Jin-Yu Yang¹ · Shuai Cao¹ · Yun Wang^{1,2}

Received: 5 January 2019 / Accepted: 21 May 2019 / Published online: 21 August 2019
© Shanghai Institutes for Biological Sciences, CAS 2019

Abstract With the shifting role of placebos, there is a need to develop animal models of placebo analgesia and elucidate the mechanisms underlying the effect. In the present study, male Sprague-Dawley rats with chronic inflammatory pain caused by complete Freund's adjuvant (CFA) underwent a series of conditioning procedures, in which morphine was associated with different cues, but they failed to induce placebo analgesia. Then, conditioning with the conditioned place preference apparatus successfully induced analgesic expectancy and placebo analgesia in naïve rats but only induced analgesic expectancy and no analgesic effect in CFA rats. Subsequently, we found enhanced c-fos expression in the nucleus accumbens and reduced expression in the anterior cingulate cortex in naïve rats while c-fos expression in the anterior cingulate cortex in CFA rats was not altered. In summary, the behavioral conditioning model demonstrated the difficulty of

establishing a placebo analgesia model in rats with a pathological condition.

Keywords Placebo analgesia · Morphine · Conditioning · Inflammatory pain · Rat

Introduction

Chronic pain affects at least 20% of people worldwide and is a difficult problem to solve [1]. It affects many aspects of patients' quality of life and has caused the crisis of prescription opioid-related addiction and overdose [2, 3]. Recently, clinical and experimental studies have shown the efficacy of placebo analgesia, which could contribute to addressing this growing problem [4, 5]. In randomized controlled trials, placebo-associated improvements occur in 10%–60% of individuals with chronic pain [6–9]. The proper application of placebos may result in patients needing a lower cumulative amount of medication and thus having less severe side-effects [10, 11].

With the increasing interest in placebo treatments [12], a number of potential mechanisms have been proposed, including neurobiological mechanisms and psychological theories such as expectancy and classical conditioning [13]. Modern neuroimaging techniques suggest that placebos reduce pain-related brain responses and engage endogenous pain modulation circuitry *via* a μ -opioid or non-opioid mechanism [14–16]. Although human studies have successfully offered new insights into the mechanisms of placebo effects, there is still a strong need for animal models of placebo analgesia [17]. In human research, it is difficult to investigate mechanisms at the molecular and cellular levels while in animal models it is possible to conduct studies using techniques such as brain lesioning,

Xiang-Sha Yin and Jin-Yu Yang have contributed equally to this work.

Electronic supplementary material The online version of this article (<https://doi.org/10.1007/s12264-019-00420-6>) contains supplementary material, which is available to authorized users.

✉ Yun Wang
wangy66@bjmu.edu.cn

¹ Department of Neurobiology, School of Basic Medical Sciences and Neuroscience Research Institute, Key Laboratory for Neuroscience, Ministry of Education of China, and National Health Commission, State key Laboratory of Natural and Biomimetic Drugs, Peking University, Beijing 100083, China

² PKU-IDG/McGovern Institute for Brain Research, Peking University, Beijing 100871, China

genetic modification, and direct measurement of pain-related neurochemicals in the brain. Furthermore, it is easier to control environmental factors, drug administration, and previous experience in animal studies [18, 19].

Although a number of studies have reported non-analgesic placebo effects in animals in the past few decades [20, 21], there have been few reports on analgesic responses in mice or rats, and almost all existing animal models employ Pavlovian conditioning paradigms and measure behavioral pain responses in naïve animals [22–27]. However, studies using physiological pain do not resemble the real clinical situation. So far, only one study has used rats with severe neuropathic pain, but the results were not in agreement with other studies and they concluded that placebo analgesia in rats is not particularly robust [28]. Thus, there is still a need for a robust and easily-reproducible model of placebo analgesia in animals with pathological pain.

To overcome the limitations of previous models and elucidate the specific mechanisms underlying placebo analgesia in patients, we conducted a series of experiments in an attempt to develop a model of placebo analgesia in rats with inflammatory pain.

Materials and Methods

Animals

Male Sprague-Dawley rats (150–200 g) were used. The animals were housed under a 12 h light/dark cycle and the temperature was maintained at $(23 \pm 1)^\circ\text{C}$. Food and water were supplied to every cage *ad libitum*. The animals were given 5 days to acclimate after arrival. All experimental procedures were approved by the Animal Care and Use Committee of Peking University. Complete Freund's adjuvant (CFA) (100 μL per rat, Sigma-Aldrich, St. Louis, MO) was injected into the plantar surface of the hind paw while animals were under brief isoflurane anesthesia. The 50% CFA was a 1:1 mixture of complete and incomplete Freund's adjuvants. Morphine hydrochloride was dissolved in saline solution and administered by intraperitoneal injection at 5 mg/kg. Animals were randomly assigned into groups using a Microsoft Excel random number generator.

Hargreaves Test and Hot Plate Test

Thermal hyperalgesia was evaluated by measuring the paw-withdrawal latency in response to a radiant heat stimulus applied to the core of the plantar surface of the hind paw. Rats were placed on a clean glass platform and each rat had a transparent restraint shell. The radiant heat

source was adjusted to a range of 12 s–15 s as the baseline latency with a cutoff time of 30 s to prevent tissue damage. All rats were tested 3 times at 5-min intervals. The mean latency was used for statistical analysis.

The hot plate test was performed using a previously-described protocol [29]. The apparatus contained a metal plate and a removable transparent wall. The plate temperature was set at 50°C or 52°C and the latency to the first lick of the hind paw was recorded, with 30 s as the cutoff time. The tester of pain behavior assays was blinded to the animal groups (another experimenter injected drugs or saline).

Spontaneous Paw-Licking Measurements

The rats were placed on the apparatus used for the Hargreaves test and a video camera was set up under the transparent glass platform. Rats were left in the test room for 40 min of video recording. The first 10 min of video were not used, as during this time the rats were acclimating to the glass apparatus and test room. The video analyst was blinded to animal groups (another experimenter used a random number list to re-number the videos).

Conditioning Paradigms

Context Conditioning

Conditioning paradigms were simplified from a previous study [26]. Briefly, after CFA injection into the left hind paw, rats had two days to recover and reach a state of steady hyperalgesia after inflammation (Fig. 2A). The context conditioning included 4 consecutive days of training, with two injections of morphine (5 mg/kg) or saline at 08:00 or 20:00 each day. For instance, rats received a saline injection at 08:00 on day 1, 20:00 on day 2, 08:00 on day 3, and 20:00 on day 4 (Fig. 2A), with morphine injection at the vacant times. The interval between injections was 12 h to ensure complete metabolism and excretion of morphine. To associate the context cues with morphine analgesia, rats were placed in their home cages after saline injection, while after morphine injection, they were placed on the Hargreaves apparatus in the testing room for 30 min, after which they underwent the Hargreaves test.

After training, the rats received saline injections in the same routine as the 4 days of training at 08:00 on day 5. The Hargreaves test was used to measure the conditioned response to saline injection. The 30 min on the Hargreaves apparatus in a particular room along with the injection was assumed to be the conditioned stimulus (mainly context stimulus), and the morphine injection was the

unconditioned stimulus; the analgesia induced by morphine was considered to be the unconditioned response, whereas pain relief from the saline injection was the conditioned response (placebo effect).

At 20:00 on day 5, rats were given an injection of saline and the Hargreaves test to ensure that the CFA inflammation prevailed at the end of the context paradigms.

Refined Context Conditioning

To validate the context conditioning paradigms and enhance the link between morphine injection (unconditioned stimulus) and its analgesic effect (unconditioned response), we further refined the context conditioning (Fig. 2C) by eliminating the saline injections and adding a positive control (morphine injection every day) and a negative control (saline injection every day).

Before CFA injection, the baseline (day 1) thresholds for the Hargreaves test were measured. On day 3 before training, the thresholds were recorded to ensure equal inflammatory pain and the rats were randomly assigned into three groups. The morphine and placebo groups received morphine (5 mg/kg) each day and were placed on the Hargreaves apparatus for 30 min, whereas the saline group received saline each day. On day 8, the morphine group received a morphine injection, while the placebo and saline groups received a saline injection. The conditioned response was measured as the pain threshold of the Hargreaves test and compared with the placebo and saline groups.

Refined Context Conditioning Without the Hargreaves Test in Training

To avoid the unpleasant stimulus of the Hargreaves test every day, we further deleted Hargreaves test from training (Fig. 2E). Training and testing on day 7 was exactly same as previously. At 20:00 on day 7, all rats were given an injection of saline and the Hargreaves test to ensure that CFA inflammation prevailed at the end of the context paradigms. On day 8, the morphine and placebo groups were given morphine and the Hargreaves test to ensure that there was no tolerance to the repetitive injection of morphine.

Refined Context Conditioning with the Hot Plate Test

The hot plate was introduced to replace the Hargreaves test in a later training paradigm (Fig. 2G). Rats were randomly assigned into two groups. The 4 days of training and pain threshold testing were same as previously (refined context conditioning without the Hargreaves test in training).

Refined Context Conditioning with Conditioned Place Preference (CPP) Chambers

The conditioning paradigms were simplified from a previous study [29]. Briefly, rats were conditioned using a two-chamber CPP apparatus, with differences in litter (crushed corncob or sawdust) and in the shape of the lights. Before training, a preference test was performed. For the placebo group, the preferred chamber of an individual rat was paired with a saline injection; and the other chamber was paired with a morphine injection. The control group had the same pairing as the placebo group for two days and the opposite pairing for the other two days to avoid CPP for morphine. In 4 days of training, rats received one morphine and one saline injection each day at 08:00 and at 20:00. The morphine and saline injections were randomly arranged to avoid unwanted pairing to the injection time. After injection, each rat was placed in the paired chamber for 40 min and removed for the hot plate test. On day 5, the control and placebo groups received a saline injection and were placed in the saline-paired chamber and morphine-paired chamber, respectively, before the hot plate test. The test for place preference was carried out before the placebo test. The time in the morphine-paired chamber (t_1) and time in the saline-paired chamber (t_2) were used to calculate the CPP coefficient = $(t_1 - t_2)/(t_1 + t_2) \times 100$.

Rats with a CPP coefficient larger than 10 or smaller than -10 were given morphine in the least-preferred chamber in a 15-min pre-test, while rats with a CPP coefficient between -10 and 10 were paired in a counterbalanced pattern.

This experimental design assumed that morphine injection was the unconditioned stimulus, the analgesic effect induced by morphine was the unconditioned response, the morphine-paired chamber was the conditioned stimulus, and the pain relief after saline injection and being in the morphine-paired chamber were the conditioned response.

The tester in the pain behavior assays was blinded to animal groups (another experimenter injected drugs and placed animals in different chambers in CPP).

c-fos Immunofluorescence Assay

At 120 min after the placebo test, rats were anesthetized with 10% chloral hydrate (0.4 g/kg, i.p.) and perfused with 0.1 mol/L phosphate-buffered saline (PBS) followed by perfusion with 4% paraformaldehyde. The brains were then removed, post-fixed for 12 h, and cryo-protected in 20% and 30% sucrose in 0.1 mol/L PBS. Coronal sections were cut at 30 μ m on a cryostat (Leica 1900, Leica Microsystems Ltd., Nussloch, Germany). Nucleus accumbens (NAc) and anterior cingulate cortex (ACC) sections were determined using the Paxinos and Watson rat brain atlas.

Sections were rinsed 3 times in 0.1 mol/L PBS (5 min each) before blocking with a blocking solution (1% bovine serum albumin (BSA), 0.3% Triton X-100, 0.1 mol/L PBS) for 1 h at room temperature. The sections were then incubated with c-fos antibody (cat26192-1-AP-50, 1:200 dilution in 1% BSA, 0.3% Triton X-100, 0.1 mol/L PBS) for 24 h at 4 °C. The sections were rinsed 3 times in PBS (10 min each) and incubated with antibody tagged with Alexa Fluor 488 nm (catO-11038, 1:1000, 1% BSA, 0.3% Triton X-100, 0.1 mol/L PBS) for 12 h at 4 °C, then rinsed 3 times in PBS (10 min each) and covered with 1% glycerol.

Statistical Analysis

Data are presented as the mean \pm SEM. Statistics were calculated using GraphPad Prism 6.0. Comparisons between two groups were made using Student's unpaired two-tailed *t*-test, or one-way ANOVA, or two-way repeated-measures ANOVA. Post-tests are named individually and were used in comparing two groups in particular columns. Statistical significance was defined as $P < 0.05$.

Results

Intraperitoneal Administration of Morphine Relieves the Thermal Hyperalgesia Induced by CFA Injection into the Hind Paw of Rats

A previous report indicated that Pavlovian conditioning with a cue induces placebo analgesia in naïve animals [26]. We used a similar paradigm to measure placebo analgesia in rats with inflammatory pain. We used CFA injection as an inflammatory pain model and the Hargreaves and hot plate tests (Fig. 1A). The latency to withdraw or lick the paw decreased after CFA injection, and this effect persisted for 12 days (Fig. 1B, $n = 5$ animals, two-way ANOVA, group effect: $F(1, 8) = 234.9$, $P < 0.001$; Sidak multiple comparisons test: $P > 0.05$ at baseline and $P < 0.001$ for 1–12 days). The degree of swelling had no correlation with the hyperalgesia (Fig. 1D). We measured changes in the thermal pain response after different doses of morphine in CFA rats (Fig. 1C, $n = 4$ animals, two-way ANOVA, group effect: $F(3,12) = 19.44$, $P < 0.001$; Turkey's multiple comparisons test: $P > 0.05$ for each group compared to saline pre-treatment, $P = 0.13$ for 2.5 mg/kg compared to saline treatment, $P < 0.001$ for 5.0 mg/kg and 10.0 mg/kg compared to saline treatment); 2.5 mg/kg morphine did not reduce the paw withdrawal latency and 10 mg/kg morphine had an apparent sedative effect. Moreover, 5 mg/kg morphine had a modest analgesic effect and little sedative

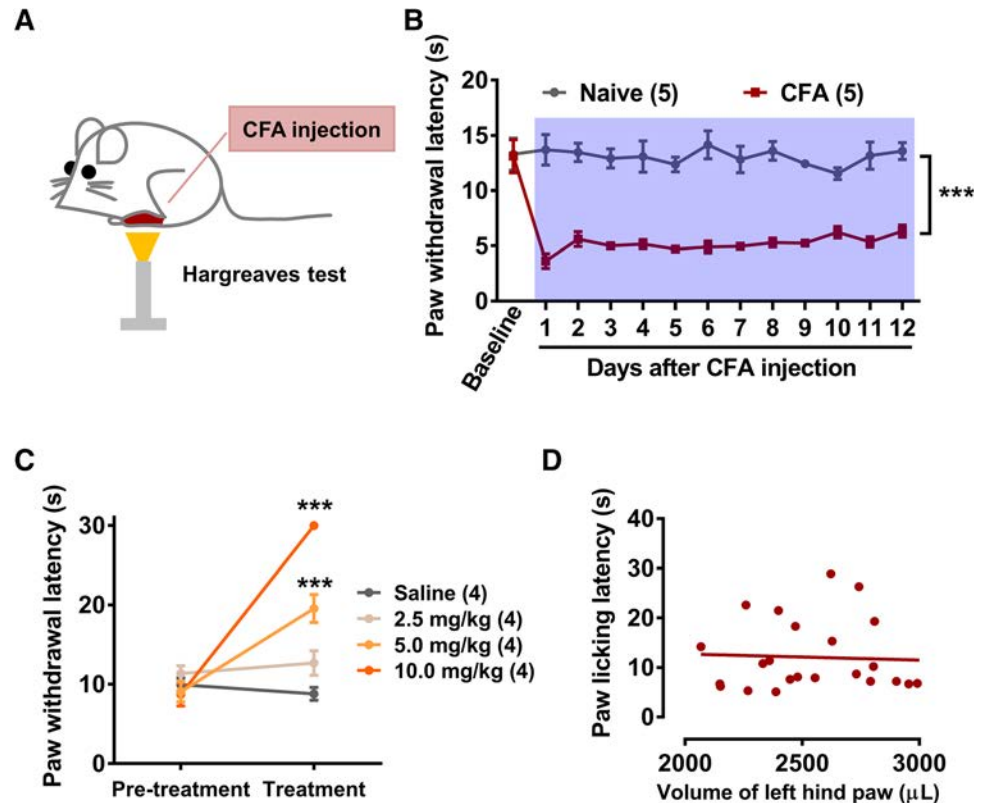
effect, so we used 5 mg/kg for the conditioning training paradigms.

Conditioning with Distinct Environmental Cues does not Elicit Placebo Analgesia in Rats

We found that i.p. morphine had a significant analgesic effect on CFA rats, with no accumulation or tolerance side-effects during training. However, the placebo injection group had no significant increase in paw withdrawal latency in the morning on day 5 compared to the saline injection in the afternoon on day 4 (Fig. 2B, $n = 12$ animals, $F(9,110) = 60.62$, one-way ANOVA with Dunnett's multiple comparison test, compared to baseline in the morning on day 1, $P < 0.001$, adjusted $P_{(5AM)} = 0.71$), indicating that conditioning with context does not induce placebo analgesia.

In the inflammatory hyperalgesia model, rats with cognitive deficits may ignore context in training so it is more difficult to induce placebo analgesia in them than in naïve rats [30, 31]. Thus we simplified the training paradigm by removing the saline injection (Figs. 2C and S1A). Rats received a morphine injection once a day and the pain response was measured 30 min after injection. We added a positive control group to verify morphine potency and a negative control group to confirm persistent hyperalgesia induced by CFA. We found that the negative control group had a shorter latency to withdraw the CFA-injected hind paw than the morphine-injected groups, and the positive control group had a longer latency to withdraw the hind paw, indicating a steady analgesic effect without any tolerance. The placebo group received saline at the same time as the morphine-injection training; the rats had no significant increase of paw withdrawal latency compared to the negative control group in CFA rats (Fig. 2D, $n = 8$ animals/group, two-way ANOVA, Turkey's multiple comparison test: $P < 0.01$ on days 4–7 for morphine *versus* saline and placebo *vs* saline, $P < 0.01$, morphine *vs* saline and morphine *vs* placebo at day 8, adjusted $P_{(8)} = 0.998$, placebo *vs* saline on day 8). However, we trained naïve rats with the training paradigm and found the placebo group had longer paw withdrawal latency than the control group on the test day (Fig. S1B, $n = 6$ animals/group, two-way ANOVA, Turkey's multiple comparison test: $P < 0.01$ on days 2–5 morphine *vs* saline and placebo *vs* saline; $P < 0.01$ on day 6, morphine *vs* saline and placebo *vs* saline; $P < 0.01$ on day 6, placebo *vs* morphine). In addition, there was no significant increase of paw withdrawal latency in 50% of CFA rats (Fig. S1C–D, $n = 8$ animals, two-way ANOVA, group effect: $F(1, 14) = 185.3$, $P < 0.01$; Sidak multiple comparison test: $P > 0.05$ on days 1, 3, and 8, and $P < 0.001$ on days 4–7).

Fig. 1 Morphine injection relieved CFA-induced hyperalgesia in rats. **A** Illustration of the CFA injection and Hargreaves test. **B** Paw withdrawal latency of the left hind paw in naïve and CFA rats ($n = 5$ animals, $***P < 0.001$, two-way ANOVA with Bonferroni *post hoc* tests). All the training paradigms and tests were performed from 3 to 8 days after CFA injection, when the thermal hyperalgesia was stable. **C** Paw withdrawal latency of the left hind paw in CFA rats after morphine injection ($n = 4$ animals, $***P < 0.001$, two-way ANOVA with Bonferroni *post hoc* tests). **D** Correlations between volume of swelling in the hind paw and paw withdrawal latency ($n = 24$ animals, Pearson $r = -0.05$, $P = 0.82$). The data are presented as the mean \pm SEM.



Considering that the measurement of pain response is a negative experience for rats and interferes with attention and context-pairing learning during training [32], we further omitted everyday Hargreaves testing. However, we still found similar results on the test day (Fig. 2E–F, $n = 14$ animals/group, two-way ANOVA, Turkey's multiple comparisons test: $P < 0.001$ on day 7 (AM) for morphine *vs* saline and morphine *vs* placebo, adjusted $P_{(TPM)} = 0.68$ for placebo *vs* saline, $P < 0.001$ on day 8 for morphine *vs* saline and placebo *vs* saline).

The Hargreaves test measures paw-withdrawal behavior, and indicates a mainly reflexive response at the spinal level. However, the hot plate test integrates the pain response of the spinal cord and brain, and placebo analgesia is thought to occur in the brain [33]. Hence, we used the hot plate test to replace the Hargreaves test, but still did not succeed in conditioning placebo analgesia (Fig. 2G–H, $n = 15$ animals, two-way ANOVA, group effect: $F(1,28) = 10.39$, $P < 0.01$; Sidak multiple comparisons test: $P > 0.05$ on days 1, 3, and 8, and $P < 0.001$ on day 9).

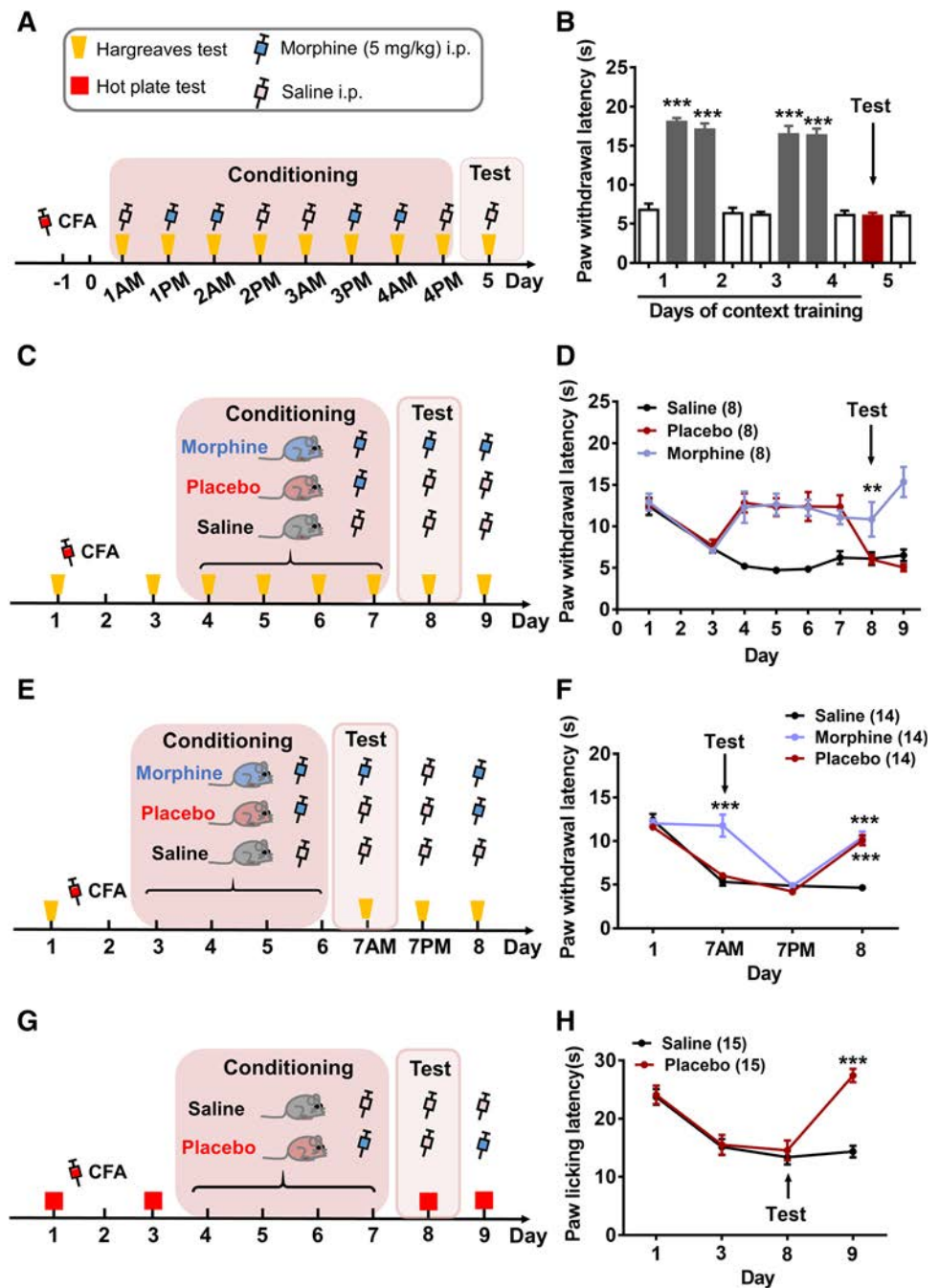
In summary, all four paradigms of conditioning with context failed to elicit placebo analgesia in CFA rats.

Conditioning with CPP Chambers does not Elicit Placebo Analgesia in CFA Rats, while Reward Expectation is Intact

In a study of healthy rats [29], researchers divided the conditioning placebo model into two continuous segments: reward learning and placebo analgesia. Reward expectation is necessary for placebo analgesia formation. In CFA rats, consistent inflammation causes deficit in some parts of the establishment of placebo analgesia compared to naïve rats.

To further investigate which part is weakened in conditioning training models, we performed conditioning similar to that described by Lee *et al.* [29]. First, we trained naïve rats with conditioning procedures (Fig. 3A) and found that the placebo group had a longer paw licking latency than the control group on the test day when saline was injected (Fig. 3B–E). In particular, the placebo group had a significantly longer latency to lick the hind paw on the test day ($n = 10$ animals/group. Control, 9.68 ± 0.44 ; placebo, 14.39 ± 0.84 . Unpaired two tailed t -test: $t_{18} = 4.962$, $P < 0.001$), indicating a placebo analgesia in naïve rats. The CPP coefficient indicates a preference for the morphine-paired chamber; before training, the rats had no preference, and afterwards they established preference as presented by an increase in the CPP coefficient. The placebo group had an increased preference for the morphine-paired chamber (which represented the formation of

Fig. 2 Context conditioning did not produce placebo analgesia in CFA rats. **A** Schematic of the first context conditioning paradigm. **B** Paw withdrawal latency in CFA rats after first conditioning with context ($n = 12$ animals, $***P < 0.001$, one-way ANOVA with Turkey's test compared 1PM, 2AM, 3PM, 4AM to 1AM). **C** Schematic of the second context conditioning paradigm. **D** Paw withdrawal latency in CFA rats after second conditioning with context ($n = 8$ animals/group, $**P < 0.01$, two-way ANOVA with Turkey's test compared to day 8). **E** Schematic of the third context conditioning paradigm. **F** Paw withdrawal latency in CFA rats after third conditioning with context ($n = 14$ animals/group, $***P < 0.001$, two-way ANOVA with Turkey's test compared to day 6). **G** Schematic of fourth context conditioning paradigm. **H** Paw withdrawal latency in CFA rats after fourth conditioning with context ($n = 15$ animals/group, $***P < 0.001$, two-way ANOVA with Turkey's test compared to day 8). The data are presented as the mean \pm SEM.

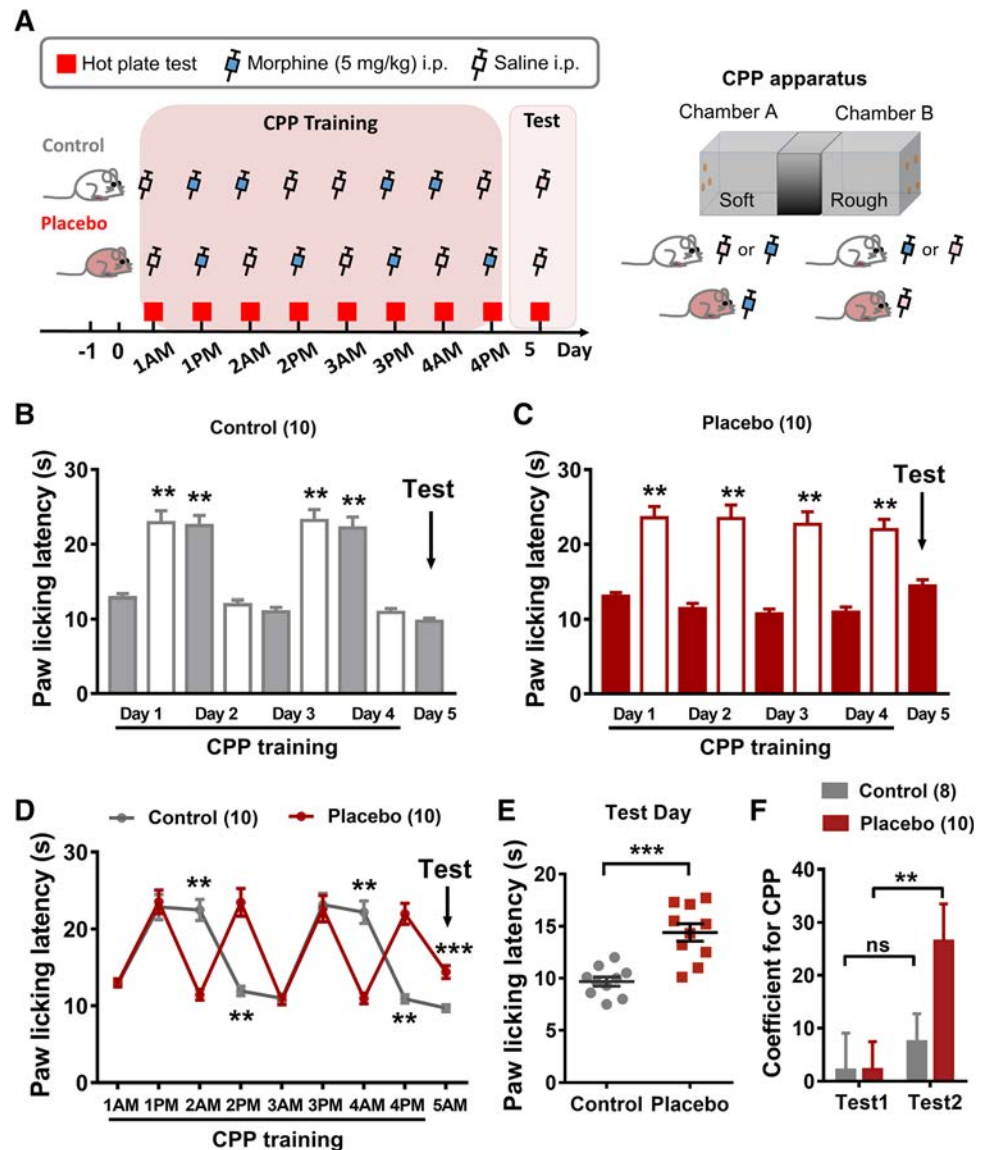


reward expectation); the control group did not exhibit this preference (Fig. 3F, $n = 8$ and 10 animals, two-way ANOVA, group effect: $F(1,16) = 1.753$, $P = 0.20$; time effect (CPP training): $F(1,16) = 8.366$, $P = 0.01$; Sidak multiple comparisons test: Test1 vs Test2, $**P < 0.01$ for placebo group, $P > 0.05$ for control group; control vs placebo, $P_{\text{test2}} = 0.077$). These results in naïve rats showed that our conditioning course is convincing and reliable.

Interestingly, the placebo group had no significant change in paw licking latency when compared to the control group in CFA rats (Fig. 4A–F). Most importantly,

the placebo group showed no difference in paw licking latency on the test day ($n = 16$ animals/group, Control, 5.86 ± 0.43 s; placebo, 5.96 ± 0.63 s; $P = 0.89$, two-tailed unpaired t test), indicating that no placebo analgesia was induced by CPP training. However, only the placebo group shifted their preference to the morphine-paired chamber ($n = 16$ animals/group, two-way ANOVA, group effect: $F(1,30) = 0.997$, $P = 0.326$; time effect (CPP training): $F(1,16) = 13.72$, $P < 0.001$; Sidak multiple comparisons test: Test 1 vs Test 2, $P < 0.01$ for placebo group, $P > 0.05$ for control group; control vs placebo,

Fig. 3 The conditioning procedure induced placebo analgesia and preference for the morphine-associated chamber in naïve rats. **A** Cartoons of the conditioning procedure with the CPP apparatus. **B–D** Hind paw licking latency in naïve rats during conditioning training and testing in the control and placebo groups ($n = 10$ animals/group, $**P < 0.01$, $***P < 0.001$, two-way ANOVA with Sidak *post hoc* tests). **E** Hind paw licking latency in naïve rats that received conditioning training (control and placebo groups) on the test day after receiving saline injection ($***P < 0.001$, unpaired *t* test with Welch correction). **F** CPP scores of CFA rats before and after conditioning training ($**P < 0.01$, two-way ANOVA with Sidak *post hoc* tests). The data are presented as the mean \pm SEM.



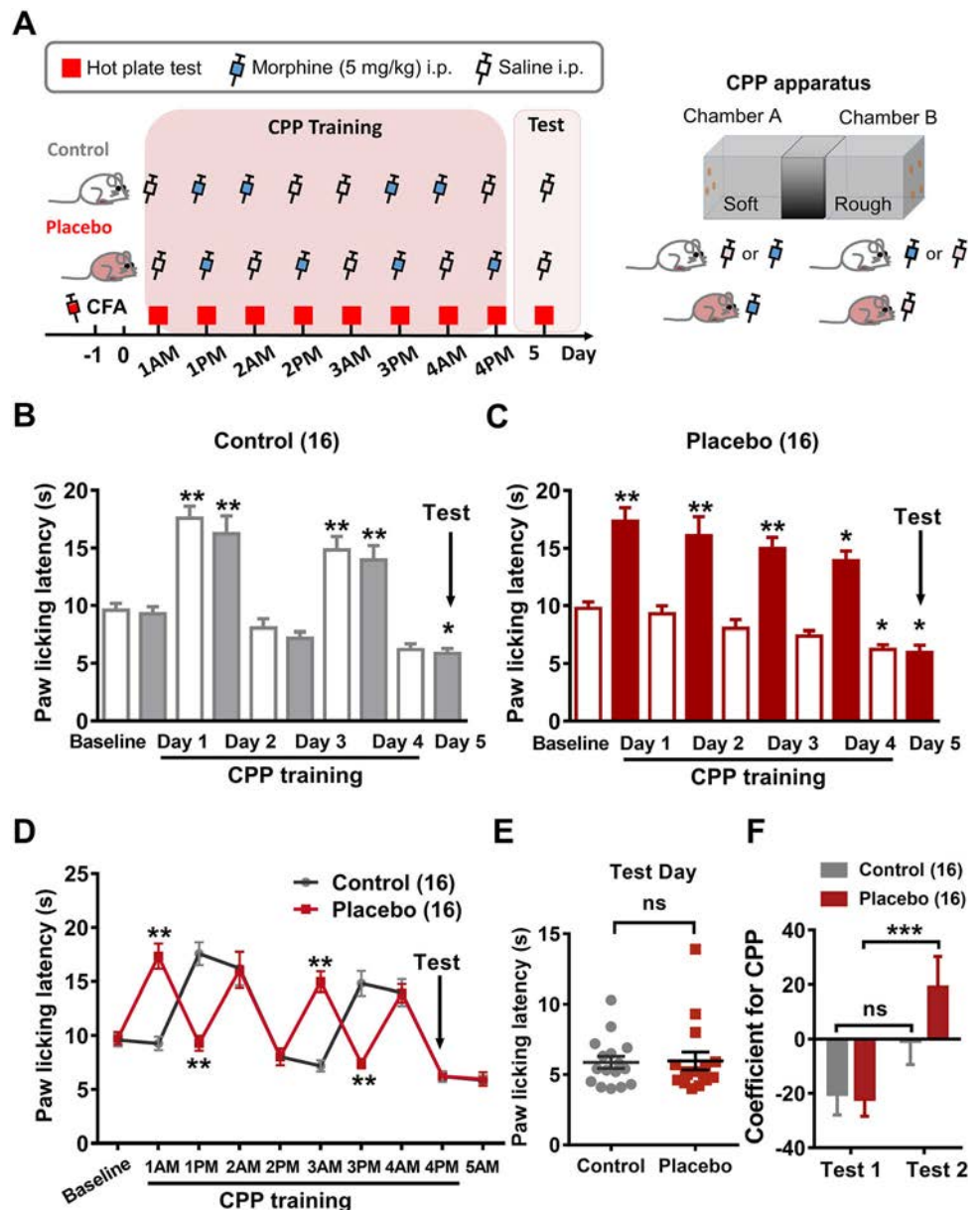
$P > 0.05$ for Test 1 and Test 2). This finding indicates that CFA rats do not experience placebo analgesia, yet they still display reward expectation.

To confirm the behavioral changes in naïve and CFA rats, we used immunofluorescence to investigate *c-fos* activation in the brain regions associated with reward-learning (NAc) and pain-processing (ACC) (Fig. 5A–B). In naïve rats (Fig. 5C–F), the placebo group had fewer *c-fos*-positive cells in the ACC than the control group (Fig. 5D; 11.4% of cells were *c-fos*-positive in the control group compared to 24% in the placebo group, $P < 0.01$). Naïve rats also had more *c-fos*-positive cells in the NAc (Fig. 5F; 20.8% of cells were *c-fos*-positive in the control group compared to 3.0% in the placebo group, $P < 0.01$). In CFA rats (Fig. 5G–J), the placebo group had more *c-fos*-positive cells in the NAc (Fig. 5H; 2.1% of cells were *c-fos*-positive in the control group compared to 17.1% in the placebo

group, $P < 0.001$). However, the *c-fos*-positive cells in the ACC were not significantly different from the control group (Fig. 5J; 31% of cells were *c-fos*-positive in the control group compared to 30.2% in the placebo group, $P > 0.05$). These findings were consistent with the behavioral changes.

Since the pain response induced by noxious stimuli like von Frey filaments can disturb the measurement of placebo analgesia [28], we recorded the number of occurrences as well as the total duration of spontaneous hind paw-licking behavior during a 30-min period (Fig. 6A–F). Intraperitoneal administration of morphine reduced the spontaneous licking time of CFA rats (53.8 s for the control group, 8.4 s for the placebo group at day 7, $P < 0.001$) and the counts of licking behaviors (2.1 for the control group, 0.7 for the placebo group at day 8, $P < 0.001$). Nevertheless, we

Fig. 4 Conditioning procedure induced preference for the morphine-associated chamber, with no placebo analgesia in CFA rats. **A** Cartoons of conditioning procedure with CPP apparatus. **B–D** Hind paw licking latency in CFA rats that received conditioning training (control and placebo groups) ($n = 16$ animals/group, $**P < 0.01$, two-way ANOVA with Sidak *post hoc* tests). **E** Paw licking latency of hind paws in CFA rats with conditioning training (control and placebo groups) on the test day after receiving a saline injection ($P = 0.89$, unpaired *t* test). **F** CPP score of CFA rats before and after conditioning training ($***P < 0.001$, two-way ANOVA with Sidak *post hoc* tests). Data are presented as the mean \pm SEM.



found no success in repeated conditioning placebo analgesia in CFA rats.

Discussion

As previously noted, there is a strong need for animal models of placebo analgesia at present, especially in animals with pathological pain; these models will contribute to elucidating the mechanism underlying placebo effects in patients and may provide patients with additional placebo-based benefits [34, 35]. However, our experiments illustrate the difficulty in eliciting robust placebo analgesia in rats with pathological pain (Fig. 7). None of our

experiments found evidence of the placebo effect, which is in agreement with the research on rats with an L5 spinal nerve lesion [28] but contrasts with other experiments on healthy rats [23, 24, 26]. Therefore, our research confirms that a model of placebo analgesia in rats with pathological pain is quite elusive and that placebo analgesia is more difficult to induce in rats than in humans. The primary findings of our study can be separated into two parts.

In part one, we tried to establish a placebo analgesia model in rats with inflammatory pain using context conditioning paradigms, which have successfully induced placebo analgesia in naïve rats in previous studies as well as our experiments. Unfortunately, there were no statistically significant differences between the placebo and

Fig. 5 The conditioning procedure increased the percentage of c-fos-positive cells in the NAc in both naïve and CFA rats, but decreased it in ACC in naïve rats. **A, B** Illustration of the ACC and NAc according to the brain atlas. Scale bars, 500 μ m. **C–F** Left, representative images of c-fos immunofluorescence in the ACC (**C**) and NAc (**D**) in naïve rats and in the ACC (**E**) and NAc (**F**) of CFA rats; right, statistics for c-fos-positive cells in the corresponding groups. Scale bars, 100 μ m. ($n = 4$ animals/group, $**P < 0.01$, $***P < 0.001$, unpaired t test).

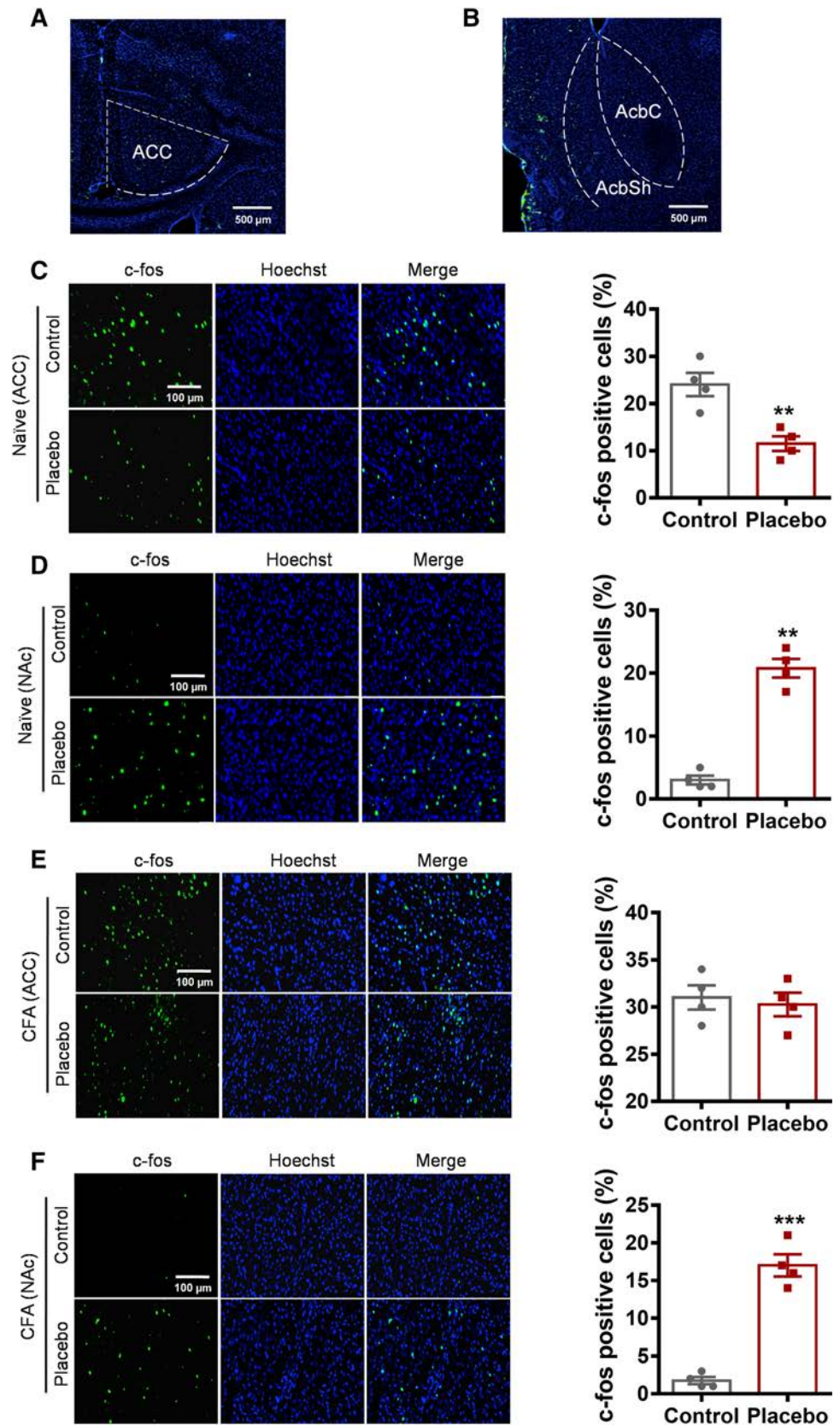


Fig. 6 Spontaneous pain behaviors did not change after the conditioning procedure in CFA rats. **A** Cartoon of the context conditioning paradigms. **B, D** Numbers (**B**) and durations (**D**) of spontaneous paw-licking behavior of CFA rats during conditioning and placebo testing ($*P < 0.05$, $**P < 0.01$ on day 7, two-way ANOVA with Sidak *post hoc* tests). **C, E** Statistics of **B** and **D**, respectively ($P > 0.05$, unpaired *t* test).

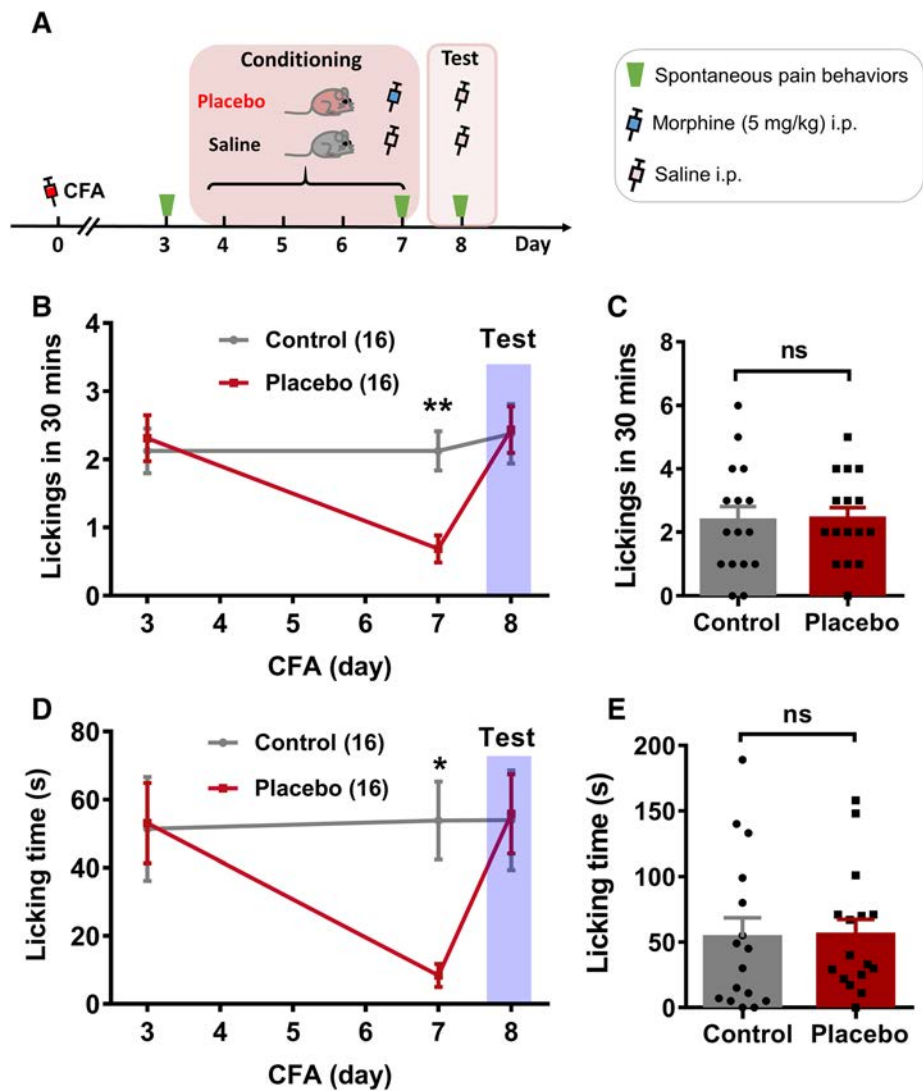
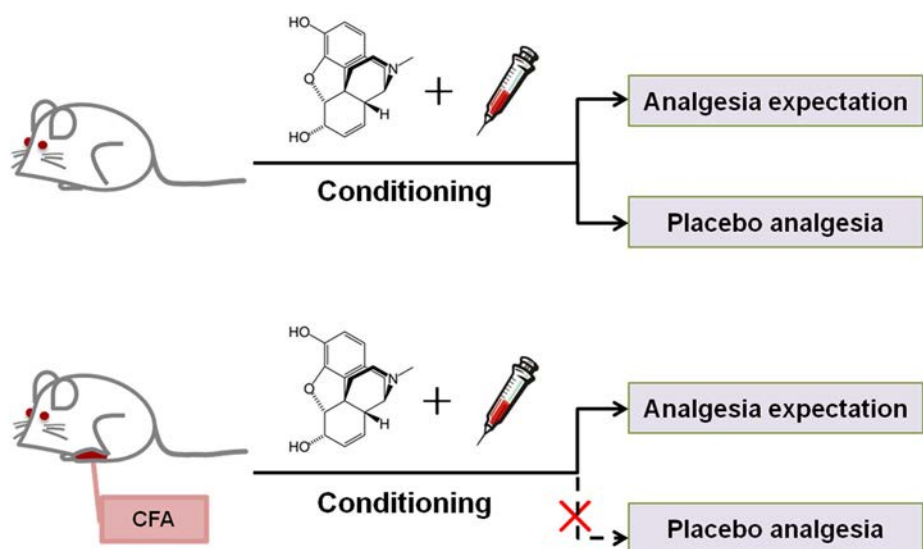


Fig. 7 Schematic of placebo analgesia in naive and CFA rats. Behavioral tests and immunostaining demonstrate that naive rats have both analgesia expectation and placebo analgesia, whereas CFA rats have intact brain function in reward learning yet diminished placebo analgesia under pathological conditions.



control groups on the test day. We explain these results as a lack of placebo analgesia in rats with pathological pain, which was further shown in the second part of our study. Here, we list some advantages of our models that contribute to the credibility of this study.

First, we used an appropriate model of pathological pain in rats. The previous model in rats with severe neuropathic pain that failed to induce the placebo effects recommended a milder pain condition [36, 37]. Most human studies of placebo analgesia were tested with mild experimental pain [38]. Furthermore, immune activation and inflammatory responses were involved in the processing of pathological pain states [39] and NSAIDs were used in healthy volunteers [40] and naïve animals [26] to induce robust placebo analgesia. Therefore, it can be inferred that placebo analgesia plays a role in the treatment of inflammatory pain. In addition, the CFA-induced chronic inflammatory pain model is relatively suitable. Our results suggest that this painful condition remained stable during the entire experiment. A challenge for most clinical experiments is controlling the spontaneous remission or fluctuation of disease symptoms [41–44].

Second, we attempted to develop a model of placebo analgesia in rats. We followed the most common model and failed to induce it, which suggests that placebo analgesia is more difficult to elicit in rats with pathological pain than in healthy rats. Therefore, we simplified the training paradigm and maximized the association between sensory cues and the experience of analgesia [45]. However, this strategy was also ineffective. And we also chose a dose of 50% CFA to rule out the possibility that the degree of inflammatory pain affected the manifestation of the placebo effect. Then, we thought that the daily measurement might have been an interference factor, so we repeated the experiments without it. Finally, we used the hot plate test to replace the Hargreaves test, because the former integrates the spinal and brain levels of the pain response while the latter mainly tests the reflexive response at the spinal level [46, 47]. Although we did not obtain positive results, we provided sufficient evidence to demonstrate that it is difficult to create a placebo analgesia model in rats with pathological pain using conventional context conditioning procedures.

Finally, we carefully selected the proper experimental design. For example, we selected the optimum dose of morphine to suppress pain (5 mg/kg) and our results suggested that this dose did not induce tolerance effects and was appropriate for our repeated-dose conditioning paradigm [48, 49]. Furthermore, no opiate-induced hyperalgesia was found in any of the experiments, in agreement with other studies [28, 50]. We also designed multiple controls, including comparisons between groups and self-controls.

In part two, we tried to determine why we failed to develop a model of placebo analgesia in rats with inflammatory pain. It is known that expectation plays an important role in the human placebo response [51, 52], which mainly results from learning and previous experience [53, 54]. Similarly, one animal study divided the placebo effect model into two parts (reward learning and the expression of placebo analgesia) and suggested that reward expectation is necessary for the formation of placebo analgesia [29]. To further investigate which part was affected in our models in rats with inflammatory pain, we designed a more complicated model that successfully induced placebo analgesia and preference for the morphine-associated chamber in naïve rats. We found that the reward expectation was unaffected in the rats with inflammatory pain, but there was no analgesia. It is known that humans can be classified as high- or low-responders to placebo effects [55–57], and it is possible that such subpopulations may exist in rats. We determined the distribution of individual data on the test day which revealed no deference between the two groups. In addition, we quantified the expression of c-fos in the ACC and the NAc as these areas are important for the pain response and reward expectation [58–61]. We found increased c-fos expression in the NAc but no differences in c-fos expression in the ACC of the placebo groups with inflammatory pain, which directly corresponded with the observed behaviors. Yet we must acknowledge that our interpretation of the brain regions activated has limitations. One of the reasons is that ACC is involved not only in sensory pain, but also in attention, emotion, cognition, and motivation [62–64]. Moreover, as NAc function in reward expectation and noxious stimuli changes [65, 66], we could not rule out the possibility that ACC activation may reflect motivational and emotional changes, and NAc activation may have implication for pain responses.

In general, the most plausible explanation is that the conditioning paradigm successfully elicited an expectation of treatment in rats that was then broken by the altered treatment on the test day. Reviewing past studies, most placebo research in naïve rats used thermal assays to measure placebo effects while human studies used subjective self-reports to measure pain [67]. In our experiments, we used the established method of testing the thermal pain response, which is a better measurement of evoked or reflexive pain and which may therefore violate the expression of placebo effects. In light of this, we next tested spontaneous pain [68, 69], a better indicator of affective pain, without any other change on the test day but this did not produce placebo analgesia either. Given this result, we must consider that the expectation of reward in rats in pathological condition is not enough to elicit placebo effects even though expectation is strongly

associated with placebo analgesia in humans. Chronic inflammatory pain results in hyperalgesia, which decreases the heat pain threshold in patients and animals, therefore the placebo effect may be too weak to relieve the severe pathological pain. Moreover, since placebo analgesia is a complex process involving multiple brain functions and psychological factors, it is difficult to completely mimic placebo analgesia in rats due to the cognitive gap between human and rats, especially under pathological conditions.

In summary, this series of experiments demonstrates the failure of placebo analgesia in rats with inflammatory pain. Rodents are unable to adequately model a phenomenon as complex as humans. We conclude that, at least in the present paradigm, placebo analgesia in rats with pathological pain is not feasible, and therefore we recommend considering the possibility that the topic is best studied in humans.

Acknowledgements This work was supported by grants from the National Natural Science Foundation of China (31720103908, 31530028, and 81821092) and the National Basic Research Development Program of the Ministry of Science and Technology of China (2017YFA0701300).

Conflict of interest The authors declare no conflict of interest.

References

- Andrews P, Steultjens M, Riskowski J. Chronic widespread pain prevalence in the general population: a systematic review. *Eur J Pain* 2018, 22: 5–18.
- Voon P, Karamouzian M, Kerr T. Chronic pain and opioid misuse: a review of reviews. *Subst Abuse Treat Prev Policy* 2017, 12: 36.
- Duenas M, Ojeda B, Salazar A, Mico JA, Failde I. A review of chronic pain impact on patients, their social environment and the health care system. *J Pain Res* 2016, 9: 457–467.
- Buchel C, Geuter S, Sprenger C, Eippert F. Placebo analgesia: a predictive coding perspective. *Neuron* 2014, 81: 1223–1239.
- Klinger R, Colloca L, Bingel U, Flor H. Placebo analgesia: clinical applications. *Pain* 2014, 155: 1055–1058.
- Tuttle AH, Tohyama S, Ramsay T, Kimmelman J, Schweinhardt P, Bennett GJ, *et al.* Increasing placebo responses over time in U.S. clinical trials of neuropathic pain. *Pain* 2015, 156: 2616–2626.
- Petersen GL, Finnerup NB, Grosen K, Pilegaard HK, Tracey I, Benedetti F, *et al.* Expectations and positive emotional feelings accompany reductions in ongoing and evoked neuropathic pain following placebo interventions. *Pain* 2014, 155: 2687–2698.
- Kaptchuk TJ, Friedlander E, Kelley JM, Sanchez MN, Kokkotou E, Singer JP, *et al.* Placebos without deception: a randomized controlled trial in irritable bowel syndrome. *PLoS One* 2010, 5: e15591.
- Arakawa A, Kaneko M, Narukawa M. An investigation of factors contributing to higher levels of placebo response in clinical trials in neuropathic pain: a systematic review and meta-analysis. *Clin Drug Investig* 2015, 35: 67–81.
- Enck P, Bingel U, Schedlowski M, Rief W. The placebo response in medicine: minimize, maximize or personalize? *Nat Rev Drug Discov* 2013, 12: 191–204.
- Doering BK, Rief W. Utilizing placebo mechanisms for dose reduction in pharmacotherapy. *Trends Pharmacol Sci* 2012, 33: 165–172.
- Benedetti F, Carlino E, Piedimonte A. Increasing uncertainty in CNS clinical trials: the role of placebo, nocebo, and Hawthorne effects. *Lancet Neurol* 2016, 15: 736–747.
- Tracey I. Getting the pain you expect: mechanisms of placebo, nocebo and reappraisal effects in humans. *Nat Med* 2010, 16: 1277–1283.
- Tetreault P, Mansour A, Vachon-Pressseau E, Schnitzer TJ, Apkarian AV, Baliki MN. Brain connectivity predicts placebo response across chronic pain clinical trials. *PLoS Biol* 2016, 14: e1002570.
- Benedetti F, Amanzio M, Thoen W. Disruption of opioid-induced placebo responses by activation of cholecystokinin type-2 receptors. *Psychopharmacology (Berl)* 2011, 213: 791–797.
- Zubieta JK, Bueller JA, Jackson LR, Scott DJ, Xu Y, Koeppel RA, *et al.* Placebo effects mediated by endogenous opioid activity on mu-opioid receptors. *J Neurosci* 2005, 25: 7754–7762.
- Dodd S, Dean OM, Vian J, Berk M. A review of the theoretical and biological understanding of the nocebo and placebo phenomena. *Clin Ther* 2017, 39: 469–476.
- Klinger R, Flor H. Clinical and ethical implications of placebo effects: enhancing patients' benefits from pain treatment. *Handb Exp Pharmacol* 2014, 225: 217–235.
- Hrobjartsson A. What are the main methodological problems in the estimation of placebo effects? *J Clin Epidemiol* 2002, 55: 430–435.
- Ben-Shaanan TL, Azulay-Debby H, Dubovik T, Starosvetsky E, Korin B, Schiller M, *et al.* Activation of the reward system boosts innate and adaptive immunity. *Nat Med* 2016, 22: 940–944.
- Wendt L, Albring A, Schedlowski M. Learned placebo responses in neuroendocrine and immune functions. *Handb Exp Pharmacol* 2014, 225: 159–181.
- Bryant CD, Roberts KW, Culbertson CS, Le A, Evans CJ, Fanselow MS. Pavlovian conditioning of multiple opioid-like responses in mice. *Drug Alcohol Depend* 2009, 103: 74–83.
- Zhang RR, Zhang WC, Wang JY, Guo JY. The opioid placebo analgesia is mediated exclusively through mu-opioid receptor in rat. *Int J Neuropsychopharmacol* 2013, 16: 849–856.
- Nolan TA, Price DD, Caudle RM, Murphy NP, Neubert JK. Placebo-induced analgesia in an operant pain model in rats. *Pain* 2012, 153: 2009–2016.
- Guo JY, Yuan XY, Sui F, Zhang WC, Wang JY, Luo F, *et al.* Placebo analgesia affects the behavioral despair tests and hormonal secretions in mice. *Psychopharmacology (Berl)* 2011, 217: 83–90.
- Guo JY, Wang JY, Luo F. Dissection of placebo analgesia in mice: the conditions for activation of opioid and non-opioid systems. *J Psychopharmacol* 2010, 24: 1561–1567.
- Xu L, Wan Y, Ma L, Zheng J, Han B, Liu FY, *et al.* A context-based analgesia model in rats: involvement of prefrontal cortex. *Neurosci Bull* 2018, 34: 1047–1057.
- McNabb CT, White MM, Harris AL, Fuchs PN. The elusive rat model of conditioned placebo analgesia. *Pain* 2014, 155: 2022–2032.
- Lee IS, Lee B, Park HJ, Olausson H, Enck P, Chae Y. A new animal model of placebo analgesia: involvement of the dopaminergic system in reward learning. *Sci Rep* 2015, 5: 17140.
- Bushnell MC, Ceko M, Low LA. Cognitive and emotional control of pain and its disruption in chronic pain. *Nat Rev Neurosci* 2013, 14: 502–511.

31. Wiech K. Deconstructing the sensation of pain: the influence of cognitive processes on pain perception. *Science* 2016, 354: 584–587.
32. Fiorio M, Recchia S, Corra F, Simonetto S, Garcia-Larrea L, Tinazzi M. Enhancing non-noxious perception: behavioural and neurophysiological correlates of a placebo-like manipulation. *Neuroscience* 2012, 217: 96–104.
33. Deuis JR, Dvorakova LS, Vetter I. Methods used to evaluate pain behaviors in rodents. *Front Mol Neurosci* 2017, 10: 284.
34. Benedetti F. Placebo responses in animals. *Pain* 2012, 153: 1983–1984.
35. Pecina M, Zubieta JK. Molecular mechanisms of placebo responses in humans. *Mol Psychiatry* 2015, 20: 416–423.
36. Gregory NS, Harris AL, Robinson CR, Dougherty PM, Fuchs PN, Sluka KA. An overview of animal models of pain: disease models and outcome measures. *J Pain* 2013, 14: 1255–1269.
37. Jaggi AS, Jain V, Singh N. Animal models of neuropathic pain. *Fundamental & Clinical Pharmacology* 2011, 25: 1–28.
38. Manchikanti L, Boswell MV, Kaye AD, Helm I S, Hirsch JA. Therapeutic role of placebo: evolution of a new paradigm in understanding research and clinical practice. *Pain Physician* 2017, 20: 363–386.
39. Watkins LR, Maier SF, Goehler LE. Immune activation: the role of pro-inflammatory cytokines in inflammation, illness responses and pathological pain states. *Pain* 1995, 63: 289–302.
40. Benedetti F, Amanzio M, Rosato R, Blanchard C. Nonopioid placebo analgesia is mediated by CB1 cannabinoid receptors. *Na Med* 2011, 17: 1228–1230.
41. Weimer K, Enck P. Traditional and innovative experimental and clinical trial designs and their advantages and pitfalls. *Handb Exp Pharmacol* 2014, 225: 237–272.
42. Rutherford BR, Mori S, Sneed JR, Pimontel MA, Roose SP. Contribution of spontaneous improvement to placebo response in depression: a meta-analytic review. *J Psychiatr Res* 2012, 46: 697–702.
43. Quessy SN, Rowbotham MC. Placebo response in neuropathic pain trials. *Pain* 2008, 138: 479–483.
44. He JH, Xu L, Shen Y, Kong MJ, Shi LY, Ma ZL. The changes of monocarboxylate transporter-2 in spinal cord horn in a rat model of chronic inflammatory pain. *Zhongguo Ying Yong Sheng Li Xue Za Zhi* 2015, 31: 19–22.
45. Miller FG, Kaptchuk TJ. The power of context: reconceptualizing the placebo effect. *J R Soc Med* 2008, 101: 222–225.
46. Allen JW, Yaksh TL. Assessment of acute thermal nociception in laboratory animals. *Methods Mol Med* 2004, 99: 11–23.
47. Lavich TR, Cordeiro RS, Silva PM, Martins MA. A novel hot-plate test sensitive to hyperalgesic stimuli and non-opioid analgesics. *Braz J Med Biol Res* 2005, 38: 445–451.
48. Mehalick ML, Ingram SL, Aicher SA, Morgan MM. Chronic inflammatory pain prevents tolerance to the antinociceptive effect of morphine microinjected into the ventrolateral periaqueductal gray of the rat. *J Pain* 2013, 14: 1601–1610.
49. Beaudry H, Gendron L, Moron JA. Implication of delta opioid receptor subtype 2 but not delta opioid receptor subtype 1 in the development of morphine analgesic tolerance in a rat model of chronic inflammatory pain. *Eur J Neurosci* 2015, 41: 901–907.
50. Bekhit MH. Opioid-induced hyperalgesia and tolerance. *Am J Ther* 2010, 17: 498–510.
51. Atlas LY, Wager TD. How expectations shape pain. *Neurosci Lett* 2012, 520: 140–148.
52. Schwarz KA, Pfister R, Buchel C. Rethinking explicit expectations: connecting placebos, social cognition, and contextual perception. *Trends Cogn Sci* 2016, 20: 469–480.
53. Carlino E, Benedetti F. Different contexts, different pains, different experiences. *Neuroscience* 2016, 338: 19–26.
54. Vase L, Norskov KN, Petersen GL, Price DD. Patients' direct experiences as central elements of placebo analgesia. *Philos Trans R Soc Lond B Biol Sci* 2011, 366: 1913–1921.
55. Hall KT, Loscalzo J, Kaptchuk TJ. Genetics and the placebo effect: the placeboome. *Trends Mol Med* 2015, 21: 285–294.
56. Colagiuri B, Schenk LA, Kessler MD, Dorsey SG, Colloca L. The placebo effect: From concepts to genes. *Neuroscience* 2015, 307: 171–190.
57. Colloca L, Grillon C. Understanding placebo and nocebo responses for pain management. *Curr Pain Headache Rep* 2014, 18: 419.
58. Qiu YH, Wu XY, Xu H, Sackett D. Neuroimaging study of placebo analgesia in humans. *Neurosci Bull* 2009, 25: 277–282.
59. Wager TD, Atlas LY. The neuroscience of placebo effects: connecting context, learning and health. *Nat Rev Neurosci* 2015, 16: 403–418.
60. Faria V, Fredrikson M, Furmark T. Imaging the placebo response: a neurofunctional review. *Eur Neuropsychopharmacol* 2008, 18: 473–485.
61. de la Fuente-Fernandez R, Schulzer M, Stoessl AJ. Placebo mechanisms and reward circuitry: clues from Parkinson's disease. *Biol Psychiatry* 2004, 56: 67–71.
62. Bush G, Luu P, Posner MI. Cognitive and emotional influences in anterior cingulate cortex. *Trends Cogn Sci* 2000, 4: 215–222.
63. Bush G, Vogt BA, Holmes J, Dale AM, Greve D, Jenike MA, *et al.* Dorsal anterior cingulate cortex: a role in reward-based decision making. *Proc Natl Acad Sci U S A* 2002, 99: 523–528.
64. Devinsky O, Morrell MJ, Vogt BA. Contributions of anterior cingulate cortex to behaviour. *Brain* 1995, 118: 279–306.
65. Stuber GD, Sparta DR, Stamatakis AM, van Leeuwen WA, Hardjoprajitno JE, Cho S, *et al.* Excitatory transmission from the amygdala to nucleus accumbens facilitates reward seeking. *Nature* 2011, 475: 377–380.
66. Baliki MN, Geha PY, Fields HL, Apkarian AV. Predicting value of pain and analgesia: nucleus accumbens response to noxious stimuli changes in the presence of chronic pain. *Neuron* 2010, 66: 149–160.
67. Linde K, Fassler M, Meissner K. Placebo interventions, placebo effects and clinical practice. *Philos Trans R Soc Lond B Biol Sci* 2011, 366: 1905–1912.
68. Kabadi R, Kouya F, Cohen HW, Banik RK. Spontaneous pain-like behaviors are more sensitive to morphine and buprenorphine than mechanically evoked behaviors in a rat model of acute postoperative pain. *Anesth Analg* 2015, 120: 472–478.
69. Tappe-Theodor A, Kuner R. Studying ongoing and spontaneous pain in rodents—challenges and opportunities. *Eur J Neurosci* 2014, 39: 1881–1890.



Hes1 Knockdown Exacerbates Ischemic Stroke Following tMCAO by Increasing ER Stress-Dependent Apoptosis *via* the PERK/eIF2 α /ATF4/CHOP Signaling Pathway

Yueyong Li^{1,2} · Yingjun Zhang³ · Huangde Fu⁴ · Huadong Huang⁴ · Qifeng Lu⁵ · Houji Qin⁵ · Yingning Wu⁵ · Huatuo Huang⁵ · Guizhen Mao⁵ · Zhongheng Wei⁵ · Pinhu Liao⁶

Received: 23 January 2019 / Accepted: 16 April 2019 / Published online: 15 July 2019
© Shanghai Institutes for Biological Sciences, CAS 2019

Abstract Apoptosis induced by endoplasmic reticulum (ER) stress plays a crucial role in mediating brain damage after ischemic stroke. Recently, Hes1 (hairy and enhancer of split 1) has been implicated in the regulation of ER stress, but whether it plays a functional role after ischemic stroke and the underlying mechanism remain unclear. In this study, using a mouse model of ischemic stroke *via* transient middle cerebral artery occlusion (tMCAO), we found that Hes1 was induced following brain injury, and that siRNA-mediated knockdown of Hes1 increased the cerebral infarction and worsened the neurological outcome, suggesting that Hes1 knockdown exacerbates ischemic stroke. In addition, mechanistically, Hes1 knockdown

promoted apoptosis and activated the PERK/eIF2 α /ATF4/CHOP signaling pathway after tMCAO. These results suggest that Hes1 knockdown promotes ER stress-induced apoptosis. Furthermore, inhibition of PERK with the specific inhibitor GSK2606414 markedly attenuated the Hes1 knockdown-induced apoptosis and the increased cerebral infarction as well as the worsened neurological outcome following tMCAO, implying that the protection of Hes1 against ischemic stroke is associated with the amelioration of ER stress *via* modulating the PERK/eIF2 α /ATF4/CHOP signaling pathway. Taken together, these results unveil the detrimental role of Hes1 knockdown after ischemic stroke and further relate it to the regulation of ER stress-induced apoptosis, thus highlighting the importance of targeting ER stress in the treatment of ischemic stroke.

Yueyong Li, Yingjun Zhang and Huangde Fu have contributed equally to this work.

✉ Zhongheng Wei
weizhongh1968@163.com

✉ Pinhu Liao
liaopinhu@163.com

- ¹ Department of Interventional Medicine, The First Affiliated Hospital of Jinan University, Guangzhou 510630, China
- ² Department of Interventional Medicine, Affiliated Hospital of Youjiang Medical University for Nationalities, Baise 533000, China
- ³ Department of Medical Imageology, Hunan University of Medicine, Huaihua 418000, China
- ⁴ Department of Neurosurgery, Affiliated Hospital of Youjiang Medical University for Nationalities, Baise 533000, China
- ⁵ Department of Emergency Intervention, Affiliated Hospital of Youjiang Medical University for Nationalities, Baise 533000, China
- ⁶ Department of Emergency, The First Affiliated Hospital of Jinan University, Guangzhou 510630, China

Keywords Hes1 · Ischemic stroke · PERK/eIF2 α /ATF4/CHOP pathway · ER stress · Transient MCAO

Introduction

Ischemic stroke-induced brain damage is common, devastates the central nervous system, and causes death and disability across the world [1]. Currently, the first-choice therapeutic strategy applied to cope with the ischemic insult is timely reperfusion, which is aimed at restoring the cerebral blood supply [2]. However, reperfusion undesirably causes further damage to the vulnerable ischemic brain tissue, by ischemia/reperfusion (IR) injury, and eventually worsens the clinical outcome [3]. To date, there is overwhelming evidence that I/R injury causes brain damage by triggering a series of distinct but overlapping cell signaling pathways involved in such processes as

oxidative stress, inflammation, excitotoxicity, and acidosis [4]. Despite this knowledge, however, the mechanisms underlying I/R injury are still far from fully understood, and no effective therapy for preventing or limiting ischemic stroke-induced brain damage has been developed.

In the last decade, accumulating evidence has demonstrated that neuronal apoptosis induced by endoplasmic reticulum (ER) stress plays an important role in mediating brain damage after ischemic stroke [5, 6]. ER stress activates the unfolded protein response (UPR) pathways by inducing protein kinase RNA-like endoplasmic reticulum kinase (PERK), which increases the phosphorylation level of eukaryotic initiation factor 2 alpha (eIF2 α) and triggers a pro-adaptive response by inhibiting global protein synthesis and the selective translation of activating transcription factor 4 (ATF4). In contrast, prolonged ER stress results in apoptosis and damage, such as that reported in rat models of I/R injury [7–9]. The notion that ER stress may be a promising target in I/R injury is further supported by evidence that inhibiting ER stress protects neurons against ischemic damage [10]. Therefore, elucidating the regulatory mechanisms of ER stress during ischemic stroke holds the promise of discovering novel therapeutic targets for reducing brain damage.

Hes1 (hairy and enhancer of split 1) is a basic helix-loop-helix transcription factor that is important for several activities in the nervous system, such as development, differentiation, and proliferation [11]. Recently, Hes1 has been connected with the regulation of UPR pathways and ER stress-induced apoptosis [12]. However, whether it plays a role in regulating ER stress and subsequent brain damage during ischemic stroke is unknown. In this study, by using an animal model of ischemic stroke developed by transient middle cerebral artery occlusion (tMCAO), we report a detrimental role of Hes1 knockdown in ischemic stroke, which is dependent on increasing ER stress-dependent apoptosis *via* its modulatory function in the PERK/eIF2 α /ATF4/CHOP signaling pathway.

Materials and Methods

Antibodies and Reagents

The primary antibodies against Hes1, Bax, and Bcl-2 were from Abcam (Cambridge, MA, USA). The primary antibodies against p-PERK (Thr980, #3179), PERK (#3192), p-eIF2 α (Ser51, #9721), eIF2 α (#5324), and cleaved caspase-3 (#9661) were from Cell Signaling Technology (Beverly, MA, USA). The primary antibodies against ATF4 (sc-200), CHOP (sc-166682), and β -actin (sc-47778) were from Santa Cruz Biotechnology (Santa Cruz, CA, USA). The secondary antibodies conjugated with

horseradish peroxidase were from Santa Cruz. The PERK inhibitor GSK2606414 was from Selleck Chemicals (Houston, TX, USA).

Animals and Cerebral Ischemic Stroke Model

Twelve-week-old wild-type male C57BL/6 mice were used in this study to establish the ischemic stroke model. Mice were housed in pathogen-free conditions throughout the study. Mice for all experiments were randomized and grouped prior to cerebral I/R induction by tMCAO [13, 14]. Briefly, mice were anesthetized with pentobarbital sodium (50 mg/kg) via intraperitoneal (i.p.) injection. A midline neck incision was made to isolate the left external carotid and pterygopalatine arteries, which were then ligated with silk. The internal carotid artery (ICA) at the peripheral site of its bifurcation and the pterygopalatine artery were occluded with a small clip and the common carotid artery (CCA) was ligated with silk. The external carotid was cut and a nylon monofilament with a blunted tip (0.20 mm) using a coagulator was inserted; a silk suture was tightened to prevent bleeding. The monofilament was advanced after removal of the clip on the ICA. The parietal bone turned pale on the occluded side during MCA occlusion, and a laser Doppler flowmeter was used to monitor the blood flow and assure successful occlusion [15]. The monofilament and the CCA ligature were removed after 1 h of occlusion and reperfused for 72 h with the release of blood flow from ICA. The mice in the sham group receiving surgery without ligation were used as controls. Each group included 12 mice. All animal experimental procedures were conducted in accordance with protocols approved by the Ethics Committee of The First Affiliated Hospital of Jinan University.

RNA Extraction and Real-time Quantitative RT-PCR

Total RNA was extracted from the ipsilateral cortex and striatum using TRIzol reagent (ThermoFisher Scientific, San Jose, CA, USA) and then complementary DNA was synthesized using the RevertAid First Strand cDNA Synthesis Kit (ThermoFisher Scientific) according to the manufacturer's instructions. Real-time quantitative RT-PCR was performed to quantify gene expression using the SYBR Green Realtime PCR Master Mix (ThermoFisher Scientific) and CFX96 Touch Real-Time PCR Detection System (Bio-Rad, Hercules, CA, USA). The mouse house-keeping *Actb* gene was used as an endogenous control. The primers were as follows:

Hes1 sense 5'-TCCCCGGCATTCCAAGCTAG-3', anti-sense 5'-GTCACCTCGTTCATGCACTC-3'; *Actb* sense

5'-ACTGGGACGACATGGAGAAG-3', antisense 5'-GTCTCCGGAGTCCATCACAA-3'.

Western Blotting Analysis

Total protein was extracted from the ipsilateral cortex and striatum using the Tissue Protein Extraction Kit (Phygene Life Sciences, Shanghai, China). After denaturation and quantification, the protein samples were loaded onto 8%–10% gel for separation using sodium dodecyl sulfate-polyacrylamide gel electrophoresis as previously described [16]. Briefly, the separated proteins were transferred onto PVDF membranes (Millipore, Bedford, MA, USA), followed by blocking for 1 h at room temperature (RT) with 5% non-fat dry milk diluted in TBST. The membrane was cut based on the molecular weights of the protein targets and probed with the corresponding primary antibodies overnight at 4°C. After washing with TBST for 30 min, the membranes were incubated with the corresponding secondary antibodies for 1 h at RT. The blots were detected using the ECL Plus Detection System (GE Healthcare, Piscataway, NJ, USA). The band intensity was quantified using ImageJ software (<http://rsbweb.nih.gov/ij>).

In Vivo Administration and siRNA-mediated Knockdown

The administration of inhibitor and siRNA transfection in mice subjected to tMCAO or sham surgery was performed as adapted from a previous report [17]. A volume of 4 µL of the PERK inhibitor GSK2606414 (20 µmol/L) or 4 µL siRNA targeting mouse Hes1 or scrambled siRNA were injected through a Hamilton microsyringe (0.5 µL/min, 8-min duration) into the left cerebral ventricle at 1.0 mm posterior to bregma, 2.0 mm lateral to the midline, and 4.0 mm ventral to the skull surface 24 h before tMCAO or sham surgery. siRNAs were synthesized by GenePharma (Shanghai, China). The sequences were as follows: Hes1 siRNA: 5'-AAGGUUUUAUUAUGUCUUAGGG-3'; scrambled siRNA: 5'-CCUACGCCACCAAUUUCGU-3'.

Infarct Evaluation and Neurological Assessment

Brains harvested from euthanized (pentobarbital sodium, 50 mg/kg, i.p.) mice were cut into 2-mm coronal slices and stained for 0.5 h in the dark with 2% 2,3,5-triphenyltetrazolium chloride (TTC) (Sigma Aldrich, St. Louis, MO, USA) at 37°C. Infarct sizes were quantified from digitized images using ImageJ software and expressed as the damaged area normalized to the total area of the contralateral hemisphere. After 24, 48, and 72 h of reperfusion, each mouse was scored based on a five-point system to

assess the neurological outcome [18]. The scoring system was as follows: 0, without deficits; 1, unable to extend right paw; 2, circling to the right; 3, falling to the right; 4, unable to walk. The final score was expressed as the median value of 12 mice in each group.

TUNEL Staining

TUNEL staining was used to detect neuronal apoptosis following ischemic stroke [19]. Briefly, sections 10 µm thick were fixed in 4% paraformaldehyde for 1 h at RT and incubated with 0.2% H₂O₂ for 1 h to block endogenous peroxidase activity. The sections were then incubated for 1 h in the dark with TUNEL reaction mixture (Millipore) at 37°C. After the counterstaining with DAPI, the fluorescence signal was captured with a Nikon A1 laser confocal microscope. In each animal, the number of TUNEL-positive cells was counted across three random fields within the region of the penumbra, and its percentage among the total cells was calculated using ImageJ.

Statistical Analysis

All data are presented as the mean ± SD, except for the neurological scores which are expressed as median values. Statistical significance was calculated by one-way ANOVA followed by Dunnett's test using SPSS 11.5 (SPSS Inc., Chicago, IL, USA). *P* < 0.05 were considered to be significant.

Results

Hes1 Expression is Induced in Mouse Brain After tMCAO

As a downstream effector gene of the Notch receptor, Hes1 expression varies during the differentiation of neurons [20]. However, how its expression changed following reperfusion in ischemic stroke was unknown. To address this, we used the tMCAO cerebral stroke model followed by reperfusion in wild-type C57BL/6 mice [21], and then compared the expression of Hes1 in brains with and without I/R injury. We found that, compared with sham surgery, the transcript level of Hes1 was significantly upregulated in the brain tissue with I/R injury followed by reperfusion for 12, 24, 48, and 72 h, as analyzed by qRT-PCR (Fig. 1A). Likewise, the results of Western blotting analysis showed that the protein expression of Hes1 was also upregulated after I/R injury (Fig. 1B). These findings showed that Hes1 expression is upregulated in the brain following I/R injury.

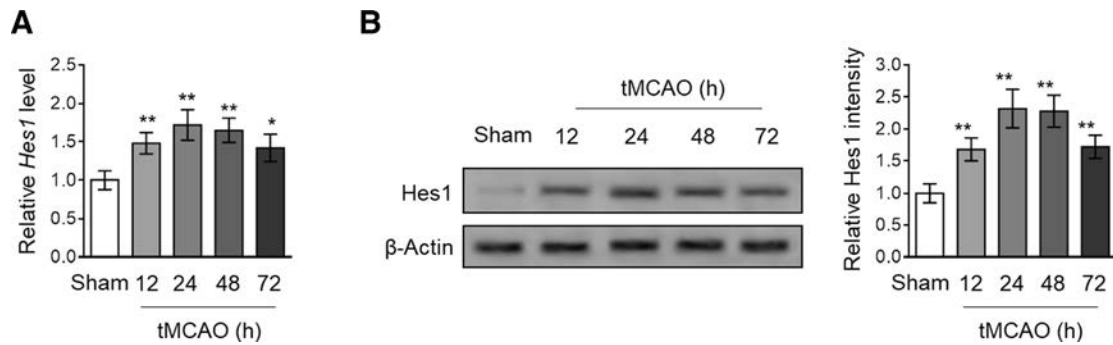


Fig. 1 Hes1 expression is induced in brain tissue following tMCAO. **A** The mRNA levels of Hes1 determined by qRT-PCR analysis. Data are presented relative to the sham group. **B** The protein levels of Hes1 determined by immunoblotting analysis. β-Actin was used as a

loading control. Left, representative images; right (band intensity analysis). Data are the mean ± SD. ***P* < 0.01, **P* < 0.05, one-way ANOVA followed by Dunnett’s test.

Hes1 Knockdown Exacerbates Cerebral Infarction and Neurological Deficit After tMCAO

The expression change of brain Hes1 following I/R injury led us to ask whether it plays a functional role during this pathological process. To address this, we depleted the expression of brain Hes1 by siRNA-mediated knockdown *in vivo*. Compared with sham surgery, tMCAO consistently resulted in an increased expression of brain Hes1, which was efficiently depleted when transfected with siRNA targeting Hes1 (siHes1) (Fig. 2A). Specifically, siHes1 transfection led to Hes1 knockdown in non-ischemic and

ischemic (core and penumbra) regions (Fig. 2B), indicating an efficient and broad knockdown effect. Next, the effect of Hes1 knockdown on I/R injury was examined by quantifying the cerebral infarct size delineated by TTC-stained brain slices [22]. As shown by the stained brain slices of tMCAO mice, the cerebral infarct size was increased when Hes1 was depleted by siHes1 as compared to the siRNA control (Fig. 2C, D). Moreover, at the same time, the extent of neurological deficit, as measured by a five-point system [18], was also significantly higher in tMCAO mice depleted of brain Hes1 (Fig. 2E). Together, these functional studies indicated that Hes1 knockdown increases the

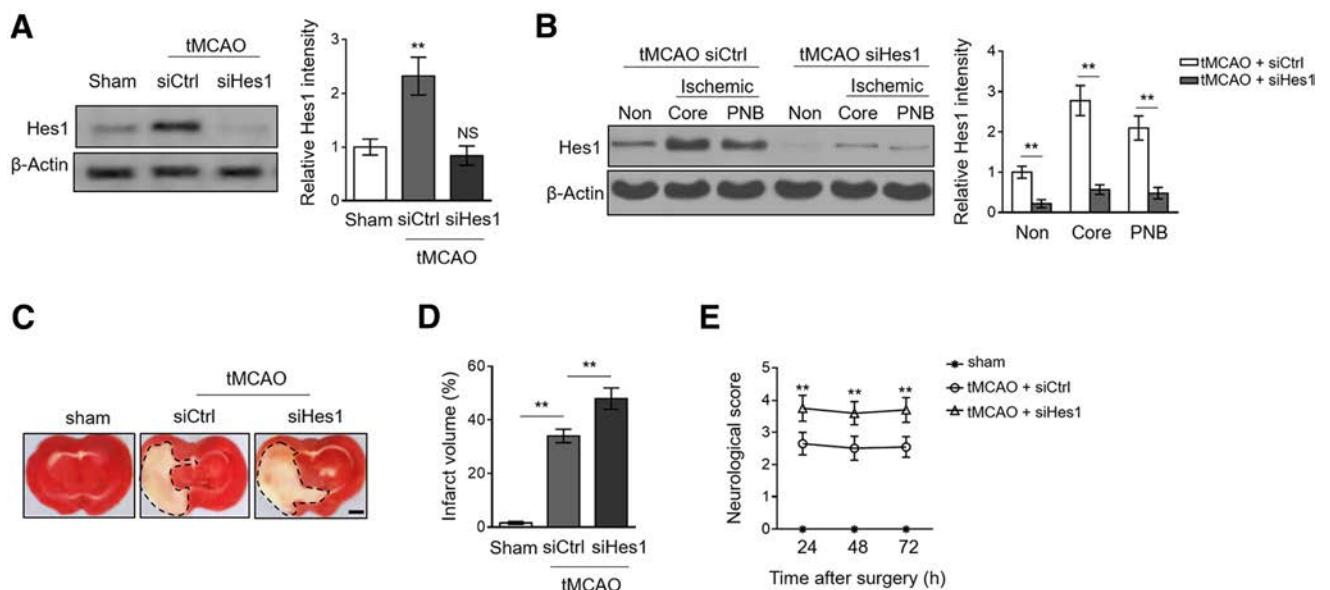


Fig. 2 Hes1 knockdown increases the cerebral infarction and exacerbates the neurological outcome following tMCAO. **A, B** At 24 h of reperfusion, the ipsilateral brain tissues were harvested and the Hes1 protein level was measured by immunoblotting analysis. β-actin was used as a loading control. Left, representative images; right, band intensity analysis. Non, non-ischemic; PNB, penumbra. **C, D** Representative images of brain TTC staining from 3 representative mice in

each group (**C**) and the percentage infarct volume (**D**) (dashed outline, infarct area; scale bar, 2 mm). **E** Neurological scores after 24, 48, and 72 h of reperfusion. Data are mean ± SD, except for neurological scores which are expressed as median values. ***P* < 0.01; NS, not significant, one-way ANOVA followed by Dunnett’s test.

cerebral infarction and worsens the neurological outcome after tMCAO, and thus suggested that Hes1 plays a protective role against I/R injury.

Hes1 Knockdown Promotes Neuronal Apoptosis After tMCAO

The apoptosis of neurons is a fundamental event mediating I/R injury-induced brain damage [23, 24]. To understand how Hes1 knockdown exaggerates I/R injury, we examined its effect on neuronal apoptosis following tMCAO. As shown by TUNEL staining of brain slices, tMCAO induced prominent apoptosis of neurons within the penumbra compared with sham surgery, and moreover, this extent of apoptosis induction was further significantly increased when Hes1 was depleted by siRNA transfection (Fig. 3A). Then, we confirmed this result by measuring the expression of apoptosis-related markers. As expected, Western blotting analysis showed that, in contrast to the sham group, tMCAO resulted in elevated expression of pro-apoptotic cleaved caspase-3 and Bax, and conversely decreased the expression of anti-apoptotic Bcl-2 (Fig. 3B, C). In addition, consistent with the TUNEL staining results (Fig. 3A), Hes1 knockdown markedly intensified the expression change of these apoptosis-related markers, compared with siCtrl group (Fig. 3B, C), showing that Hes1 knockdown promotes neuronal apoptosis after tMCAO. Taken together, given the important role of neuronal apoptosis in I/R injury,

these results suggested that the increased neuronal apoptosis at least partly explains the detrimental effect of Hes1 knockdown on exaggerating the cerebral infarction and the neurological deficit after tMCAO.

Hes1 Knockdown Promotes Activation of the PERK/eIF2 α /ATF4/CHOP Pathway After tMCAO

Recently, depletion of Hes1 in mouse and human cells has been reported to increase apoptosis in response to ER stress induced by dithiothreitol and thapsigargin; this is associated with its modulation of the PERK pathway [12]. Further, accumulating evidence has suggested that the dysregulation of ER stress plays a key role in inducing neuronal apoptosis and subsequent ischemic stroke-induced brain damage [25–27]. Hence, to elucidate how Hes1 knockdown promotes neuronal apoptosis following I/R injury, we next focused on examining the effect on ER stress. The results showed that the expression of p-PERK, p-eIF2 α , ATF4, and CHOP was increased in the I/R-injured brain (Fig. 4D), indicating activation of the PERK/eIF2 α /ATF4/CHOP signaling pathway and consistent with previous studies demonstrating that ER stress is induced in the rat model of stroke [9, 28]. Moreover, we found that the expression of p-PERK, p-eIF2 α , ATF4 and CHOP was further enhanced by Hes1 knockdown (Fig. 4A–D). These data suggested that activation of the PERK/eIF2 α /ATF4/CHOP pathway after tMCAO is enhanced in the absence of Hes1.

Fig. 3 Hes1 knockdown promotes apoptosis after tMCAO. **A** At 24 h after reperfusion, the ipsilateral brain tissue was harvested and the apoptosis within the penumbra was assessed by TUNEL staining. Left, representative images; right, percentages of TUNEL-positive cells. **B, C** Protein expression of cleaved caspase-3, Bax, and Bcl-2 determined by immunoblotting analysis. β -Actin was used as a loading control. **B** Representative images. **C** Analysis of cleaved caspase-3 band intensity and the Bax/Bcl-2 ratio. Data are the mean \pm SD. ** P < 0.01, one-way ANOVA followed by Dunnett's test.

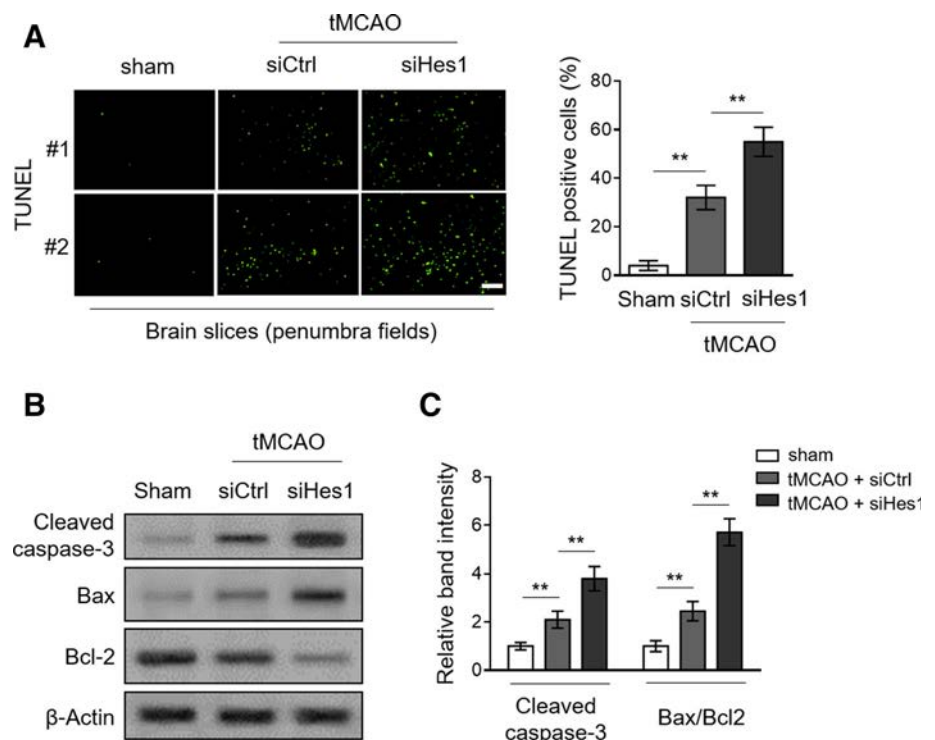
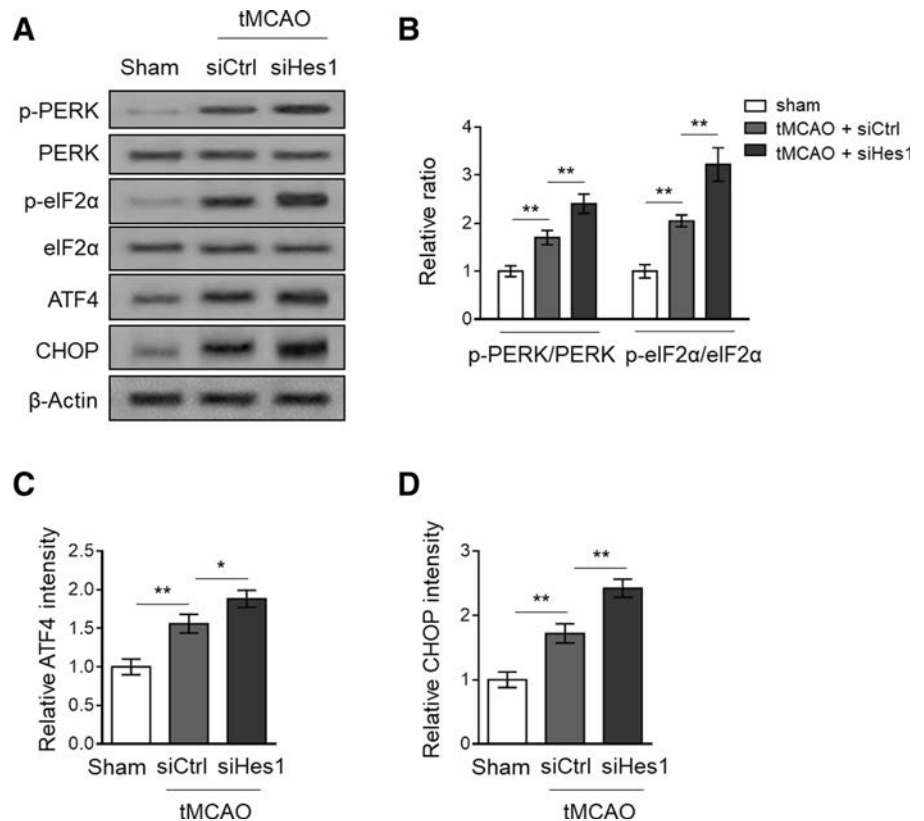


Fig. 4 Hes1 knockdown promotes activation of the PERK/eIF2 α /ATF4/CHOP pathway. Protein expression of p-PERK, PERK, p-eIF2 α , eIF2 α , ATF4, and CHOP analyzed by immunoblotting. β -actin was used as a loading control. **A** Representative images. **B** Statistical analysis of p-PERK/PERK, and p-eIF2 α /eIF2 α ratios. **C**, **D** Band intensity of ATF4 (**C**) and CHOP (**D**). Data are the mean \pm SD. ** $P < 0.01$, * $P < 0.05$, one-way ANOVA followed by Dunnett's test.



PERK Inhibitor Attenuates Effects of Hes1 Knockdown After tMCAO

To establish a potential causal link between promotion of the PERK signaling pathway and exaggerated neuronal apoptosis, cerebral infarction, and neurological deficit by Hes1 knockdown after tMCAO, we gave mice GSK2606414, a selective inhibitor of PERK [29]. Western blotting analysis showed that treatment with 4 μ L GSK2606414 (20 μ mol/L) at 24 h prior to tMCAO surgery effectively inhibited the activation of PERK and the downstream signaling pathway in the I/R-injured brain, irrespective of Hes1 expression (Fig. 5A). More importantly, along with the abrogated activation of PERK/eIF2 α /ATF4/CHOP signaling pathway, Hes1 knockdown-induced expression changes of the apoptosis-related markers cleaved caspase-3, Bax, and Bcl-2, were all remarkably attenuated (Fig. 5A, B), suggesting that activation of PERK/eIF2 α /ATF4/CHOP pathway promoted by Hes1 knockdown is responsible for the increased neuronal apoptosis after cerebral I/R injury. Furthermore, consistent with the attenuated apoptosis, the exaggeration of infarct size (Fig. 5C) and neurological deficit by Hes1 knockdown (Fig. 5D) was also significantly diminished when PERK was inhibited by GSK2606414. Thus, these lines of evidence together suggest that Hes1 knockdown aggravates ischemic stroke following tMCAO at least through

promoting ER stress-dependent neuronal apoptosis mediated by the PERK/eIF2 α /ATF4/CHOP pathway.

Discussion

Since neuronal apoptosis is one of the major pathogenic factors that cause brain damage following ischemic stroke, reducing apoptosis during this condition is a potential therapeutic strategy to prevent the loss of neurons in the affected tissue and minimize the ischemic stroke-induced damage, holding promise to improve the clinical outcome of patients with acute ischemic stroke [3, 23]. Several signaling pathways lead to the initiation of apoptosis after cerebral ischemia, including the most studied mitochondrial apoptotic pathway [30, 31]. However, ER stress-induced apoptosis has emerged as another important factor during the pathophysiology of cerebral ischemia, as evidenced by investigations using rat and mouse models as well as *in vitro* systems [9, 32–34]. Accordingly, it has been proposed that drugs shown to attenuate ER stress after experimental cerebral ischemia may serve as strong candidates in the treatment of stroke patients [25], such as dantrolene [35], (-)-epigallocatechin-3-gallate [28], and sodium phenylbutyrate [36]. Nonetheless, ER stress signaling is initially aimed to restore ER homeostasis, and manipulating such stress may have deleterious side-effects

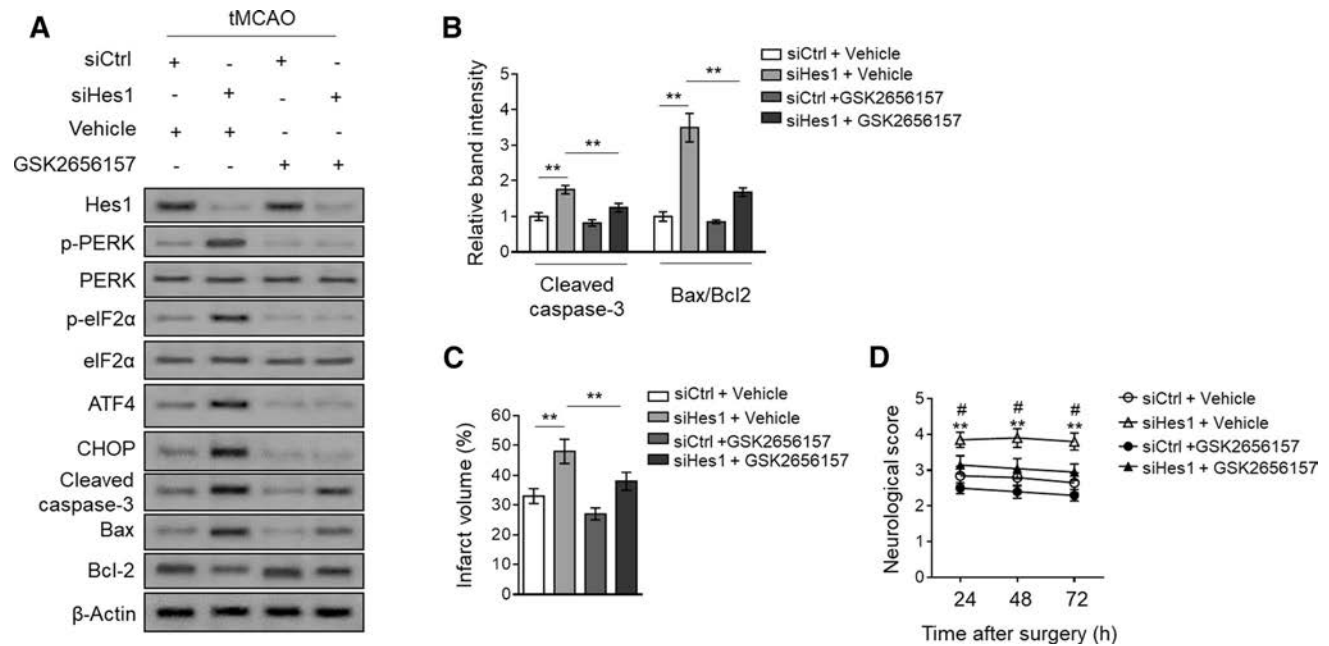


Fig. 5 PERK inhibitor attenuates Hes1 knockdown-induced effects following tMCAO. **A, B** At 24 h of reperfusion, ipsilateral brain tissue was harvested and the protein expression of targets as indicated was analyzed by immunoblotting. β -Actin was used as a loading control. **A** Representative images. **B** Analysis of band intensity of cleaved caspase-3 and of Bax/Bcl-2 ratio. **C** Percentages of infarct

volume from TTC staining. **D** Neurological scores after 24, 48, and 72 h of reperfusion. Data are the mean \pm SD, except for neurological scores, which are expressed as median values. ** $P < 0.01$; in **D**, ** $P < 0.01$, siCtrl + Vehicle vs siHes1 + Vehicle; # $P < 0.01$, siHes1 + Vehicle vs siHes1 + GSK2656157, one-way ANOVA followed by Dunnett's test.

[37], so a comprehensive knowledge of the mechanisms underlying ER regulation following ischemic stroke is essential to better exploit the therapeutic potential.

It is known that UPR induced by severe or prolonged ER stress can eventually result in the activation of proapoptotic pathways through mediators such as CHOP, caspase-12, and JNK [38]. But the regulation of ER stress-induced apoptosis following ischemic stroke is still not completely understood. In this study, by using stroke mouse model established *via* tMCAO, we showed that Hes1 knockdown increased neuronal apoptosis and the cerebral infarction and exacerbated the neurological outcome partly by promoting the activation of the PERK/eIF2 α /ATF4/CHOP pathway, thus suggesting that Hes1 may function as a novel regulator of ER stress to affect the process of ER stress-induced neuronal apoptosis following cerebral I/R injury. Given the evidence from the animal model and mechanistic studies, we provide a molecular basis for the possible application of Hes1 as a target in stroke treatment.

The Notch pathway is an evolutionarily conserved cell-to-cell communication system that plays indispensable roles in a variety of cellular activities such as differentiation, proliferation, and apoptosis [39]. Hes1 is a target gene downstream of Notch signaling that is activated by the binding of a Notch ligand to its cognate receptor [40]. One previous study has reported that, after renal I/R injury,

I/R activates Notch2/Hes1 signaling, which plays an important role in the renal I/R injury-associated inflammation and apoptosis [41]. Besides, activation of Notch1/Hes1 signaling has cardioprotective effects and attenuate myocardial I/R injury [42, 43]. We found that Hes1 expression was upregulated in brain tissue following tMCAO, suggesting that this increased expression of Hes1 is derived from the activated Notch/Hes1 signaling in response to cerebral I/R injury. This is possible, since increased expression of Notch signaling molecules has been reported in the ischemic brain of animal models [44, 45]. In mammalian cells, four Notch receptors (Notch1–4) and five ligands (Delta-like1/3/4 and Jagged1/2) have been identified [46]. However, so far the upstream Notch receptor ligand that mediates the upregulation of Hes1 following tMCAO-induced cerebral I/R injury is unknown, and this needs to be resolved by future investigations.

The increased neuronal apoptosis, cerebral infarction, and neurological deficit by Hes1 knockdown following tMCAO was remarkably rescued by treatment with a selective PERK inhibitor; this not only suggests that the promoted activation of the PERK/eIF2 α /ATF4/CHOP pathway and the resulting elevated ER stress act as critical events to account for these effects, but also implies that other mechanisms may also exist. Coincidentally, the Notch1/Hes1 signaling pathway has also been associated

with the attenuation of ER stress-induced apoptosis and protects the heart against I/R injury [47]. On the other hand, it has been reported that a lack of Hes1 in human and mouse cell lines induces apoptosis during ER stress, and this is associated with the enhanced dephosphorylation of eIF2 α via upregulating the expression of GADD34, a pro-apoptotic protein [12]. Although whether this mechanism could also explain the Hes1-regulated ER stress following cerebral I/R injury is unclear, it provides a useful clue for further studies to uncover how Hes1 knockdown promotes activation of the PERK/eIF2 α /ATF4/CHOP pathway. Addressing this issue may help to advance our understanding of the mechanism by which Hes1 participates in the pathophysiology of ischemic stroke. Moreover, it should be noted that all the functional and mechanistic results presented in the current study were obtained from *in vivo* siRNA-mediated knockdown experiments. Further investigations using Hes1-deficient mice or gain-of-function tactics would be helpful to consolidate the protective role of Hes1 in cerebral ischemic stroke.

Acknowledgements This work was supported by grants from the Guangxi Zhuang Autonomous Region Health and Family Planning Commission Science and Technology Project (Z2016419), Guangxi Natural Science Foundation Project (No.: 2018JJA140853) and the Science and Technology Project of Hunan Province, China (2014FJ4233).

Conflict of interest The authors declare that they have no conflict of interest.

References

- Strong K, Mathers C, Bonita R. Preventing stroke: saving lives around the world. *Lancet Neurol* 2007, 6: 182–187.
- Duehrkop C, Rieben R. Ischemia/reperfusion injury: effect of simultaneous inhibition of plasma cascade systems versus specific complement inhibition. *Biochem Pharmacol* 2014, 88: 12–22.
- Moskowitz MA, Lo EH, Iadecola C. The science of stroke: mechanisms in search of treatments. *Neuron* 2010, 67: 181–198.
- Nakka VP, Gusain A, Mehta SL, Raghuram R. Molecular mechanisms of apoptosis in cerebral ischemia: multiple neuro-protective opportunities. *Mol Neurobiol* 2008, 37: 7–38.
- Roussel BD, Kruppa AJ, Miranda E, Crowther DC, Lomas DA, Marciniak SJ. Endoplasmic reticulum dysfunction in neurological disease. *Lancet Neurol* 2013, 12: 105–118.
- Ozcan L, Tabas I. Role of endoplasmic reticulum stress in metabolic disease and other disorders. *Annu Rev Med* 2012, 63: 317–328.
- Rozpedek W, Pytel D, Mucha B, Leszczynska H, Diehl JA, Majsterek I. The role of the PERK/eIF2 α /ATF4/CHOP signaling pathway in tumor progression during endoplasmic reticulum stress. *Curr Mol Med* 2016, 16: 533–544.
- Cao SS, Kaufman RJ. Unfolded protein response. *Curr Biol* 2012, 22: R622–626.
- Nakka VP, Gusain A, Raghuram R. Endoplasmic reticulum stress plays critical role in brain damage after cerebral ischemia/reperfusion in rats. *Neurotox Res* 2010, 17: 189–202.
- Feng D, Wang B, Wang L, Abraham N, Tao K, Huang L, *et al.* Pre-ischemia melatonin treatment alleviated acute neuronal injury after ischemic stroke by inhibiting endoplasmic reticulum stress-dependent autophagy via PERK and IRE1 signalings. *J Pineal Res* 2017, 62.
- Shang Y, Coppo M, He T, Ning F, Yu L, Kang L, *et al.* The transcriptional repressor Hes1 attenuates inflammation by regulating transcription elongation. *Nat Immunol* 2016, 17: 930–937.
- Lee JE, Morrison W, Hollien J. Hairy and enhancer of split 1 (HES1) protects cells from endoplasmic reticulum stress-induced apoptosis through repression of GADD34. *J Biol Chem* 2018, 293: 5947–5955.
- Ito A, Fujimura M, Niizuma K, Kanoke A, Sakata H, Morita-Fujimura Y, *et al.* Enhanced post-ischemic angiogenesis in mice lacking RNF213; a susceptibility gene for moyamoya disease. *Brain Res* 2015, 1594: 310–320.
- Deppermann C, Kraft P, Volz J, Schuhmann MK, Beck S, Wolf K, *et al.* Platelet secretion is crucial to prevent bleeding in the ischemic brain but not in the inflamed skin or lung in mice. *Blood* 2017, 129: 1702–1706.
- Arumugam TV, Tang SC, Lathia JD, Cheng A, Mughal MR, Chigurupati S, *et al.* Intravenous immunoglobulin (IVIG) protects the brain against experimental stroke by preventing complement-mediated neuronal cell death. *Proc Natl Acad Sci U S A* 2007, 104: 14104–14109.
- Shindo A, Maki T, Mandeville ET, Liang AC, Egawa N, Itoh K, *et al.* Astrocyte-derived pentraxin 3 supports blood-brain barrier integrity under acute phase of stroke. *Stroke* 2016, 47: 1094–1100.
- Li L, Zhu K, Liu Y, Wu X, Wu J, Zhao Y, *et al.* Targeting thioredoxin-1 with siRNA exacerbates oxidative stress injury after cerebral ischemia/reperfusion in rats. *Neuroscience* 2015, 284: 815–823.
- Low PC, Manzanero S, Mohannak N, Narayana VK, Nguyen TH, Kvaskoff D, *et al.* PI3 Kdelta inhibition reduces TNF secretion and neuroinflammation in a mouse cerebral stroke model. *Nat Commun* 2014, 5: 3450.
- Tao Z, Zhao H, Wang R, Liu P, Yan F, Zhang C, *et al.* Neuroprotective effect of microRNA-99a against focal cerebral ischemia-reperfusion injury in mice. *J Neurol Sci* 2015, 355: 113–119.
- Kageyama R, Ohtsuka T, Shimojo H, Imayoshi I. Dynamic Notch signaling in neural progenitor cells and a revised view of lateral inhibition. *Nat Neurosci* 2008, 11: 1247–1251.
- Fluri F, Schuhmann MK, Kleinschnitz C. Animal models of ischemic stroke and their application in clinical research. *Drug Des Devel Ther* 2015, 9: 3445–3454.
- Shibata R, Sato K, Pimentel DR, Takemura Y, Kihara S, Ohashi K, *et al.* Adiponectin protects against myocardial ischemia-reperfusion injury through AMPK- and COX-2-dependent mechanisms. *Nat Med* 2005, 11: 1096–1103.
- Eltzschig HK, Eckle T. Ischemia and reperfusion—from mechanism to translation. *Nat Med* 2011, 17: 1391–1401.
- Niizuma K, Yoshioka H, Chen H, Kim GS, Jung JE, Katsu M, *et al.* Mitochondrial and apoptotic neuronal death signaling pathways in cerebral ischemia. *Biochim Biophys Acta* 2010, 1802: 92–99.
- Xin Q, Ji B, Cheng B, Wang C, Liu H, Chen X, *et al.* Endoplasmic reticulum stress in cerebral ischemia. *Neurochem Int* 2014, 68: 18–27.
- Liu X, Zhao S, Liu F, Kang J, Xiao A, Li F, *et al.* Remote ischemic postconditioning alleviates cerebral ischemic injury by attenuating endoplasmic reticulum stress-mediated apoptosis. *Transl Stroke Res* 2014, 5: 692–700.
- Yuan Y, Guo Q, Ye Z, Pingping X, Wang N, Song Z. Ischemic postconditioning protects brain from ischemia/reperfusion injury

- by attenuating endoplasmic reticulum stress-induced apoptosis through PI3K-Akt pathway. *Brain Res* 2011, 1367: 85–93.
28. Yao C, Zhang J, Liu G, Chen F, Lin Y. Neuroprotection by (-)-epigallocatechin-3-gallate in a rat model of stroke is mediated through inhibition of endoplasmic reticulum stress. *Mol Med Rep* 2014, 9: 69–76.
 29. Axten JM, Medina JR, Feng Y, Shu A, Romeril SP, Grant SW, *et al.* Discovery of 7-methyl-5-(1-([3-(trifluoromethyl)phenyl]acetyl)-2,3-dihydro-1H-indol-5-yl)-7H-pyrrolo[2,3-d]pyrimidin-4-amine (GSK2606414), a potent and selective first-in-class inhibitor of protein kinase R (PKR)-like endoplasmic reticulum kinase (PERK). *J Med Chem* 2012, 55: 7193–7207.
 30. Chan PH. Mitochondria and neuronal death/survival signaling pathways in cerebral ischemia. *Neurochem Res* 2004, 29: 1943–1949.
 31. Sims NR, Muyderman H. Mitochondria, oxidative metabolism and cell death in stroke. *Biochim Biophys Acta* 2010, 1802: 80–91.
 32. Zhang X, Yuan Y, Jiang L, Zhang J, Gao J, Shen Z, *et al.* Endoplasmic reticulum stress induced by tunicamycin and thapsigargin protects against transient ischemic brain injury: Involvement of PARK2-dependent mitophagy. *Autophagy* 2014, 10: 1801–1813.
 33. Ouyang YB, Lu Y, Yue S, Xu LJ, Xiong XX, White RE, *et al.* miR-181 regulates GRP78 and influences outcome from cerebral ischemia in vitro and in vivo. *Neurobiol Dis* 2012, 45: 555–563.
 34. Wu CX, Liu R, Gao M, Zhao G, Wu S, Wu CF, *et al.* Pinocembrin protects brain against ischemia/reperfusion injury by attenuating endoplasmic reticulum stress induced apoptosis. *Neurosci Lett* 2013, 546: 57–62.
 35. Li F, Hayashi T, Jin G, Deguchi K, Nagotani S, Nagano I, *et al.* The protective effect of dantrolene on ischemic neuronal cell death is associated with reduced expression of endoplasmic reticulum stress markers. *Brain Res* 2005, 1048: 59–68.
 36. Srinivasan K, Sharma SS. Sodium phenylbutyrate ameliorates focal cerebral ischemic/reperfusion injury associated with comorbid type 2 diabetes by reducing endoplasmic reticulum stress and DNA fragmentation. *Behav Brain Res* 2011, 225: 110–116.
 37. Hetz C, Chevet E, Harding HP. Targeting the unfolded protein response in disease. *Nat Rev Drug Discov* 2013, 12: 703–719.
 38. Hadley G, Neuhaus AA, Couch Y, Beard DJ, Adriaanse BA, Vekrellis K, *et al.* The role of the endoplasmic reticulum stress response following cerebral ischemia. *Int J Stroke* 2018, 13: 379–390.
 39. Andersson ER, Sandberg R, Lendahl U. Notch signaling: simplicity in design, versatility in function. *Development* 2011, 138: 3593–3612.
 40. Espinosa L, Cathelin S, D'Altri T, Trimarchi T, Statnikov A, Guiu J, *et al.* The Notch/Hes1 pathway sustains NF-kappaB activation through CYLD repression in T cell leukemia. *Cancer Cell* 2010, 18: 268–281.
 41. Huang R, Zhou Q, Veeraragoo P, Yu H, Xiao Z. Notch2/Hes-1 pathway plays an important role in renal ischemia and reperfusion injury-associated inflammation and apoptosis and the gamma-secretase inhibitor DAPT has a nephroprotective effect. *Ren Fail* 2011, 33: 207–216.
 42. Pei H, Yu Q, Xue Q, Guo Y, Sun L, Hong Z, *et al.* Notch1 cardioprotection in myocardial ischemia/reperfusion involves reduction of oxidative/nitrative stress. *Basic Res Cardiol* 2013, 108: 373.
 43. Yu L, Li F, Zhao G, Yang Y, Jin Z, Zhai M, *et al.* Protective effect of berberine against myocardial ischemia reperfusion injury: role of Notch1/Hes1-PTEN/Akt signaling. *Apoptosis* 2015, 20: 796–810.
 44. Lou YL, Guo F, Liu F, Gao FL, Zhang PQ, Niu X, *et al.* MiR-210 activates notch signaling pathway in angiogenesis induced by cerebral ischemia. *Mol Cell Biochem* 2012, 370: 45–51.
 45. Wang L, Chopp M, Zhang RL, Zhang L, Letourneau Y, Feng YF, *et al.* The Notch pathway mediates expansion of a progenitor pool and neuronal differentiation in adult neural progenitor cells after stroke. *Neuroscience* 2009, 158: 1356–1363.
 46. Arboleda-Velasquez JF, Zhou Z, Shin HK, Louvi A, Kim HH, Savitz SI, *et al.* Linking Notch signaling to ischemic stroke. *Proc Natl Acad Sci U S A* 2008, 105: 4856–4861.
 47. Zhang M, Yu LM, Zhao H, Zhou XX, Yang Q, Song F, *et al.* 2,3,5,4'-Tetrahydroxystilbene-2-O-beta-D-glucoside protects murine hearts against ischemia/reperfusion injury by activating Notch1/Hes1 signaling and attenuating endoplasmic reticulum stress. *Acta Pharmacol Sin* 2017, 38: 317–330.



Chemical Stimulation of Renal Tissue Induces Sympathetic Activation and a Pressor Response *via* the Paraventricular Nucleus in Rats

Chao Ye¹ · Yun Qiu¹ · Feng Zhang¹ · Ai-Dong Chen¹ · Hong Zhou¹ · Jue-Jin Wang¹ · Qi Chen² · Yue-Hua Li² · Yu-Ming Kang³ · Guo-Qing Zhu^{1,2}

Received: 3 January 2019 / Accepted: 3 June 2019 / Published online: 7 August 2019
© Shanghai Institutes for Biological Sciences, CAS 2019

Abstract Sympathetic activation and the kidney play critical roles in hypertension and chronic heart failure. The role of the kidney in sympathetic activation is still not well known. In this study, we revealed an excitatory renal reflex (ERR) in rats induced by chemical stimulation of the kidney that regulated sympathetic activity and blood pressure. The ERR was induced by renal infusion of capsaicin, and evaluated by the changes in renal sympathetic outflow, blood pressure, and heart rate. Renal infusion of capsaicin dose-dependently increased the contralateral renal sympathetic nerve activity, mean arterial pressure, and heart rate. Capsaicin in the cortico-medullary border had greater effects than in the cortex or medulla. Intravenous infusion of capsaicin had no significant effects. The effects of renal infusion of capsaicin were abolished by ipsilateral renal denervation, but were not affected by bilateral sinoaortic denervation. Renal infusion of capsaicin increased the ipsilateral renal afferent activity. The ERR was also induced by renal infusion of

bradykinin, adenosine, and angiotensin II, but not by ATP. Renal infusion of capsaicin increased c-Fos expression in the paraventricular nucleus (PVN) of hypothalamus. Lesion of neurons in the PVN with kainic acid abolished the capsaicin-induced ERR. These findings indicate that chemical stimulation of kidney causes an excitatory reflex, leading to sympathetic activation, pressor response, and accelerated heart rate. The PVN is an important central nucleus in the pathway of the ERR.

Keywords Sympathetic activity · Blood pressure · Renal afferents · Renal reflex · Paraventricular nucleus

Introduction

Sympathetic activity is enhanced in hypertension [1, 2], chronic heart failure [3, 4], and chronic kidney disease [5, 6]. Excessive sympathetic activation contributes greatly to the occurrence and development of hypertension and related organ damage [7]. Intervention in sympathetic overactivity has been used as an important strategy for attenuating hypertension and its complications [8, 9]. On the other hand, most patients with chronic kidney disease have high blood pressure and excessive sympathetic activation, which are closely associated with the increases in morbidity and mortality of cardiovascular events [5]. The excessive sympathetic activity not only plays a crucial role in the pathogenesis of hypertension but also contributes greatly to the development of chronic kidney diseases that are independent of hypertension [5]. Accumulating evidence has shown that the kidney plays critical roles in sympathetic activation in hypertension and chronic kidney diseases [10–15]. However, the mechanisms

Electronic supplementary material The online version of this article (<https://doi.org/10.1007/s12264-019-00417-1>) contains supplementary material, which is available to authorized users.

✉ Guo-Qing Zhu
gqzhucn@njmu.edu.cn

¹ Key Laboratory of Targeted Intervention of Cardiovascular Disease, Collaborative Innovation Center of Translational Medicine for Cardiovascular Disease, and Department of Physiology, Nanjing Medical University, Nanjing 211166, China

² Department of Physiology, Nanjing Medical University, Nanjing 211166, China

³ Department of Physiology and Pathophysiology, Cardiovascular Research Center, Xi'an Jiaotong University School of Medicine, Xi'an 710061, China

leading to excessive sympathetic activation are complex and not completely understood.

Renal nerves consist of afferent sensory and efferent sympathetic nerves. The afferents are activated by stimulation of mechanoreceptors and chemoreceptors in the kidney [16]. The mechanoreceptors are mainly distributed in the renal pelvis wall, and are activated by increased pelvic pressure. The chemoreceptors respond to the chemical environment in the renal tissue and pelvis, such as hypertonic NaCl, capsaicin, bradykinin, and adenosine. Immunoreactivity for substance P has been found in the interlobar branches of the renal artery, the walls of the renal pelvis, and the proximal ureter, which are involved in chemoreceptor function [17]. It has been shown that the activation of renal afferents reduces renal sympathetic nerve activity (RSNA) in normotensive rats, but increases the RSNA in several pathophysiological conditions such as chronic heart failure, hypertension, and ischemic acute renal failure [10, 18, 19]. The role of renal afferent nerve activity in the reflex control of sympathetic outflow is controversial or opaque [20]. Renal denervation or catheter-based radiofrequency renal denervation which interrupts both the afferent and efferent renal nerves has been used as an interventional approach to treat hypertension [16, 21, 22]. Therefore, it is important to reveal the roles of renal afferents in the reflex regulation of blood pressure and sympathetic activity. The present study was designed to determine the roles of an excitatory renal reflex (ERR) induced by chemical stimulation of the kidney in regulating sympathetic activity and blood pressure. Furthermore, whether the hypothalamic paraventricular nucleus (PVN) is critical for the central neurocircuitry of the ERR was investigated.

Methods

Animals and General Procedures

Experiments were carried out on 132 male Sprague–Dawley rats weighing 280 g–320 g. The protocols were approved by the Experimental Animal Care and Use Committee in Nanjing Medical University. The experimental procedures were carried out in accordance with the Guide for the Care and Use of Laboratory Animals (US National Institutes of Health, NIH publication, 8th edition, 2011). The rats were kept at a controlled humidity and temperature under a 12-h light/dark cycle with free access to lab chow and tap water. Each rat was anesthetized with a mixture of α -chloralose (40 mg/kg) and urethane (800 mg/kg) *via* intraperitoneal injection. The depth of anesthesia was confirmed before surgery by the absence of both corneal reflexes and paw withdrawal responses to a noxious

pinch [23]. The trachea and right carotid artery were exposed by a midline incision in the neck. The trachea was intubated for positive-pressure ventilation with room air using a small-animal ventilator (model 51600, Stoelting, Chicago, IL). The right carotid artery was cannulated to record blood pressure. The arterial blood pressure, mean arterial pressure (MAP), heart rate (HR), and RSNA were simultaneously recorded using a PowerLab data acquisition system (8SP, ADInstruments, Bella Vista, NSW, Australia). The rat was euthanized at the end of the experiment with pentobarbital sodium (100 mg/kg) *via* intravenous injection.

RSNA Recording

RSNA was recorded as we reported previously [24]. Briefly, the left renal artery and nerves were exposed *via* a left flank incision. The renal nerve was isolated and cut at its distal end to abolish afferent activity from the kidney. The nerve was then placed on a pair of parallel silver electrodes, and immersed in mineral oil at 37 °C. The nerve activity was amplified with an AC/DC differential amplifier (model DP-304, Warner Instruments, Hamden, CT). The signals were low-pass filtered at 3,000 Hz and high-pass filtered at 100 Hz, and then integrated at a 100-ms time constant. After each experiment, the central end of the renal nerve was cut to record background noise. The RSNA value was obtained by the integrated RSNA value minus the background noise value, and expressed as a percentage change of the control value.

Recording of Renal Afferent Nerve Activity

The right renal nerve was exposed, isolated, and sectioned at its central end to abolish the renal efferent activity. Renal afferent nerve activity was recorded as for RSNA recording.

Chemical Stimulation of Kidney to Induce the ERR

The right kidney was exposed and a stainless-steel tube (0.31 mm outer diameter) was horizontally inserted into the kidney for the infusion of chemicals. The tube was inserted from the right side of the kidney to the left side, except in the protocol used to compare the effects of capsaicin at different sites in the kidney. The tip of the tube was held at the cortico-medullary border or at different depths from the renal surface to compare the effects of capsaicin. The insertion of the tube stopped when a slight resistance was encountered, indicating that the tip reached the cortico-medullary border, which was about 2 mm below the renal surface. The ERR was induced by renal infusion of capsaicin (1 nmol/ μ L), or bradykinin

(0.5 nmol/ μ L), adenosine (0.5 nmol/ μ L), ATP (1.5 nmol/ μ L), or angiotensin II (Ang II, 0.01 nmol/ μ L). The tube was connected to a microinjector through a PE50 polyethylene catheter. The infusion was carried out using a programmable pressure injector (PM2000B, MicroData Instrument, NJ) at 1.0 μ L/min for 20 min. The ERR was evaluated by the RSNA, MAP, and HR responses to the renal infusion of chemicals.

Microinjection into the PVN

Microinjections were performed as we reported previously [25]. Briefly, each rat was fixed in a stereotaxic frame in the prone position (Stoelting, Chicago, IL). The coordinates of the PVN used in the present study were 0.4 mm lateral to the midline, 1.8 mm caudal to bregma, and 7.9 mm below the dorsal surface. The PVN microinjection was performed with a glass micropipette (50 μ m tip diameter). The volume of the microinjection for each side was 50 nL, and it was completed in 1 min. After each experiment, the same volume of Evans Blue was microinjected. The injection sites were localized histologically [26]. The visible extent of dye was <300 μ m in diameter. The data from rats with microinjection sites outside the PVN were excluded.

Identification of PVN Lesion

Toluidine blue staining of brain sections was used to identify the lesion in the PVN. The nuclei of cells stained blue. The standard for the effectiveness of a PVN lesion was that the number of nuclei within 0.2 mm around the injection site in the bilateral PVN was reduced by >60%.

Sinoaortic Denervation (SAD)

SAD was carried out in only one of the experimental protocols to examine the secondary effect of the baroreflex on the ERR. The bilateral vagal and carotid sinus nerves in the neck were individually identified and sectioned. All other nerve fibers visible in the carotid sinus area were cut. The common carotid arteries and carotid bifurcation were stripped of adventitial tissues 4 mm above and below the bifurcation. Phenol solution (10%) was applied to this area to destroy any remaining nerve fiber. The denervation was confirmed by showing that the HR change was <5 beats/min after intravenous administration of phenylephrine (20 μ g/kg) [27].

Immunohistochemistry

Immunohistochemistry for c-Fos expression was examined as we previously described [28, 29]. Mouse monoclonal antibody against c-Fos (sc-271243) was from Santa Cruz (Dallas, TX) and diluted 1:1000 for use. Biotinylated secondary antibody was from Santa Cruz (ABC staining system kit).

Chemicals

Capsaicin was from MedChem Express (Monmouth Junction, NJ); bradykinin, Ang II, adenosine, and ATP were from Sigma Chemical Co. (St Louis, MO); and kainic acid (KA) was from Abcam (Cambridge, MA). Capsaicin was dissolved in ethanol and stored as stock solution. The capsaicin solution was diluted before use; it contained 1% stock solution, 1% Tween 80, and 98% normal saline. The vehicle was used as the control for capsaicin. Other chemicals were dissolved in saline.

Statistics

The changes of RSNA, MAP, and HR were determined by the average values for 1 min when their maximal response was reached. Comparisons between two groups were assessed by Student's *t*-test. One-way or two-way ANOVA was used for multiple comparisons followed by *post hoc* Bonferroni's test. All data are expressed as the mean \pm SEM. A *P* value <0.05 was considered statistically significant.

Results

Dose- and Time-Effects of Renal Infusion of Capsaicin

Unilateral renal infusion of capsaicin at the cortico-medullary border of the kidney caused immediate increases in the contralateral RSNA, MAP, and HR in a dose-dependent manner (Fig. 1A). The infusion sites in kidneys were confirmed by Evans blue staining (Fig. 1B). The capsaicin had its maximal effects at \sim 1 nmol/min for 20 min (Fig. 2A), so we used this dose in all subsequent experiments. The maximal effects of capsaicin began at \sim 15 min after the beginning of infusion (RSNA, +18.3% \pm 3.2%; MAP, +8.2 \pm 1.3 mmHg; HR, +8.1 \pm 2.9 bpm), and lasted 40 min–50 min. Renal infusion of vehicle did not have significant effects on the RSNA, MAP, and HR (Fig. 2B).

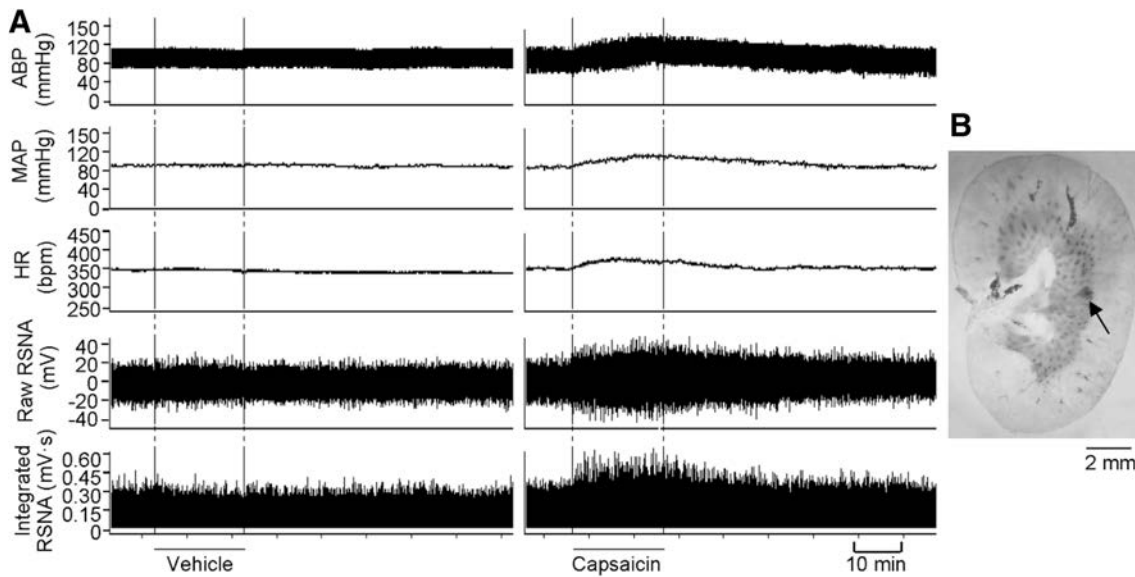


Fig. 1 Capsaicin-induced excitatory renal reflex (ERR). **A** Representative recordings showing the capsaicin-induced reflex changes of arterial blood pressure (ABP), mean arterial pressure (MAP), heart rate (HR), and contralateral renal sympathetic nerve activity (RSNA).

The capsaicin was infused into the cortico-medullary border of the right kidney at 1 nmol/min for 20 min. **B** Representative section of kidney showing the infusion site.

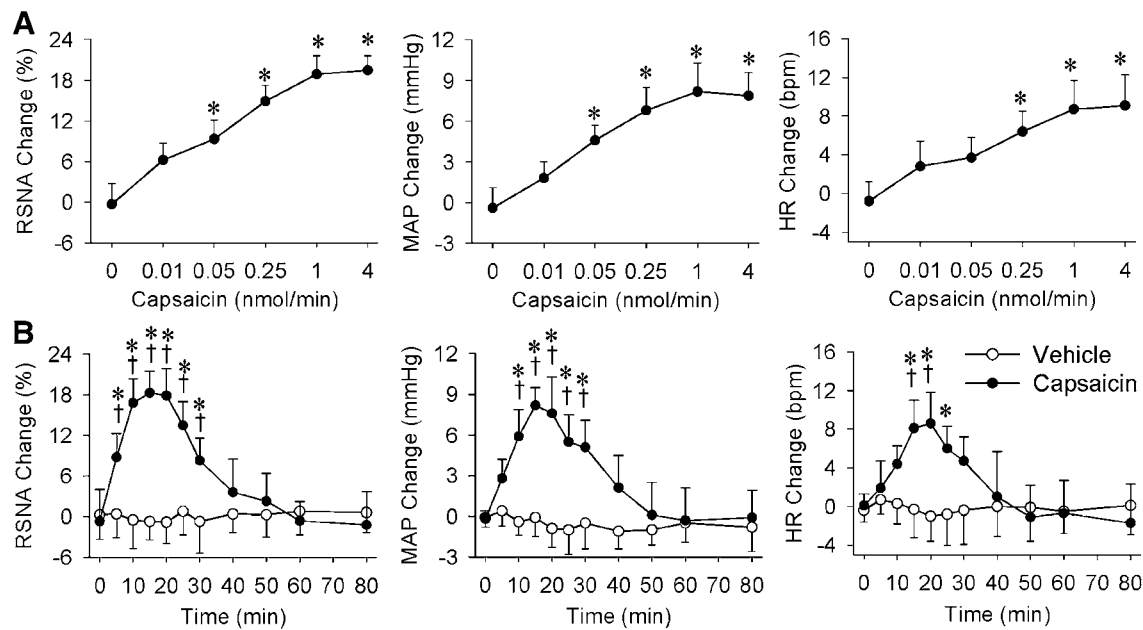


Fig. 2 Dose- and time-effects of the capsaicin-induced excitatory renal reflex (ERR). Capsaicin was infused into the cortico-medullary border of the right kidney to induce reflex changes in contralateral renal sympathetic nerve activity (RSNA), mean arterial pressure (MAP) and heart rate (HR). **A** Dose-response curves for capsaicin

(0 nmol/min, 0.01 nmol/min, 0.05 nmol/min, 0.25 nmol/min, 1 nmol/min, and 4 nmol/min for 20 min). **B** Time-courses for capsaicin (1 nmol/min for 20 min). Values are the mean \pm SEM. * $P < 0.05$ vs 0 nmol or 0 min; † $P < 0.05$ vs Vehicle. $n = 6$ per group.

Effects of Capsaicin in Different Sites in the Kidney

Renal infusion of capsaicin 1 mm, 2 mm, or 4 mm below the kidney surface (corresponding to the cortex, cortico-medullary border, and medulla) increased the contralateral RSNA, MAP, and HR. However, the effects of capsaicin at

the cortico-medullary border were significantly greater than those in the cortex and medulla (Fig. 3A). Infusion of capsaicin into the cortico-medullary border of the upper, lateral, or lower parts of the kidney showed similar increases in the contralateral RSNA, MAP, and HR (Fig. 3B). There were no significant differences in the

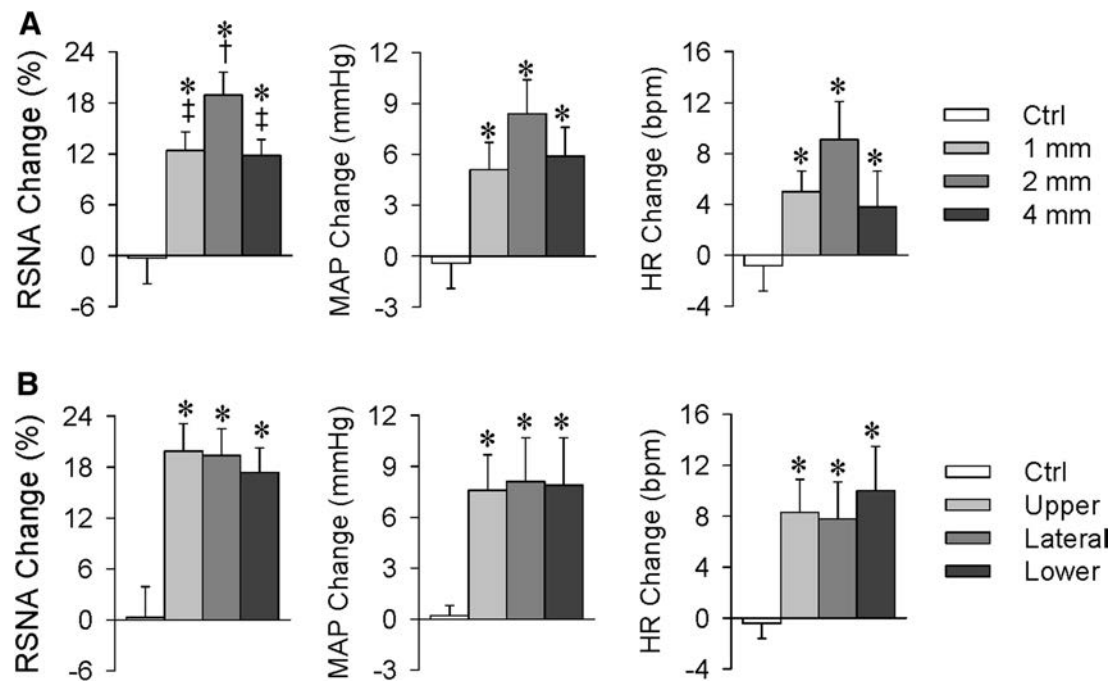


Fig. 3 Excitatory renal reflex (ERR) induced by capsaicin at different sites in the kidney. Capsaicin (1 nmol/min for 20 min) was infused into the right kidney to induce reflex changes in the contralateral renal sympathetic nerve activity (RSNA), mean arterial pressure (MAP), and heart rate (HR). **A** Effects of capsaicin at

different depths in the kidney (1 mm, 2 mm, and 4 mm below the lateral surface). **B** Effects of capsaicin at different locations in the kidney (upper, lateral, and lower parts, 2 mm below the surface). Values are the mean \pm SEM. * $P < 0.05$ vs Ctrl; † $P < 0.05$ vs 1 mm; ‡ $P < 0.05$ vs 2 mm. $n = 6$ per group.

baseline RSNA, MAP, and HR among these groups (Tables S1 and S2). The cortico-medullary border in the lateral kidney was selected as the infusion site in all other experiments.

Excluding the Possibility of Extra-Renal Effects Due to Capsaicin Diffusion

Although renal infusion of capsaicin increased the contralateral RSNA, MAP, and HR, intravenous infusion of same dose failed to have any significant effects on these parameters (Fig. 4A). The results excluded the possibility that the effects of renal infusion might be due to leakage of capsaicin into the circulation. Our previous studies have shown that administration of capsaicin to white adipose tissue induces an adipose afferent reflex that causes sympathetic activation and pressor responses [30–32]. Similar effects were found for capsaicin infusion into the perirenal fat in the present study. However, the effects of capsaicin in the perirenal fat were smaller than those at the same dose in the kidney (RSNA, $11.3\% \pm 1.5\%$ vs $18.9\% \pm 2.7\%$, $P < 0.05$; MAP, 3.9 ± 1.5 mmHg vs 8.4 ± 2.2 mmHg, $P < 0.05$; HR, 1.4 ± 2.2 bpm vs 9.1 ± 3.0 bpm, $P < 0.05$). Furthermore, the effects of capsaicin in perirenal fat were completely abolished by denervation of the perirenal fat (Fig. 4B). More

importantly, the effects of renal infusion of capsaicin were completely abolished by ipsilateral renal denervation, but not affected by ipsilateral perirenal lipectomy (Fig. 5A). These results indicate that the effects of renal infusion of capsaicin are caused by stimulation of the kidney rather than perirenal fat.

Renal Infusion of Capsaicin Increases Ipsilateral Renal Afferent Nerve Activity

Renal infusion of capsaicin increased the ipsilateral renal afferent activity (Fig. 5B). There were no significant differences in baseline afferent activity between the vehicle- and the capsaicin-treated groups (Table S3). Representative recordings showed that capsaicin in the kidney induced an immediate increase in the afferent activity (Fig. 5C). The results showed that capsaicin stimulates renal afferents in the kidney and increases their activity. Taking into account all the above results, we concluded that the effects of capsaicin in the kidney are primarily caused by increased renal afferent nerve activity due to their activation rather than capsaicin-induced release of chemicals or signal molecules into the circulation.

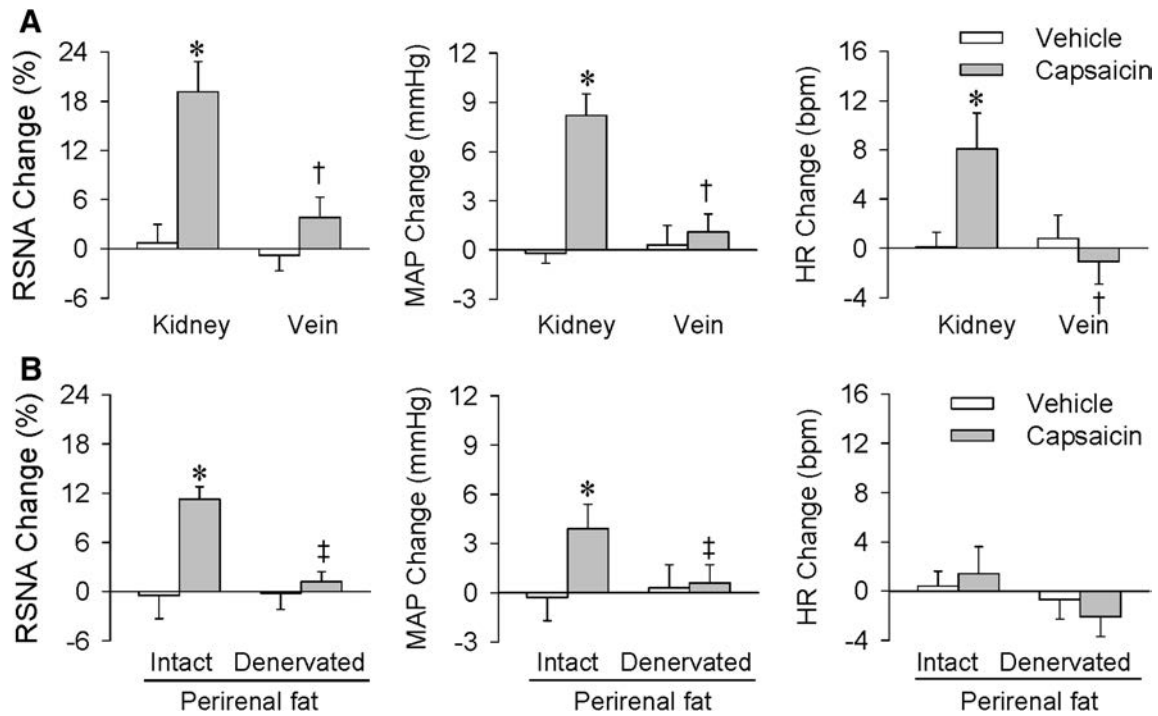


Fig. 4 Effects of infusion of capsaicin into the right kidney, jugular vein, and perirenal fat on contralateral renal sympathetic nerve activity (RSNA), mean arterial pressure (MAP), and heart rate (HR). **A** Effects of capsaicin infusion into the cortico-medullary border of

the right kidney and the jugular vein. **B** Effects of capsaicin infusion into intact or denervated perirenal fat. Capsaicin was infused at 1 nmol/min for 20 min. Values are the mean ± SEM. **P* < 0.05 vs Vehicle; †*P* < 0.05 vs Kidney; ‡*P* < 0.05 vs Intact. *n* = 6 per group.

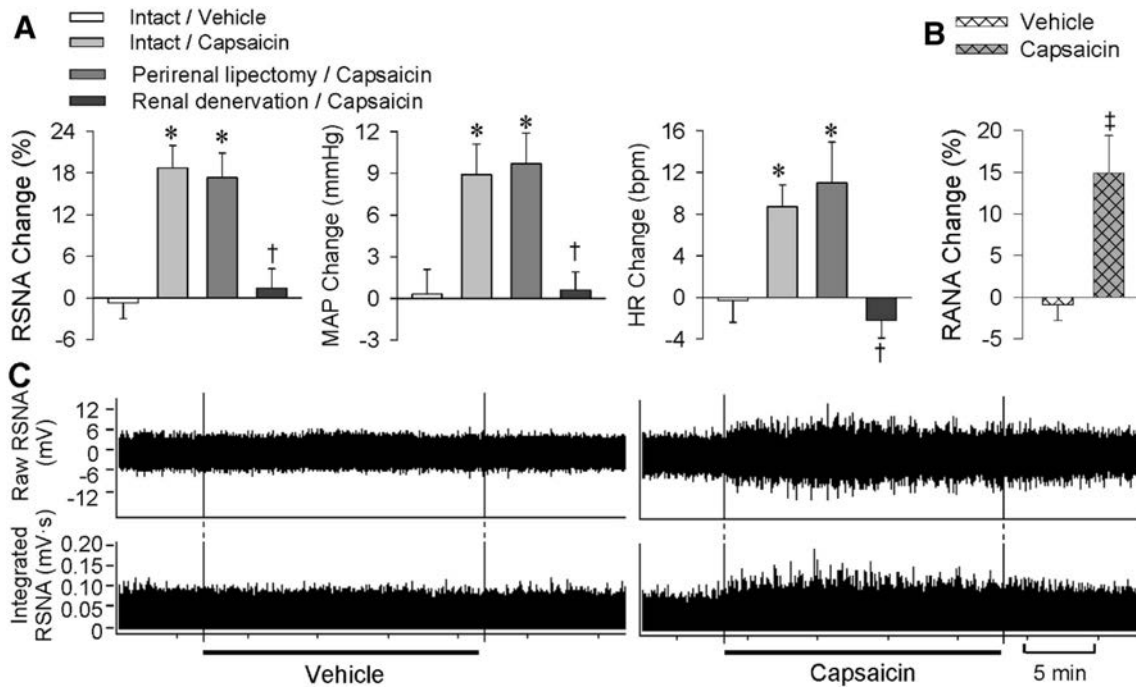


Fig. 5 Role of renal afferents in the capsaicin-induced excitatory renal reflex (ERR). Capsaicin (1 nmol/min for 20 min) was infused into the cortico-medullary border of the right kidney to induce reflex changes in the contralateral renal sympathetic nerve activity (RSNA), mean arterial pressure (MAP), and heart rate (HR). **A** Effects of capsaicin in kidney were not affected by ipsilateral perirenal

lipectomy, but were abolished by ipsilateral renal denervation. **B** Effect of intrarenal infusion of capsaicin on renal afferent nerve activity (RANA). **C** Representative recordings of RANA. Values are the mean ± SEM. **P* < 0.05 vs Intact/Vehicle; †*P* < 0.05 vs Intact/Capsaicin; ‡*P* < 0.05 vs Vehicle. *n* = 6 per group.

ERR Induced by Different Chemicals

Capsaicin is the main pungent ingredient in hot chili peppers, and selectively activates sensory neurons *via* acting on a non-selective ligand-gated cation channel, transient receptor potential vanilloid-1. Capsaicin is used to stimulate sensory afferents [33–35]. It was of interest to determine whether ERR can be induced by other chemicals. We found that renal infusion of bradykinin, adenosine, and Ang II had effects similar to capsaicin on the contralateral RSNA, MAP, and HR. However, renal infusion of ATP failed to induce the ERR (Fig. 6A).

Effects of SAD on Capsaicin-Induced ERR

The ERR was examined 1 h after SAD surgery to determine whether the baroreflex plays a role in capsaicin-induced ERR. SAD had no significant effects on baseline RSNA, MAP, and HR (Table S4). The SAD rats showed a tendency towards an enhanced ERR, but the difference from sham-operated rats failed to reach significance (Fig. 6B), suggesting that the inhibitory effect of the baroreflex on the ERR is very weak under normal conditions. Therefore, all other experiments were carried out in rats without SAD, better representing the true state of the ERR in regulating sympathetic and cardiovascular activity in intact animals.

The PVN is Important in Mediating the Capsaicin-Induced ERR

The PVN is critical in the cardiac sympathetic afferent reflex [36] and adipose afferent reflex [30], so we investigated its role in the ERR. Immunohistochemistry showed that unilateral renal infusion of capsaicin increased c-Fos expression in the bilateral PVN (Fig. 7A). The increased c-Fos expression involved both the parvocellular and magnocellular parts of the PVN (Fig. 7B). KA is strongly neurotoxic [37] and is widely used to destroy neurons in brain nuclei without lesioning terminals and axons of passage in the injection site [38]. Neurons immediately fire at a very high rate after KA injection, and no neuronal activity is recorded 1 h later [38]. Bilateral PVN microinjection of KA induces a great and immediate increase in sympathetic outflow, blood pressure, and HR, which recovers within 1 h, and then remains at baseline levels [30, 36]. In the present study, microinjection of KA into the bilateral PVN prevented the capsaicin-induced ERR 2 h later (Fig. 7C). There were no significant differences in baseline RSNA, MAP, and HR before the PVN microinjection of saline or KA (Table S5). The effectiveness of PVN lesioning by KA was confirmed by toluidine blue staining (Fig. S1). Microinjection of KA into anterior hypothalamic areas near the PVN failed to prevent the capsaicin-induced ERR, indicating that the PVN is involved in the central pathway of the ERR.

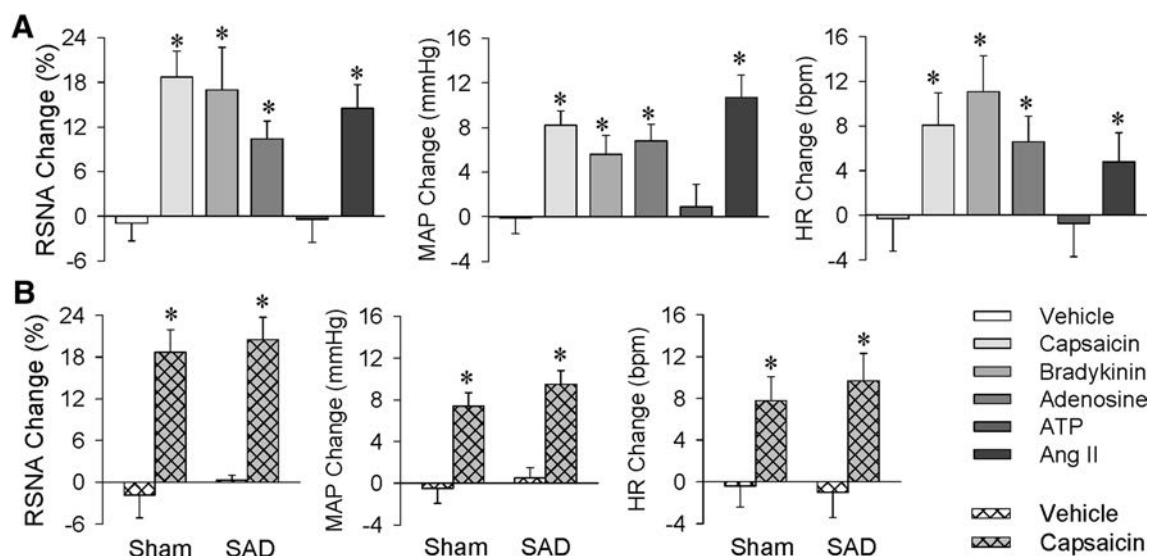


Fig. 6 Excitatory renal reflex (ERR) induced by different chemicals and effects of sinoaortic denervation (SAD) on capsaicin-induced ERR as evaluated by the reflex changes in contralateral renal sympathetic nerve activity (RSNA), mean arterial pressure (MAP), and heart rate (HR). **A** Effects of renal infusion of capsaicin (1 nmol/

min), bradykinin (0.5 nmol/min), adenosine (0.5 nmol/min), ATP (1.5 nmol/min), and Ang II (0.01 nmol/min) for 20 min. **B** Effects of bilateral SAD on the ERR. Renal infusion of vehicle or capsaicin was carried out 1 h after sham operation (Sham) or bilateral SAD. Values are the mean \pm SEM. * $P < 0.05$ vs Vehicle. $n = 6$ per group.

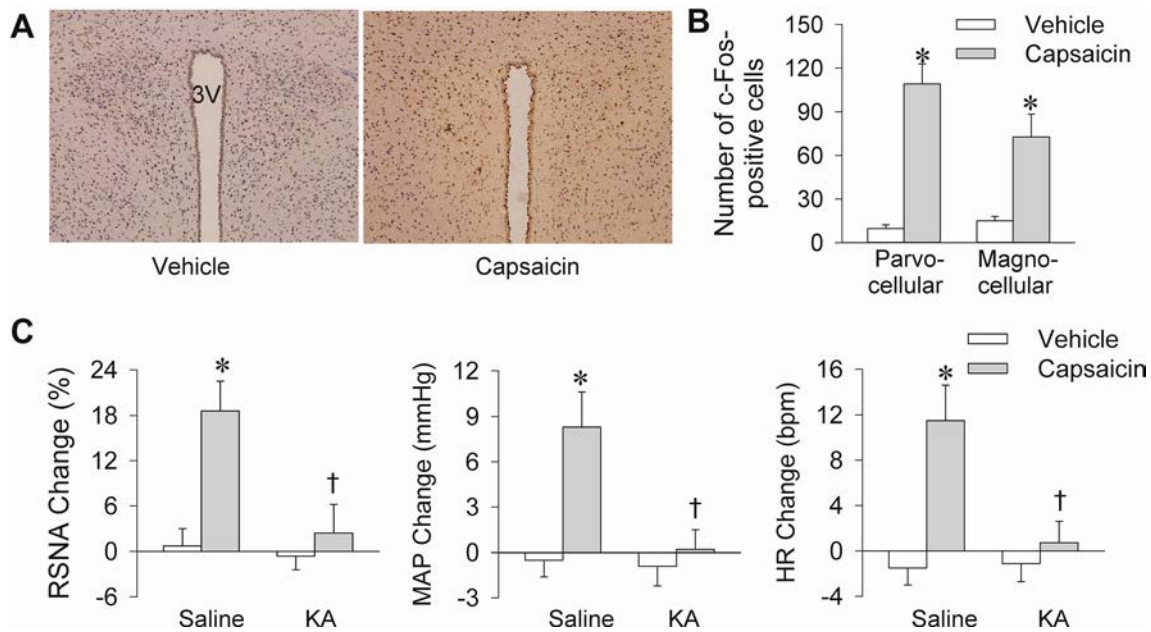


Fig. 7 The PVN is involved in the capsaicin-induced excitatory renal reflex (ERR). **A** Representative immunohistochemical sections showing the c-Fos expression (yellow) in the PVN 30 min after renal infusion of capsaicin. **B** Numbers of c-Fos-positive cells in the parvocellular and magnocellular parts of the PVN 30 min after renal

infusion of capsaicin. **C** Effects of bilateral PVN lesions with kainic acid (KA) on the capsaicin-induced ERR. Vehicle or capsaicin (1 nmol/min for 20 min) was infused 120 min after the PVN microinjection of saline or KA (2 nmol). Values are the mean \pm SEM. * $P < 0.05$ vs Vehicle; † $P < 0.05$ vs Saline. $n = 6$ per group.

Discussion

The kidney is critical in the sympathetic activation in hypertension and chronic kidney diseases [10–15]. Numerous studies have focused on renal sympathetic activity and its underlying mechanism, but the role of renal afferent activity in sympathetic activation is obscure or controversial. In the present study, we established a method to induce an ERR. Chemical stimulation of renal afferents induces the ERR, which leads to an increase in sympathetic activity, blood pressure, and HR. The PVN is an important component of the central neurocircuitry of the ERR.

In a preliminary study, we found that the responses to renal infusion of capsaicin were much more stable than that to a single renal injection of capsaicin, so we used infusion for 20 min to induce the ERR. Activation of renal afferents with capsaicin increased sympathetic activity, blood pressure and HR. That the ERR might involve the activation of renal chemoreceptors was supported by the findings that the infusion of bradykinin, adenosine, or Ang II induced ERR effects similar to capsaicin. Substance P immunoreactivity has been reported in the interlobar branches of the renal artery, the walls of the renal pelvis, and the proximal ureter, which are involved in chemoreceptor function [17]. That the ERR induced by capsaicin at the cortico-medullary border was greater than that in cortex or medulla may be related to the arcuate arteries or interlobar branches

of the renal artery containing chemoreceptors near the cortico-medullary border.

Renal infusion of capsaicin increased the ipsilateral renal afferent activity and the capsaicin-induced ERR was not affected by ipsilateral perirenal lipectomy, but was completely abolished by ipsilateral renal denervation. These results indicate that the renal afferent nerves are responsible for the effects of capsaicin in the kidney, and this is supported by the fact that the afferent nerves from the kidney enter the spinal cord through the T6-L2 dorsal root ganglia, and terminate in ipsilateral laminae I–III [39].

Neuroanatomical evidence has shown that renal afferent activity is closely connected with various sites in the brain associated with sympathetic outflow and cardiovascular regulation, including the nucleus of the solitary tract, rostral ventrolateral medulla, PVN, subfornical organ, and preoptic area [10]. The PVN is important in the control of cardiovascular activity and sympathetic outflow *via* its descending projections to the rostral ventrolateral medulla and intermediolateral column of spinal cord [40–43]. Stimulation of the renal afferent nerve altered the activity of 197 neurons in 407 neurons in the PVN, most of which were excited, but 8% were suppressed [44]. We found that renal infusion of capsaicin increased c-Fos expression in the bilateral PVN. Lesioning of bilateral PVN with KA abolished the effects of capsaicin in the kidney. These findings indicate that the PVN is important in the ERR pathway. It has been reported that afferent activity from

one kidney can modulate contralateral efferent renal nerve activity to regulate diuresis and natriuresis to balance overall renal function between the two kidneys [10, 45]. In this study, we found that renal infusion of capsaicin increased c-Fos expression in both the parvocellular and magnocellular parts of the PVN. The latter may be related to its reflex effects in regulating sodium balance.

Sympathetic overactivity contributes greatly to the development and progress of chronic heart failure, hypertension, and chronic kidney disease [16]. Increased renal input may play critical roles in the excessive sympathetic activity in these diseases. Numerous studies have shown that catheter-based radiofrequency renal denervation, which abolishes both afferent and efferent renal activity, has been used as an interventional therapy for chronic heart failure, chronic kidney disease, and hypertension [16, 21, 22]. Selective renal afferent and efferent denervation may be new therapeutic approaches in the treatment of hypertension.

In summary, chemical stimulation of the kidney causes the ERR, which results in increased sympathetic outflow, blood pressure, and HR. The PVN is critical in the central neurocircuitry of the ERR.

Acknowledgements This work was supported by the National Natural Science Foundation of China (31871148, 91639105, 31571167, and 31571168).

Conflict of interest The authors declare no competing financial interests.

References

- Grassi G, Ram VS. Evidence for a critical role of the sympathetic nervous system in hypertension. *J Am Soc Hypertens* 2016, 10: 457–466.
- Mrowka R. Arterial hypertension. *Acta Physiol (Oxf)* 2017, 219: 697–699.
- Zhang DY, Anderson AS. The sympathetic nervous system and heart failure. *Cardiol Clin* 2014, 32: 33–45, vii.
- Floras JS. Sympathetic nervous system activation in human heart failure: clinical implications of an updated model. *J Am Coll Cardiol* 2009, 54: 375–385.
- Kaur J, Young BE, Fadel PJ. Sympathetic overactivity in chronic kidney disease: consequences and mechanisms. *Int J Mol Sci* 2017, 18: E1682.
- Park J. Cardiovascular risk in chronic kidney disease: role of the sympathetic nervous system. *Cardiol Res Pract* 2012, 2012: 319432.
- Grassi G, Mark A, Esler M. The sympathetic nervous system alterations in human hypertension. *Circ Res* 2015, 116: 976–990.
- Esler M. Sympathetic nervous system moves toward center stage in cardiovascular medicine: from Thomas Willis to resistant hypertension. *Hypertension* 2014, 63: e25–e32.
- Seravalle G, Mancina G, Grassi G. Role of the sympathetic nervous system in hypertension and hypertension-related cardiovascular disease. *High Blood Press Cardiovasc Prev* 2014, 21: 89–105.
- Kopp UC. Role of renal sensory nerves in physiological and pathophysiological conditions. *Am J Physiol Regul Integr Comp Physiol* 2015, 308: R79–R95.
- Esler M, Guo L. The future of renal denervation. *Auton Neurosci* 2017, 204: 131–138.
- Iliescu R, Lohmeier TE, Tudorancea I, Laffin L, Bakris GL. Renal denervation for the treatment of resistant hypertension: review and clinical perspective. *Am J Physiol Renal Physiol* 2015, 309: F583–F594.
- Rettig R, Folberth C, Stauss H, Kopf D, Waldherr R, Unger T. Role of the kidney in primary hypertension: a renal transplantation study in rats. *Am J Physiol* 1990, 258: F606–F611.
- Rettig R, Stauss H, Folberth C, Ganten D, Waldherr B, Unger T. Hypertension transmitted by kidneys from stroke-prone spontaneously hypertensive rats. *Am J Physiol* 1989, 257: F197–F203.
- Bie P, Evans RG. Normotension, hypertension and body fluid regulation: brain and kidney. *Acta Physiol (Oxf)* 2017, 219: 288–304.
- Frame AA, Carmichael CY, Wainford RD. Renal afferents. *Curr Hypertens Rep* 2016, 18: 69.
- Zheng H, Patel KP. Integration of renal sensory afferents at the level of the paraventricular nucleus dictating sympathetic outflow. *Auton Neurosci* 2017, 204: 57–64.
- Johns EJ, Kopp UC, DiBona GF. Neural control of renal function. *Compr Physiol* 2011, 1: 731–767.
- Kalaitzidis RG, Karasavvidou D, Siamopoulos KC. Renal sympathetic denervation and renal physiology. *Curr Clin Pharmacol* 2013, 8: 189–196.
- Abdulla MH, Johns EJ. The innervation of the kidney in renal injury and inflammation: a cause and consequence of deranged cardiovascular control. *Acta Physiol (Oxf)* 2017, 220: 404–416.
- Veelken R, Schmieder RE. Renal denervation—implications for chronic kidney disease. *Nat Rev Nephrol* 2014, 10: 305–313.
- Carlstrom M. Therapeutic value of renal denervation in cardiovascular disease? *Acta Physiol (Oxf)* 2017, 220: 11–13.
- Zhang LL, Ding L, Zhang F, Gao R, Chen Q, Li YH, *et al.* Salusin-beta in rostral ventrolateral medulla increases sympathetic outflow and blood pressure via superoxide anions in hypertensive rats. *J Hypertens* 2014, 32: 1059–1067.
- Han Y, Shi Z, Zhang F, Yu Y, Zhong MK, Gao XY, *et al.* Reactive oxygen species in the paraventricular nucleus mediate the cardiac sympathetic afferent reflex in chronic heart failure rats. *Eur J Heart Fail* 2007, 9: 967–973.
- Chen AD, Zhang SJ, Yuan N, Xu Y, De W, Gao XY, *et al.* AT₁ receptors in paraventricular nucleus contribute to sympathetic activation and enhanced cardiac sympathetic afferent reflex in renovascular hypertensive rats. *Exp Physiol* 2011, 96: 94–103.
- Geng KW, He T, Wang RR, Li CL, Luo WJ, Wu FF, *et al.* Ethanol increases mechanical pain sensitivity in rats via activation of GABAA receptors in medial prefrontal cortex. *Neurosci Bull* 2016, 32: 433–444.
- Schreihöfer AM, Sved AF. Use of sinoaortic denervation to study the role of baroreceptors in cardiovascular regulation. *Am J Physiol* 1994, 266: R1705–R1710.
- Li C, Yan Y, Cheng J, Xiao G, Gu J, Zhang L, *et al.* Toll-like receptor 4 deficiency causes reduced exploratory behavior in mice under approach-avoidance conflict. *Neurosci Bull* 2016, 32: 127–136.
- He F, Ai H, Wang M, Wang X, Geng X. Altered neuronal activity in the central nucleus of the amygdala induced by restraint water-immersion stress in rats. *Neurosci Bull* 2018, 34: 1067–1076.
- Shi Z, Chen WW, Xiong XQ, Han Y, Zhou YB, Zhang F, *et al.* Sympathetic activation by chemical stimulation of white adipose tissues in rats. *J Appl Physiol* 2012, 112: 1008–1014.

31. Xiong XQ, Chen WW, Zhu GQ. Adipose afferent reflex: sympathetic activation and obesity hypertension. *Acta Physiol (Oxf)* 2014, 210: 468–478.
32. Xiong XQ, Chen WW, Han Y, Zhou YB, Zhang F, Gao XY, *et al.* Enhanced adipose afferent reflex contributes to sympathetic activation in diet-induced obesity hypertension. *Hypertension* 2012, 60: 1280–1286.
33. Pingle SC, Matta JA, Ahern GP. Capsaicin receptor: TRPV1 a promiscuous TRP channel. *Handb Exp Pharmacol* 2007, 179: 155–171.
34. Nakagawa H, Hiura A. Capsaicin, transient receptor potential (TRP) protein subfamilies and the particular relationship between capsaicin receptors and small primary sensory neurons. *Anat Sci Int* 2006, 81: 135–155.
35. Holzer P. Capsaicin: cellular targets, mechanisms of action, and selectivity for thin sensory neurons. *Pharmacol Rev* 1991, 43: 143–201.
36. Zhong MK, Duan YC, Chen AD, Xu B, Gao XY, De W, *et al.* Paraventricular nucleus is involved in the central pathway of cardiac sympathetic afferent reflex in rats. *Exp Physiol* 2008, 93: 746–753.
37. Li Z, You Z, Li M, Pang L, Cheng J, Wang L. Protective effect of resveratrol on the brain in a rat model of epilepsy. *Neurosci Bull* 2017, 33: 273–280.
38. Metzner W, Juranek J. A method to biotinylate and histochemically visualize ibotenic acid for pharmacological inactivation studies. *J Neurosci Methods* 1997, 76: 143–150.
39. Ciriello J, Calaresu FR. Central projections of afferent renal fibers in the rat: an anterograde transport study of horseradish peroxidase. *J Auton Nerv Syst* 1983, 8: 273–285.
40. Badoer E. The role of the hypothalamic PVN in the regulation of renal sympathetic nerve activity and blood flow during hyperthermia and in heart failure. *Am J Physiol Renal Physiol* 2010, 298: F839–F846.
41. Sun J, Ren XS, Kang Y, Dai HB, Ding L, Tong N, *et al.* Intermedin in paraventricular nucleus attenuates sympathoexcitation and decreases TLR4-mediated sympathetic activation via adrenomedullin receptors in rats with obesity-related hypertension. *Neurosci Bull* 2019, 35: 34–46.
42. Yu XJ, Miao YW, Li HB, Su Q, Liu KL, Fu LY, *et al.* Blockade of endogenous angiotensin-(1-7) in hypothalamic paraventricular nucleus attenuates high salt-induced sympathoexcitation and hypertension. *Neurosci Bull* 2019, 35: 47–56.
43. Zhou JJ, Ma HJ, Shao JY, Pan HL, Li DP. Impaired hypothalamic regulation of sympathetic outflow in primary hypertension. *Neurosci Bull* 2019, 35: 124–132.
44. Calaresu FR, Ciriello J. Renal afferent nerves affect discharge rate of medullary and hypothalamic single units in the cat. *J Auton Nerv Syst* 1981, 3: 311–320.
45. Kopp UC, Grisk O, Cicha MZ, Smith LA, Steinbach A, Schluter T, *et al.* Dietary sodium modulates the interaction between efferent renal sympathetic nerve activity and afferent renal nerve activity: role of endothelin. *Am J Physiol Regul Integr Comp Physiol* 2009, 297: R337–R351.



Ketamine Alleviates Fear Generalization Through GluN2B-BDNF Signaling in Mice

Muhammad Asim^{1,2} · Bo Hao^{1,2} · Yu-Han Yang^{1,2} · Bu-Fang Fan^{1,2} ·
Li Xue^{1,2,3} · Yan-Wei Shi^{1,2,3} · Xiao-Guang Wang^{1,2,3} · Hu Zhao^{1,2,3}

Received: 2 February 2019 / Accepted: 21 June 2019 / Published online: 23 August 2019
© Shanghai Institutes for Biological Sciences, CAS 2019

Abstract Fear memories are critical for survival. Nevertheless, over-generalization of these memories, depicted by a failure to distinguish threats from safe stimuli, is typical in stress-related disorders. Previous studies have supported a protective role of ketamine against stress-induced depressive behavior. However, the effect of ketamine on fear generalization remains unclear. In this study, we investigated the effects of ketamine on fear generalization in a fear-generalized mouse model. The mice were given a single sub-anesthetic dose of ketamine (30 mg/kg, i.p.) 1 h before, 1 week before, immediately after, or 22 h after fear conditioning. The behavioral measure of fear (indicated by freezing level) and synaptic protein expression in the basolateral amygdala (BLA) and inferior-limbic pre-frontal cortex (IL-PFC) of mice were examined. We found that only ketamine administered 22 h after fear conditioning significantly decreased the fear generalization, and the

effect was dose-dependent and lasted for at least 2 weeks. The fear-generalized mice showed a lower level of brain-derived neurotrophic factor (BDNF) and a higher level of GluN2B protein in the BLA and IL-PFC, and this was reversed by a single administration of ketamine. Moreover, the GluN2B antagonist ifenprodil decreased the fear generalization when infused into the IL-PFC, but had no effect when infused into the BLA. Infusion of ANA-12 (an antagonist of the BDNF receptor TrkB) into the BLA or IL-PFC blocked the effect of ketamine on fear generalization. These findings support the conclusion that a single dose of ketamine administered 22 h after fear conditioning alleviates the fear memory generalization in mice and the GluN2B-related BDNF signaling pathway plays an important role in the alleviation of fear generalization.

Keywords Ketamine · Fear generalization · Post-traumatic stress disorder · BDNF · GluN2B · GluN2A

Muhammad Asim and Bo Hao have contributed equally to this work.

Electronic supplementary material The online version of this article (<https://doi.org/10.1007/s12264-019-00422-4>) contains supplementary material, which is available to authorized users.

✉ Yan-Wei Shi
shiyaw@mail.sysu.edu.cn

✉ Xiao-Guang Wang
wxguang@mail.sysu.edu.cn

¹ Faculty of Forensic Medicine, Zhongshan School of Medicine, Sun Yat-sen University, Guangzhou, China

² Guangdong Province Translational Forensic Medicine Engineering Technology Research Center, Zhongshan School of Medicine, Sun Yat-sen University, Guangzhou, China

³ Guangdong Province Key Laboratory of Brain Function and Disease, Zhongshan School of Medicine, Sun Yat-sen University, Guangzhou, China

Introduction

Post-traumatic stress disorder (PTSD) is an excessive generalization of fear memory that is characterized not only by a strong response to a previously learned threatening cue but also a debilitating failure to suppress these responses even in the presence of cues that indicate safety [1, 2]. Epidemiological studies have estimated that the incidence of life-time PTSD is ~8% in the general population [3]. Current PTSD treatment includes pharmacotherapy, psychotherapy, or a combination of both. However, there is still a high proportion of PTSD patients without remission after multiple trials of both pharmacotherapy and psychotherapy [4–7].

Ketamine, a non-competitive N-methyl-D-aspartate receptor (NMDAR) antagonist, has rapid and sustained antidepressant effects both in humans and in a mouse model of depression [8–10]. Brachman *et al.* [11] showed that prophylactic ketamine attenuates stress-induced depressive behavior in three mouse models of stress. A previous study found that burned soldiers receiving perioperative ketamine have a lower prevalence of PTSD [12]. However, a follow-up study from the same research group did not support their initial findings [13]. Results from studies in animal models investigating the anxiety-related effect of ketamine are not always consistent, with reports of anxiolytic [14], anxiogenic [15], and null results [16], which raise new questions such as the heterogeneity and translatability of animal models, and how the dosage and timing of ketamine administration influence its affectivity for PTSD treatment.

Clinical studies have reported exaggerated amygdala and medial prefrontal responses in anxiety disorders [17, 18]. Previous studies found that fear generalization increases the overall activity of neurons in the lateral amygdala of mice [19]. Trace fear conditions increase the spiking of projection neurons in the inferior-limbic prefrontal cortex (IL-PFC) and basolateral amygdala (BLA) [20]. NMDARs are required for learning and memory and their subunits undergo dynamic modification following fear conditioning [21–24]. Inhibition of NMDARs prevents the loss of brain-derived neurotrophic factor (BDNF) function [25]. Importantly, BDNF modulates fear generalization in humans [26]. Recently, it was shown that ketamine regulates the expression of BDNF in the medial PFC of the single prolonged stress and electric foot shock (SPS&S) rat model [27]. Protein kinase M zeta (PKM ζ) and Ca²⁺/calmodulin-dependent protein kinase II- α (CAMKII- α) are pivotal in learning and memory [28, 29]. However, the roles of NMDAR/BDNF, PKM ζ , and CAMKII- α signaling in cued fear memory generalization remain unclear and the effects of ketamine on these molecules during fear generalization remain to be defined.

In the present study, we used a fear generalized mouse model to study the effects of ketamine on fear generalization and the molecular mechanisms underlying the effects.

Material and Methods

Animals

Male C57BL/6 mice weighing 20 g–25 g (6–8 weeks old) were maintained on a 14-h/10-h light/dark cycle with food and water available *ad libitum* at the Laboratory Animal Center of Sun Yat-sen University. All animal procedures

were approved by the Animal Care and Use Committee of Sun Yat-sen University.

Drugs

Ketamine (Gutian Pharma Co., Fujian, China, 30 mg/kg [30, 31]) was administered intraperitoneally, while ifenprodil (MedChemExpress, NJ, 2.0 μ g/ μ L [24]) and ANA-12 (Sigma Aldrich, St. Louis, MO, 1 μ g/ μ L [32]) were infused bilaterally into the BLA or IL-PFC.

Behavioral Protocol

The procedure was a modification of the rat model of fear generalization described previously [19]. All behavioral experiments were performed during the light phase (daytime). Fear conditioning and fear memory recall tests were conducted in different contexts in a sound isolation chamber (Coulbourn Instruments, MA). The freezing behavior of mice was recorded and quantified with a video camera attached to the roof of the sound isolation chamber. Infrared LED cues placed on the wall of the chamber coincided with sound stimuli to check the sound-evoked freezing behavior. The floor, walls, lighting conditions, and odor differed between the conditioning and testing (retrieval) contexts. Before starting experiments, all chambers were cleaned with 70% ethanol. On day 1, the mice were habituated to context A (12 inches wide \times 10 inches deep \times 12 inches high), receiving 5 presentations of two sounds (duration 10 s, composed of either 5 kHz clicks or a continuous sound at 1 kHz, with a 5-ms rise and fall time, and 70 \pm 5 dB sound pressure). Immediately after habituation, fear conditioning was applied, where one of the two sounds (conditioned stimulus, CS+) (10 presentations of each sound at an average interval of 70 s, with a range of 40 s–100 s) was paired with a 1-s foot-shock delivered through metal grids on the floor (weak shock group, 0.4 mA for 1 s; strong shock group, 1.2 mA for 1 s, co-terminated with the CS+). After 24 h (on day 2), the behavioral test was performed in context B with presentations of 5 trials of each CS– (clicks tone, which was not paired with electric shock during training) and CS+ (continuous tone, which was paired with electric shock during training) sounds (10 s duration, with an average inter-trial interval of 70 s, in a range of 40 s–100 s), and the freezing levels in response to the two sounds were measured by taking an average freezing level to all CS– tones, and an average freezing levels to all CS+ tones during behavioral test (Fig. 1A). The difference in freezing response to CS–/CS+ was evaluated as the index of behavioral generalization (IBG), which was defined as the ratio of average freezing response to CS– to the average freezing response to CS+ in the testing session.

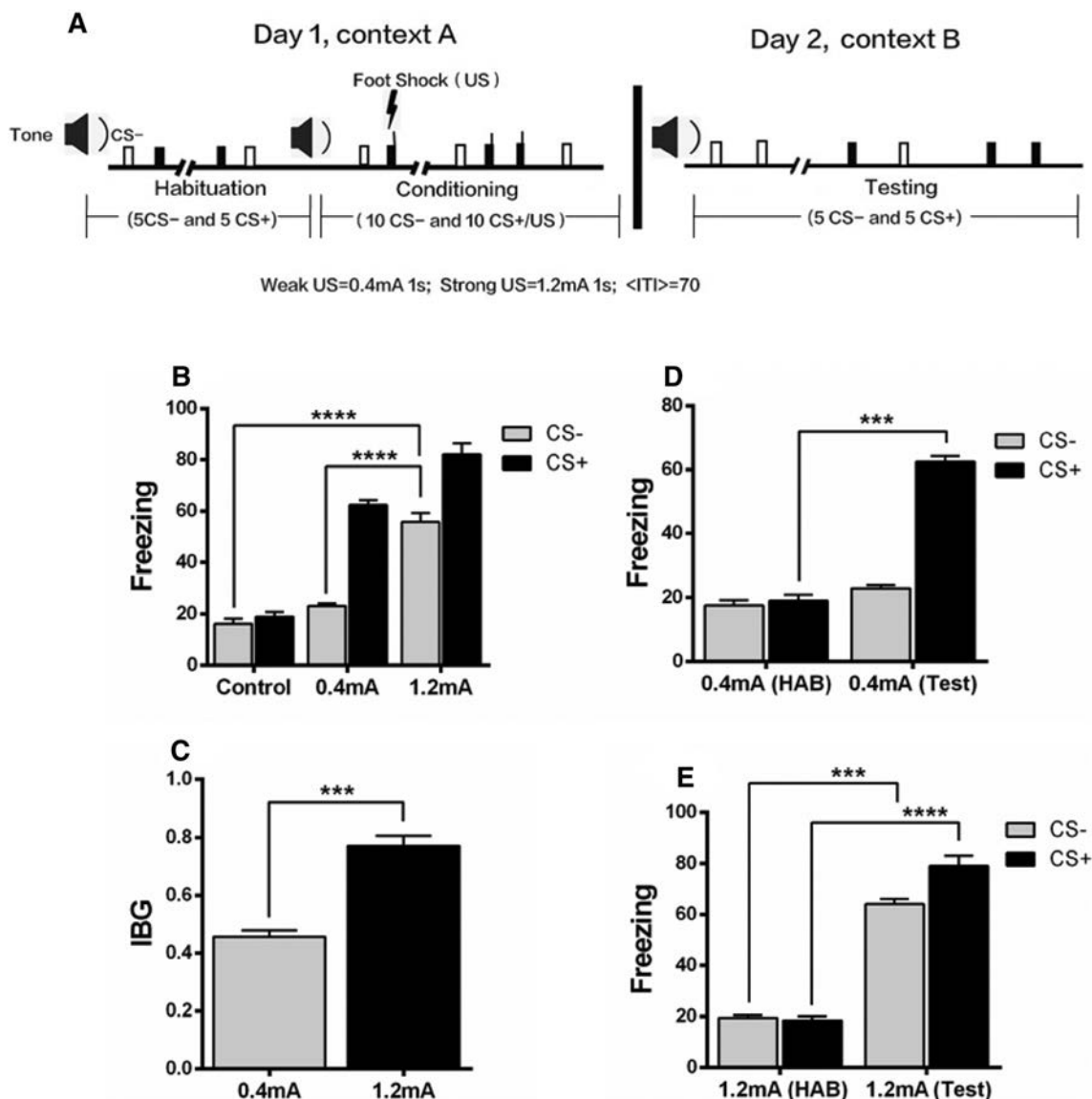


Fig. 1 A strong shock causes fear generalization. **A** Schematic of the behavioral protocol. **B** Mice with the strong shock (1.2 mA) showed a greater freezing level to the CS- (Clicks tone, which was not paired with shock during training) tone than those with the weak shock (0.4 mA) and controls (0 mA). **C** The index of behavioral generalization (IBG) was higher in the strong shock group than in the weak shock group. **D** In the weak shock group, the fear response to a CS+ (Continuous tone, which was paired with shock during training, but not

paired with shock during behavioral testing) tone during the behavioral test (Test) was significantly higher than that of the habituation session (HAB); while there was no significant difference in the fear response to the CS- tone between HAB and Test. **E** The strong shock group showed an increased freezing level in response to both the CS- and CS+ tones, indicating fear generalization. $n = 8$ –10 mice/group; mean \pm SEM; *** $P < 0.001$, **** $P < 0.0001$.

Immunoblotting

Mice were sacrificed immediately, 1 week, or 2 weeks following behavior test. The brain was removed, and IL-PFC and BLA tissues were collected. Samples were homogenized for 1 min in RIPA sample buffer containing a protease inhibitor mixture (1:100; Millipore, Bedford, MA) and 1 mmol/L PMSF. The homogenates were centrifuged at 12000 g for 20 min at 4 °C. Supernatant liquids were assessed for protein concentration using a

BCA assay (Pierce, Waltham, MA, Catalog# 23225). Proteins were resolved by SDS-PAGE and transferred to a PVDF membrane (Immobilon-P, Millipore). Blots were incubated overnight at 4 °C with rabbit polyclonal anti-PKC ζ (1:500, Catalog# ab59364, Abcam, Cambridge, UK), anti-phospho PKC ζ (T560) (1:500, Catalog# ab59412, Abcam), anti-GluN2A (1:1000, Catalog# 07-632, Millipore), anti-GluN2B (1:1000, Catalog# 14544, Cell Signaling Technology, MA), anti-BDNF (1:500, Catalog# 3160-1, Epitomics, CA), or anti-CaMKII- α (1:1000,

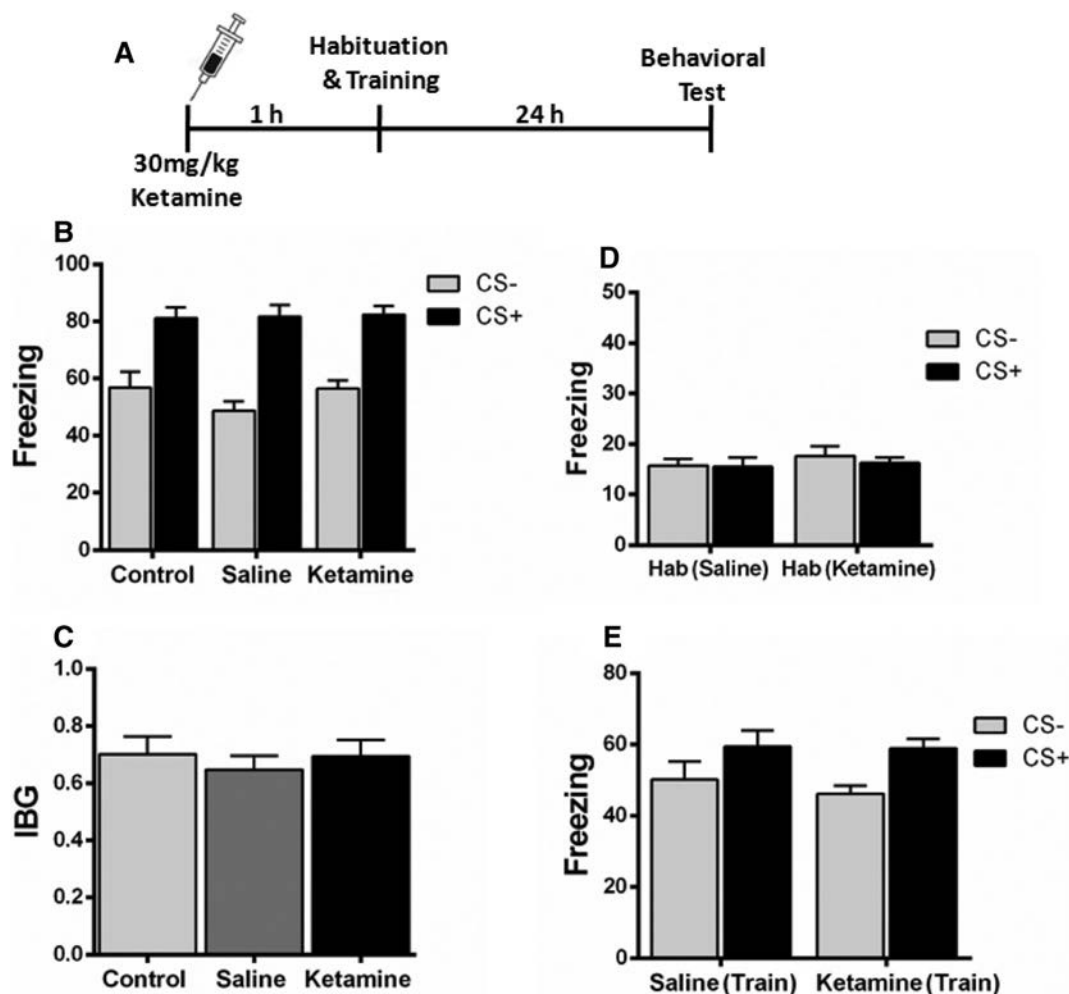


Fig. 2 Effect of ketamine on fear generalization when administered 1 h before fear conditioning. **A** Experimental design. **B** Mice injected with saline or ketamine 1 h before fear conditioning expressed comparable levels of freezing behavior. **C** No significant difference

was found in the index of behavioral generalization (IBG) between the saline and ketamine groups. **D**, **E** Mice injected with saline or ketamine expressed comparable levels of freezing during habituation (**D**) and training (**E**). $n = 8$ mice/group; mean \pm SEM.

Catalog# 50049, Cell Signaling Technology), and bands were amplified with HRP-conjugated secondary antibody (1:1000, Catalog# HAF008, R&D, MN). Protein signals were developed using Immobilon Western Chemiluminescent HRP Substrate (Millipore). The target protein immunoreactivity was normalized to GAPDH (1:1000, Catalog# 2118, Cell Signaling Technology) and quantified by densitometry using ImageJ (NIH, MD).

Cannula Infusion Experiment

Mice were anesthetized with sodium pentobarbital, and then positioned into a stereotaxic instrument (RWD Life Science, Shenzhen, China). They were placed on a heating pad, and the temperature was continuously monitored with a rectal thermometer. The body temperature was maintained at 37.5 °C–38.5 °C. Eye cream was applied to both corneas to prevent dehydration. Guide cannulas were

implanted bilaterally in the BLA (−1.6 mm posterior, \pm 3.35 mm lateral, and −4.8 mm dorsal to bregma) or the IL-PFC (+1.78 mm posterior, \pm 0.4 mm lateral, and −2.5 mm dorsal to bregma), and fixed to the skull with dental cement. The coordinates were based on a mouse brain atlas [33]. Stainless-steel obturators were placed into the guide cannulas, and were changed every day to ensure patency until infusions were completed. Mice were kept in home cages to recover for at least 1 week after surgery.

After recovery, the mice were trained in the fear conditioning protocol, and 22 h later they received bilateral infusions of 0.5 μ L ANA-12 (1 μ g/ μ L) or saline into the BLA or IL-PFC through the cannulas, and intraperitoneal injection of 30 mg/kg ketamine or saline, while another group of mice only received 0.5 μ L ifenprodil (Ifen, 2.0 μ g/ μ L) or saline in the BLA or IL-PFC bilaterally. Drugs were infused (0.1 μ L/min) through tip-sharpened 33-gauge double injector cannulas, which were attached to a

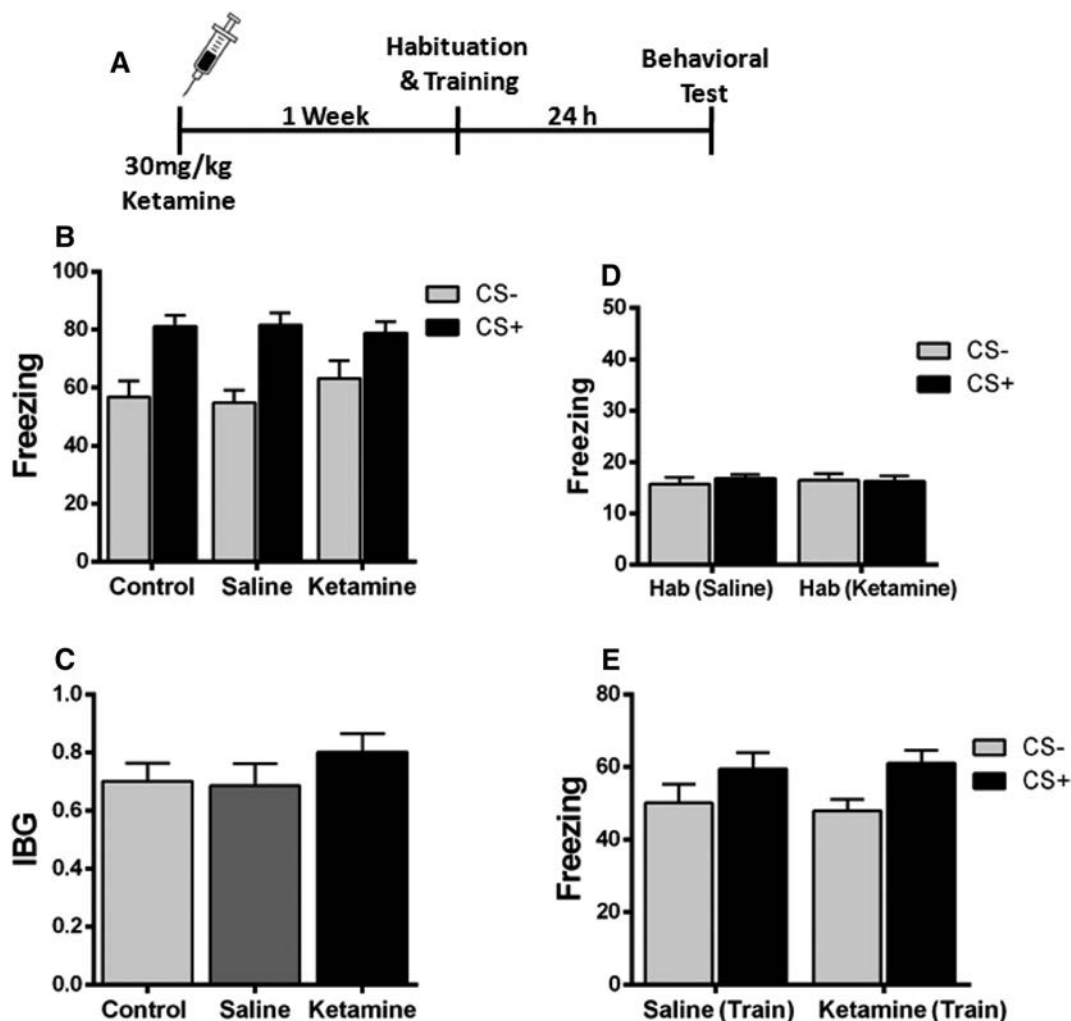


Fig. 3 Prophylactic effect of ketamine on fear generalization when injected 1 week before fear conditioning. **A** Experimental design. **B** Mice injected with saline or ketamine 1 week before fear conditioning showed comparable levels of freezing during behavioral

tests. **C** The two groups of mice showed comparable values of the index of behavioral generalization (IBG). **D, E** Mice in both groups showed comparable freezing levels during habituation and training. $n = 8$ mice/group; mean \pm SEM.

micro-syringe. The injector cannulas were kept in place for another 2 min to decrease the spread of the drug. The behavioral tests were performed 2 h after the bilateral infusions.

Statistical Significance

All data are presented as the mean \pm SEM. $P < 0.05$ was considered statistically significant. Data were analyzed with the unpaired *t*-test or one-way ANOVA, using repeated measures where appropriate. Significant ANOVAs were followed by a *post-hoc* Turkey's test where appropriate.

Results

Strong Shock Causes Generalization of Conditioned Fear

To determine the effects of weak and strong shocks on fear generalization, mice were divided into control, weak shock (0.4 mA), and strong shock (1.2 mA) groups. The mice with strong shock showed a significantly increased freezing level in response to the CS- tone as compared with the control and weak shock groups (Fig. 1B). The IBG was also higher in the strong shock group than in the weak shock group (Fig. 1C). Furthermore, the mice discriminated between the CS+ and CS- 24 h after weak shock fear conditioning, as evidenced by selectively higher freezing level in response to the CS+ than the CS- (Fig. 1D). However, the mice with strong shock expressed

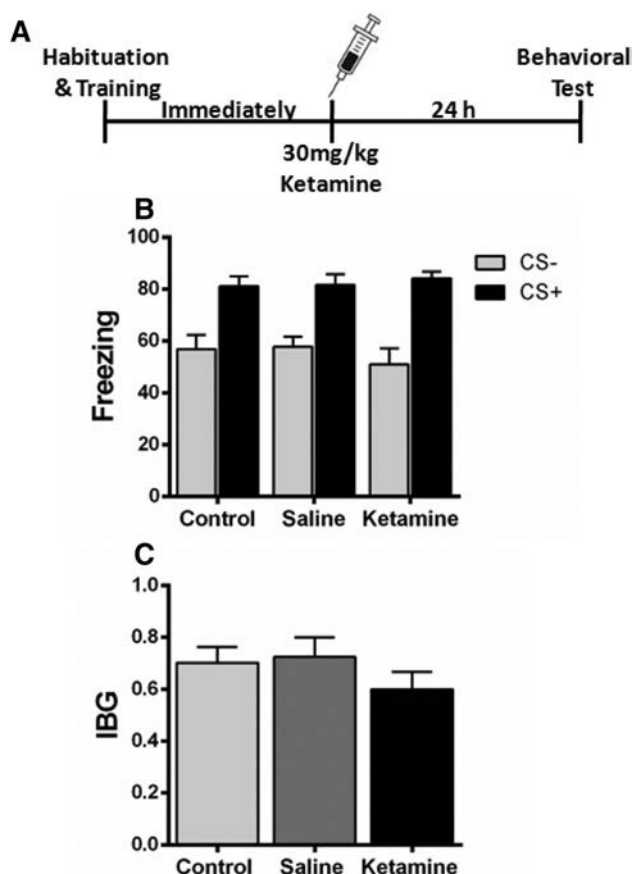


Fig. 4 Effect of ketamine when administered immediately after fear conditioning. **A** Experimental design. **B, C** Ketamine when administered immediately after fear conditioning did not alter the fear generalization (**B**) or the index of behavioral generalization (IBG) (**C**) compared with the saline group. $n = 8$ mice/group; mean \pm SEM.

significantly increased freezing behavior in response to both the CS- and CS+ tones during behavioral tests compared to the habituation (Fig. 1E). These results suggest that a strong shock causes generalization of conditioned fear.

Ketamine Injection 1 h Before Fear Conditioning Does Not Alleviate Fear Generalization

A recent study found that in contextual fear-conditioned mice, a single dose of ketamine (30 mg/kg) attenuates the contextual fear memory only when given a week before as a prophylactic, but had no effect when given immediately before or after a stress-inducing episode [34]. To determine the prophylactic effect of ketamine on fear generalization, we administered a single dose of ketamine (30 mg/kg) or saline intraperitoneally 1 h before fear conditioning (Fig. 2A). These mice expressed comparable freezing levels when tested 24 h after conditioning (Fig. 2B). Also, no significant difference was found in the IBG level

(Fig. 2C). Furthermore, the freezing level during habituation and training was similar in the saline and ketamine groups (Fig. 2D, E). These results suggest that ketamine administered 1 h prior to fear conditioning does not alter fear generalization.

Ketamine Injection 1 Week Before Fear Conditioning Does Not Inhibit Fear Generalization

To further determine the prophylactic effect of ketamine on fear generalization, ketamine (30 mg/kg) was administered intraperitoneally 1 week prior to fear conditioning (Fig. 3A). The results showed that ketamine did not alter the fear response when compared to the saline-injected mice (Fig. 3B). Moreover, the IBG level was similar in ketamine- and saline-injected mice (Fig. 3C). The freezing levels during habituation and training were comparable between the two groups (Fig. 3D, E). These data showed that ketamine injection 1 week before fear conditioning does not change fear generalization in mice.

Ketamine Injection Immediately After Fear Conditioning Does Not Alleviate Fear Generalization

A single dose of ketamine (30 mg/kg) immediately after fear conditioning did not affect the freezing and IBG levels of mice when compared to the control and saline groups (Fig. 4). These results indicate that ketamine does not affect fear generalization when injected immediately after fear conditioning.

Ketamine Administration 22 h Following Fear Conditioning Alleviates Fear Generalization

Ketamine when administered 22 h after fear conditioning significantly reduced the fear response to the CS- tone (Fig. 5B). There was a significant difference in the IBG between the control, saline, and ketamine groups (Fig. 5C). It has been reported that the antidepressant effect of ketamine remains significant for 1 week [35], so we tested its effects on fear generalization at 2 h (test 1), 1 week (test 2), and 2 weeks (test 3) after ketamine administration. The results showed that the ketamine-induced alleviation of fear generalization remained significant for at least 2 weeks (Fig. 5D, E). In addition, to investigate whether the effect of ketamine was dose-dependent, 7.5 mg/kg, 15 mg/kg, and 30 mg/kg ketamine was applied 22 h after fear conditioning (Fig. S1). Ketamine at 15 mg/kg and 30 mg/kg significantly decreased the fear generalization when compared with the control group, while 7.5 mg/kg did not (Fig. S1).

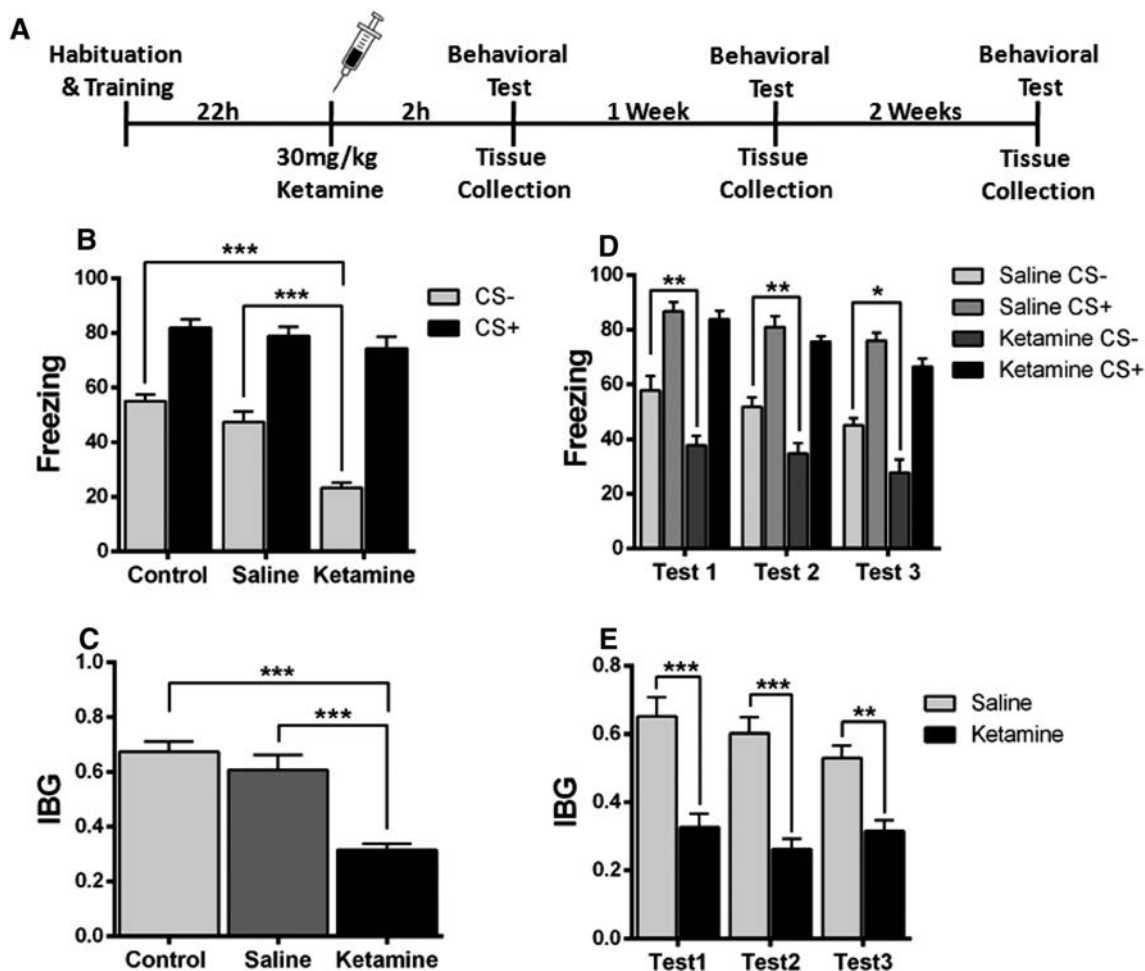


Fig. 5 Ketamine administered 22 h after fear conditioning decreases fear generalization. **A** Experimental design. **B** Injection of ketamine 22 h after fear conditioning showed a significantly lower fear response to the CS- tone than the saline group. **C** Ketamine-injected mice expressed lower levels of the index of behavioral generalization

(IBG) than the saline group. **D, E** The effect of ketamine remained significant for at least 2 weeks. $n = 8$ mice/group; mean \pm SEM; $*P < 0.05$, $**P < 0.01$, $***P < 0.001$. Test 1, 2 h after ketamine injection; Test 2, 1 week after ketamine injection; Test 3, 2 weeks after ketamine injection.

Ketamine Alters the Expression of GluN2B and BDNF in the BLA and IL-PFC

NMDAR subunits undergo modification following training [21–24]. Ketamine is an antagonist of NMDARs, which is critical in learning and memory [36]. We first used Western blot to examine the expression of GluN2A and GluN2B in the BLA and IL-PFC 24 h after fear conditioning, and found that GluN2B was significantly increased after fear memory generalization; this was reversed by a single dose of ketamine (Figs. 6C, 7C). Interestingly, GluN2A was also increased, but the increment was not reversed by ketamine (Figs. 6D, 7D). A previous study reported that inhibition of NMDARs prevented the loss of BDNF function [25]. Therefore, we investigated the expression of BDNF in the BLA and IL-PFC and found that the BDNF level was decreased after formation of generalized fear memory; this was reversed by ketamine (Figs. 6B, 7B).

These results highlight an important role of GluN2B-related BDNF signaling in the expression of generalized fear. Previous studies have reported that PKM ζ and CAMKII- α are involved in long-term memory formation [28, 29]. To investigate the role of these proteins in fear generalization, the expression of PKM ζ , P-PKM ζ , and CAMKII- α in the BLA and IL-PFC was examined. We did not find any significant difference in their expression in either region after the formation of generalization of conditioned fear. Moreover, ketamine administration did not affect their expression in these regions of mice exposed to the fear conditioning protocol (Figs. 6, 7E, F, G). These results indicate that PKM ζ and CAMKII- α in the BLA and IL-PFC are not necessary for the generalization of conditioned fear.

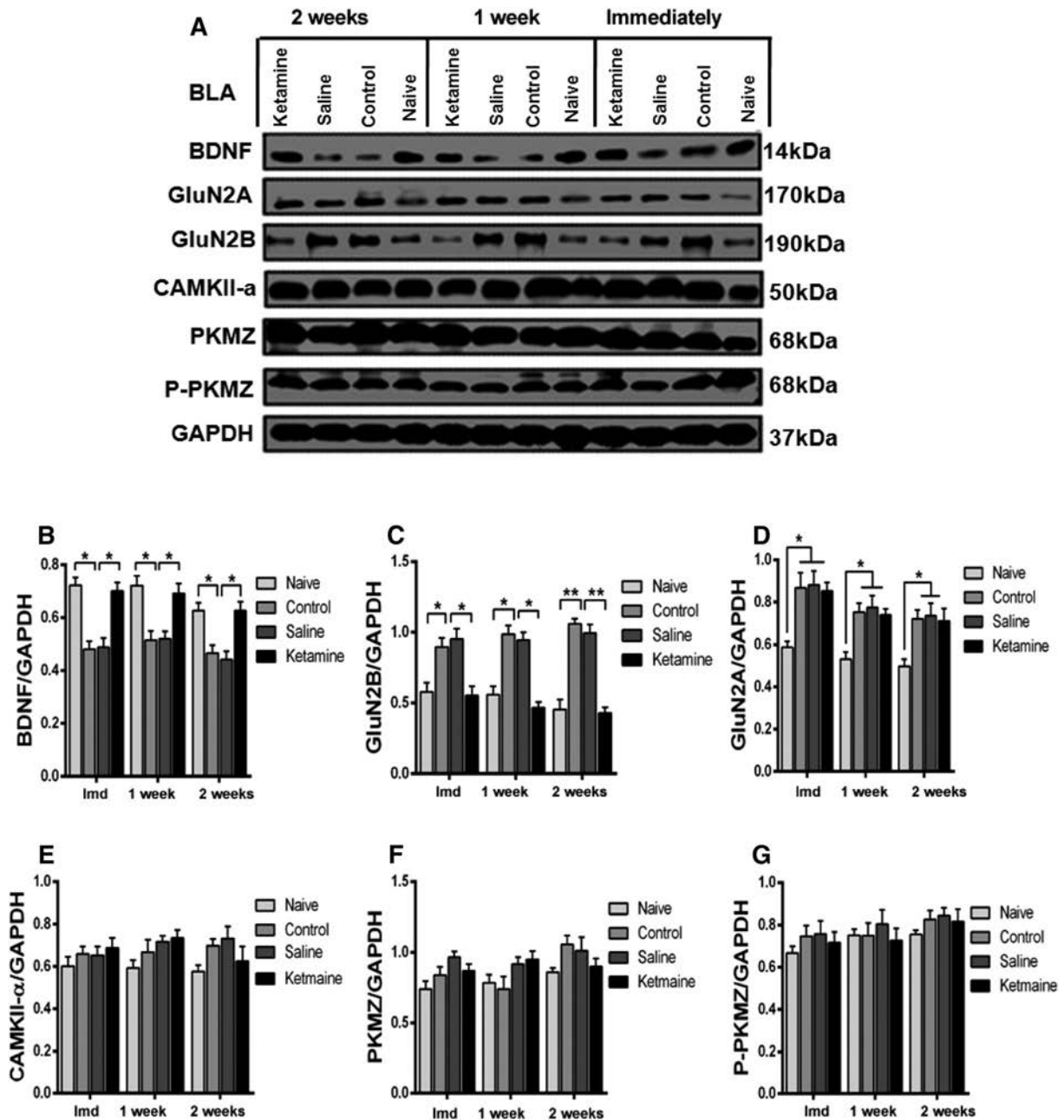


Fig. 6 Effects of ketamine on the expression of postsynaptic proteins in the BLA. **A** Western blots of synaptic protein levels in the BLA. **B**, **C** Fear generalization decreased the expression of BDNF and increased the expression of GluN2B, which were reversed by ketamine. **D** GluN2A was significantly increased in fear-generalized

mice but this increase was not reversed by ketamine. **E–G** The expression of PKM ζ , P-PKM ζ , and CAMKII- α did not differ among the naïve, control, saline, and ketamine groups. $n = 5$ mice/group; mean \pm SEM. * $P < 0.05$, ** $P < 0.001$; lmd, immediately; BLA, basolateral amygdala; IL-PFC, inferior-limbic prefrontal cortex.

Effect of GluN2B and BDNF Receptor Antagonists on Fear Generalization

To investigate whether ketamine alleviates fear generalization by regulating GluN2B-related BDNF signaling in the BLA and IL-PFC, mice were either injected with a GluN2B antagonist, or the BDNF receptor TrkB antagonist ANA-12, bilaterally into the BLA or IL-PFC. The GluN2B

antagonist ifenprodil did not decrease the fear generalization when infused bilaterally into the BLA (Fig. 8B, C). However, bilateral infusion of ifenprodil into the IL-PFC significantly decreased the fear generalization as compared with the saline group (Fig. 8D, E). Moreover, ANA-12 infused either into the BLA or IL-PFC blocked the effect of ketamine on fear generalization (Fig. 8F–I). These results support an important role of GluN2B-related BDNF

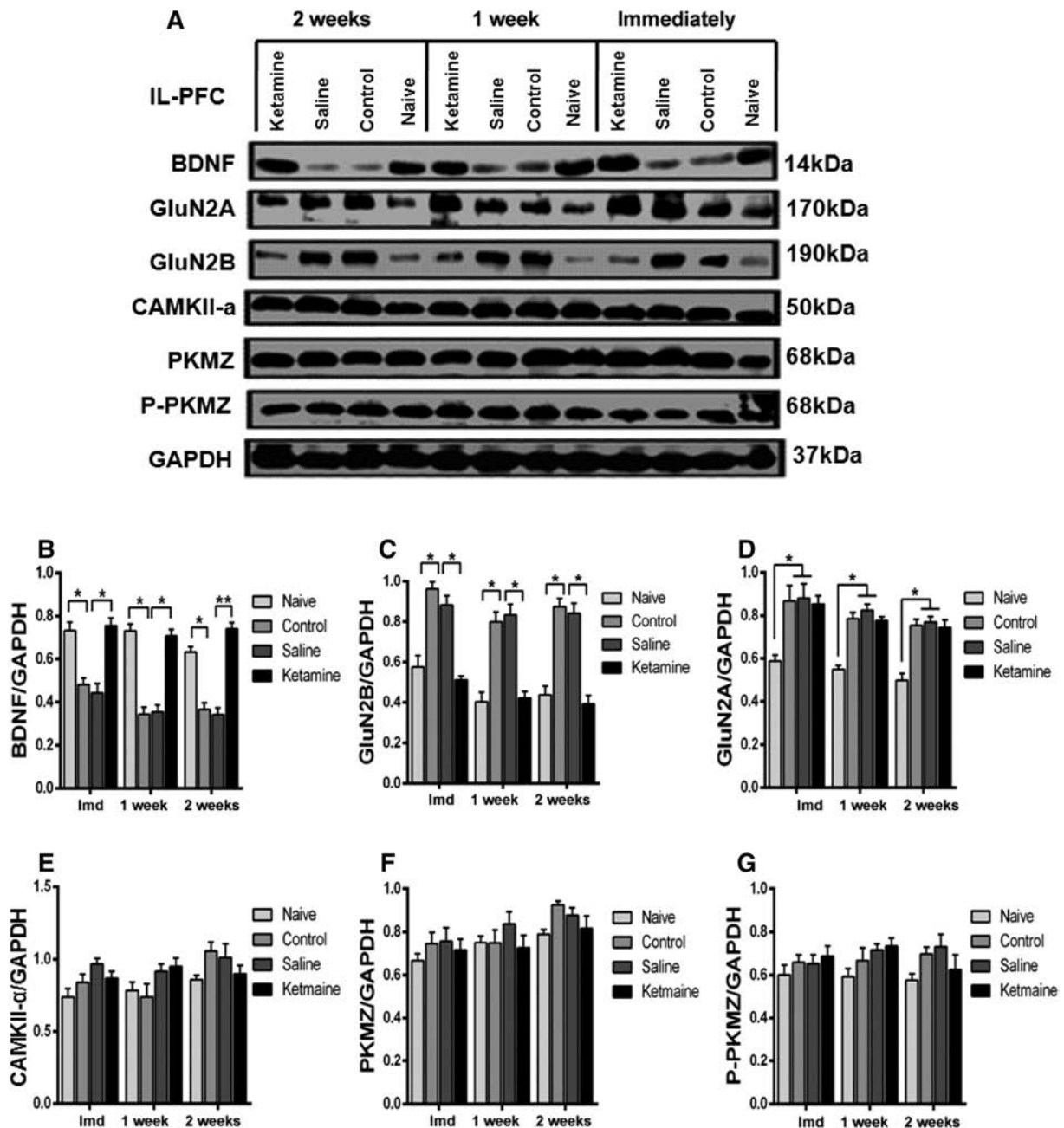


Fig. 7 Effect of ketamine on the expression of postsynaptic proteins in the IL-PFC. **A** Western blots of synaptic protein levels in the IL-PFC. **B, C** Fear generalization decreased the expression of BDNF and increased the expression of GluN2B, which were reversed by ketamine. **D** GluN2A was significantly higher in fear-generalized

mice but this increase was not reversed by ketamine. **E–G** The expression of PKM ζ , P-PKM ζ , and CAMKII- α did not differ among the naïve, control, saline, and ketamine groups. $n = 5$ mice/group; mean \pm SEM; * $P < 0.05$; Imd, immediately; BLA, basolateral amygdala; IL-PFC, inferior-limbic prefrontal cortex.

signaling in fear generalization and modulation of the GluN2B/BDNF signaling pathway is involved at least in part in the alleviation of fear generalization by ketamine.

Discussion

We investigated the role of ketamine in fear generalization. A strong stress induced the enduring generalization of conditioned fear. The fear-generalized mice developed PTSD-like behaviors, unable to discriminate dangerous from safe stimuli. A single sub-anesthetic dose of ketamine intraperitoneally administered 22 h after fear conditioning

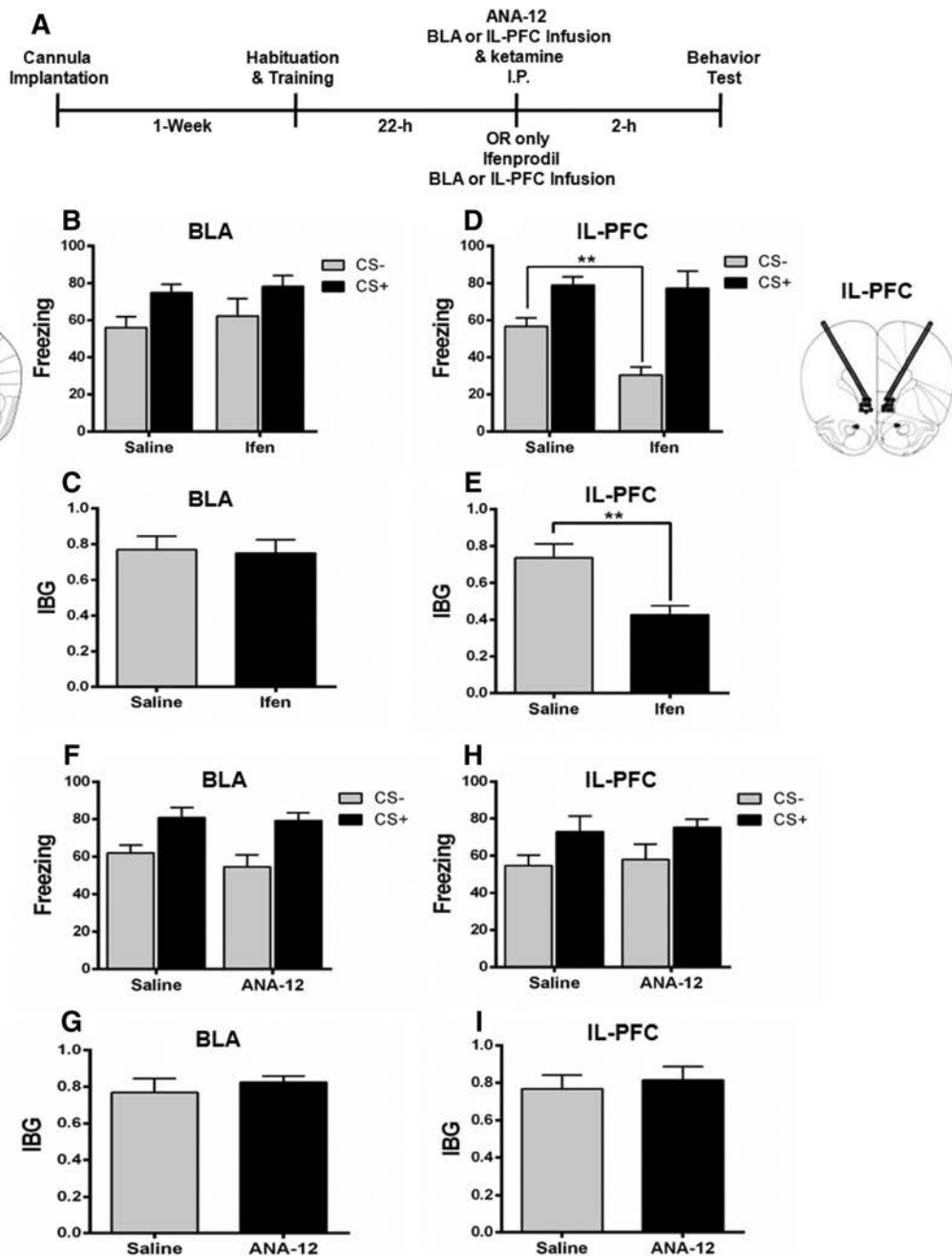


Fig. 8 Effects of GluN2B and BDNF antagonists on fear generalization. **A** Schematic of the experimental procedure. **B, C** Infusion of the GluN2B-selective antagonist ifenprodil into the BLA did not decrease the fear generalization as shown by similar freezing levels (**B**) and IBG (**C**) in the ifenprodil (Ifen) and saline groups. **D, E** Ifenprodil infusion into the IL-PFC decreased the fear generalization, as shown by a significantly lower response to the CS- in terms of

freezing level (**D**) and IBG (**E**) in the Ifen group than in the saline group. **F–I** The BDNF receptor TrkB antagonist ANA-12 infused either into the BLA (**F, G**) or the IL-PFC (**H, I**) blocked the effect of ketamine on fear generalization as shown by comparable freezing levels and IBG in the ANA-12 and saline groups. $n=6$ mice per group; mean \pm SEM; ** $P < 0.001$; BLA, basolateral amygdala; IL-PFC, inferior-limbic prefrontal cortex.

led to significant inhibition of fear generalization and the effect lasted at least 2 weeks. Fear-generalized mice had a lower level of BDNF and a higher level of GluN2B protein in the BLA and IL-PFC, which were reversed by a single administration of ketamine. Moreover, the GluN2B antagonist ifenprodil decreased the fear generalization when

infused into the IL-PFC, but had no effect when infused into the BLA. The BDNF receptor TrkB antagonist ANA-12 blocked the effect of ketamine on fear generalization when infused into either the BLA or the IL-PFC. The results support the conclusion that ketamine suppresses fear generalization by modulating GluN2B/BDNF signaling.

According to theoretical models of Pavlovian conditioning, fear learning can also be modulated by changing the unconditioned stimulus itself [37, 38]. A recent study showed that increasing the intensity of electrical shocks strengthens the fear generalization response, which was presented as a novel PTSD model [19]. Fear generalization produces more robust symptoms, including increased freezing in response to a safe cue and impaired safety signal learning, which has been proposed as a biomarker for PTSD patients [1]. Interestingly, clinical studies have reported exaggerated amygdala and medial PFC responses in anxiety disorders [17, 18]. In fear-generalized rats, the overall activity of neurons in the lateral amygdala is significantly enhanced [19], and the freezing level is positively correlated with the excitability of IL-PFC and BLA projection neurons after conditioning [20]. Consistent with these studies, we found that fear-generalized mice had a lower level of BDNF and a higher level of GluN2B protein in the BLA and IL-PFC, which were reversed by a single intraperitoneal dose of ketamine. Recently, it has been shown that blockade of NMDAR-dependent bursting activity in the lateral habenula mediates the antidepressant actions of ketamine in rat and mouse models of depression [39]. It would therefore be interesting to investigate the effects of ketamine on the activity of neurons in the BLA and PFC.

Ketamine increased the BDNF expression in the BLA and IL-PFC in a short period of time (~ 2 h) after administration, which is consistent with a previous study showing that 1 h–5 h are sufficient for significant upregulation of protein expression [40]. A recent study confirmed that ketamine increases pro-BDNF expression within 40 min after a single dose [41]. These results indicate that ketamine might prevent the degradation of protein or enhance the expression of protein *via* the cytoplasmic mRNA pool. Acute ketamine administration increased BDNF protein in the BLA and IL-PFC. This is consistent with the antidepressant effects of ketamine, which may depend on rapid activation of the mammalian target of BDNF protein in the PFC [42, 43], and ketamine alleviates the PTSD-like effect by modifying the BDNF and HCN1 expression in the SPS&S animal model [27].

In addition, we found that GluN2B and GluN2A protein expression was increased as a result of fear generalization and ketamine reversed the expression of GluN2B, but interestingly GluN2A expression remained the same. Growing evidence supports the idea that the expression and subunit composition of NMDARs can be dynamically modulated by individual experiences. Interestingly, the expression of membrane GluN2B, not the total amount of GluN1, GluN2A, and GluN2B, is increased in the hippocampal CA1 after contextual fear conditioning in a stress-strength-dependent manner [24], highlighting an

important role of NMDAR trafficking in NMDA-dependent synaptic plasticity. Accumulating data indicate that NMDARs dynamically sense and integrate neural signaling in a stimulus-dependent manner, by the regulation of expression, subunit composition, or cellular trafficking. Notably, previous studies revealed that loss of GluN2B function [44] or GluN2B deletion [45] impairs long-term fear memory. Our recent data also supported an important role of GluN2B in long-term fear memory formation [22]. Moreover, inhibition of NMDARs prevents the loss of BDNF function [25]. Our results together with previous data indicate that ketamine up-regulates BDNF signaling by decreasing GluN2B protein to alleviate PTSD-like symptoms.

Acknowledgements This work was supported by grants from the National Natural Science Foundation of China (81530061 and 81471829), the Pearl River Nova Program of Guangzhou (201610010154), and the Natural Science Foundation of Guangdong Province China (2017A030313095).

Conflict of interest All authors claim that there are no conflicts of interest.

References

- Jovanovic T, Kazama A, Bachevalier J, Davis M. Impaired safety signal learning may be a biomarker of PTSD. *Neuropharmacology* 2012, 62: 695–704.
- Ciocchi S, Herry C, Grenier F, Wolff SB, Letzkus JJ, Vlachos I, *et al.* Encoding of conditioned fear in central amygdala inhibitory circuits. *Nature* 2010, 468: 277–282.
- Kessler RC, Sonnega A, Bromet E, Hughes M, Nelson CB. Posttraumatic stress disorder in the National Comorbidity Survey. *Arch Gen Psychiatry* 1995, 52: 1048–1060.
- Pradhan B, Kluever D'Amico J, Makani R, Parikh T. Nonconventional interventions for chronic post-traumatic stress disorder: Ketamine, repetitive trans-cranial magnetic stimulation (rTMS), and alternative approaches. *J Trauma Dissociation* 2016, 17: 35–54.
- Stein DJ, Ipser JC, Seedat S. Pharmacotherapy for post traumatic stress disorder (PTSD). *Cochrane Database Syst Rev* 2006: CD002795.
- Golub Y, Mauch CP, Dahloff M, Wotjak CT. Consequences of extinction training on associative and non-associative fear in a mouse model of Posttraumatic Stress Disorder (PTSD). *Behav Brain Res* 2009, 205: 544–549.
- Bernardini F, Attademo L, Cleary SD, Luther C, Shim RS, Quartesan R, *et al.* Risk prediction models in psychiatry: toward a new frontier for the prevention of mental illnesses. *J Clin Psychiatry* 2017, 78: 572–583.
- Berman RM, Cappiello A, Anand A, Oren DA, Heninger GR, Charney DS, *et al.* Antidepressant effects of ketamine in depressed patients. *Biol Psychiatry* 2000, 47: 351–354.
- Zanos P, Moaddel R, Morris PJ, Georgiou P, Fischell J, Elmer GI, *et al.* NMDAR inhibition-independent antidepressant actions of ketamine metabolites. *Nature* 2016, 533: 481–486.
- Zarate CA, Jr., Mathews D, Ibrahim L, Chaves JF, Marquardt C, Ukoh I, *et al.* A randomized trial of a low-trapping nonselective

- N-methyl-D-aspartate channel blocker in major depression. *Biol Psychiatry* 2013, 74: 257–264.
11. Brachman RA, McGowan JC, Perusini JN, Lim SC, Pham TH, Faye C, *et al.* Ketamine as a prophylactic against stress-induced depressive-like behavior. *Biol Psychiatry* 2016, 79: 776–786.
 12. McGhee LL, Maani CV, Garza TH, Gaylord KM, Black IH. The correlation between ketamine and posttraumatic stress disorder in burned service members. *J Trauma* 2008, 64: S195–198; Discussion S197–198.
 13. McGhee LL, Maani CV, Garza TH, Slater TM, Petz LN, Fowler M. The intraoperative administration of ketamine to burned U.S. service members does not increase the incidence of post-traumatic stress disorder. *Mil Med* 2014, 179: 41–46.
 14. Silvestre JS, Pallares M, Nadal R, Ferre N. Opposite effects of ethanol and ketamine in the elevated plus-maze test in Wistar rats undergoing a chronic oral voluntary consumption procedure. *J Psychopharmacol* 2002, 16: 305–312.
 15. Hayase T, Yamamoto Y, Yamamoto K. Behavioral effects of ketamine and toxic interactions with psychostimulants. *BMC Neurosci* 2006, 7: 25.
 16. Becker A, Peters B, Schroeder H, Mann T, Huether G, Grecksch G. Ketamine-induced changes in rat behaviour: A possible animal model of schizophrenia. *Prog Neuropsychopharmacol Biol Psychiatry* 2003, 27: 687–700.
 17. Bryant RA, Kemp AH, Felmingham KL, Liddell B, Olivieri G, Peduto A, *et al.* Enhanced amygdala and medial prefrontal activation during nonconscious processing of fear in posttraumatic stress disorder: an fMRI study. *Hum Brain Mapp* 2008, 29: 517–523.
 18. Bremner JD, Vermetten E, Schmahl C, Vaccarino V, Vythilingam M, Afzal N, *et al.* Positron emission tomographic imaging of neural correlates of a fear acquisition and extinction paradigm in women with childhood sexual-abuse-related post-traumatic stress disorder. *Psychol Med* 2005, 35: 791–806.
 19. Ghosh S, Chattarji S. Neuronal encoding of the switch from specific to generalized fear. *Nat Neurosci* 2015, 18: 112–120.
 20. Song C, Ehlers VL, Moyer JR, Jr. Trace fear conditioning differentially modulates intrinsic excitability of medial prefrontal cortex-basolateral complex of amygdala projection neurons in infralimbic and prelimbic cortices. *J Neurosci* 2015, 35: 13511–13524.
 21. Wang SH, de Oliveira Alvares L, Nader K. Cellular and systems mechanisms of memory strength as a constraint on auditory fear reconsolidation. *Nat Neurosci* 2009, 12: 905–912.
 22. Chen YF, Chen ZX, Wang RH, Shi YW, Xue L, Wang XG, *et al.* Knockdown of CLC-3 in the hippocampal CA1 impairs contextual fear memory. *Prog Neuropsychopharmacol Biol Psychiatry* 2019, 89: 132–145.
 23. Holehonnur R, Phensy AJ, Kim LJ, Milivojevic M, Vuong D, Daison DK, *et al.* Increasing the GluN2A/GluN2B ratio in neurons of the mouse basal and lateral amygdala inhibits the modification of an existing fear memory trace. *J Neurosci* 2016, 36: 9490–9504.
 24. Sun YY, Cai W, Yu J, Liu SS, Zhuo M, Li BM, *et al.* Surface expression of hippocampal NMDA GluN2B receptors regulated by fear conditioning determines its contribution to memory consolidation in adult rats. *Sci Rep* 2016, 6: 30743.
 25. Tanqueiro SR, Ramalho RM, Rodrigues TM, Lopes LV, Sebastiao AM, Diogenes MJ. Inhibition of NMDA receptors prevents the loss of BDNF function induced by amyloid beta. *Front Pharmacol* 2018, 9: 237.
 26. Muhlberger A, Andreatta M, Ewald H, Glotzbach-Schoon E, Troger C, Baumann C, *et al.* The BDNF Val66Met polymorphism modulates the generalization of cued fear responses to a novel context. *Neuropsychopharmacology* 2014, 39: 1187–1195.
 27. Hou L, Qi Y, Sun H, Wang G, Li Q, Wang Y, *et al.* Applying ketamine to alleviate the PTSD-like effects by regulating the HCN1-related BDNF. *Prog Neuropsychopharmacol Biol Psychiatry* 2018, 86: 313–321.
 28. Wang S, Sheng T, Ren S, Tian T, Lu W. Distinct roles of PKC α /lambda and PKMzeta in the initiation and maintenance of hippocampal long-term potentiation and memory. *Cell Rep* 2016, 16: 1954–1961.
 29. Rossetti T, Banerjee S, Kim C, Leubner M, Lamar C, Gupta P, *et al.* Memory erasure experiments indicate a critical role of CaMKII in memory storage. *Neuron* 2017, 96: 207–216.e202.
 30. Iijima M, Fukumoto K, Chaki S. Acute and sustained effects of a metabotropic glutamate 5 receptor antagonist in the novelty-suppressed feeding test. *Behav Brain Res* 2012, 235: 287–292.
 31. Koike H, Iijima M, Chaki S. Involvement of AMPA receptor in both the rapid and sustained antidepressant-like effects of ketamine in animal models of depression. *Behav Brain Res* 2011, 224: 107–111.
 32. Lepack AE, Fuchikami M, Dwyer JM, Banasr M, Duman RS. BDNF release is required for the behavioral actions of ketamine. *Int J Neuropsychopharmacol* 2014, 18.
 33. Paxinos G, Franklin KBJ. *The Mouse Brain in Stereotaxic Coordinates*. San Diego: Academic Press, 2001.
 34. McGowan JC, LaGamma CT, Lim SC, Tsitsiklis M, Neria Y, Brachman RA, *et al.* Prophylactic ketamine attenuates learned fear. *Neuropsychopharmacology* 2017, 42: 1577–1589.
 35. Zarate CA Jr., Singh JB, Carlson PJ, Brutsche NE, Ameli R, Luckenbaugh DA, *et al.* A randomized trial of an N-methyl-D-aspartate antagonist in treatment-resistant major depression. *Arch Gen Psychiatry* 2006, 63: 856–864.
 36. Muir WW. NMDA receptor antagonists and pain: ketamine. *Vet Clin North Am Equine Pract* 2010, 26: 565–578.
 37. Baldi E, Lorenzini CA, Bucherelli C. Footshock intensity and generalization in contextual and auditory-cued fear conditioning in the rat. *Neurobiol Learn Mem* 2004, 81: 162–166.
 38. Laxmi TR, Stork O, Pape HC. Generalisation of conditioned fear and its behavioural expression in mice. *Behav Brain Res* 2003, 145: 89–98.
 39. Yang Y, Cui Y, Sang K, Dong Y, Ni Z, Ma S, *et al.* Ketamine blocks bursting in the lateral habenula to rapidly relieve depression. *Nature* 2018, 554: 317–322.
 40. Ben-Ari Y, Brody Y, Kinor N, Mor A, Tsukamoto T, Spector DL, *et al.* The life of an mRNA in space and time. *J Cell Sci* 2010, 123: 1761–1774.
 41. Nguyen L, Lucke-Wold BP, Logsdon AF, Scandinaro AL, Huber JD, Matsumoto RR. Behavioral and biochemical effects of ketamine and dextromethorphan relative to its antidepressant-like effects in Swiss Webster mice. *Neuroreport* 2016, 27: 1004–1011.
 42. Autry AE, Adachi M, Nosyreva E, Na ES, Los MF, Cheng PF, *et al.* NMDA receptor blockade at rest triggers rapid behavioural antidepressant responses. *Nature* 2011, 475: 91–95.
 43. Bocchio-Chiavetto L, Bagnardi V, Zanardini R, Molteni R, Nielsen MG, Placentino A, *et al.* Serum and plasma BDNF levels in major depression: a replication study and meta-analysis. *World J Biol Psychiatry* 2010, 11: 763–773.
 44. Brigman JL, Wright T, Talani G, Prasad-Mulcare S, Jinde S, Seabold GK, *et al.* Loss of GluN2B-containing NMDA receptors in CA1 hippocampus and cortex impairs long-term depression, reduces dendritic spine density, and disrupts learning. *J Neurosci* 2010, 30: 4590–4600.
 45. Akashi K, Kakizaki T, Kamiya H, Fukaya M, Yamasaki M, Abe M, *et al.* NMDA receptor GluN2B (GluR epsilon 2/NR2B) subunit is crucial for channel function, postsynaptic macromolecular organization, and actin cytoskeleton at hippocampal CA3 synapses. *J Neurosci* 2009, 29: 10869–10882.



L-type Calcium Channels are Involved in Iron-induced Neurotoxicity in Primary Cultured Ventral Mesencephalon Neurons of Rats

Yu-Yu Xu¹ · Wen-Ping Wan¹ · Sha Zhao¹ · Ze-Gang Ma^{1,2}

Received: 31 January 2019 / Accepted: 5 May 2019 / Published online: 3 September 2019
© Shanghai Institutes for Biological Sciences, CAS 2019

Abstract In the present study, we investigated the mechanisms underlying the mediation of iron transport by *L*-type Ca²⁺ channels (LTCCs) in primary cultured ventral mesencephalon (VM) neurons from rats. We found that co-treatment with 100 μmol/L FeSO₄ and MPP⁺ (1-methyl-4-phenylpyridinium) significantly increased the production of intracellular reactive oxygen species, decreased the mitochondrial transmembrane potential and increased the caspase-3 activation compared to MPP⁺ treatment alone. Co-treatment with 500 μmol/L CaCl₂ further aggravated the FeSO₄-induced neurotoxicity in MPP⁺-treated VM neurons. Co-treatment with 10 μmol/L isradipine, an LTCC blocker, alleviated the neurotoxicity induced by co-application of FeSO₄ and FeSO₄/CaCl₂. Further studies indicated that MPP⁺ treatment accelerated the iron influx into VM neurons. In addition, FeSO₄ treatment significantly increased the intracellular Ca²⁺ concentration. These effects were blocked by isradipine. These results suggest that elevated extracellular Ca²⁺ aggravates iron-induced neurotoxicity. LTCCs mediate iron transport in dopaminergic neurons and this, in turn, results in elevated intracellular Ca²⁺ and further aggravates iron-induced neurotoxicity.

Keywords *L*-type Ca²⁺ channels · Iron overload · Parkinson's disease · Isradipine · Dopamine neuron

Introduction

Parkinson's disease (PD) is a common neurodegenerative disease. It is characterized by a selective loss of dopamine (DA) neurons in the substantia nigra pars compacta (SNpc), and results in DA exhaustion in the striatum. Many factors have been implicated in the pathological process of PD [1–6]. Recently, growing evidence has indicated that iron accumulation plays a key role in the pathogenesis of DA neuron degeneration [7–10]. Iron is an important co-factor in maintaining cellular functions. It is extensively involved in metabolic processes [11, 12]. When the dynamic balance of iron is interrupted, it leads to mitochondrial DNA damage [13, 14], mitochondrial dysfunction, lipid peroxidation, and DNA breakage [15]. Excessive deposition of iron in the brain and the consequent oxidative stress are considered to play key roles in the pathogenesis of PD [16]. However, the precise mechanisms underlying iron-selective accumulation in the SN and iron-mediated neuronal toxicity remain unclear.

There is evidence that *L*-type Ca²⁺ channels (LTCCs) are involved in the DA neuron degeneration [17–20]. Epidemiological studies have shown that the risk of PD is significantly decreased by dihydropyridines, LTCC blockers, in patients with hypertension [21, 22]. It has been reported that LTCCs may mediate iron entry into cardiomyocytes under high-iron conditions [23]. In addition to cardiomyocytes, iron may compete with Ca²⁺ for entry into nerve growth factor-treated PC12 cells and mouse N-2α cells *via* LTCCs [24]. Our previous study also demonstrated that the LTCC blocker nifedipine attenuates iron aggregation in the SN of iron-overloaded rats [25]. However, the mechanisms underlying LTCC-mediated iron accumulation in the SN are not fully understood.

✉ Ze-Gang Ma
mazegang@qdu.edu.cn

¹ Department of Physiology, School of Basic Medicine, Qingdao University, Qingdao 266071, China

² Institute of Brain Science and Disorders, Qingdao University, Qingdao 266071, China

It is well known that excessive iron reacts with hydrogen peroxide to produce hydroxyl radicals by the Fenton reaction, thus aggravating oxidative stress. Recently, studies have indicated that iron overload increases the level of intracellular Ca^{2+} ($[\text{Ca}^{2+}]_i$), thereby aggravating the iron-mediated neurotoxicity. In addition, inhibition of Ca^{2+} signals prevents the mitochondrial fragmentation and neuronal death induced in hippocampal neurons by iron-overload [26]. However, the effects of extracellular Ca^{2+} on iron-overload-induced neurotoxicity remain unclear. In the present study, we investigated the mechanisms underlying LTCC-mediated iron transport and the effects of Ca^{2+} on iron-induced neuronal toxicity in primary cultured ventral mesencephalon (VM) neurons from rats.

Materials and Methods

Materials

All the reagents were from Sigma Chemical Co. (St. Louis, MO, USA) unless otherwise indicated. Dulbecco's modified Eagle's medium Nutrient Mixture-F12 (DMEM/F12) and B27 were from Gibco (Grand Island, NY, USA).

Culture of VM Primary Neurons

All procedures were carried out in accordance with the National Institutes of Health Guide for Care and Use of Laboratory Animals and were approved by the Animal Ethics Committee of Qingdao University. Primary cultures of VM neurons were prepared from the mesencephalon of embryonic Wistar rats (14 days) as previously reported, with some modifications [27, 28]. Briefly, the abdomen of female rats was cleaned with 70% ethanol, and then the abdominal wall and the uterine horns were opened. Each embryo was collected from the uterine horns and the amniotic membranes were removed. For dissection, the embryos were placed in a Petri dish containing pre-cooled DMEM/F12 under a stereomicroscope and the VM was isolated using ultra-fine forceps. Cells were suspended in serum-free DMEM/F12 supplemented with 2% B27, and then seeded onto poly-D-lysine-coated culture plates. Neurons were cultured for 7 days before use. Neuron purity was approximately 90% based on immunofluorescence staining with the specific neuron marker microtubule-associated protein 2.

Assessment of Mitochondrial Transmembrane Potential ($\Delta\Psi_m$)

After culture for 7 days, changes in the $\Delta\Psi_m$ of VM neurons were measured with rhodamine123, using flow

cytometry as described previously [29, 30]. The uptake of rhodamine123 into mitochondria is an indicator of the $\Delta\Psi_m$. The neurons were pre-incubated with 5 $\mu\text{mol/L}$ 1-methyl-4-phenylpyridinium (MPP^+) for 24 h, and then treated with FeSO_4 and/or CaCl_2 for 3 h. The neurons were divided into control, MPP^+ treatment, $\text{MPP}^+/\text{CaCl}_2$ treatment, $\text{MPP}^+/\text{CaCl}_2/\text{isradipine}$ treatment, $\text{MPP}^+/\text{FeSO}_4$ treatment, $\text{MPP}^+/\text{FeSO}_4/\text{isradipine}$ treatment, $\text{MPP}^+/\text{CaCl}_2/\text{FeSO}_4$ treatment, and $\text{MPP}^+/\text{CaCl}_2/\text{FeSO}_4/\text{isradipine}$ treatment groups (500 $\mu\text{mol/L}$ CaCl_2 , 100 $\mu\text{mol/L}$ FeSO_4 , 10 $\mu\text{mol/L}$ isradipine). After different treatments, the neurons were incubated in HEPES-buffered saline (HBS) containing rhodamine123 in a final concentration of 5 $\mu\text{g/mL}$ for 30 min at 37 °C. After washing twice with HBS, the fluorescence intensity was recorded at 488 nm excitation and 525 nm emission. Results were presented as a Fluorescence 1-Histogram, setting the gated regions M1 and M2 as a marker to measure the changing levels of fluorescence intensity with Cellquest software.

Reactive Oxygen Species (ROS) Assay

Intracellular ROS in the VM neurons were measured using $\text{H}_2\text{DCF-DA}$ (2,7-dichlorodihydrofluorescein) as previously described [30]. The fluorescence emitted by $\text{H}_2\text{DCF-DA}$ reflects intracellular ROS generation. After the different treatments, the neurons were incubated in HBS containing $\text{H}_2\text{DCF-DA}$ in a final concentration of 5 $\mu\text{mol/L}$ for 30 min at 37°C. After washing twice with HBS, fluorescent intensity was recorded at 488 nm excitation and 525 nm emission. The results were presented as for the $\Delta\Psi_m$ assay.

Western Blot Analysis

The VM neurons were seeded in six-well plates and treated as described above. After washing with PBS, the cells were digested on culture plates with RIPA lysis buffer (50 mmol/L Tris-HCl, 150 mmol/L NaCl, 1% Nonidet, 0.5% deoxycholate, 1 mmol/L EDTA, and 1 mmol/L PMSF) with 1% phenylmethylsulfonyl fluoride on ice for 30 min. Then, the samples were centrifuged at 12,000 rpm for 20 min at 4 °C. Protein concentration was determined with a bicinchoninic acid kit. The lysates containing 40 μg of protein sample were separated on 12% sodium dodecyl sulfate polyacrylamide gel and transferred to polyvinylidene difluoride membranes with a diameter of 0.22 μm . The membranes were blocked with 5% non-fat milk at room temperature for 2 h. Blots were probed with rabbit anti-mouse cleaved caspase-3 (Cell Signaling, Boston, MA, USA, 1:1000) and rabbit anti-mouse β -actin primary antibody (Bioss, Boston, MA, USA, 1:10000) overnight at 4 °C. After washing with TBST, the membranes were incubated with goat anti-rabbit and goat anti-mouse

secondary antibodies conjugated with horseradish peroxidase (Bioss, Boston, MA, USA, 1:10,000) for 1 h at room temperature. The antigen-antibody complexes were visualized with enhanced chemiluminescence reagent and then analyzed by scanning densitometry on a Tanon Image System (Shanghai, China).

Calcein Loading of Cells and Iron Influx Assay

Calcein-AM is a membrane-permeable, non-fluorescent molecule that becomes fluorescent upon intracellular cleavage by cytoplasmic esterases to calcein (which is membrane impermeable). It is pH-independent and is rapidly quenched by divalent metals and reversed easily by their chelators. Ferrous iron influx into VM neurons was determined by the quenching of calcein fluorescence as described previously [31]. The VM neurons were divided into 4 groups. Control: VM neurons were cultured in serum-free DMEM/F12 supplemented with 2% B27 for 24 h; MPP⁺: VM neurons were cultured in serum-free DMEM/F12 supplemented with 2% B27 with 5 $\mu\text{mol/L}$ MPP⁺ for 24 h; MPP⁺ with isradipine or Bayk8644: MPP⁺-treated cells underwent the same procedures except that isradipine or 10 $\mu\text{mol/L}$ Bayk8644 was included in the perfusion fluid. The cells were incubated with calcein-AM at a final concentration of 1 $\mu\text{mol/L}$ in HBS for 30 min at 37 °C. Excess calcein on the cell surface was washed 3 times with HBS. Calcein fluorescence was recorded at 488 nm excitation and 525 nm emission. Fluorescence intensity was measured every 3 min for the next 30 min during perfusion with 100 $\mu\text{mol/L}$ ferrous iron (FeSO₄ in ascorbic acid solution, 1:44 molar ratio, pH 6.0). The mean fluorescence intensity of 30–35 cells in 4 separate fields was monitored at 200 \times magnification and processed with Leica Application Suite X (Leica, Mannheim, Germany).

Determination of Intracellular Ca²⁺ Concentration

Fluo-3 AM is a fluorescent probe used to assess the [Ca²⁺]_i. Fluo-3 AM can penetrate the cell membrane and it is cleaved by esterase to form Fluo-3, which binds to Ca²⁺ and produces strong fluorescence. The excitation wavelength is 488 nm and emission is 525 nm–530 nm. VM neurons were divided into 6 groups. Control: VM neurons were cultured in serum-free DMEM/F12 supplemented with 2% B27 for 24 h; MPP⁺: VM neurons were cultured in serum-free DMEM/F12 supplemented with 2% B27 with 5 $\mu\text{mol/L}$ MPP⁺ for 24 h; MPP⁺/FeSO₄ treatment: MPP⁺-treated cells underwent the same procedures except that 100 $\mu\text{mol/L}$ FeSO₄ was included in the perfusion fluid; MPP⁺/CaCl₂ treatment: MPP⁺-treated cells underwent the same procedures except that 2.5 mmol/L CaCl₂ was included in the perfusion fluid; MPP⁺/FeSO₄/CaCl₂

treatment: MPP⁺-treated cells underwent the same procedures except that 100 $\mu\text{mol/L}$ FeSO₄ and 2.5 mmol/L CaCl₂ were included in the perfusion fluid; and MPP⁺/FeSO₄/CaCl₂/isradipine treatment: MPP⁺-treated cells underwent the same procedures except that 100 $\mu\text{mol/L}$ FeSO₄, 2.5 mmol/L CaCl₂, and 10 $\mu\text{mol/L}$ isradipine were included in the perfusion fluid. The cells were incubated with Fluo-3 AM at a final concentration of 5 $\mu\text{mol/L}$ in HBS for 30 min at 37°C and then perfused with Krebs–Henseliet buffer (K–H buffer). Fluo-3 AM fluorescence was recorded at 488 nm excitation and 525 nm emission. Fluorescence intensity was measured every 2 min for the next 20 min during perfusion with K–H buffer. The mean fluorescence intensity of 30–35 cells in 4 separate fields was monitored at 200 \times magnification and processed with Leica Application Suite X (Leica, Mannheim, Germany) [32].

Statistical Analysis

The results are expressed as the mean \pm SEM. Data were analyzed using Prism Graphpad 5.0 software (Graphpad Software, San Diego, CA, USA). One-way analysis of variance (ANOVA) followed by the Newman-Keuls test was used to compare the differences between the means. For iron influx and [Ca²⁺]_i imaging experiments, regular two-way ANOVA followed by Bonferroni *post hoc* comparison of the means was performed. $P < 0.05$ was considered to be significant.

Results

Isradipine Prevents FeSO₄-induced $\Delta\Psi\text{m}$ Reduction in VM Neurons

$\Delta\Psi\text{m}$ is a key index of mitochondrial function, which is closely related to oxidative stress and apoptosis. By flow cytometry, we assessed the $\Delta\Psi\text{m}$ changes in VM neurons after FeSO₄ and/or CaCl₂ treatment. The $\Delta\Psi\text{m}$ in the MPP⁺ and MPP⁺/CaCl₂ groups were slightly lower than that in the control group, however the difference was not statistically significant (Fig. 1). The $\Delta\Psi\text{m}$ in the MPP⁺/FeSO₄ group was decreased by 26% compared to the MPP⁺ group, and the difference was statistically significant ($P < 0.001$). Co-treatment with isradipine alleviated the FeSO₄-induced decrease of $\Delta\Psi\text{m}$ in VM neurons ($P < 0.01$). The $\Delta\Psi\text{m}$ in the MPP⁺/FeSO₄/CaCl₂ group was decreased by 11% compared to the MPP⁺/FeSO₄ group ($P < 0.01$). Treatment with isradipine alleviated the neurotoxicity induced by co-treatment with FeSO₄ and CaCl₂ ($P < 0.001$).

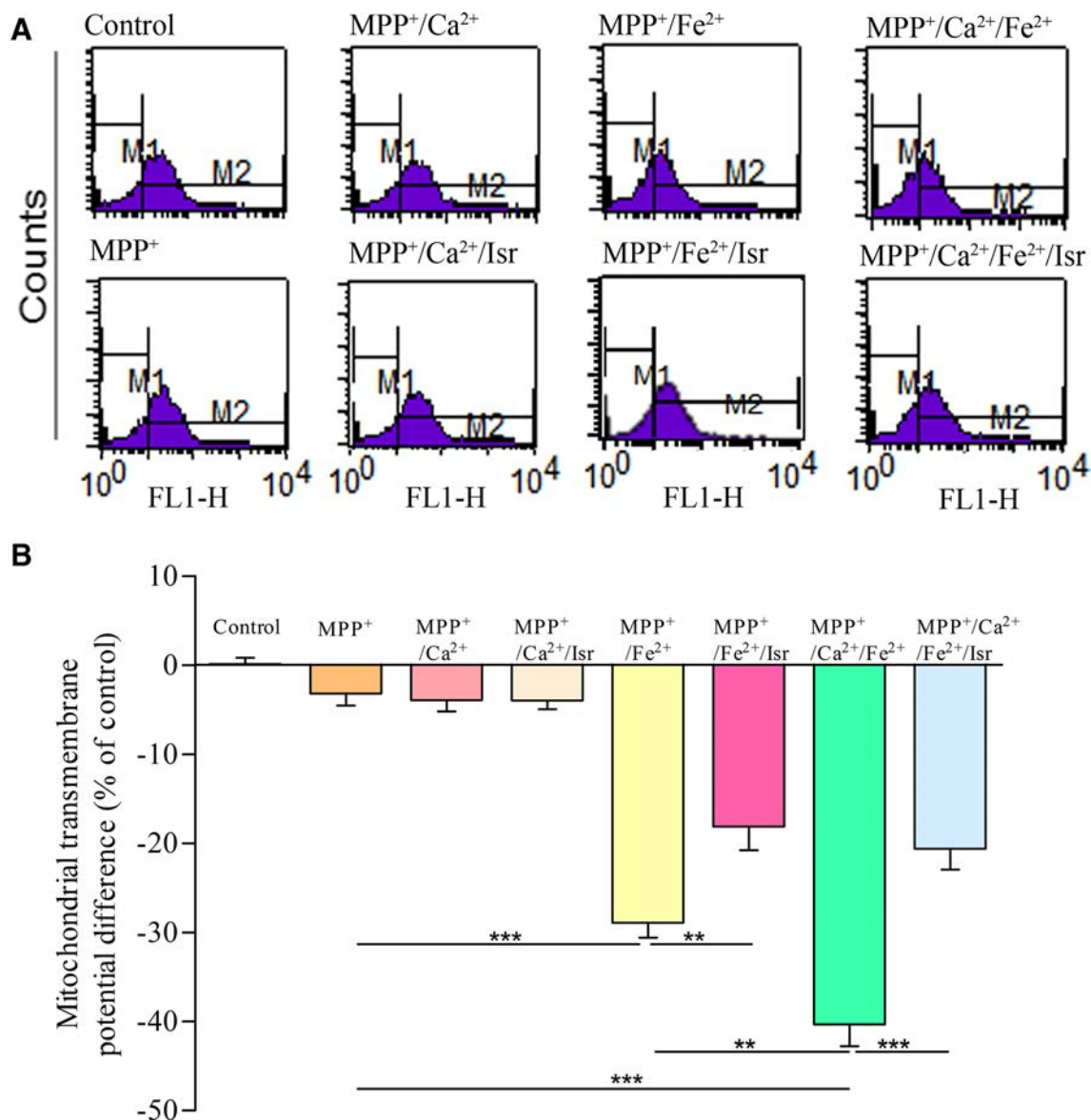


Fig. 1 Isradipine prevents FeSO₄-induced $\Delta\Psi_m$ reduction in VM neurons. **A** Representative fluorometric assays of the $\Delta\Psi_m$ in different groups of VM neurons. **B** Summary of the changes in

$\Delta\Psi_m$ in different treatment groups (mean \pm SEM of 6 independent experiments; ** $P < 0.01$, *** $P < 0.001$).

Isradipine Prevents FeSO₄-induced ROS Production in VM Neurons

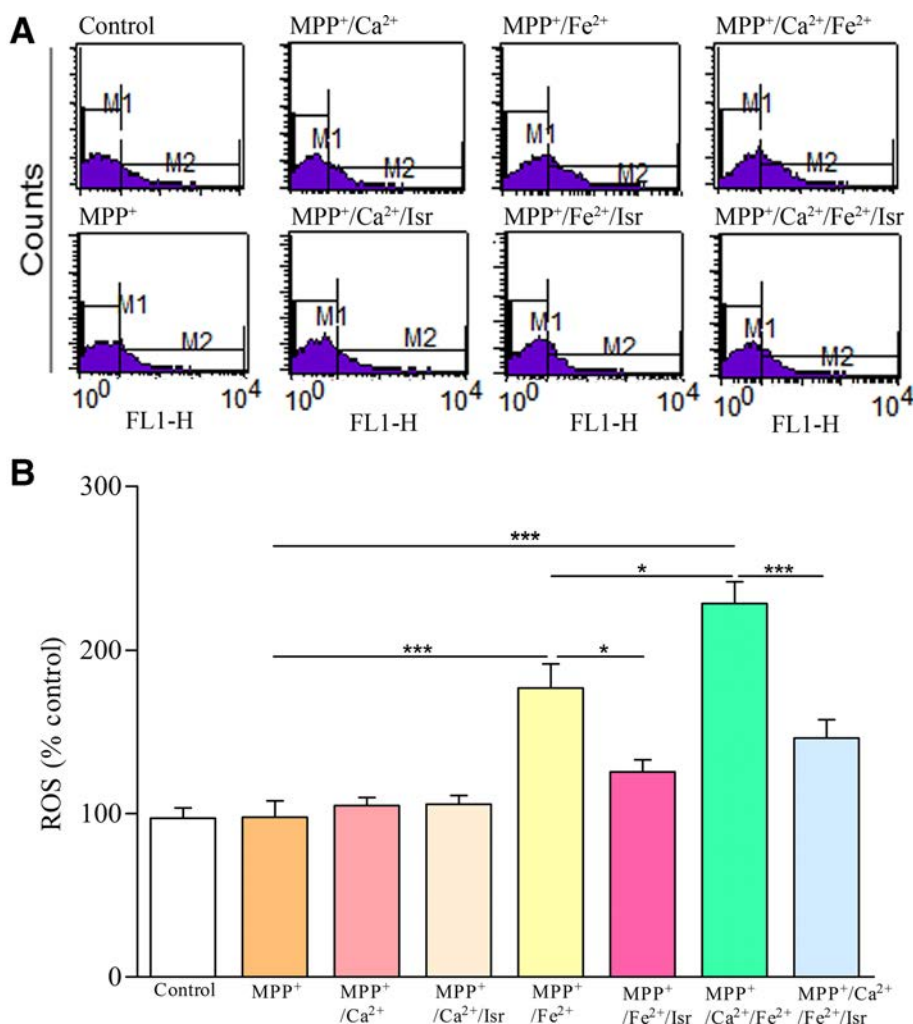
We further measured the changes of ROS production in VM neurons using the fluorescence dye H₂DCF-DA. The fluorescence value of the control was set to 100%. Co-application of MPP⁺ with FeSO₄ significantly increased the intracellular ROS production (Fig. 2). The intracellular ROS production in the MPP⁺/FeSO₄ group was increased by 80% compared to the MPP⁺ group ($P < 0.001$). Co-treatment with isradipine inhibited FeSO₄-induced ROS production ($P < 0.05$). The ROS production in the MPP⁺/FeSO₄/CaCl₂ group was increased by 28% compared to the

MPP⁺/FeSO₄ group ($P < 0.05$). Isradipine markedly inhibited the ROS production induced by FeSO₄ and CaCl₂ co-treatment ($P < 0.001$).

Isradipine Inhibits FeSO₄-induced Caspase-3 Activation in VM Neurons

Caspase-3 is a key protein in the process of apoptosis. We further assessed the caspase-3 activity in the different treatment groups. The expression of cleaved caspase-3 in the MPP⁺/FeSO₄ group was up-regulated by 202% compared to the MPP⁺ group ($P < 0.001$). This increase was alleviated by isradipine ($P < 0.05$ versus the MPP⁺/FeSO₄

Fig. 2 Isradipine prevents FeSO_4 -induced ROS production in VM neurons. **A** Representative fluorometric assays of ROS in different groups. **B** Statistical analysis of the ROS production in different treatment groups. Fluorescence values of the control were set to 100% (mean \pm SEM of 6 independent experiments; * $P < 0.05$, *** $P < 0.001$).



group). The cleaved caspase-3 expression in the MPP⁺/FeSO₄/CaCl₂ group was up-regulated by 59% compared to the MPP⁺/FeSO₄ group ($P < 0.01$). The up-regulation of cleaved caspase-3 induced by MPP⁺/FeSO₄/CaCl₂ co-treatment was alleviated by isradipine ($P < 0.001$ versus MPP⁺/FeSO₄/CaCl₂ group) (Fig. 3).

Isradipine Inhibits MPP⁺-induced Iron Influx in VM Neurons

Iron influx into VM neurons was determined by the quenching of calcein fluorescence. Time-dependent intracellular fluorescence quenching occurred with 100 $\mu\text{mol/L}$ ferrous iron perfusion (control), indicating increased intracellular iron levels. After treatment with 5 $\mu\text{mol/L}$ MPP⁺ for 24 h, the quenching was more rapid than in the control. The quenching was further accelerated when neurons were perfused with 10 $\mu\text{mol/L}$ Bayk8644, a Ca²⁺ channel agonist, compared with the MPP⁺ group, indicating a further iron influx. Fluorescence quenching in the MPP⁺ group was inhibited by both 1 $\mu\text{mol/L}$ and 10 $\mu\text{mol/L}$

isradipine, indicating that iron influx was blocked by isradipine (Fig. 4).

Intracellular Ca²⁺ Levels Increase with Iron Treatment

We did not find a significant difference in the $[\text{Ca}^{2+}]_i$ between the MPP⁺ group and MPP⁺/CaCl₂ (2.5 mmol/L) co-perfusion groups ($P > 0.05$ vs control). However, the $[\text{Ca}^{2+}]_i$ significantly increased with FeSO₄ perfusion in K-H buffer. A marked increase in $[\text{Ca}^{2+}]_i$ occurred when 2.5 mmol/L CaCl₂ was perfused in K-H buffer compared to the MPP⁺/FeSO₄ co-application group. Bath application of isradipine inhibited iron-induced elevation of $[\text{Ca}^{2+}]_i$ (Fig. 5).

Discussion

In the present study, we found that isradipine, a specific antagonist of LTCCs, prevented the iron-induced reduction in $\Delta\Psi_m$ and inhibited iron-induced ROS production and

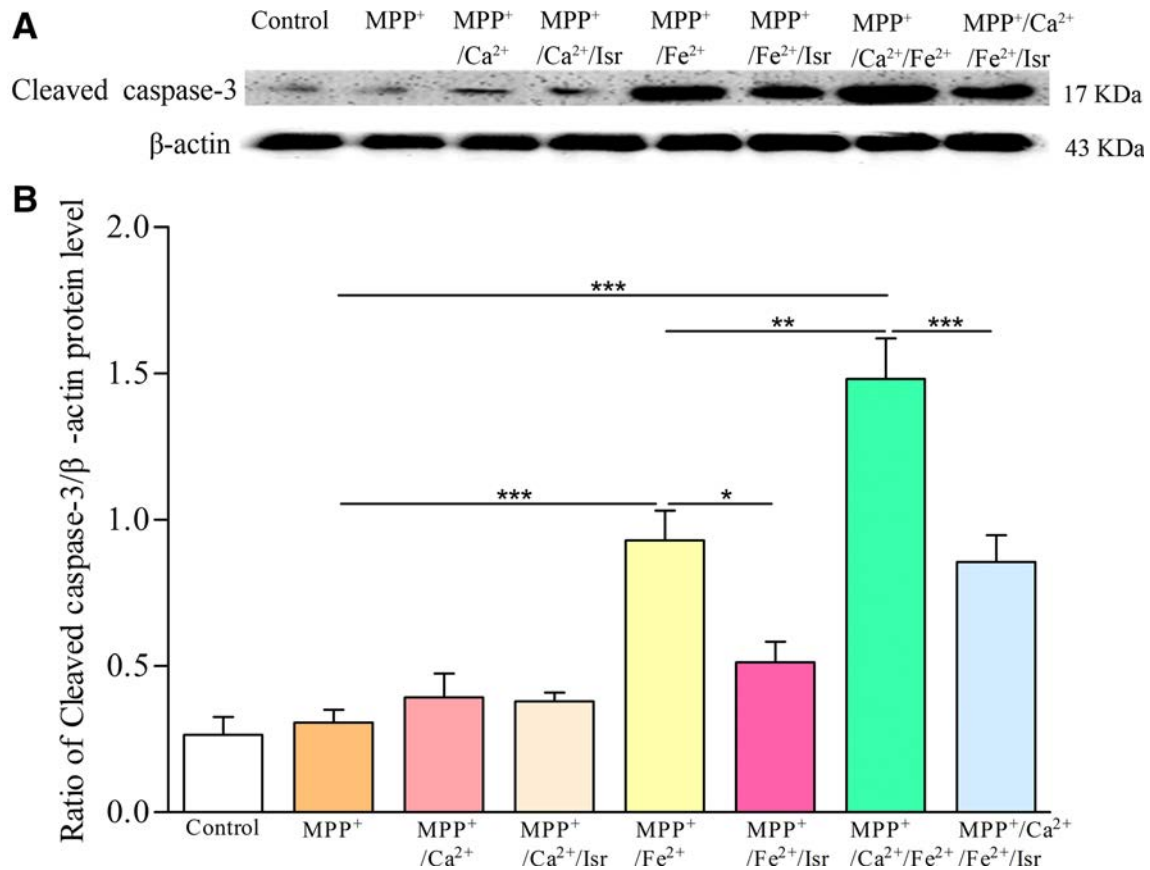


Fig. 3 Isradipine inhibits FeSO₄-induced caspase-3 activation in VM neurons. **A** Original bands showing the expression of cleaved caspase-3 in VM neurons. β-actin was used as a loading control. **B** Statistical

summary of the expression of cleaved caspase-3 in the different treatment groups (ratio of cleaved caspase-3 to β-actin from 6 independent experiments; **P* < 0.05, ***P* < 0.01, ****P* < 0.001).

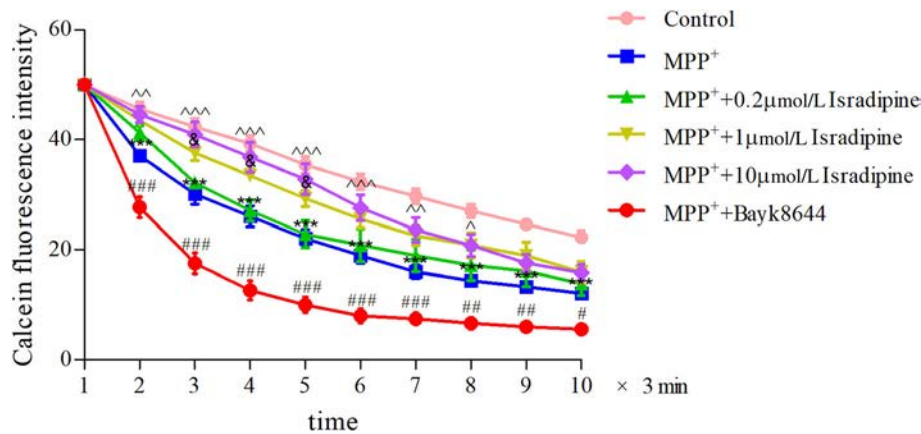


Fig. 4 Time-course of calcein fluorescence in VM neurons. The mean fluorescence intensity was calculated from 30–35 separate cells from 4 separate fields at each time point (mean ± SEM of 6 independent experiments; ****P* < 0.001, MPP⁺ group versus control;

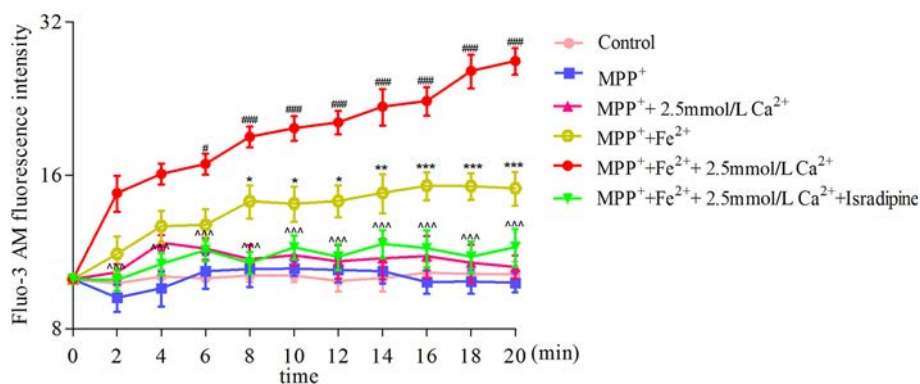
#*P* < 0.05, ##*P* < 0.01, ###*P* < 0.001, Bayk8644 group vs MPP⁺ group; ^*P* < 0.05, ^^*P* < 0.01, ^^*P* < 0.001, 10 μmol/L isradipine group vs MPP⁺ group; &*P* < 0.05, 1 μmol/L isradipine group vs MPP⁺ group)

caspase-3 activation in VM neurons. These findings suggest that LTCCs are involved in iron-induced DA neuron degeneration in the pathogenesis of PD.

Iron overload in the SN plays a key role in the etiology and pathogenesis of PD [33]. However, the precise

mechanisms underlying such an overload remain unknown. The uptake of iron by neurons is divided into a transferrin-dependent pathway and a non-transferrin-bound iron (NTBI) pathway [34]. Studies have revealed that iron enters DA neurons in the SN of PD patients mainly via the

Fig. 5 Time-course of fluo-3 AM fluorescence in VM neurons. The mean fluorescence intensity was calculated from 30 to 35 separate cells from 4 separate fields at each time point (mean \pm SEM of 6 independent experiments; * $P < 0.05$, ** $P < 0.01$, *** $P < 0.001$ vs MPP⁺ group; # $P < 0.05$, ### $P < 0.001$ vs MPP⁺/FeSO₄ group, ^^ $P < 0.001$ vs MPP⁺/FeSO₄/CaCl₂ group)



NTBI-dependent pathway [35]. Therefore, NTBI pathways, including divalent metal transporter 1 (DMT1) and voltage-gated Ca²⁺ channel-mediated iron transport, have attracted more attention. Previous studies have confirmed that the expression of DMT1 protein is up-regulated in the pathogenesis of PD and is involved in the uptake of iron by DA neurons in the SN [36, 37]. Other studies have shown that iron can enter neurons through LTCCs, and this is associated with the pathology and progression of neurodegenerative diseases [38, 39]. LTCCs may also provide an alternative route for iron import in neuronal cells [24]. However, there is no direct evidence for LTCC-mediated iron transport in DA neurons in the pathogenesis of PD. In this study, we found that activation or blockade of LTCCs altered the intracellular iron content in MPP⁺-treated VM neurons, which implied that LTCCs might mediate iron influx. These results indicate that LTCCs can contribute to iron accumulation in the SN. It has been shown that dihydropyridines such as nitrendipine and nimodipine block LTCC-mediated iron transport in the micromolar range [24, 40]. Indeed, we found that both 1 and 10 $\mu\text{mol/L}$ isradipine protect cells against iron-induced toxicity. Previous studies have also shown that isradipine in the nanomolar range inhibits the LTCCs in DA neurons [41, 42]. We further tested the effects of 200 nmol/L isradipine on the iron transport in MPP⁺-treated VM neurons. However, we did not find significant inhibition of iron influx by 200 nmol/L isradipine perfusion. It has been reported that 1 $\mu\text{mol/L}$ isradipine is a saturating concentration that is known to inhibit Cav1 channels, but not to disrupt the gating of other plasma membrane channels [41]. Both Cav1.2 and Cav1.3 Ca²⁺ channels are functionally expressed in DA neurons. It is still unclear which type of Ca²⁺ channel mediates iron transport in DA neurons. Further studies are needed to determine the sub-type selectivity of LTCC-mediated iron transport.

In addition, we found that the intensity of Ca²⁺ fluorescence in VM neurons was enhanced by iron stimulation, which suggested that iron promotes Ca²⁺ release and/or Ca²⁺ influx in VM neurons. It has been

reported that iron overload might delay LTCC inactivation and cause more Ca²⁺ influx in cardiomyocytes [40]. Therefore, we hypothesized that the iron-induced Ca²⁺ influx might further aggravate the iron-induced neurotoxicity in DA neurons.

Consistent with our hypothesis, we also found that the neurons reacted more to the stress of iron and Ca²⁺ co-application, which suggests that an increase in extracellular Ca²⁺ aggravates the iron-induced neurotoxicity by decreasing $\Delta\Psi\text{m}$ and aggravating intracellular oxidative stress. Ca²⁺ is an important second messenger and Ca²⁺ overload may lead to cell death. Our study focused on the effects of Ca²⁺ on iron-induced neuronal toxicity, and attempted to minimize the effect of Ca²⁺ itself on cell damage. So a relatively low Ca²⁺ concentration was chosen, based on preliminary studies. As expected, 500 $\mu\text{mol/L}$ Ca²⁺ itself did not induce significant changes in ROS, $\Delta\Psi\text{m}$, and caspase-3 activation; however, it markedly increased the iron-induced toxicity. It has been shown that iron overload increases [Ca²⁺]_i and affects the calcineurin-dependent regulation of nuclear factor in the activated T-cell signaling pathway during cardiomyopathy [43]. Recently, Lee *et al.* demonstrated that iron overload results in the elevation of [Ca²⁺]_i. Chelation of Ca²⁺ by BAPTA attenuates the mitochondrial fragmentation and neuron death induced by iron overload [26, 44]. It is known that iron homeostasis is vital for cellular metabolism and important for maintaining cellular functions. Elevated cellular iron may induce hydroxyl radical production by the Fenton reaction, which in turn leads to mitochondrial dysfunction, oxidative stress, caspase-3 activation, and ultimately apoptosis in the pathogenesis of PD. Previous studies have shown that ROS production causes the release of Ca²⁺ by activating redox-sensitive Ca²⁺ channels [45, 46]. Munoz *et al.* [47] also showed that iron overload increases intracellular ROS levels and stimulates RyR-mediated Ca²⁺ release from the endoplasmic reticulum in primary hippocampal neurons. Lee *et al.* [26] confirmed that iron overload induces Drp1 (Ser637)-dependent mitochondrial damage and neuronal death *via* Ca²⁺ signaling, including Ca²⁺/calmodulin and

Ca²⁺/calpain-calcineurin signaling. Taken together, all these studies support the concept that an interaction of iron and Ca²⁺ may aggravate the damage to neurons.

In conclusion, our studies indicate that LTCCs mediate iron influx in DA neurons. An elevation of extracellular Ca²⁺ concentration aggravates iron-induced neurotoxicity. The LTCC antagonist isradipine might protect neurons against iron-induced neurodegeneration.

Acknowledgements This work was supported by grants from the National Natural Science Foundation of China (81671249) and the Natural Science Foundation of Shandong Province, China (ZR2016CM04).

Conflict of interest The authors declare that they have no conflict of interest.

References

- Carocci A, Catalano A, Sinicropi MS, Genchi G. Oxidative stress and neurodegeneration: the involvement of iron. *Biometals* 2018, 31: 715–735.
- Chan CS, Gertler TS, Surmeier DJ. Calcium homeostasis, selective vulnerability and Parkinson's disease. *Trends Neurosci* 2009, 32: 249–256.
- Ju C, Hou L, Sun F, Zhang L, Zhang Z, Gao H, *et al.* Antioxidation and antiapoptotic effects of chondroitin sulfate on 6-Hydroxydopamine-induced injury through the up-regulation of Nrf2 and inhibition of mitochondria-mediated pathway. *Neurochem Res* 2015, 40: 1509–1519.
- Liu Q, Xu Y, Wan W, Ma Z. An unexpected improvement in spatial learning and memory ability in alpha-synuclein A53T transgenic mice. *J Neural Transm (Vienna)* 2018, 125: 203–210.
- McNaught KS, Perl DP, Brownell AL, Olanow CW. Systemic exposure to proteasome inhibitors causes a progressive model of Parkinson's disease. *Ann Neurol* 2004, 56: 149–162.
- Xue Y, Yang YT, Liu HY, Chen WF, Chen AQ, Sheng Q, *et al.* Orexin-A increases the activity of globus pallidus neurons in both normal and parkinsonian rats. *Eur J Neurosci* 2016, 44: 2247–2257.
- Berg D, Hochstrasser H. Iron metabolism in Parkinsonian syndromes. *Mov Disord* 2006, 21: 1299–1310.
- Guan X, Xu X, Zhang M. Region-specific iron measured by MRI as a biomarker for Parkinson's disease. *Neurosci Bull* 2017, 33: 561–567.
- Song N, Xie J. Iron, dopamine, and alpha-synuclein interactions in at-risk dopaminergic neurons in Parkinson's disease. *Neurosci Bull* 2018, 34: 382–384.
- Wang QM, Xu YY, Liu S, Ma ZG. Isradipine attenuates MPTP-induced dopamine neuron degeneration by inhibiting up-regulation of L-type calcium channels and iron accumulation in the substantia nigra of mice. *Oncotarget* 2017, 8: 47284–47295.
- Greminger AR, Mayer-Proschel M. Identifying the threshold of iron deficiency in the central nervous system of the rat by the auditory brainstem response. *ASN Neuro* 2015, 7.
- Hidalgo C, Nunez MT. Calcium, iron and neuronal function. *IUBMB Life* 2007, 59: 280–285.
- Gao X, Campian JL, Qian M, Sun XF, Eaton JW. Mitochondrial DNA damage in iron overload. *J Biol Chem* 2009, 284: 4767–4775.
- Horowitz MP, Greenamyre JT. Mitochondrial iron metabolism and its role in neurodegeneration. *J Alzheimers Dis* 2010, 20 Suppl 2: S551–S568.
- Kristinsson J, Snaedal J, Torsdottir G, Johannesson T. Ceruloplasmin and iron in Alzheimer's disease and Parkinson's disease: a synopsis of recent studies. *Neuropsychiatr Dis Treat* 2012, 8: 515–521.
- Martin WR, Wieler M, Gee M. Midbrain iron content in early Parkinson disease: a potential biomarker of disease status. *Neurology* 2008, 70: 1411–1417.
- Chan CS, Guzman JN, Ilijic E, Mercer JN, Rick C, Tkatch T, *et al.* 'Rejuvenation' protects neurons in mouse models of Parkinson's disease. *Nature* 2007, 447: 1081–1086.
- Ilijic E, Guzman JN, Surmeier DJ. The L-type channel antagonist isradipine is neuroprotective in a mouse model of Parkinson's disease. *Neurobiol Dis* 2011, 43: 364–371.
- Kupsch A, Gerlach M, Puppeter SC, Sautter J, Dirr A, Arnold G, *et al.* Pretreatment with nimodipine prevents MPTP-induced neurotoxicity at the nigral, but not at the striatal level in mice. *Neuroreport* 1995, 6: 621–625.
- Surmeier DJ, Guzman JN, Sanchez-Padilla J. Calcium, cellular aging, and selective neuronal vulnerability in Parkinson's disease. *Cell Calcium* 2010, 47: 175–182.
- Berger SM, Bartsch D. The role of L-type voltage-gated calcium channels Cav1.2 and Cav1.3 in normal and pathological brain function. *Cell Tissue Res* 2014, 357: 463–476.
- Lee YC, Lin CH, Wu RM, Lin JW, Chang CH, Lai MS. Antihypertensive agents and risk of Parkinson's disease: a nationwide cohort study. *PLoS One* 2014, 9: e98961.
- Oudit GY, Sun H, Trivieri MG, Koch SE, Dawood F, Ackerley C, *et al.* L-type Ca²⁺ channels provide a major pathway for iron entry into cardiomyocytes in iron-overload cardiomyopathy. *Nat Med* 2003, 9: 1187–1194.
- Gaasch JA, Geldenhuys WJ, Lockman PR, Allen DD, Van der Schyf CJ. Voltage-gated calcium channels provide an alternate route for iron uptake in neuronal cell cultures. *Neurochem Res* 2007, 32: 1686–1693.
- Ma Z, Zhou Y, Xie J. Nifedipine prevents iron accumulation and reverses iron-overload-induced dopamine neuron degeneration in the substantia nigra of rats. *Neurotox Res* 2012, 22: 274–279.
- Lee DG, Park J, Lee HS, Lee SR, Lee DS. Iron overload-induced calcium signals modulate mitochondrial fragmentation in HT-22 hippocampal neuron cells. *Toxicology* 2016, 365: 17–24.
- McNaught KS, Mytilineou C, Jnobaptiste R, Yabut J, Shashidharan P, Jennert P, *et al.* Impairment of the ubiquitin-proteasome system causes dopaminergic cell death and inclusion body formation in ventral mesencephalic cultures. *J Neurochem* 2002, 81: 301–306.
- Pardo B, Paino CL, Casarejos MJ, Mena MA. Neuronal-enriched cultures from embryonic rat ventral mesencephalon for pharmacological studies of dopamine neurons. *Brain Res Brain Res Protoc* 1997, 1: 127–132.
- Sanelli T, Ge W, Leystra-Lantz C, Strong MJ. Calcium mediated excitotoxicity in neurofilament aggregate-bearing neurons in vitro is NMDA receptor dependant. *J Neurol Sci* 2007, 256: 39–51.
- Zhang S, Wang J, Song N, Xie J, Jiang H. Up-regulation of divalent metal transporter 1 is involved in 1-methyl-4-phenylpyridinium (MPP(+))-induced apoptosis in MES23.5 cells. *Neurobiol Aging* 2009, 30: 1466–1476.
- Wetli HA, Buckett PD, Wessling-Resnick M. Small-molecule screening identifies the selanazol drug ebselen as a potent inhibitor of DMT1-mediated iron uptake. *Chem Biol* 2006, 13: 965–972.
- Jiang H, Song N, Xu H, Zhang S, Wang J, Xie J. Up-regulation of divalent metal transporter 1 in 6-hydroxydopamine intoxication is IRE/IRP dependent. *Cell Res* 2010, 20: 345–356.

33. Youdim MB, Stephenson G, Ben Shachar D. Ironing iron out in Parkinson's disease and other neurodegenerative diseases with iron chelators: a lesson from 6-hydroxydopamine and iron chelators, desferal and VK-28. *Ann N Y Acad Sci* 2004, 1012: 306–325.
34. Umbreit JN, Conrad ME, Moore EG, Latour LF. Iron absorption and cellular transport: the mobilferrin/paraferritin paradigm. *Semin Hematol* 1998, 35: 13–26.
35. Xu HM, Jiang H, Wang J, Luo B, Xie JX. Over-expressed human divalent metal transporter 1 is involved in iron accumulation in MES23.5 cells. *Neurochem Int* 2008, 52: 1044–1051.
36. Faucheux BA, Herrero MT, Villares J, Levy R, Javoy-Agid F, Obeso JA, *et al.* Autoradiographic localization and density of [¹²⁵I]ferrotransferrin binding sites in the basal ganglia of control subjects, patients with Parkinson's disease and MPTP-lesioned monkeys. *Brain Res* 1995, 691: 115–124.
37. Song N, Jiang H, Wang J, Xie JX. Divalent metal transporter 1 up-regulation is involved in the 6-hydroxydopamine-induced ferrous iron influx. *J Neurosci Res* 2007, 85: 3118–3126.
38. Bostanci MO, Bagirici F. Blocking of L-type calcium channels protects hippocampal and nigral neurons against iron neurotoxicity. The role of L-type calcium channels in iron-induced neurotoxicity. *Int J Neurosci* 2013, 123: 876–882.
39. Lockman JA, Geldenhuys WJ, Bohn KA, Desilva SF, Allen DD, Van der Schyf CJ. Differential effect of nimodipine in attenuating iron-induced toxicity in brain- and blood-brain barrier-associated cell types. *Neurochem Res* 2012, 37: 134–142.
40. Tsushima RG, Wickenden AD, Bouchard RA, Oudit GY, Liu PP, Backx PH. Modulation of iron uptake in heart by L-type Ca²⁺ channel modifiers: possible implications in iron overload. *Circ Res* 1999, 84: 1302–1309.
41. Guzman JN, Ilijic E, Yang B, Sanchez-Padilla J, Wokosin D, Galtieri D, *et al.* Systemic isradipine treatment diminishes calcium-dependent mitochondrial oxidant stress. *J Clin Invest* 2018, 128: 2266–2280.
42. Guzman JN, Sanchez-Padilla J, Chan CS, Surmeier DJ. Robust pacemaking in substantia nigra dopaminergic neurons. *J Neurosci* 2009, 29: 11011–11019.
43. Lin H, Li HF, Lian WS, Chen HH, Lan YF, Lai PF, *et al.* Thromboxane A₂ mediates iron-overload cardiomyopathy in mice through calcineurin-nuclear factor of activated T cells signaling pathway. *Circ J* 2013, 77: 2586–2595.
44. Pelizzoni I, Macco R, Morini MF, Zacchetti D, Grohovaz F, Codazzi F. Iron handling in hippocampal neurons: activity-dependent iron entry and mitochondria-mediated neurotoxicity. *Aging Cell* 2011, 10: 172–183.
45. Sanmartin CD, Paula-Lima AC, Garcia A, Barattini P, Hartel S, Nunez MT, *et al.* Ryanodine receptor-mediated Ca(2+) release underlies iron-induced mitochondrial fission and stimulates mitochondrial Ca(2+) uptake in primary hippocampal neurons. *Front Mol Neurosci* 2014, 7: 13.
46. Zima AV, Blatter LA. Redox regulation of cardiac calcium channels and transporters. *Cardiovasc Res* 2006, 71: 310–321.
47. Munoz P, Humeres A, Elgueta C, Kirkwood A, Hidalgo C, Nunez MT. Iron mediates N-methyl-D-aspartate receptor-dependent stimulation of calcium-induced pathways and hippocampal synaptic plasticity. *J Biol Chem* 2011, 286: 13382–13392.



A Familial Phenotypic and Genetic Study of Mutations in *PFN1* Associated with Amyotrophic Lateral Sclerosis

Jieshan Chi¹ · Junling Chen¹ · Yan Li¹ · Zhiheng Huang¹ · Lijuan Wang¹ · Yuhu Zhang¹

Received: 25 May 2019 / Accepted: 29 July 2019 / Published online: 4 December 2019
© Shanghai Institutes for Biological Sciences, CAS 2019

Dear Editor,

Amyotrophic lateral sclerosis (ALS) is a progressive and fatal neurodegenerative disease that prominently affects both upper and lower motor neurons. The prevalence of ALS has been estimated at 2.6–3.0 per 100,000 in Europe, 5.2 per 100,000 in the USA, and 1.9–9.9 per 100,000 in Asia [1–3]. ALS is classified as sporadic (sALS) or familial (fALS), but only 5%–10% of cases are identified as familial [4, 5]. In 1993, the first mutation associated with ALS was found in the superoxide dismutase 1 (*SOD1*) gene [6]. Since then, > 30 genes with such mutations have been reported, of which four genes *SOD1*, *FUS* (FUS RNA binding protein), *TARDBP* (TAR DNA binding protein), and *C9orf72* (C9orf72-SMCR8 complex subunit), account for 60%–70% of fALS cases and 10% of sALS cases [5]. The discovery of mutations in these genes has established a pivotal rationale for understanding the pathogenic processes and mechanisms in ALS. In particular, mitochondrial dysfunction, disruption of RNA metabolism, abnormal regulation of protein structure, and cytoskeletal defects are now considered to be the main pathways involved in the pathogenesis of ALS [5].

Electronic supplementary material The online version of this article (<https://doi.org/10.1007/s12264-019-00448-8>) contains supplementary material, which is available to authorized users.

Jieshan Chi and Junling Chen contributed equally to this work.

✉ Yuhu Zhang
yhzhangsd@126.com

¹ Department of Neurology, Guangdong Neuroscience Institute, Guangdong Provincial People's Hospital, Guangdong Academy of Medical Sciences, Guangzhou 510080, China

In 2012, mutations in the profilin 1 (*PFN1*) gene were identified in two large families with ALS by exome sequencing, and the *PFN1* gene was further identified as a causative gene by sequencing in 272 cases of fALS, with five other cases of fALS containing variants in this gene [7]. Since then, an additional 12 reports of *PFN1* screening have identified 10 cases from among 5,385 ALS cases, including fALS and sALS (Table S1). A total of seven ALS-causing mutations in the *PFN1* gene have been reported so far (Table S1) [7, 8]. Current reports show that fALS cases caused by *PFN1* mutations all have limb symptoms at the onset, while the specific clinical manifestations have not been described [7, 8].

In this study, we report for the first time fALS patients in Asia with a *PFN1* mutation. Peripheral blood samples were obtained from the affected and unaffected family members (II-2, II-7, III-3, III-5, III-12, IV-1, and IV-2). Next-generation exome sequencing was performed using the Illumina NextSeq 500 platform (Illumina, San Diego, CA) to screen the gene variations. Custom-designed Roche NimbleGen SeqCap probe libraries were used to capture all coding regions and 10 bp of the flanking intronic regions of genes. The gene detection interval included 182 causative genes and 2,851 coding regions, which contained a total of 465,264 bases (Table S2). Sanger sequencing was used to validate the identified variant in the proband's mother and other relatives for segregation analysis.

The proband (Patient 1: III-3) of the pedigree first started to experience progressive right lower extremity weakness at the age of 56. The proband's symptoms gradually worsened, and the left lower extremity was also involved, resulting in instability while walking. As the disease progressed over the next 11 months, muscle atrophy and fasciculation appeared in both lower extremities. Findings from neurological examination of the

proband and other affected family members are summarized in Table 1. Electromyographic (EMG) examination of the proband showed neurogenic damage in both lower limbs and the thoracic paraspinal muscles. No significant abnormality was found on magnetic resonance imaging (MRI) of the brain and the whole spinal cord. Cerebrospinal fluid (CSF) testing showed no abnormalities in color of the fluid, CSF pressure, the presence of white and red blood cells, protein, or glucose levels. Anti-GD1b IgM antibody was weakly positive, and the remaining human anti-ganglioside antibodies were negative.

The mother of the proband (Patient 2: II-2) was unable to stand and was wheelchair-bound from the age of 78. By 86 years of age, she could not lift her head, and had developed dysarthria within the previous few months. Clinical information on this patient was limited. Due to her stiff muscles, muscle twitching, and muscle atrophy, a neurological examination could not be performed. Patient 3 (II-7) started to experience weakness of her right lower limb, especially the distal extremity, at the age of 64. The weakness became worse, and the left lower limb was involved at the age of 66. The patient had muscle atrophy in both lower extremities with fasciculation. Patient 4 (III-12) first started to experience progressive right lower limb weakness at the age of 50. This weakness gradually worsened with muscle atrophy, and the left lower extremity was also involved two years after the onset of symptoms. The patient had complained of numbness in both lower extremities, but no sensory abnormalities were observed on neurological examination. The EMG result suggested neurogenic damage in both lower extremities, consistent with anterior horn cell damage in the L2–S2 spinal segments. No significant abnormality was found on MRI of the lumbosacral spinal cord. CSF testing showed no abnormalities and serum human anti-ganglioside antibodies were all negative.

The proband’s grandfather (I-1) had died in his 40s due to an accident, before which he was asymptomatic. The proband’s grandmother and great-grandparents were asymptomatic and died at 80–90 years of age. Patient 5 (II-5) had symptoms of lower limb weakness since the age of 63; these started on the right and then involved the left side. He was diagnosed with ALS and died in 2014 at the age of 70. Limb weakness, muscle atrophy, and stiffness were not present in family member III-5.

Next-generation sequencing analysis indicated a heterozygous c.353G > T missense mutation (p.G118V) of the *PFNI* gene in the proband (III-3) (Fig. 1B); this had been identified as a clinically significant pathogenic mutation. Sanger sequencing showed that the other symptomatic family members (II-2, II-7, III-3, and III-12) and an asymptomatic family member (IV-1) also had the p.G118V mutation of *PFNI* (Fig. S1). All the affected

Table 1 Clinical features of patients from the family with a p.G118V mutation in the *PFNI* gene

Patient	Onset site	Age	Age at onset	Muscle strength					Muscle ten- sion of LL	Deep tendon reflexes		Babinski’s sign	Cognitive impairment	Sensory abnormalities	
				RPLL	RDUL	LPLL	LPLL	LDLL		UL	LL				UL
Patient 1 (III-3)	RLL	58	56	2	1–2	3	1–2	3	1–2	5	Increased	Weakness	Weakness	–	–
Patient 2 (II-2)	Not sure	88	Not sure	NA	NA	NA	NA	NA	NA	NA	Increased	Weakness	Weakness	–	NA
Patient 3 (II-7)	RLL	68	64	4	3	5	4	5	4	5	Normal	Weakness	Weakness	–	–
Patient 4 (III-12)	RLL	53	50	4	3	5	4	5	4	5	Normal	Weakness	Briskness	±	–
Patient 5 (II-5)	RLL	Died at 70	63	NA	NA	NA	NA	NA	NA	NA	NA	Weakness	Weakness	–	NA

RLL right lower limb, RPLL right proximal lower limb, RDUL right distal upper limb, LPLL left proximal lower limb, LDLL left distal lower limb, UL upper limb, LL lower limb, NA not applicable (unknown), ±, suspicious positive; –, negative.

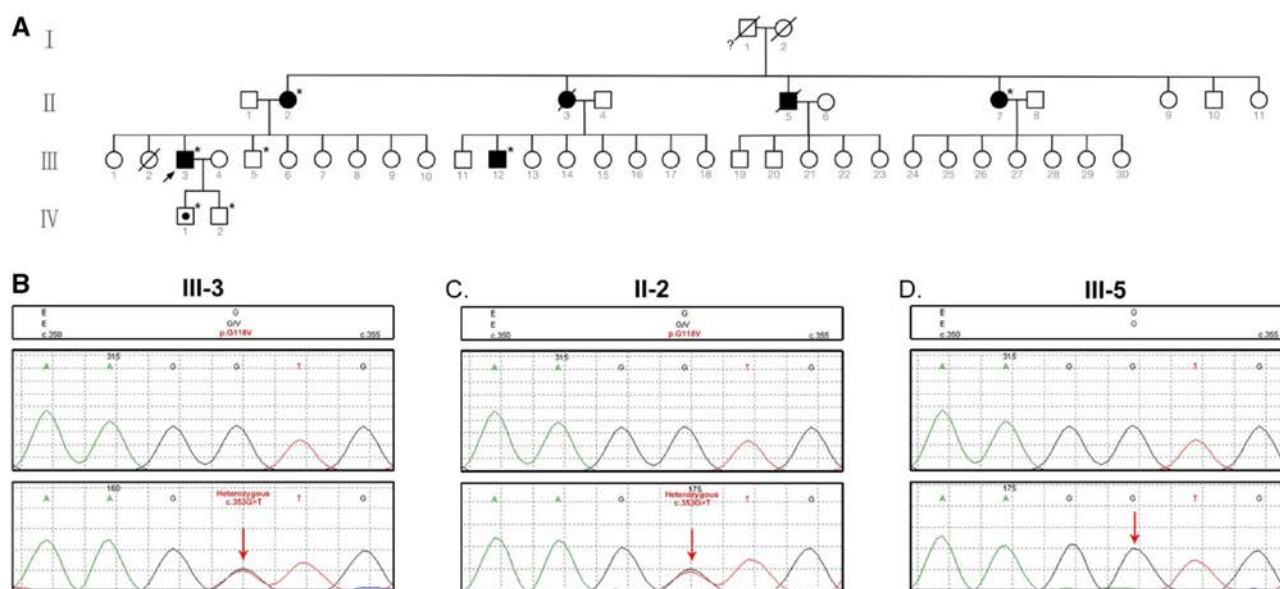


Fig. 1 The family pedigree and results of gene sequencing. **A** The family pedigree. Patient III-3 is the proband. The proband's grandfather (I-1) died in his 40s due to an accident, before which he was asymptomatic, and the question mark (?) means that it is unclear whether he was a patient or not. Family member IV-1 was

found to have the p.G118V mutation in the *PFNI* gene, but relevant clinical symptoms had not yet occurred (*genetic testing performed). **B–D** Genetic testing results for the proband (III-3), the proband's mother (II-2), and the proband's brother (III-5).

family members were older than 50 years, and the asymptomatic family member was less than 40 years old. Genetic testing of the other two asymptomatic family members, III-5 and IV-2, showed that both had negative results for the gene mutation (Fig. S1). According to the genetic results and the clinical phenotypic manifestations in the affected family members (Fig. 1A), an autosomal dominant inheritance pattern was confirmed.

In this study, we describe a missense mutation (c.353G > T, p.G118V) in the *PFNI* gene in a family with a phenotype proposed to be ALS. In 2013, a case of sALS associated with the p.R136W mutation in the *PFNI* gene was found in China [9]. However, our study is the first report of fALS in the Asian population with a mutation in the *PFNI* gene. This gene encodes the 140-amino-acid protein profilin 1, which is essential for the regulation of actin polymerization in response to extracellular signals. Mutations in the *PFNI* gene have been previously identified as a cause of ALS. Cells expressing a *PFNI* gene mutation have shown cytoskeletal defects [7] and altered stress granule dynamics [10]. Higher expression levels of TAR DNA-binding protein 43 (TDP-43), which is encoded by the *TARDBP* gene, have been reported in cells expressing ALS-associated *PFNI* mutations than in the wild-type *PFNI* [11]. The p.G118V mutation was discussed in 2012 when the *PFNI* gene was first identified to be associated with fALS [7], and was further confirmed as a pathological site rather than a benign polymorphism by examining 7,560 control samples [7]. And this variant has

not been reported in population databases, including the 1000 Genomes Project, the Database of Single Nucleotide Polymorphisms (dbSNP), and the Genome Aggregation Database (GnomAD). Cells expressing the p.G118V mutation in the *PFNI* gene have been found to contain a pathological aggregation of TDP-43 and show cytoskeletal defects that are known to be associated with motor neuron diseases [7]. Transgenic mice expressing *PFNI* with the p.G118V mutation have been shown to develop ALS-associated clinical and pathological features, including loss of upper and lower motor neurons, muscular atrophy, and reduced survival [12]. Based on *in vivo* and *in vitro* studies, there is evidence to support the hypothesis that the p.G118V missense mutation in the *PFNI* gene leads to the development of ALS.

Clinically, the proband presented with predominant lower motor neuron damage but no abnormalities in upper motor neurons in the current course of the disease. This does not meet the traditional ALS diagnostic criteria that require upper and lower motor neuron involvement and spread within a region or from one region to another (bulbar, cervical, thoracic, or lumbar). However, the 2015 revised El Escorial diagnostic criteria describe limited presenting phenotypes of ALS, including progressive bulbar palsy, flail arm syndrome and flail leg syndrome, progressive muscular atrophy, and primary lateral sclerosis [13]. These restricted phenotypes may develop into disseminated ALS or may be confirmed to carry pathogenic ALS mutations or pathological ALS changes [13].

Therefore, considering the manifestation of upper motor neuron signs in the proband's mother at a relatively late stage, based on the progressive nature of their symptoms and signs as well as the EMG results, the diagnosis of ALS was also established. It is worth noting that genetic testing and family history contribute to a diagnosis when early clinical symptoms are atypical.

In this family study, the same mutation in the *PFN1* gene resulted in similar clinical presentations and clinical features of ALS in the affected family members. First, all patients had a spinal onset that involved the lower limbs, characterized by initial asymmetric (mainly right lower extremity) and primarily distal symptoms and signs. The symptoms gradually progressed, and the involvement of both lower extremities occurred over a period of about two years. Previous studies have shown that cases of fALS with a *PFN1* gene mutation present with initial spinal rather than bulbar symptoms and signs [7, 8]. Second, at the onset, the involvement of lower motor neurons predominates, with subtle upper motor neuron signs usually emerging at a later stage. It is particularly important to emphasize the need to distinguish ALS from Charcot-Marie-Tooth disease, a hereditary peripheral motor and sensory neuropathy, at an early stage, so genetic testing plays a vital role in diagnosis. Third, dysphagia and respiratory failure are the major causes of death in ALS. In this report, bulbar symptoms were observed in the proband's mother more than eight years after onset, indicating that patients with ALS caused by *PFN1* mutations survive longer.

Finally, cognitive impairment was not observed; this is consistent with previous research in patients with ALS with a *PFN1* gene mutation [8]. It is worth noting that the anti-GD1b IgM antibody was weakly positive in the proband, highlighting the importance of awareness of the presence of related diseases. However, clinical symptoms such as sensory ataxia and ophthalmoplegia were not observed, and anti-GD1b IgM antibody was not detected in family member III-12. The early clinical symptoms and signs in the patients in this family might have included a differential diagnosis of flail leg syndrome, which is a rare restricted phenotype of ALS. However, as flail leg syndrome progresses, patients usually develop stiffness and muscle atrophy of almost the entire body, resulting in inactivity, and bulbar symptoms also inevitably occur, which is inconsistent with classic ALS.

This study had several limitations. First, the duration of follow-up was limited, and the pedigree in this type of study should be followed for an extended period to record the changing symptoms and signs of ALS associated with the *PFN1* gene mutation. Also, only one family pedigree has been identified so far. Therefore, it might be advisable to screen for *PFN1* gene mutations in patients with flail leg

syndrome or progressive muscular atrophy, and this deserves further study. More cases of fALS can be collected to explore further the pathogenic mechanisms of fALS and provide a theoretical basis for the development of improved diagnostic and therapeutic methods.

In this study, we describe the first ALS family in Asia with a *PFN1* mutant and a detailed phenotypic analysis was performed due to the specific clinical manifestations. In patients with progressive asymmetrical lower extremity weakness, muscle atrophy, and gradual involvement of other regions that occur at an older age, with or without upper motor neuron involvement, a diagnosis of ALS should be considered, and genetic testing would help to make an accurate diagnosis.

Acknowledgements We sincerely thank the patients and their families for their cooperation. This work was supported by the Key Program of the Natural Science Foundation of Guangdong Province, China (2017B030311015), Guangzhou Municipal People's Livelihood Science and Technology Project (201803010085), and the National Key R&D Program of China (2017YFC1310200).

Conflict of interest The authors declare that they have no conflict of interest.

References

- Logroscino G, Traynor BJ, Hardiman O, Chio A, Mitchell D, Swingler RJ, *et al.* Incidence of amyotrophic lateral sclerosis in Europe. *J Neurol Neurosurg Psychiatry* 2010, 81: 385–390.
- Mehta P, Kaye W, Raymond J, Punjani R, Larson T, Cohen J, *et al.* Prevalence of amyotrophic lateral sclerosis - United States, 2015. *MMWR Morb Mortal Wkly Rep* 2018, 67: 1285–1289.
- Shahzaila N, Sobue G, Kuwabara S, Kim SH, Birks C, Fan DS, *et al.* Amyotrophic lateral sclerosis and motor neuron syndromes in Asia. *J Neurol Neurosurg Psychiatry* 2016, 87: 821–830.
- Nguyen HP, Van Broeckhoven C, van der Zee J. ALS genes in the genomic era and their implications for FTD. *Trends Genet* 2018, 34: 404–423.
- Taylor JP, Brown RH, Jr., Cleveland DW. Decoding ALS: from genes to mechanism. *Nature* 2016, 539: 197–206.
- Renton AE, Chio A, Traynor BJ. State of play in amyotrophic lateral sclerosis genetics. *Nat Neurosci* 2014, 17: 17–23.
- Wu CH, Fallini C, Ticozzi N, Keagle PJ, Sapp PC, Piotrowska K, *et al.* Mutations in the profilin 1 gene cause familial amyotrophic lateral sclerosis. *Nature* 2012, 488: 499–503.
- Ingre C, Landers JE, Rizik N, Volk AE, Akimoto C, Birve A, *et al.* A novel phosphorylation site mutation in profilin 1 revealed in a large screen of US, Nordic, and German amyotrophic lateral sclerosis/frontotemporal dementia cohorts. *Neurobiol Aging* 2013, 34: 1708. e1–6.
- Chen Y, Zheng ZZ, Huang R, Chen K, Song W, Zhao B, *et al.* *PFN1* mutations are rare in Han Chinese populations with amyotrophic lateral sclerosis. *Neurobiol Aging* 2013, 34: 1922. e1–5.
- Figley MD, Bieri G, Kolaitis RM, Taylor JP, Gitler AD. Profilin 1 associates with stress granules and ALS-linked mutations alter stress granule dynamics. *J Neurosci* 2014, 34: 8083–8097.

11. Tanaka Y, Nonaka T, Suzuki G, Kametani F, Hasegawa M. Gain-of-function profilin 1 mutations linked to familial amyotrophic lateral sclerosis cause seed-dependent intracellular TDP-43 aggregation. *Hum Mol Genet* 2016, 25: 1420–1433.
12. Fil D, DeLoach A, Yadav S, Alkam D, MacNicol M, Singh A, *et al.* Mutant Profilin1 transgenic mice recapitulate cardinal features of motor neuron disease. *Hum Mol Genet* 2017, 26: 686–701.
13. Ludolph A, Drory V, Hardiman O, Nakano I, Ravits J, Robberecht W, *et al.* A revision of the El Escorial criteria - 2015. *Amyotroph Lateral Scler Frontotemporal Degener* 2015, 16: 291–292.



A *De Novo* Variant Identified in the *PPP2R1A* Gene in an Infant Induces Neurodevelopmental Abnormalities

Yanghui Zhang¹ · Haoxian Li¹ · Hua Wang¹ · Zhengjun Jia¹ · Hui Xi¹ · Xiao Mao¹

Received: 21 March 2019 / Accepted: 12 June 2019 / Published online: 17 September 2019
© Shanghai Institutes for Biological Sciences, CAS 2019

Dear Editor,

Neurodevelopmental disorders include a wide range of conditions such as epilepsy, intellectual disability, and autism spectrum disorder. These disorders commonly co-occur in patients, which suggests that they share a common etiology [1, 2]. Genetic advances resulting from sequencing techniques over the past few years have greatly expanded our understanding of neurodevelopmental disorders. Numerous specific genes have been identified in patients with neurodevelopmental disorders that have pedigrees with Mendelian inheritance [3]. However, the majority of patients with neurodevelopmental disorders of possible genetic causes remain without specific diagnoses. The clinical heterogeneity and low incidence rate of these undefined disorders present a challenge for determining genetic diagnoses. Recently, using an unbiased genotype-driven approach, the United Kingdom Deciphering Developmental Disorders project has identified a total of 12 novel genes that have been suggested to be associated with developmental disorders [4]. In particular, *de novo* pathogenic variants in *PPP2R5D* (OMIM#601646) and *PPP2R1A* (OMIM#605983) were found for the first time to be involved in phenotypically similar patients with putatively novel neurodevelopmental disorders. More recently, these findings have been further confirmed in additional patients with intellectual disabilities [5]. In the present

study, we report a *de novo* variant in the *PPP2R1A* gene as a likely pathogenic variant in an infant patient who manifested neurodevelopmental abnormalities.

The patient, a 9-month-old male, was the second child of non-consanguineous parents who had no previous family history of neurodevelopmental disorders. The infant was conceived by *in vitro* fertilization and was born by cesarean-section delivery following a full-term pregnancy. His mother and father were 24 and 27 years old, respectively. No abnormalities were noted during pregnancy. The infant had a birth weight of 3.4 kg, a head circumference of 33 cm, and a body length of 49 cm. Birth asphyxia and dysmorphism of external organs were not reported. A description of frequent milk-vomiting was recalled by his mother during times of breast-feeding. The infant was able to smile at 1 month, raise his head at 3 months, and sit at 6 months. At 6 months of age, the infant experienced his first seizure, during which he exhibited an ocular gaze in both eyes and had a clonic convulsion of the extremities for approximately 2 min. Subsequently, seizures occurred several times during hospitalization. Levetiracetam was administered and was successful at controlling subsequent seizures. A physical examination showed that the patient had a weight of 6.0 kg (< 3rd percentile), a head circumference of 42 cm (15th percentile), and a height of 65 cm (10th percentile). At 9 months of age, a neurological examination showed that he could sit with slight assistance and was capable of receiving and understanding simple instructions from adults. No other neurological abnormalities were found.

Magnetic resonance imaging revealed a reduction of brain parenchyma, widening of the cerebral sulci and fissures, enlargement of the ventricular system, and agenesis of the corpus callosum (Fig. 1A). Brainstem auditory evoked potentials suggested peripheral and central

✉ Xiao Mao
gbtechies@outlook.com

¹ National Health Commission Key Laboratory of Birth Defects Research, Prevention and Treatment, Hunan Provincial Maternal and Child Health Care Hospital, Changsha 410008, China

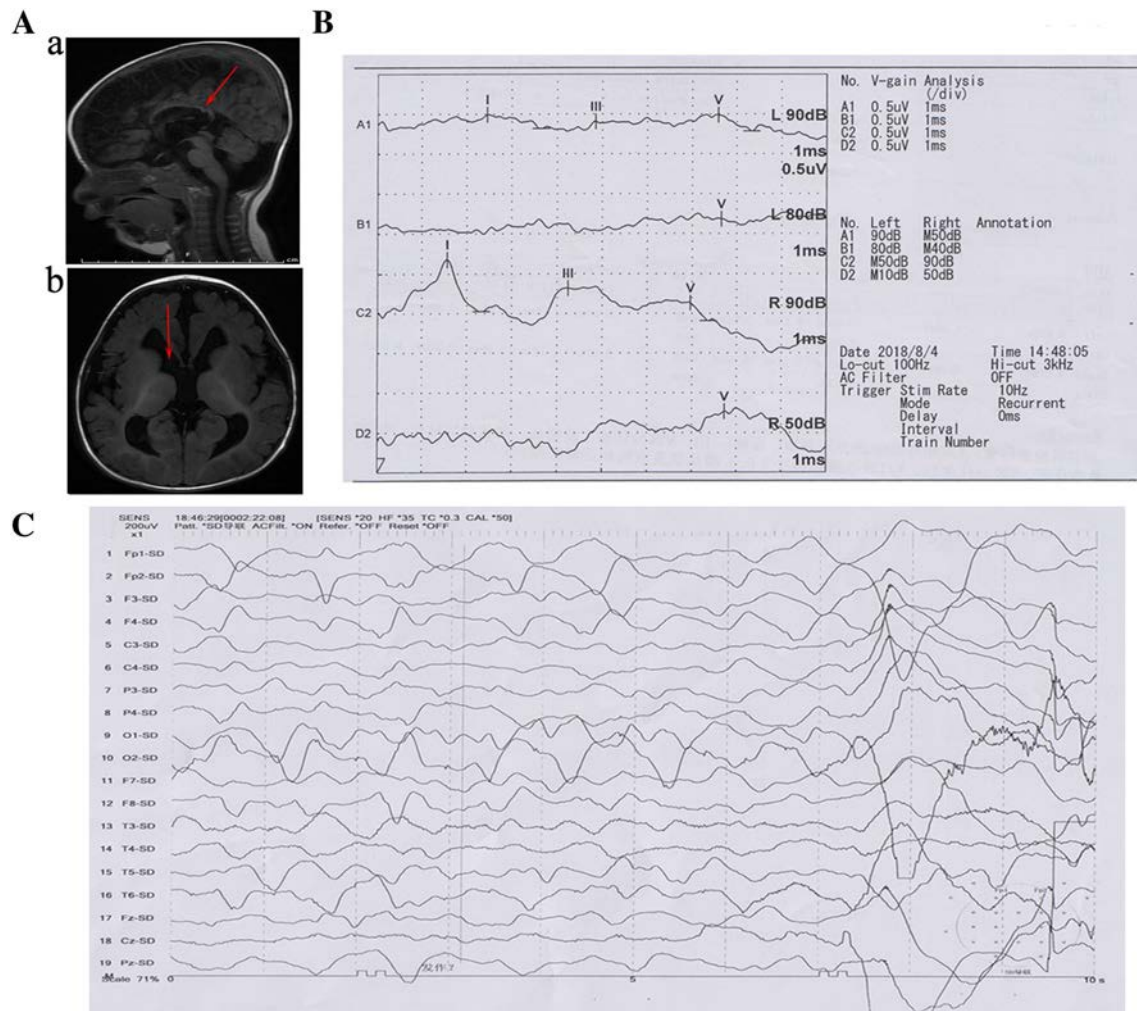


Fig. 1 Clinical and genetic data of the patient. **A** Brain MRI showing agenesis of the corpus callosum (**a**), enlargement of the ventricular system, and retardation of myelination of the white matter (**b**). **B** Brainstem auditory evoked potentials showing that the I, III, and V waves were hardly detectable and the latency to each wave was

prolonged on the left side; the waveform of the V wave was poorly differentiated with a normal range of latency to each wave on the right side; the auditory brainstem response thresholds were increased. **C** EEG demonstrating synchronous discharges of high-amplitude δ -waves spreading from the frontal lobe.

impairment of the auditory pathways and increased auditory brainstem response thresholds (Fig. 1B). Video electroencephalography (EEG) monitored a focal seizure and recorded synchronous discharges of high-amplitude δ -waves spreading from the frontal lobe to the entire brain (Fig. 1C). No abnormalities were found in laboratory tests. No other abnormalities—including dysmorphic features or complications of the heart, kidney, or liver—were found.

Karyotyping based on low-coverage genome-sequencing did not detect possible causative copy-number variants in the patient. An average sequence depth of 100 \times was achieved and > 90% of the target exome was captured at 20 \times coverage or higher for each sample *via* whole-exome sequencing (WES). Sequencing data were processed by a computational pipeline for WES data processing and analysis, following a previously-described workflow [6].

We found a *de novo* variant (chr19:52716212, NM_014225.5, c.656C>T, p.S219L) in *PPP2RIA*, a disease-associated gene previously classified as likely to be pathogenic according to the guidelines of the American College of Medical Genetics and Genomics [7]. In addition, this variant has been identified as a likely pathogenic variant in a patient with epilepsy and intellectual disability [8], which is useful information for further assessing its potential pathogenicity.

Protein phosphatase 2A (PP2A) is a heterodimeric core enzyme [9], which comprises a scaffolding subunit (A), a catalytic subunit (C), and a specific substrate-binding regulatory subunit (B) that regulates substrate specificity, cellular localization, and enzymatic activity. The scaffolding A subunit (also called PR65) and regulatory B subunit are encoded by the *PPP2RIA* and *PPP2R5D* genes,

respectively. *De novo* missense pathogenic variants of *PPP2R5D* [MRD35 (OMIM#616355)] and *PPP2R1A* [MRD36 (OMIM#616362)] have been reported to cause autosomal-dominant mental retardation [5].

Patients with MRD36 were more severely affected than patients with MRD35 in terms of mental retardation [5], which is consistent with the vital function of active PP2A holoenzymes in biogenesis. Patients with MRD36 were characterized as having severely delayed psychomotor development, agenesis of the corpus callosum, enlarged ventricles, and possible facial dysmorphism. In the present study, although our patient presented roughly normal developmental milestones in early infancy, the imaging findings of the infant's brain morphology and epileptic signatures in the EEG were in accord with the infant's reported symptoms. Furthermore, sensorineural hearing loss and delayed myelination in the white matter might be a unique feature of our patient, which suggests clinical heterogeneity among patients with *PPP2R1A* variants. The infant reported in the present study should be followed up to document any other emerging phenotypes.

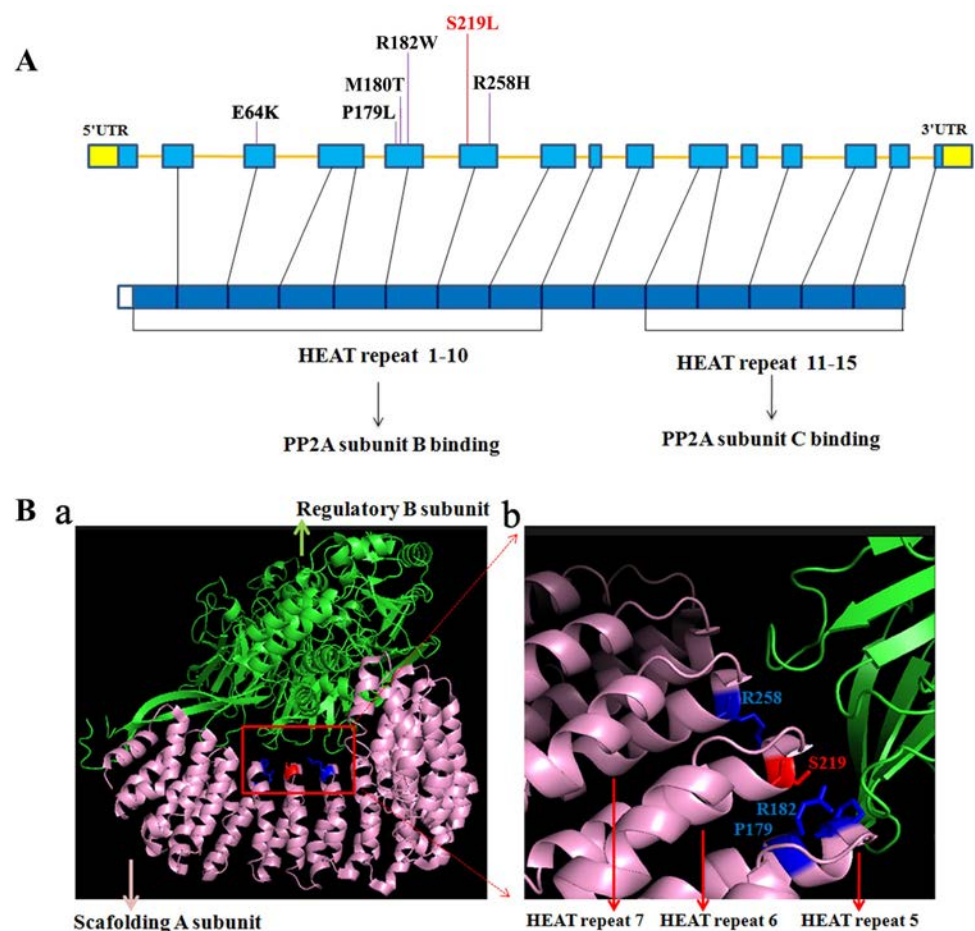
To date, only six variants in the *PPP2R1A* gene have been reported in patients with mental retardation (Fig. 2A),

and all six were *de novo* in sporadic patients. Interestingly, the reported positions—P179, R182, and R258—have also been documented as hotspots in malignancies [10]. These findings indicate that *PPP2R1A* has a high spontaneous mutation rate. Regional variant rates are subject to a variety of intrinsic characteristics and extrinsic factors [11]. Several factors (e.g., CpG sites, DNase hypersensitivity, and high GC content) may explain the high regional variant rates in this gene.

The *PPP2R1A* is composed of 15 HEAT (huntingtin, elongation factor 3, protein phosphatase 2A, and yeast kinase TOR1) repeat motifs, of which HEATs 1–8 mediate interactions with a specific regulatory B subunit [9]. The reported causative variants in previous studies are located in HEAT domains 5 and 7 of *PPP2R1A*. The variant in our present study was positioned in the sixth HEAT motif. The amino-acids of these variants are closely linked with the B subunit of the PP2A complex. Taken together, these findings suggest that these sites may be critical for interactions with other subunits and that mutants may exhibit altered interactions among subunits (Fig. 2B).

In summary, we report a novel *de novo* variant in the *PPP2R1A* gene as a likely pathogenic variant. Although

Fig. 2 Pathogenic variant of *PPP2R1A* and its protein structure. **A** The six reported variants (E64K [12], P179L [4], M180T [13], R182W [4], S219L, and R258H [5]) and their relative locations in the causative gene and its encoded protein. We report a likely pathogenic variant at S219 (red). **B** (a) Structure of *PPP2R1A* interacting with the regulatory B subunit. (b) Enlargement showing the causative amino-acids located in the center of this interaction.



rare, this *PPP2R1A* variant-induced condition should be considered in patients with unknown neurodevelopmental abnormalities, especially if such patients have agenesis of the corpus callosum. At present, a variant-driven approach to unrecognized disorders may be an effective strategy for determining the etiology of potential genetic disorders.

Acknowledgements This work was supported by the Science and Technology Department of Hunan Province, China (2017JJ3142).

Conflict of interest The authors claim no conflicts of interest.

References

1. Srivastava AK, Schwartz CE. Intellectual disability and autism spectrum disorders: causal genes and molecular mechanisms. *Neurosci Biobehav Rev* 2014, 46 Pt 2: 161–174.
2. Xu M, Ji Y, Zhang T, Jiang X, Fan Y, Geng J, *et al.* Clinical application of chromosome microarray analysis in Han Chinese children with neurodevelopmental disorders. *Neurosci Bull* 2018, 34: 981–991.
3. Vissers LE, Gilissen C, Veltman JA. Genetic studies in intellectual disability and related disorders. *Nat Rev Genet* 2016, 17: 9–18.
4. Fitzgerald TW, Gerety SS, Jones WD, Kogelenberg MV, King DA, McRae J, *et al.* Large-scale discovery of novel genetic causes of developmental disorders. *Nature* 2015, 519: 223–228.
5. Houge G, Haesen D, Vissers LE, Mehta S, Parker MJ, Wright M, *et al.* B56δ-related protein phosphatase 2A dysfunction identified in patients with intellectual disability. *J Clin Invest* 2015, 125: 3051–3062.
6. Wang JL, Cao L, Li XH, Hu ZM, Li JD, Zhang JG, *et al.* Identification of PRRT2 as the causative gene of paroxysmal kinesigenic dyskinesias. *Brain* 2011, 134: 3490–3498.
7. Richards S, Aziz N, Bale S, Bick D, Das S, Gastier-Foster J, *et al.* Standards and guidelines for the interpretation of sequence variants: a joint consensus recommendation of the American College of Medical Genetics and Genomics and the Association for Molecular Pathology. *Genet Med* 2015, 17: 405–424.
8. Hamdan FF, Myers CT, Cossette P, Lemay P, Spiegelman D, Laporte AD, *et al.* High rate of recurrent *de novo* mutations in developmental and epileptic encephalopathies. *Am J Hum Genet* 2017, 101: 664–685.
9. Cho US, Xu W. Crystal structure of a protein phosphatase 2A heterotrimeric holoenzyme. *Nature* 2007, 445: 53–57.
10. McConechy MK, Anglesio MS, Kalloger SE, Yang W, Senz J, Chow C, *et al.* Subtype-specific mutation of PPP2R1A in endometrial and ovarian carcinomas. *J Pathol* 2011, 223: 567–573.
11. Ségurel L, Wyman MJ, Przeworski M. Determinants of mutation rate variation in the human germline. *Annu Rev Genomics Hum Genet* 2014, 15: 47–70.
12. Anazi S, Maddirevula S, Salpietro V, Asi YT, Alshahli S, Alhashem A, *et al.* Expanding the genetic heterogeneity of intellectual disability. *Hum Genet* 2017, 136: 1419–1429.
13. Lelieveld SH, Wiel L, Venselaar H, Pfundt R, Vriend G, Veltman JA, *et al.* Spatial clustering of *de novo* missense mutations identifies candidate neurodevelopmental disorder-associated genes. *Am J Hum Genet* 2017, 101: 478–484.



Biomarkers for Parkinson's Disease: How Good Are They?

Tianbai Li^{1,2} · Weidong Le^{1,2}

Received: 27 July 2019 / Accepted: 17 September 2019 / Published online: 23 October 2019
© Shanghai Institutes for Biological Sciences, CAS 2019

Abstract Parkinson's disease (PD) is a complex neurodegenerative disorder with no cure in sight. Clinical challenges of the disease include the inability to make a definitive diagnosis at the early stages and difficulties in predicting the disease progression. The unmet demand to identify reliable biomarkers for early diagnosis and management of the disease course of PD has attracted a lot of attention. However, only a few reported candidate biomarkers have been tried in clinical practice at the present time. Studies on PD biomarkers have often overemphasized the discovery of novel identity, whereas efforts to further evaluate such candidates are rare. Therefore, we update the new development of biomarker discovery in PD and discuss the standard process in the evaluation and assessment of the diagnostic or prognostic value of the identified potential PD biomarkers in this review article. Recent developments in combined biomarkers and the current status of clinical trials of biomarkers as outcome measures are also discussed. We believe that the combination of different biomarkers might enhance the specificity and sensitivity over a single measure that might not be sufficient for such a multiplex disease.

Keywords Parkinson's disease · Biomarkers · Combined biomarkers · Clinical trials

✉ Weidong Le
wdle@sibs.ac.cn

¹ Center for Clinical Research on Neurological Diseases, the First Affiliated Hospital, Dalian Medical University, Dalian 116021, China

² Liaoning Provincial Key Laboratory for Research on the Pathogenic Mechanisms of Neurological Diseases, the First Affiliated Hospital, Dalian Medical University, Dalian 116021, China

Introduction

Parkinson's disease (PD) is a chronic and progressive neurodegenerative disorder that results from the loss of dopamine neurons within the substantia nigra (SN) and manifests with a broad range of motor and non-motor symptoms [1, 2]. As the second most common neurodegenerative disorder, PD affects 1% of people older than age 60, and 3% at the age of 80 years or older [3]. Although great achievements in the understanding of PD have been made during the over 200-year history of PD research [4], the diagnostic criteria for PD are still based on the identification of only motor symptoms, namely bradykinesia plus rigidity and resting tremor, which occur years after the neurodegenerative process has started [2]. Moreover, even when the new diagnostic criteria are correctly applied, the misdiagnosis rate is still high (16%–20% by movement disorder experts) due to substantial clinical overlap among parkinsonian disorders [5]. Delayed diagnosis and misdiagnosis militate against the therapeutic benefits of disease-modifying therapies. Therefore, there is an urgent need to make an effort to discover and identify reliable and accurate biomarkers for PD.

In 1998, the National Institutes of Health Biomarkers Definitions Working Group defined a biomarker as “a measurable indicator of some biological state or condition that is objectively measured and evaluated to examine normal biological processes, pathogenic processes, or pharmacologic responses to a therapeutic intervention” [6]. Biomarkers can be classified according to their functional characteristics: susceptibility risk biomarkers representing the potential for developing PD [7]; diagnostic biomarkers are used to confirm the presence of PD; and prognostic biomarkers indicating disease progression, treatment-associated changes, or disease recurrence [8].

For over 20 years, given the urgency of early diagnosis and effective disease-modifying treatments of PD, great efforts have been made to discover diagnostic and prognostic biomarkers [9]. A robust and accurate diagnostic biomarker can help recognize PD before the motor symptoms appear or when the motor or non-motor signs are inadequate to make the clinical diagnosis. It can also be used to make a differential diagnosis between PD and other neurological disorders, especially differentiating idiopathic PD from other forms of parkinsonism. It would be preferable if the biomarker could be verified in neuropathologically demonstrated cases of PD [10]. In general, biomarkers include physiological measurements, bodily fluid or tissue examinations, genetic or metabolic data, imaging measures, and even rating scales or survey measures that could represent candidate biomarkers [6].

Although various studies have been conducted in discovering potential PD biomarkers, only a few biomarkers have been translated into clinical practice [11]. PD biomarker studies have often overemphasized the discovery of novel potential biomarkers, whereas efforts to further evaluate such candidates are rare [12]. In this review, we summarize the evaluation measures of biomarkers and provide an update on the discovery of promising candidates in the diagnosis and prognosis of PD. Some recent developments on combined biomarkers and the current status of clinical trials using biomarkers as outcome measures are also discussed.

Process for the Evaluation of PD Biomarkers

Concerning the lack of a coherent pipeline connecting biomarker discovery with well-established methods for validation, it is important to establish standard protocols for the method of biomarker evaluation. Many studies on biomarkers have suggested pipelines for evaluating and validating novel biomarkers [8, 13]. In 2010, the National Academy of Sciences of America recommended a framework for the evaluation of biomarkers at the request of the Food and Drug Administration, with critical components of analytical validity, qualification, and utilization [14]. The framework provides guidelines for the previously non-uniform process in the evaluation of biomarkers.

Analytical Validation

Analytical validation can be employed to evaluate the assays and measurement performance characteristics of potential biomarkers, determining the accuracy and repeatability of biomarkers [14]. As an assessment of a

biomarker test, analytical validation includes the detection approaches and the discrimination of the biomarkers.

Establishing appropriate and standard approaches is crucial to biomarker discovery studies, which can ensure the quality and reproducibility of results, especially when comparing across multiple laboratories and clinical settings [15]. Studies of biomarker discovery usually start by establishing an accessible and confirmed PD patient cohort according to clinical diagnostic criteria with specialists. A meta-analysis of longitudinally-followed participants with autopsy-confirmed diagnoses shows that a good correlation between clinical diagnosis and neuropathological diagnosis can be established if a specialist follows international diagnostic criteria, and continues follow-up to correct any initial diagnostic error [10]. It is equally important to set up a standard sample collection process, and storage procedures for samples such as cerebrospinal fluid (CSF) and blood. In addition, harmonization of access to biobank samples streamlines the process of PD biomarker discovery [11]. Overall, standard metrics exist for all the processes from biomarker discovery to validation.

As an important evaluation index in characterizing the performance of a diagnostic biomarker, discrimination indicates the capability of a test to distinguish between disease and control, or those with and without an outcome of interest. When it comes to the discrimination of a diagnostic biomarker of PD, the ability to distinguish PD from healthy controls (HCs) is usually not enough. The inclusion of non-PD neurological disease controls (NDCs), especially parkinsonian syndrome, is critical in biomarker validation studies [11]. Sensitivity and specificity are most commonly regarded in the discrimination analysis. Here, the receiver operating curve (ROC) is a graphical plot to illustrate the diagnostic ability of a binary classifier system by plotting the true-positive rate (sensitivity) against the false-positive rate (1-specificity) at a range of cutoff points [13]. Every possible cutoff point of a test result corresponds to the resulting sensitivity and specificity. The area under the ROC curve (AUC) is the most widely used measure of testing discrimination, and can directly compare the diagnostic accuracy of biomarkers. A perfectly discriminating test would have an AUC of 1. Currently, a particular AUC value of 0.8 is considered a “good” performance of a test. Many PD biomarker studies have evaluated the performance characteristics of biomarkers with relatively small sample sizes, and these approaches may not yield clinically useful AUC characteristics. However, in some cases, a higher AUC value may not be so helpful either, since the clinician may only care about a single cutoff point selected from the curve to meet special demands, whereas the AUC refers to the entire curve.

Qualification

Qualifications can furnish available evidence on associations between biomarkers and disease states or clinical outcomes. One of the most important components in qualification is to evaluate the prognostic value of the biomarker-disease relationship [14]. Prognostic biomarkers as indicators of disease progression or treatment-associated changes that must be conducted by prospective or cohort studies, allow for causal inferences to be made since biomarkers and measurements of PD occur simultaneously [16]. Follow-up work in the prospective studies always takes years or decades, especially in PD because of its chronic course. On the contrary, cross-sectional studies enroll a population of interest and collect data on the characteristics of interest almost at the same time, but biomarkers found by cross-sectional studies cannot reveal a prognostic or predictive value [17].

When assessing the relevance for predicting future events, the calibration of biomarkers should also be considered. Calibration is used to estimate probabilities that closely correspond with the outcomes in reality. A simple way of presenting the calibration value is by plotting observed *versus* predicted results [8]. Under some circumstances, biomarkers may improve the accuracy of a test through an improvement in calibration without altering the AUC.

Utilization

Utilization is a contextual analysis of the available evidence about the risks and benefits associated with the use of biomarkers [14]. The safety and efficacy of biomarkers should be weighed against their risk of failure to determine a range of proper performance for each specific biomarker [8]. Cost-effectiveness analysis is a key tool in considering the utilization of biomarkers, and can represent the outcome probabilities and assign values to particular outcomes [8]. A great deal of research has been done on how to conduct such studies [18], although definitive estimates of costs can be made only after the measurement of clinical outcomes.

Recent Advances in PD Biomarkers

Clinical Biomarkers

It is widely accepted that before the classical motor symptoms occur, subtle motor dysfunction or non-motor symptoms may already appear. Non-motor symptoms such as rapid eye movement sleep behavior disorder (RBD), hyposmia, constipation, and mood disorders are referred to as promising biomarkers in the detection of prodromal PD [19]. RBD as the

most common and best-characterized parasomnia in PD, is assumed to be an original symptom of progressive neurodegeneration. Numerous studies have revealed that RBD can serve as an anticipatory biomarker of prodromal PD and other synucleinopathies. RBD is strongly associated with PD with a 45% risk of developing neurodegeneration at 5 years and a 76% risk at 10 years, according to a 7-year follow-up study [20]. Aiming to assess the diagnostic accuracy of the prodromal criteria introduced by the International Parkinson and Movement Disorder Society in 2015, one RBD cohort study found that 39.7% of individuals with RBD converted to PD/dementia with Lewy bodies. The prodromal criteria had 81.3% sensitivity and 67.9% specificity for conversion to PD in RBD cohorts at 4-year follow-up [21].

Data on the prevalence of olfactory dysfunction in PD range from 45% to 90% [22]. There is good evidence that most PD patients develop olfactory dysfunction 4–6 years before the motor impairment occurs [23]. However, the specificity of olfactory dysfunction is lower than RBD and motor markers [24]. This could be because olfactory dysfunction is also common in other synucleinopathies and in older adults. Combined assessment of olfactory dysfunction, motor asymmetry, and a typical finding at ultrasound (midbrain hyper-echogenicity) can improve diagnostic accuracy in early PD [25]. Since the specificity of these non-motor symptoms is generally not sufficient for the early diagnosis of PD, constructing other objective measures and auxiliary methods in combination with the results of non-motor signs would enhance the predictive value of the clinical biomarkers for PD.

Imaging Biomarkers

An increasing number of imaging tests are promising for indicating early changes in PD patients and as an independent measure of disease progression, with the character of less susceptibility to the effects of subjectivity, medication, and placebo [26]. Among the imaging studies on PD, neuroimaging of the dopamine system has received the most attention. Dopamine transporter single-photon emission computed tomography (DAT-SPECT) and fluorodopa positron emission tomography (F-DOPA PET) have been used to detect neurochemical changes in the dopamine system [27]. The majority of studies on DAT-SPECT imaging of PD patients have shown a high accuracy of diagnostic performance with a sensitivity of 79%–100% and specificity of 80%–100% [27, 28]. Various SPECT radiotracers for imaging DAT also have been used to evaluate the severity of disease and differentiate PD from other forms of parkinsonism [29]. In a 4-year clinical follow-up study, the combination of hyposmia and DAT deficit revealed by DAT-SPECT is able to identify the risk of PD onset, with a 5% reduction in DAT binding annually [30]. Similar to studies with DAT-SPECT, F-DOPA

PET imaging recognizes decreased F-DOPA uptake in the caudate and putamen of PD patients [31]. Reduced F-DOPA uptake has been reported to occur contralateral to the hypokinesia-rigidity symptoms and is correlated with its severity [quantified by the Unified Parkinson's Disease Rating Scale (UPDRS)].

Advanced magnetic resonance imaging (MRI) techniques, including several specific sequences and high field-strength scanners, have shown promise in the early diagnosis of PD and monitoring disease progression [32, 33]. Neuromelanin MRI (NM-MRI) is a novel technique that reflects the loss of neurons containing neuromelanin, and the signal intensity of the SN is greatly reduced on NM-MRI in PD patients [34]. Nigrosome-1 (N1) indicates an area of high signal intensity in the dorsal part of the SN and is visualized as a “swallow-tail” sign on high-resolution susceptibility-weighted imaging (SWI) [35]. Calloni *et al.* have assessed the loss of N1 on multiple-echo SWI of 126 PD patients, 30 with non-PD parkinsonism, and 24 HCs [36]. They found that the sensitivity and specificity of N1 in discriminating PD from controls is 96.43% and 85.00%, whereas N1 does not play a leading role in the differentiation of PD from non-PD parkinsonism, with a low level of specificity [36]. While promising, the utility of MRI in early diagnosis and monitoring the course of PD remains to be defined.

Biofluid-Based Biomarkers

α-Synuclein

Misfolded and aggregated α -synuclein is the major protein component of Lewy bodies, and is thought to be the pathological hallmark of PD [37]. Genetic mutations and post-translational modifications of the α -synuclein protein, such as phosphorylation, ubiquitination, and oxidization, participate in the process of protein misfolding [7]. Since α -synuclein is both genetically and pathologically associated with PD and can be detected in biofluids, it has become a widely-used approach in PD biomarker studies [37, 38]. Rapid progress has been made in the identification and validation of α -synuclein species as biomarkers for PD in recent years.

Studies from different laboratories on total α -synuclein in the CSF have produced consistent results with high analytical precision and inter-laboratory correlation, collectively showing that total CSF α -synuclein is significantly lower in PD patients than in HCs and patients with NDCs [38–41]. Other α -synuclein species such as oligomeric α -synuclein and phosphorylated α -synuclein have also been evaluated as potential biomarkers for PD [42–44]. However, none of these alone has a satisfactory diagnostic accuracy in distinguishing PD patients from controls [7]. A meta-analysis of data from 34

studies on total CSF, as well as oligomeric and phosphorylated α -synuclein in patients with PD, NDCs, or other forms of parkinsonism, and HCs has been reported. The results revealed that the sensitivity and specificity of total α -synuclein for distinguishing PD from controls are 0.72 and 0.65, respectively, and the sensitivity and specificity of oligomeric α -synuclein are 0.71 and 0.64 [45]. In longitudinal studies, no significant change of total α -synuclein in CSF has been found in patients with early PD and HCs over 6–24 months [46, 47]. A study assessing the combined α -synuclein species showed that the ratio of CSF oligomeric α -synuclein to total α -synuclein, together with phosphorylated α -synuclein and neurodegenerative biomarkers improves the diagnostic performance of oligomeric α -synuclein alone, with an AUC of 0.86%, sensitivity 79%, and specificity 67% [42]. For these reasons, the majority view is that a single species of CSF α -synuclein cannot be regarded as a reliable biomarker for PD, while the combination of α -synuclein species, or with other CSF biomarkers may furnish encouraging results.

α -Synuclein aggregation in the CSF has aroused great interest among researchers in recent years for its remarkable diagnostic accuracy in distinguishing PD patients from controls [48–50]. α -Synuclein seeding aggregation assays including protein-misfolding cyclic amplification and real-time quaking-induced conversion (RT-QuIC) are the main techniques for measuring pathogenic α -synuclein aggregates in biofluids [50]. An RT-QuIC assay study showed α -synuclein aggregation in the CSF of PD patients with a sensitivity of 95% and a specificity of 100% compared to HCs, while patients with Alzheimer's disease (AD), progressive supranuclear palsy, or corticobasal degeneration give negative results for α -synuclein aggregation [48]. A more recent study has detected oligomeric α -synuclein in the CSF of 105 PD patients and 79 HCs from the BioFIND cohort, a North American multicenter study of PD patients with standardized clinical and biospecimen acquisition protocols [17], by independently cross-validating two different platforms of α -synuclein seeding aggregation assays [51]. The AUC value for the diagnosis of PD vs HCs reached 0.95 with a sensitivity of 97.1% and a specificity of 92.5%. Given that these assays represent a process central to the pathogenesis of PD, and support the hypothesis that α -synuclein pathology spreads by a “prion-like” mechanism [52], α -synuclein aggregation assays in CSF may have the potential to be a surrogate for the presence of α -synuclein pathology. As for whether α -synuclein aggregation can be considered acceptable for its introduction into clinical practice as a biomarker for PD, larger cohorts of patients with pathological confirmation of PD and ongoing longitudinal assessment of prodromal individuals are needed.

α -Synuclein can be detected in blood due to its high level of expression and production by red blood cells (RBCs). Since blood is more easily accessible than CSF in

clinical circumstances, a body of studies has assessed the levels of α -synuclein species in RBC, serum, and plasma as a candidate biomarker of PD [37]. However, these studies have yielded inconsistent results for the changes in the α -synuclein level in the blood of PD patients compared to HCs [53–55]. This could be due to the easy contamination of RBC and different approaches to sample collection and determination across studies.

Extracellular Vesicles

Extracellular vesicles (EVs) are a subset of small membranous vesicles derived from the endosomes and released into biofluids by almost all kinds of tissue, including the central nervous system (CNS) [56]. They can be categorized into exosomes (50 nm–150 nm), microvesicles (100 nm–1000 nm), and apoptotic bodies (> 1000 nm) [57]. EVs harbor a cargo of proteins and nucleic acids that are likely to indicate pathogenic processes in CNS. Therefore, CNS-derived EVs may hold promise for biomarker discovery in PD.

Increasing evidence has demonstrated that EVs mediate the transfer and transport of toxic α -synuclein between cells, suggesting a pivotal mechanism underlying the spread of α -synuclein aggregates and the acceleration of pathology in PD [58]. It has been reported that exosomes derived from the CNS occur in the blood and the level of α -synuclein from CNS-derived exosomes in plasma is significantly higher in PD patients, but the performance of plasma exosomal α -synuclein is only moderate (AUC 0.654, sensitivity 70.1%, specificity 52.9%) [59]. Recent findings on α -synuclein from EVs in plasma are consistent with these results and also lack sufficient diagnostic performance [60, 61]. Apart from α -synuclein, changes in other proteins or nucleic acids such as microRNAs have also been detected [58, 62, 63]. Proteomic analysis of urinary EVs has shown that the combination of SNAP23 and calbindin attains a diagnostic performance at an AUC of 0.86 with 77% sensitivity and 85% specificity [64]. It would be worth evaluating candidate biomarkers in EVs using a larger clinical PD cohort and investigating panels of combined biomarkers in EVs to enhance the accuracy of diagnosis.

MicroRNAs

Recent studies have demonstrated that microRNAs are involved in the regulation of PD-related genes and alterations of certain microRNAs possibly relevant to either disease onset or disease progression [65, 66]. MicroRNAs have been considered as potential biomarkers for the early detection of PD as well as monitoring the progression of the pathology for their characteristics of detectability and stable expression in biofluids [67]. Altered expression levels of microRNAs in patients with

PD *versus* controls have been widely reported. A recent meta-analysis has shown hsa-miR-221-3p, hsa-miR-214-3p, and hsa-miR-29c-3p to be significantly differentially expressed in the blood of PD patients [68]. Yang and colleagues measured the level of hsa-miR-105-5p in the plasma of 319 PD patients, 305 patients with NDCs, and 273 HCs and found that it was significantly higher in PD patients than in HCs (0.163 ± 0.018 vs 0.065 ± 0.011 , $P < 0.001$), or patients with NDCs (0.163 ± 0.018 vs 0.047 ± 0.007 , $P < 0.001$). The discriminative values (AUC) in differentiating PD from HCs, essential tremor (ET), and AD are 0.768, 0.786, and 0.787, respectively [69]. A comprehensive analysis of the microRNA combinations of hsa-miR-335-5p/hsa-miR-3613-3p (95% CI, 0.87–0.94), hsa-miR-3355p/hsa-miR-6865-3p (95% CI, 0.87–0.93), and miR-335-5p/miR-3613-3p/miR-6865-3p (95% CI, 0.87–0.94) showed that they are closely related to a high degree of discriminatory accuracy (AUC 0.9–1.0) [70]. Although several microRNAs have been demonstrated to be relevant to the onset and progression of PD, and their combination could present a relatively high diagnostic accuracy for PD, more effort is needed to further evaluate the potential of microRNAs and other small molecules as candidate biomarkers before application in clinical practice.

Inflammation-Related Biomarkers

Mounting evidence supports the role of inflammation as a measurable driving force of PD pathology. Neuroinflammation is associated with abnormally activated microglia and altered levels of inflammatory mediators in the brains of PD patients. Many studies have shown that CSF and plasma levels of inflammatory cytokines, such as tumor necrosis factor (TNF)- α , interleukin (IL)-1 β , IL-4, IL-6, and IL-10 are significantly higher in PD than in HCs [71, 72]. On account of the expression levels of inflammatory cytokines that may not be specifically elevated in PD, combinations of inflammatory cytokines with other candidate biomarkers have been investigated to help the early diagnosis and detection of PD progression [73, 74]. Edison *et al.* identified a panel of inflammatory factors with α -synuclein in serum and CSF that can be measured with stable results regardless of sample collection time; they distinguish between PD and HCs with 82% sensitivity and 83% specificity, and monitor inflammation as disease progresses [74]. In addition, several T cell-mediated immunity-related proteins in the peripheral blood have been discovered and verified as potential biomarkers of PD. Lymphocyte activation gene-3 (sLAG-3), an important marker of helper T cell activity, has been shown to be a candidate novel biomarker for PD with an AUC of 0.82 (serum sLAG-3) in differentiating PD from HCs [75].

Recent investigations suggest an important role of gut-derived inflammation through the microbiota-gut-brain axis in the pathogenesis of PD [76]. Gut inflammation may interact with microbiota changes and facilitate the expression and aggregation of α -synuclein from gut to the brain *via* the vagus nerve [76, 77]. Studies have revealed differences in gut microbiota and microbiota metabolism between early-stage PD patients and controls [78]. The gut microbiome has also been shown to be associated with the severity of constipation and motor phenotype [78]. Pardo *et al.* found increased expression of the bacterial endotoxin-specific ligand TLR4, CD³⁺ T cells, and cytokines in colonic biopsies from PD patients [77]. These alterations of gut microbiota and gut inflammation-related indices may have the potential to be early diagnostic biomarkers for PD and deserve further investigation.

Combinations of Biomarkers

An increasing number of studies have revealed that a combination of biomarkers can improve the diagnostic accuracy of individual biomarkers. Combined biomarkers might be able to predict the motor progression or cognitive impairment of PD. Even though various types of biomarkers have been involved in the analysis of combined biomarkers, α -synuclein is still of the most concern (Table 1). It is recommended to use the combined novel biomarkers with existing clinical predictors rather than expecting a biomarker to simply substitute for clinical assessment. The use of biomarkers in combination should span multiple modes (for example, clinical, biochemical, and imaging-based biomarkers) to maximize their utility. And yet, very little research has been conducted to evaluate the performance of combined novel imaging or biofluid-based biomarkers with clinical assessment. The challenge is to establish a methodology to unite these biomarkers of disparate type and strength into merged criteria. Mollenhauer *et al.* have explored a panel of multi-modal progression biomarkers for PD in a longitudinal cohort [47]. After 24 months covering non-motor symptoms, cognitive function, and REM sleep behavior disorder by polysomnography, voxel-based morphometry of the brain by MRI, and CSF markers (including total α -synuclein, amyloid beta 1-42 (A β 42), total and phosphorylated tau protein, and neurofilament light chain proteins), they found that biomarkers with relative worsening included the sleep and imaging measures, whereas the cognitive measures and selected biofluid-based biomarkers were not significantly altered in PD compared to HCs [47]. A cohort study constructed a predictive model by the composition of multivariate measures including age, UPSIT (University of Pennsylvania Smell Inventory Test), RBDSQ (Rapid Eye Movement Sleep Behaviour Disorder Screening

Questionnaire), CSF A β 42, and caudate uptake on DAT imaging, and found that the five variables in combination showed the strongest associations with cognitive impairment, allowing prediction of cognitive impairment at 2 years in PD patients (0.80, 0.74–0.87; $P = 0.0003$ compared to age alone) [95]. Since none of the candidate biomarkers so far has provided an accurate and early diagnosis of such a complex disease, our vision for the future is that a combination of different kinds of biomarkers may solve this dilemma.

Conclusions

With an increasing number of novel candidate biomarkers, it is of great importance to establish a standard evaluation measure of PD biomarkers, which may help to connect the discovery to the validation of candidate biomarkers. Processes in the evaluation of PD biomarkers mainly consist of analytical validation, quality control, and utilization, in which standardization of approaches, discrimination value, follow-up work in cohort studies, calibration, and cost-effectiveness analysis should be taken into consideration.

Current biomarkers mainly focus on the symptomatic evaluation of PD, specific neuroimaging changes, and biochemical measurements of biofluids. Some of these candidate biomarkers have relatively high diagnostic performance or predictive value for PD and may have the potential to be applied in clinical practice after a standard evaluation. Biomarkers may address many of the critical issues in clinical trials, such as the selection of appropriate participants and the assessment of treatment effects. To date, biomarkers have been applied in several clinical trials for PD, and most of them are used as surrogate outcomes for investigating the biological efficacy of a treatment (Table 2). For instance, total α -synuclein has been proposed as a surrogate biomarker in assessing the efficacy of drugs targeting α -synuclein in phase 1–2 clinical trials. In spite of this, biomarkers with the function of identifying a population by confirming the clinical diagnosis are still rarely used. Therefore, to improve the diagnostic accuracy of individual biomarkers, an increasing number of studies have focused on developing panels of combined biomarkers or predictive models involving a combination of biomarkers. We believe that exploration for biomarkers will continue. Relative to looking for novel biomarkers, more effort should be made in systematically proceeding to the long process of confirming clinical validity and utility in future studies. As they are validated, more reliable biomarkers should begin to deliver on their full potential, with opportunities for clinical trials, personalized treatments, and primary or secondary prevention of PD.

Table 1 Overview of combined diagnostic and prognostic biomarkers.

Combined biomarkers	Diagnostic value	Prognostic value		Sample size	Study
		Motor progression	Cognitive impairment		
<i>Biofluid-based biomarkers</i>					
Oligomeric α -synuclein/total α -synuclein in CSF	NA	Correlation with UPDRS motor ($r = 0.41, P < 0.01$)	NA	121 early PD patients from the DATATOP cohort	Majbour <i>et al.</i> [79]
Oligomeric α -synuclein/total α -synuclein, phosphorylated α -synuclein, and phosphorylated tau in CSF	AUC 0.86, sensitivity 79%, specificity 67%	NA	NA	46 PD patients and 48 HC	Majbour <i>et al.</i> [42]
Total tau/total α -synuclein in CSF	AUC 0.83, sensitivity 70%, specificity 88% (PD vs AD)	NA	NA	78 PD patients and 20 AD patients	Førland <i>et al.</i> [80]
Phosphorylated tau/ α -synuclein and TNF- α in CSF	AUC 0.91, sensitivity 92.9%, specificity 75%	NA	NA	40 PD patients and 40 HC	Delgado-Alvarado <i>et al.</i> [81]
NFL, FABP3, and A β 42 in CSF	AUC 0.87 (NFL/A β 42)	NA	Higher NFL ($P = 0.0005$), lower A β 42 ($P = 0.00053$), and higher FABP3 ($P = 0.0037$) conferred high hazard ratios for PDD	104 PD patients and 30 HC	Bäckström <i>et al.</i> [82]
FABP3 with phosphorylated tau and total α -synuclein in CSF	AUC 0.96 (PDD vs AD)	NA	NA	54 PD, 20 PDD, and 48 AD patients	Chiasserini <i>et al.</i> [83]
Total tau, phosphorylated tau, α -synuclein, A β 42, NFL, MCP-1, and YKL-40 in CSF	AUC 0.95 (PD vs non-PD parkinsonism)	NA	NA	31 PD and 94 non-PD parkinsonism patients	Magdalinou <i>et al.</i> [84]
DJ-1, total tau and phosphorylated tau	AUC 0.92, sensitivity 82%, specificity 81% (PD vs MSA)	NA	NA	43 PD and 23 MSA patients	Herbert <i>et al.</i> [85]
Total α -synuclein, A β 42, GCase, β -hex, and cathepsin D	AUC 0.83, sensitivity 84%, specificity 75%	NA	NA	79 PD patients and 61 HCs from the BioFIND cohort	Parnetti <i>et al.</i> [86]
Serum TNF- α and CSF α -synuclein	AUC 0.75, sensitivity 82%, and specificity 83%	NA	NA	12 PD patients and 6 HCs at 11 time-points across 24 h	Eidson <i>et al.</i> [74]
IFN- γ , IL-10, and TNF- α in serum	AUC 0.87, sensitivity 83%, specificity 80%	Correlation with postural instability ($P < 0.001$)	Correlation with cognitive impairment ($P < 0.001$)	72 PD patients and 56 controls	Rathnayake <i>et al.</i> [87]
Nurr1, TNF- α , IL-1 β , IL-4, IL-6, and IL-10 in PBMCs	AUC 0.71	NA	NA	312 PD patients, 318 HCs, and 332 NDC patients	Le <i>et al.</i> [73]
MiR-19a, miR-19b, miR-24, miR-30c, miR-34b, miR-133b, and miR-205 in CSF	AUC 0.98	NA	NA	28 PD patients and 28 controls	Marques <i>et al.</i> [88]

Table 1 continued

Combined biomarkers	Diagnostic value	Prognostic value		Sample size	Study
		Motor progression	Cognitive impairment		
<i>Imaging-based biomarkers</i>					
NM-MRI and N1 imaging	AUC 0.935, sensitivity 0.85, specificity 0.92 (PD vs ET)	NA	NA	68 PD and 25 ET patients	Jin <i>et al.</i> [89]
DAT-SPECT, DTI, and sMRI	NA	Correlation with the UPDRS ($P < 0.001$)	NA	205 PD patients and 105 controls at 1-year follow-up	Lorio <i>et al.</i> [90]
NM-MRI and DAT-SPECT	AUC 0.99, sensitivity 93%, specificity 100% (PD vs non-PD parkinsonism)	NA	NA	30 PD and 19 non-PD parkinsonism patients	Matsusue <i>et al.</i> [91]
<i>Multiple models of combined biomarkers</i>					
Plasma oligomer α -synuclein and multiple ESWAN imaging markers	AUC 0.827, sensitivity 0.8, specificity 0.8	NA	NA	60 PD patients and 30 HCs	Chen <i>et al.</i> [92]
PIGD score, caudate DAT imaging, and CSF A β 42	NA	Accuracy (AUC 0.684, 95% CI 0.628–0.740) in prediction of later development of FOG	NA	393 patients with newly diagnosed PD without FOG at 4 years of follow-up	Kim <i>et al.</i> [93]
Age, CSF oligomeric/total α -synuclein, and β -glucocerebrosidase activity	AUC 0.87, sensitivity 82%, specificity 71%	NA	NA	71 PD and 45 NDC patients	Parnetti <i>et al.</i> [94]
Age, UPSIT, RBDSQ, CSF A β 42, and caudate DAT imaging	NA	Accuracy of prediction of cognitive impairment (AUC 0.8)	NA	390 PD patients at 2 years of follow-up	Schrag <i>et al.</i> [95]

PD, Parkinson's disease; HC, healthy controls; AD, Alzheimer's disease; PDD, PD dementia; ET, essential tremor; CSF, cerebrospinal fluid; AUC, area under the curve; UPDRS, Unified Parkinson's Disease Rating Scale; NA, not analyzed; DATATOP, Deprenyl and Tocopherol Antioxidative Therapy for Parkinsonism study; NFL, neurofilament light chain protein; FABP3, fatty-acid-binding protein 3; PBMCs, peripheral blood mononuclear cells; NM-MRI, neuromelanin-sensitive magnetic resonance imaging; N1, nigrosome-1; DAT-SPECT, dopamine-transporter SPECT; DTI, diffusion tensor imaging; sMRI, structural magnetic resonance imaging; ESWAN, multiple enhanced T2 star-weighted angiography; PIGD, postural instability gait difficulty; FOG, freezing of gait; UPSIT, smell identification test; RBDSQ, REM sleep behavior disorder screening questionnaire.

Table 2 Clinical trials using biomarkers as outcome measures

Study title	Biomarkers	Participants	Phase	Clinical Trials. gov identifier
The Swedish BioFINDER 2 Study	A β 42, tau, and phosphorylated tau	1505	Not applicable	NCT03174938
KM-819 for patients with PD	KM-819, oligomeric α -synuclein, total tau, phosphorylated tau	88	1	NCT03022799
Evaluation of a multimodal neuroimaging method for diagnosis in PD	Combination of biomarkers in multimodal imaging	60	1	NCT02428816
Development of a novel 18F-DTBZ PET imaging as a biomarker to monitor neurodegeneration of PARK6 and PARK8 parkinsonism	18F-DTBZ PET imaging	49	2	NCT01759888
Single ascending dose study of MEDI1341 in healthy volunteers	Total α -synuclein	40	1	NCT03272165
Effect of undenatured cysteine-rich whey protein isolate (HMS 90 [®]) in patients with PD	Plasma glutathione, urinary 8-hydroxydeoxyguanosine, and urinary total antioxidant status	38	4	NCT01662414
Florbetapir F18-PET imaging of beta-amyloid in PD patients	A β , tau, and phosphorylated tau	31	2	NCT00857532
Ambroxol in disease modification in PD	GCcase	20	2	NCT02941822
Modulation of gut microbiota by Rifaximin in PD patients	Blood biomarkers of neuroinflammation and exosomal α -synuclein	20	2	NCT03958708

BioFINDER, biomarkers for identifying neurodegenerative disorders early and reliably; KM-819, Fas-associated factor 1 inhibitor; DTBZ, dihydrotetabenazine; PET, positron emission tomography; GCcase, β -glucocerebrosidase.

Acknowledgements This review was supported by the National Natural Science Foundation of China (81430021 and 81771521) and the Key Research and Development Plan of the Science and Technology Department of Liaoning Province, China (2018225051).

References

- Dickson DW. Parkinson's disease and parkinsonism: neuropathology. *Cold Spring Harb Perspect Med* 2012, 2: a009258.
- Kalia LV, Lang AE. Parkinson's disease. *Lancet* 2015, 386: 896–912.
- Erkinen MG, Kim MO, Geschwind MD. Clinical neurology and epidemiology of the major neurodegenerative diseases. *Cold Spring Harb Perspect Biol* 2018, 10: a033118.
- Li S, Le W. Milestones of Parkinson's disease research: 200 years of history and beyond. *Neurosci Bull* 2017, 33: 598–602.
- Rizzo G, Copetti M, Arcuti S, Martino D, Fontana A, Logroscino G. Accuracy of clinical diagnosis of Parkinson disease: a systematic review and meta-analysis. *Neurology* 2016, 86: 566–576.
- Strimbu K, Tavel JA. What are biomarkers? *Curr Opin HIV AIDS* 2010, 5: 463–466.
- Parnetti L, Gaetani L, Eusebi P, Paciotti S, Hansson O, El-Agnaf O, *et al.* CSF and blood biomarkers for Parkinson's disease. *Lancet Neurol* 2019, 6: 573–586.
- Perlis R. Translating biomarkers to clinical practice. *Mol Psychiatry* 2011, 16: 1076.
- Shao Y, Le W. Recent advances and perspectives of metabolomics-based investigations in Parkinson's disease. *Mol Neurodegener* 2019, 14: 3. <https://doi.org/10.1186/s13024-018-03042>.
- Lotankar S, Prabhavalkar KS, Bhatt LK. Biomarkers for Parkinson's disease: recent advancement. *Neurosci Bull* 2017, 33: 585–597.
- Chen-Plotkin AS, Albin R, Alcalay R, Babcock D, Bajaj V, Bowman D, *et al.* Finding useful biomarkers for Parkinson's disease. *Sci Transl Med* 2018, 10: eaam6003.
- Li S, Le W. Biomarker discovery in Parkinson's disease: present challenges and future opportunities. *Neurosci Bull* 2017, 33: 481–482.
- Rifai N, Gillette MA, Carr SA. Protein biomarker discovery and validation: the long and uncertain path to clinical utility. *Nat Biotechnol* 2006, 24: 971–983.
- Ball JR, Micheel CM. Evaluation of biomarkers and surrogate endpoints in chronic disease. National Academies Press: Washington, 2010: 1–314.
- Forshed J. Experimental design in clinical 'omics biomarker discovery. *J Proteome Res* 2017, 16: 3954–3960.
- Postuma RB, Berg D. Prodromal Parkinson's disease: the decade past, the decade to come. *Mov Disord* 2019, 34: 665–675.
- Kang UJ, Goldman JG, Alcalay RN, Xie T, Tuite P, Henchcliffe C, *et al.* The BioFIND study: characteristics of a clinically typical Parkinson's disease biomarker cohort. *Mov Disord* 2016, 31: 924–932.
- Sanders GD, Maciejewski ML, Basu A. Overview of cost-effectiveness analysis. *JAMA* 2019, 14: 1400–1401.
- Fullard ME, Morley JF, Duda JE. Olfactory dysfunction as an early biomarker in Parkinson's disease. *Neurosci Bull* 2017, 33: 515–525.
- Iranzo A, Tolosa E, Gelpi E, Molinuevo JL, Valldeoriola F, Serradell M, *et al.* Neurodegenerative disease status and post-mortem pathology in idiopathic rapid-eye-movement sleep

- behaviour disorder: an observational cohort study. *Lancet Neurol* 2013, 12: 443–453.
21. Fereshtehnejad SM, Montplaisir JY, Pelletier A, Gagnon JF, Berg D, Postuma RB. Validation of the MDS research criteria for prodromal Parkinson's disease: longitudinal assessment in a REM sleep behavior disorder (RBD) cohort. *Mov Disord* 2017, 32: 865–873.
 22. Haehner A, Boesveldt S, Berendse H, Mackay-Sim A, Fleischmann J, Silburn P, *et al*. Prevalence of smell loss in Parkinson's disease—a multicenter study. *Parkinsonism Relat Disord* 2009, 15: 490–494.
 23. Reichmann H. Premotor diagnosis of Parkinson's disease. *Neurosci Bull* 2017, 33: 526–534.
 24. Le W, Dong J, Li S, Korczyn AD. Can biomarkers help the early diagnosis of Parkinson's disease? *Neurosci Bull* 2017, 33: 535–542.
 25. Poewe W, Mahlknecht P. Combined assessment of midbrain hyperechogenicity, hyposmia and motor asymmetry improves diagnostic accuracy in early Parkinson's disease. *Expert Rev Neurother* 2012, 12: 911–914.
 26. Guan X, Xu X, Zhang M. Region-specific iron measured by MRI as a biomarker for Parkinson's disease. *Neurosci Bull* 2017, 33: 85–91.
 27. Suwijn SR, van Boheemen CJ, de Haan RJ, Tissingh G, Booij J, de Bie RM. The diagnostic accuracy of dopamine transporter SPECT imaging to detect nigrostriatal cell loss in patients with Parkinson's disease or clinically uncertain parkinsonism: a systematic review. *EJNMMI Res* 2015, 5: 12. <https://doi.org/10.1186/s13550-015-0087-1>.
 28. Bajaj N, Hauser RA, Grachev ID. Clinical utility of dopamine transporter single photon emission CT (DaT-SPECT) with (123I) ioflupane in diagnosis of parkinsonian syndromes. *J Neurol Neurosurg Psychiatry* 2013, 84: 1288–1295.
 29. Ba F, Martin WW. Dopamine transporter imaging as a diagnostic tool for parkinsonism and related disorders in clinical practice. *Parkinsonism Relat Disord* 2015, 21: 87–94.
 30. Jennings D, Siderowf A, Stern M, Seibyl J, Eberly S, Oakes D, *et al*. Conversion to Parkinson disease in the PARS hyposmic and dopamine transporter–deficit prodromal cohort. *JAMA Neurol* 2017, 74: 933–940.
 31. Wing YK, Lam SP, Zhang J, Leung E, Ho CL, Chen S, *et al*. Reduced striatal dopamine transmission in REM sleep behavior disorder comorbid with depression. *Neurology* 2015, 84: 516–522.
 32. Heim B, Krismer F, De Marzi R, Seppi K. Magnetic resonance imaging for the diagnosis of Parkinson's disease. *J Neural Trans* 2017, 124: 915–964.
 33. Jonkman LE, Kenkhuis B, Geurts JJ, van de Berg WD. Post-mortem MRI and histopathology in neurologic disease: a translational approach. *Neurosci Bull* 2019, 35: 229–243.
 34. Miyoshi F, Ogawa T, Kitao SI, Kitayama M, Shinohara Y, Takasugi M, *et al*. Evaluation of Parkinson disease and Alzheimer disease with the use of neuromelanin MR imaging and 123I-metaiodobenzylguanidine scintigraphy. *AJNR Am J Neuroradiol* 2013, 34: 2113–2118.
 35. Kau T, Hametner S, Endmayr V, Deistung A, Prihoda M, Haimburger E, *et al*. Microvessels may confound the “Swallow Tail Sign” in normal aged midbrains: a postmortem 7 T SW-MRI study. *J Neuroimaging* 2019, 29: 65–69.
 36. Calloni S, Conte G, Sbaraini S, Cilia R, Contarino V, Avignone S, *et al*. Multiparametric MR imaging of Parkinsonisms at 3 Tesla: its role in the differentiation of Idiopathic Parkinson's disease versus atypical Parkinsonian disorders. *Eur J Radiol* 2018, 109: 95–100.
 37. Fayyad M, Salim S, Majbour N, Erskine D, Stoops E, Mollenhauer B, *et al*. Parkinson's disease biomarkers based on alpha-synuclein. *J Neurochem* 2019, <https://doi.org/10.1111/jnc.14809>.
 38. Hong Z, Shi M, Chung KA, Quinn JF, Peskind ER, Galasko D, *et al*. DJ-1 and α -synuclein in human cerebrospinal fluid as biomarkers of Parkinson's disease. *Brain* 2010, 133: 713–726.
 39. Zhou B, Wen M, Yu WF, Zhang CL, Jiao L. The diagnostic and differential diagnosis utility of cerebrospinal fluid α -synuclein levels in Parkinson's disease: a meta-analysis. *Parkinsons Dis* 2015, 2015: 567386.
 40. Mollenhauer B, Trautmann E, Taylor P, Manninger P, Sixel-Döring F, Ebentheuer J, *et al*. Total CSF α -synuclein is lower in de novo Parkinson patients than in healthy subjects. *Neurosci Lett* 2013, 532: 44–48.
 41. Mollenhauer B, Locascio JJ, Schulz-Schaeffer W, Sixel-Döring F, Trenkwalder C, Schlossmacher MG. α -Synuclein and tau concentrations in cerebrospinal fluid of patients presenting with parkinsonism: a cohort study. *Lancet Neurol* 2011, 10: 230–240.
 42. Majbour NK, Vaikath NN, van Dijk KD, Ardah MT, Varghese S, Vesterager LB, *et al*. Oligomeric and phosphorylated alpha-synuclein as potential CSF biomarkers for Parkinson's disease. *Mol Neurodegener* 2016, 11: 7. <https://doi.org/10.1186/s13024-016-0072-9>
 43. Conway KA, Lee SJ, Rochet JC, Ding TT, Williamson RE, Lansbury PT. Acceleration of oligomerization, not fibrillization, is a shared property of both α -synuclein mutations linked to early-onset Parkinson's disease: implications for pathogenesis and therapy. *Proc Natl Acad Sci U S A* 2000, 97: 571–576.
 44. Parnetti L, Farotti L, Eusebi P, Chiasserini D, De Carlo C, Giannandrea D, *et al*. Differential role of CSF alpha-synuclein species, tau, and A β 42 in Parkinson's disease. *Front Aging Neurosci* 2014, 6: 53. <https://doi.org/10.3389/fnagi.2014.00053>.
 45. Eusebi P, Giannandrea D, Biscetti L, Abraha I, Chiasserini D, Orso M, *et al*. Diagnostic utility of cerebrospinal fluid α -synuclein in Parkinson's disease: a systematic review and meta-analysis. *Mov Disord* 2017, 32: 1389–1400.
 46. Mollenhauer B, Caspell-Garcia CJ, Coffey CS, Taylor P, Shaw LM, Trojanowski JQ, *et al*. Longitudinal CSF biomarkers in patients with early Parkinson disease and healthy controls. *Neurology* 2017, 89: 1959–1969.
 47. Mollenhauer B, Zimmermann J, Sixel-Döring F, Focke NK, Wicke T, Ebentheuer J, *et al*. Monitoring of 30 marker candidates in early Parkinson disease as progression markers. *Neurology* 2016, 87: 168–177.
 48. Fairfoul G, McGuire LI, Pal S, Ironside JW, Neumann J, Christie S, *et al*. Alpha-synuclein RT-Qu IC in the CSF of patients with alpha-synucleinopathies. *Ann Clin Transl Neurol* 2016, 3: 812–818.
 49. Shah Nawaz M, Tokuda T, Waragai M, Mendez N, Ishii R, Trenkwalder C, *et al*. Development of a biochemical diagnosis of Parkinson disease by detection of α -synuclein misfolded aggregates in cerebrospinal fluid. *JAMA Neurol* 2017, 74: 163–172.
 50. Paciotti S, Bellomo G, Gatticchi L, Parnetti L. Are we ready for detecting α -synuclein prone to aggregation in patients? The case of “protein-misfolding cyclic amplification” and “real-time quaking-induced conversion” as diagnostic tools. *Front Neurol* 2018, 9: 415. <https://doi.org/10.3389/fneur.2018.00415>.
 51. Kang UJ, Boehme AK, Fairfoul G, Shah Nawaz M, Ma TC, Hutten SJ, *et al*. Comparative study of cerebrospinal fluid α -synuclein seeding aggregation assays for diagnosis of Parkinson's disease. *Mov Disord* 2019, 34: 536–544.
 52. Olanow CW, Brundin P. Parkinson's disease and alpha synuclein: is Parkinson's disease a prion-like disorder? *Mov Disord* 2013, 28: 31–40.

53. Lin CH, Yang SY, Horng HE, Yang CC, Chieh JJ, Chen HH, *et al.* Plasma α -synuclein predicts cognitive decline in Parkinson's disease. *J Neurol Neurosurg Psychiatry* 2017, 88: 818–824.
54. Lee P, Lee G, Park H, Bang O, Joo I, Huh K. The plasma alpha-synuclein levels in patients with Parkinson's disease and multiple system atrophy. *J Neural Transm* 2006, 113: 1435–1439.
55. Li QX, San Mok S, Laughton KM, McLean CA, Cappai R, Masters CL, *et al.* Plasma α -synuclein is decreased in subjects with Parkinson's disease. *Exp Neurol* 2007, 204: 583–588.
56. Shi M, Sheng L, Stewart T, Zabetian CP, Zhang J. New windows into the brain: Central nervous system-derived extracellular vesicles in blood. *Prog Neurobiol* 2019, 175: 96–106.
57. Croese T, Furlan R. Extracellular vesicles in neurodegenerative diseases. *Mol Aspects Med* 2018, 60: 52–61.
58. Vella L, Hill A, Cheng L. Focus on extracellular vesicles: exosomes and their role in protein trafficking and biomarker potential in Alzheimer's and Parkinson's disease. *Int J Mol Sci* 2016, 17: 173. <https://doi.org/10.3390/ijms17020173>.
59. Shi M, Liu C, Cook TJ, Bullock KM, Zhao Y, Ghingina C, *et al.* Plasma exosomal α -synuclein is likely CNS-derived and increased in Parkinson's disease. *Acta Neuropathol* 2014, 128: 639–650.
60. Cerri S, Ghezzi C, Sampieri M, Siani F, Avenali M, Dornini G, *et al.* The exosomal/total α -synuclein ratio in plasma is associated with glucocerebrosidase activity and correlates with measures of disease severity in PD patients. *Front Cell Neurosci* 2018, 12: 125. <https://doi.org/10.3389/fncel.2018.00125>.
61. Si X, Tian J, Chen Y, Yan Y, Pu J, Zhang B. Central nervous system-derived exosomal alpha-synuclein in serum may be a biomarker in Parkinson's disease. *Neuroscience* 2019; 413: 308–316.
62. Zhao ZH, Chen ZT, Zhou RL, Zhang X, Ye QY, Wang YZ. Increased DJ-1 and α -synuclein in plasma neural-derived exosomes as potential markers for Parkinson's disease. *Front Aging Neurosci* 2018, 10: 438. <https://doi.org/10.3389/fnagi.2018.00438>
63. Fraser KB, Rawlins AB, Clark RG, Alcalay RN, Standaert DG, Liu N, *et al.* Ser (P)-1292 LRRK2 in urinary exosomes is elevated in idiopathic Parkinson's disease. *Mov Disord* 2016, 31: 1543–1550.
64. Wang S, Kojima K, Mobley JA, West AB. Proteomic analysis of urinary extracellular vesicles reveal biomarkers for neurologic disease. *EBioMedicine* 2019, 45:351–361.
65. Leggio L, Vivarelli S, L'Episcopo F, Tirolo C, Caniglia S, Testa N, *et al.* MicroRNAs in Parkinson's disease: from pathogenesis to novel diagnostic and therapeutic approaches. *Int J Mol Sci* 2017, 18: 2698. <https://doi.org/10.3390/ijms18122698>.
66. Le W, Yang Z, Li T, Li S, Wei M, Qi H, *et al.* Altered expression levels of microRNA-132 and Nurr1 in peripheral blood of Parkinson's disease: potential disease biomarkers. *ACS Chem Neurosci* 2019, 10: 2243–2249.
67. Wang Y, Yang Z, Le W. Tiny but mighty: promising roles of MicroRNAs in the diagnosis and treatment of parkinson's disease. *Neurosci Bull* 2017, 33: 543–551.
68. Schulz J, Takousis P, Wohlers I, Itua IO, Dobricic V, Ruecker G, *et al.* Meta-analyses identify differentially expressed microRNAs in Parkinson's disease. *Ann Neurol* 2019, 85: 835–851.
69. Le W, Yang Z, Li T, Cui Y, Li S, Cheng C, *et al.* Elevated plasma microRNA-105-5p level in patients with idiopathic Parkinson's disease: a potential disease biomarker. *Front Neurosci* 2019, 13: 218. <https://doi.org/10.3389/fnins.2019.00218>.
70. Patil KS, Basak I, Dalen I, Hoedt E, Lange J, Lunde KA, *et al.* Combinatory microRNA serum signatures as classifiers of Parkinson's disease. *Parkinsonism Relat Disord* 2019, 64: 202–210.
71. Le W, Rowe DB, Jankovic J, Xie W, Appel SH. Effects of cerebrospinal fluid from patients with Parkinson disease on dopaminergic cells. *Arch Neurol* 1999, 56:194–200.
72. Reale M, Iarlori C, Thomas A, Gambi D, Perfetti B, Di Nicola M, Onofrij M. Peripheral cytokines profile in Parkinson's disease. *Brain Behav Immun* 2009, 231: 55–63.
73. Le W, Li T, Yang Z, Li S, Shen B. Alterations of NURR1 and cytokines in the peripheral blood mononuclear cells: combined biomarkers for Parkinson's disease. *Front Aging Neurosci* 2018, 10: 392. <https://doi.org/10.3389/fnagi.2018.00392>.
74. Eidson LN, Kannarkat GT, Barnum CJ, Chang J, Chung J, Yen M. Candidate inflammatory biomarkers display unique relationships with alpha-synuclein and correlate with measures of disease severity in subjects with Parkinson's disease. *J Neuroinflammation* 2017, 14:164. <https://doi.org/10.1186/s12974-017-0935-1>.
75. Wang G, Chen S, Cui SS, Du JJ, Liu SH, Meng J, *et al.* Serum soluble lymphocyte activation gene-3 as a diagnostic biomarker in Parkinson's disease: A pilot multicenter study. *Mov Disord* 2019, 34:138–141.
76. Nair AT, Ramachandran V, Joghee NM, Antony S, Ramalingam G. Gut microbiota dysfunction as reliable non-invasive early diagnostic biomarkers in the pathophysiology of Parkinson's disease: a critical review. *J Neurogastroenterol Motil* 2018, 24: 30–42.
77. Perez-Pardo P, Dodiya HB, Engen PA, Forsyth CB, Huschens AM, Shannon KM, *et al.* Role of TLR4 in the gut-brain axis in Parkinson's disease: a translational study from men to mice. *Gut* 2019, 68: 829–843.
78. Scheperjans F, Aho V, Pereira PA, Koskinen K, Paulin L, Kinnunen E, *et al.* Gut microbiota are related to Parkinson's disease and clinical phenotype. *Mov Disord* 2015, 30: 350–358.
79. Majbour NK, Vaikath NN, Eusebi P, Chiasserini D, Ardah M, Varghese S, *et al.* Longitudinal changes in CSF alpha-synuclein species reflect Parkinson's disease progression. *Mov Disord* 2016, 31: 1535–1542.
80. Förlund MG, Tysnes OB, Aarsland D, Maple-Grødem J, Pedersen KF, Alves G, *et al.* The value of cerebrospinal fluid α -synuclein and the tau/ α -synuclein ratio for diagnosis of neurodegenerative disorders with Lewy pathology. *Eur J Neurol* 2019, <https://doi.org/10.1111/ene.14032>.
81. Delgado-Alvarado M, Gago B, Gorostidi A, Jiménez-Urbietta H, Dacosta-Aguayo R, Navalpotro-Gómez I, *et al.* Tau/ α -synuclein ratio and inflammatory proteins in Parkinson's disease: An exploratory study. *Mov Disord* 2017, 32: 1066–1073.
82. Bäckström DC, Domellöf ME, Linder J, Olsson B, Öhrfelt A, Trupp M, *et al.* Cerebrospinal fluid patterns and the risk of future dementia in early, incident Parkinson disease. *JAMA Neurol* 2015, 72: 1175–1182.
83. Chiasserini D, Biscetti L, Eusebi P, Salvadori N, Frattini G, Simoni S, *et al.* Differential role of CSF fatty acid binding protein 3, α -synuclein, and Alzheimer's disease core biomarkers in Lewy body disorders and Alzheimer's dementia. *Alzheimers Res Ther* 2017, 9: 52. <https://doi.org/10.1186/s13195-017-0276-4>.
84. Magdalino N, Paterson R, Schott J, Fox N, Mummery C, Blennow K, *et al.* A panel of nine cerebrospinal fluid biomarkers may identify patients with atypical parkinsonian syndromes. *J Neurol Neurosurg Psychiatry* 2015, 86: 1240–1247.
85. Herbert MK, Eeftens JM, Aerts MB, Esselink RA, Bloem BR, Kuiperij HB, *et al.* CSF levels of DJ-1 and tau distinguish MSA patients from PD patients and controls. *Parkinsonism Relat Disord* 2014, 20: 112–115.
86. Parnetti L, Paciotti S, Eusebi P, Dardis A, Zampieri S, Chiasserini D, *et al.* Cerebrospinal fluid β -glucocerebrosidase activity is reduced in parkinson's disease patients. *Mov Disord* 2017, 32: 1423–1431.

87. Rathnayake D, Chang T, Udagama P. Selected serum cytokines and nitric oxide as potential multi-marker biosignature panels for Parkinson disease of varying durations: a case-control study. *BMC Neurol* 2019, 19: 56. <https://doi.org/10.1186/s12883-019-1286-6>.
88. Marques TM, Kuiperij HB, Bruinsma IB, van Rumund A, Aerts MB, Esselink RA, *et al.* MicroRNAs in cerebrospinal fluid as potential biomarkers for Parkinson's disease and multiple system atrophy. *Mol Neurobiol* 2017, 54: 7736–7745.
89. Jin L, Wang J, Wang C, Zhang Y, Lv M, Zhou Y, *et al.* Combined visualization of nigrosome-1 and neuromelanin in the substantia nigra using 3T MRI for the differential diagnosis of essential tremor and de novo Parkinson's disease. *Front Neurol* 2019, 10: 100. <https://doi.org/10.3389/fneur.2019.00100>.
90. Lorio S, Sambataro F, Bertolino A, Draganski B, Dukart J. The combination of DAT-SPECT, structural and diffusion MRI predicts clinical progression in Parkinson's disease. *Front Aging Neurosci* 2019, 11. <https://doi.org/10.3389/fnagi.2019.00057>.
91. Matsusue E, Fujihara Y, Tanaka K, Aozasa Y, Shimoda M, Nakayasu H, *et al.* The utility of the combined use of 123I-FP-CIT SPECT and neuromelanin MRI in differentiating Parkinson's disease from other parkinsonian syndromes. *Acta Radiol* 2019, 60: 230–238.
92. Chen XQ, Niu JP, Peng RQ, Song YH, Xu N, Zhang YW. The early diagnosis of Parkinson's disease through combined biomarkers. *Acta Neurol Scand* 2019, 4:268–273.
93. Kim R, Lee J, Kim HJ, Kim A, Jang M, Jeon B, *et al.* CSF β -amyloid42 and risk of freezing of gait in early Parkinson disease. *Neurology* 2019, 92: e40–e47.
94. Parnetti L, Chiasserini D, Persichetti E, Eusebi P, Varghese S, Qureshi MM, *et al.* Cerebrospinal fluid lysosomal enzymes and alpha-synuclein in Parkinson's disease. *Mov Disord* 2014, 29: 1019–1027.
95. Schrag A, Siddiqui UF, Anastasiou Z, Weintraub D, Schott JM. Clinical variables and biomarkers in prediction of cognitive impairment in patients with newly diagnosed Parkinson's disease: a cohort study. *Lancet Neurol* 2017, 16: 66–75.



RESEARCH HIGHLIGHT

Early Intervention in Alzheimer's Disease: How Early is Early Enough?

Dong-Yu Fan^{1,2} · Yan-Jiang Wang^{1,2}

Received: 20 June 2019 / Accepted: 3 July 2019 / Published online: 7 September 2019
© Shanghai Institutes for Biological Sciences, CAS 2019

In 1906, Dr. Alois Alzheimer reported a case of dementia and thought it was a new type of disease. Later, Dr. Emil Kraepelin named it Alzheimer's disease (AD). One hundred years later, AD has become the most common type of dementia affecting the elderly population and a heavy health burden. However, the pathogenesis of the disease remains unclear, and no disease-modifying therapies are available to prevent, halt, or even slow the progression of the disease [1].

Dr. Alzheimer first observed the presence of intracellular neurofibrillary tangles and extracellular plaques in the brain of the first AD patient. The plaques were identified as being composed of the fibrous β -amyloid peptide ($A\beta$) [2] and named senile plaques, which are considered to be the only specific pathological hallmark of AD. The pathology of senile plaques has become the gold standard for diagnosing AD. Accordingly, the amyloid cascade hypothesis, in which $A\beta$ accumulates in the brain and drives neurodegeneration and cognitive impairment, was proposed to explain the pathogenesis of AD [3]. A large body of evidence indicates that $A\beta$ accumulation in the brain due to $A\beta$ overproduction and/or clearance disorders is the cause of AD, so $A\beta$ -lowering is considered to be the most promising therapeutic strategy. At present, drug research for AD is mainly focused on two approaches: one is to reduce $A\beta$ production by inhibiting key enzymes, including

beta-site amyloid precursor protein (APP) cleaving enzyme 1 (BACE1) and gamma-secretase, which cleave the APP to generate $A\beta$, and the other is to clear $A\beta$ from the brain with various antibodies against $A\beta$.

During the past two decades, several enzyme inhibitors and antibodies have been tested in patients with mild-to-moderate AD [4]. Unfortunately, none of them had therapeutic effects. From these failures, a consensus was reached that the mild-to-moderate stage of dementia is too late for the drug to reverse or halt the progression of the disease. In this regard, new criteria were proposed (National Institute on Aging/Alzheimer's Association 2011) to achieve early diagnosis allowing early intervention. In addition, much hope has been placed on interventions for patients who are at prodromal and preclinical stages.

Unfortunately, two phase III clinical trials with prodromal or preclinical patients have recently been declared to fail. The tested drugs were verubecestat [5] and atabecestat [6], both of which are BACE1 inhibitors that were expected to reduce $A\beta$ generation at the early stage of AD. Egan *et al.* presented the results of a phase III trial in AD patients at the prodromal stage using verubecestat for 104 weeks [5]. The results were unexpected: although the levels of both amyloid deposition in the brain and $A\beta$ in the cerebrospinal fluid decreased, cognitive function and the results of structural brain imaging became worse with verubecestat than with placebo. Henley *et al.* reported the preliminary results of a trial using atabecestat in patients in the preclinical stage of AD who were cognitively unimpaired with an elevated deposition of amyloid in the brain [6]. That is, the patients were at an even earlier stage than prodromal AD. However, patients taking the drug had worse cognitive function than those taking the placebo. These two studies were the first wave of attempts at

✉ Yan-Jiang Wang
yanjiang_wang@tmmu.edu.cn

¹ Department of Neurology and Center for Clinical Neuroscience, Daping Hospital, Third Military Medical University, Chongqing 400042, China

² Chongqing Key Laboratory of Aging and Brain Diseases, Chongqing 400042, China

intervention at an early stage of the disease, but the results were disappointing.

The reasons for the failure of these two early intervention trials need to be addressed. This may have been because the medication was not administered early enough, and if so, how early is early enough to achieve therapeutic benefits? We believe that these two trials did not provide a clear answer to the question of whether early intervention is effective. The main reason is that the intervention in these trials was not actually early. Here, we must distinguish between the concepts of the early phase of biology and the early phase of clinical manifestations. The accumulation of A β begins 15–20 years before the onset of dementia and reaches a plateau in the prodromal stage, and there is a long period of time with the activation of secondary pathological events that forms its own vicious circle. Therefore, when patients have prodromal clinical manifestations, they are actually in the decompensation phase, that is, in the advanced stages of the disease. Even in the preclinical phase with evident brain A β deposition, the pathophysiological mechanisms have already been initiated, and they become complicated, making it difficult to achieve therapeutic effects by solely interfering with A β at this stage. Therefore, the period in which the intervention can be truly effective may be earlier, that is, the initial stage of brain A β accumulation without activation of secondary pathological events such as tau hyperphosphorylation and neuroinflammation. This requires more effective methods of early detection, the identification of high-risk individuals earlier, and the use of drugs to prevent A β production and accumulation from the very beginning of the disease.

Another striking result of these two trials was that the use of BACE1 inhibitors caused a decline in cognitive function in the preclinical and prodromal patients, while not having this effect in mild-to-moderate AD patients in previous clinical trials. This was exactly the opposite of what was expected. The researchers were unsure why BACE1 inhibitors would cause more harm earlier than later in the disease. Our view is that the deterioration of cognition was not caused by the decrease in A β but by the side-effects of BACE1 inhibition. It may be that the adverse effects of the BACE1 inhibitors masked their protective effects. Current research shows that BACE1 has a particular physiological function in addition to being responsible for the proteolytic processing of APP. BACE1 is required for myelination and the correct bundling of axons by Schwann cells and is thus directly involved in myelination of the peripheral nervous system during early postnatal development [7]. Several animal experiments have shown that BACE1-knockout mice exhibit a variety of abnormal physiological conditions, such as decreased myelination of neurons, spontaneous epilepsy and an

abnormal EEG, memory function defects, axonal growth abnormalities, and other abnormal phenotypes. Therefore, when the dose of the inhibitor is high, the physiological function of BACE1 is severely inhibited, which can mask its protective effects.

On the one hand, as discussed in Egan's report, it is possible that BACE1 inhibitors have a greater effect on relatively normal synaptic function in prodromal patients, so they may be more sensitive to the effects of substantial BACE1 inhibition [5]. This is consistent with the animal experiments noted above, so researchers believe that lowering the dose of BACE1 inhibitors may reduce the adverse effects while inhibiting A β generation. In addition, suppressing BACE1 has been reported to promote an alternate cleavage pathway, in which η -secretase snips APP to create a synaptotoxic A η fragment [8], and it has been suggested that inhibition of BACE1 leads to the accumulation of this fragment, which damages the synapses, so it could be that inhibiting the cleavage of APP itself causes problems. The third reason may be the inhibition of BACE2, as most existing inhibitors act on both BACE1 and BACE2. BACE2 levels are usually low in the brain, and BACE2 is thought to be unrelated to amyloid pathogenesis and therefore unlikely to be the culprit. However, current research has revealed little about BACE2 function, and this possibility should not be ruled out.

A safer method is needed to reduce the adverse effects. It may be a better choice to reduce the dose of BACE1. The rate of A β deposition in the brain is 30 ng/h, accounting for 5% of the total normal A β production (580 ng/h) [9]. Therefore, a first approximation would be that a 5%–10% lowering of production over the 20-year window would abrogate the effect of this degree of clearance failure. Higher levels of inhibition would be required over shorter time intervals closer to the onset of prodromal AD. The other direction is to develop more precise drugs that specifically target A β generation by BACE1.

Given the fact that none of the anti-A β clinical trials has succeeded so far, an important concern is whether A β is the cause of AD or whether it is a suitable therapeutic target. Mounting evidence from human studies supports causative or pivotal roles of A β in AD pathogenesis, such as: (1) overproduction of A β in the brain due to mutations of APP or presenilin genes, and an additional copy of the APP gene in Down syndrome clearly causes AD [10]; (2) reduction of A β generation due to a mutation of the APP gene, which inhibits the cleavage of APP by BACE1, significantly reduces AD occurrence in the Icelandic population [11]; and (3) increase of A β in the brain precedes other AD abnormalities including tau hyperphosphorylation, brain atrophy, and cognitive decline in longitudinal studies [12]. Several reasons can explain the failures of current A β -targeting trials, including the possibility that interventions

are given too late, a low capacity for A β reduction, and the adverse effects of tested drugs. Therefore, the failure of the above clinical trials cannot be used as evidence to deny the A β -lowering strategy, and this is not the time to abandon A β cascade hypothesis.

In future studies, lowering A β remains the cornerstone of AD prevention and treatment. We need more accurate early diagnostic methods to identify patients at the early biological stage of the disease for early intervention. Moreover, the future direction of AD interventions should aim at tertiary prevention strategies [13]. At the early stage of the disease, an A β -lowering intervention alone may have a preventive effect; after neurodegenerative and other pathological events have been initiated, comprehensive interventions are required.

Acknowledgements This highlight was supported by the National Natural Science Foundation of China (91749206 and 81625007).

Conflict of interest The authors declare that they have no conflict of interests.

References

1. Sun BL, Li WW, Zhu C, Jin WS, Zeng F, Liu YH, *et al.* Clinical research on Alzheimer's disease: progress and perspectives. *Neurosci Bull* 2018, 34: 1111–1118.
2. Masters CL, Simms G, Weinman NA, Multhaup G, McDonald BL, Beyreuther K. Amyloid plaque core protein in Alzheimer disease and Down syndrome. *Proc Natl Acad Sci U S A* 1985, 82: 4245–4249.
3. Selkoe DJ, Hardy J. The amyloid hypothesis of Alzheimer's disease at 25 years. *EMBO Mol Med* 2016, 8: 595–608.
4. Panza F, Lozupone M, Logroscino G, Imbimbo BP. A critical appraisal of amyloid-beta-targeting therapies for Alzheimer disease. *Nat Rev Neurol* 2019, 15: 73–88.
5. Egan MF, Kost J, Voss T, Mukai Y, Aisen PS, Cummings JL, *et al.* Randomized trial of verubecestat for prodromal Alzheimer's disease. *N Engl J Med* 2019, 380: 1408–1420.
6. Henley D, Raghavan N, Sperling R, Aisen P, Raman R, Romano G. Preliminary results of a trial of atabecestat in preclinical Alzheimer's disease. *N Engl J Med* 2019, 380: 1483–1485.
7. Willem M, Garratt AN, Novak B, Citron M, Kaufmann S, Rittger A, *et al.* Control of peripheral nerve myelination by the beta-secretase BACE1. *Science* 2006, 314: 664–666.
8. Willem M, Tahirovic S, Busche MA, Ovsepian SV, Chafai M, Kootar S, *et al.* eta-Secretase processing of APP inhibits neuronal activity in the hippocampus. *Nature* 2015, 526: 443–447.
9. Roberts BR, Lind M, Wagen AZ, Rembach A, Frugier T, Li QX, *et al.* Biochemically-defined pools of amyloid-beta in sporadic Alzheimer's disease: correlation with amyloid PET. *Brain* 2017, 140: 1486–1498.
10. Selkoe DJ. Alzheimer's disease: genes, proteins, and therapy. *Physiol Rev* 2001, 81: 741–766.
11. Jonsson T, Atwal JK, Steinberg S, Snaedal J, Jonsson PV, Bjornsson S, *et al.* A mutation in APP protects against Alzheimer's disease and age-related cognitive decline. *Nature* 2012, 488: 96–99.
12. McDade E, Wang G, Gordon BA, Hassenstab J, Benzinger TLS, Buckles V, *et al.* Longitudinal cognitive and biomarker changes in dominantly inherited Alzheimer disease. *Neurology* 2018, 91: e1295–e1306.
13. Bu XL, Jiao SS, Lian Y, Wang YJ. Perspectives on the tertiary prevention strategy for Alzheimer's disease. *Curr Alzheimer Res* 2016, 13: 307–316.



NEUROSCIENCE BULLETIN

Impact Factor

4.246

Q2

2018 Journal Citation Report
(Clarivate Analytics, 2019)

NEUROSCIENCE BULLETIN 神经科学通报 (Monthly)

Vol. 36 No. 2 February 15, 2020

Sponsored by: Shanghai Institutes for Biological Sciences, Chinese Academy of Sciences
Chinese Neuroscience Society
Second Military Medical University

Editors-in-Chief: Shumin Duan, Ru-Rong Ji

Edited by: Editorial Board of *Neuroscience Bulletin*

319 Yueyang Road, Building 31 B, Room 405, Shanghai 200031, China

Phone: +86-21-54922863; Fax: +86-21-54922833

E-mail: nsb@sibs.ac.cn; <http://www.neurosci.cn>

Editors: Bin Wei, Xu Jiang, Zhi-Rui Liu

Published by: Shanghai Institutes for Biological Sciences, Chinese Academy of Sciences (320 Yueyang Road, Shanghai)

Printed by: Shanghai Shengtong Times Printing Co., Ltd (A6, No. 2888, Caolang Highway, Jinshan District, Shanghai)

Overseas Distributed by: Springer Nature

Home Distributed by: Local Post Offices

ISSN 1673-7067

CN 31-1975/R

Post Office Code Number: 4-608

Permit of Ad. Number: 3100420130051

Price: ¥ 100.00

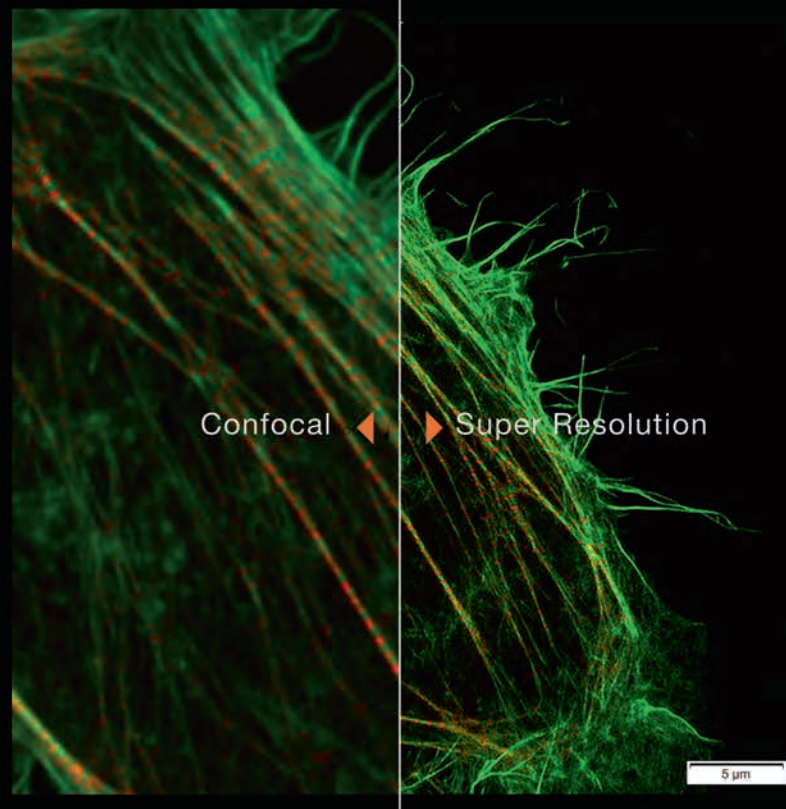
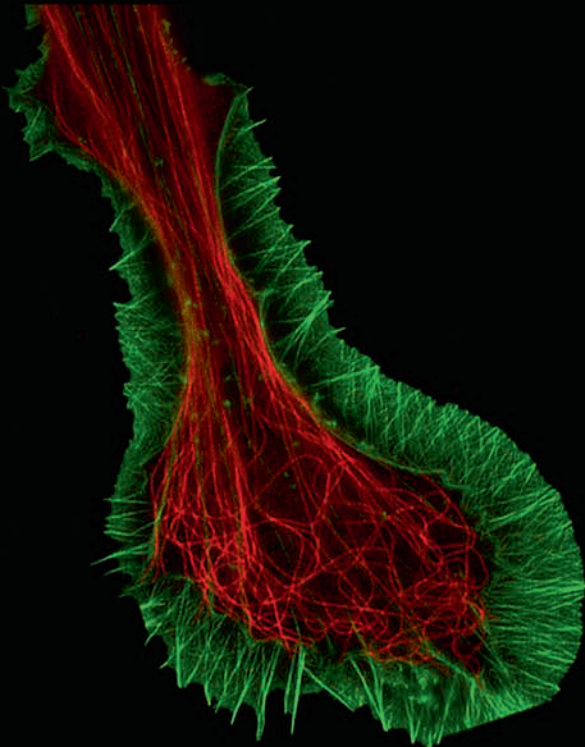
ISSN 1673-7067



9 771673 706209

兼顾分辨率和速度的

转盘共聚焦活细胞超分辨系统 **SpinSR10**



- 分辨率高达110nm的实时超分辨率成像
- 专有反卷积算法进一步提升图像质量
- 宽视野成像，速度高达 200fps
- 特色硅油物镜可以实现活细胞深层成像
- 宽场、共聚焦、超分辨率模式自由切换
- 功能强大的智能cellSens软件平台



奥林巴斯（北京）销售服务有限公司

北京朝阳区酒仙桥路10号恒通商务园B12C座2F (北京) 010-59756006
 上海市徐汇区淮海中路1010号嘉华中心11楼 (上海) 021-51582084
 广州市环市东路403号广州电子大厦16楼 (广州) 020-61227171

陕西省西安市新城区尚德路85号太平洋保险大厦8F

湖北省武汉市江岸区中山大道1628号武汉天地企业中心5号7楼701单元
 四川省成都市人民南路四段三号来福士广场T1-11楼
 辽宁省沈阳市沈河区友好街10号新地中心1号楼3501室

(西安) 029-87206108

(武汉) 027-82718838

(成都) 028-86703700

(沈阳) 024-23342084